Universitat Autònoma de Barcelona

Multifunctional nanostructured superconductors by chemical routes: towards high current conductors

Pablo Cayado Llosa

Multifunctional nanostructured superconductors by chemical routes: towards high current conductors

Dissertation presented in candidacy for the degree of

DOCTORATE OF PHILOSOPHY IN MATERIALS SCIENCE

by

Pablo Cayado Llosa

Supervisors: PROF. XAVIER OBRADORS BERENGUER AND DR. MARIONA COLL BAU
Tutor: PROF. JORDI SORT VIÑAS

Physics Department, Sciences Faculty
PhD program in Materials Science
Autonomous University of Barcelona (UAB)

Superconducting Materials and Large Scale Nanostructures
Materials Science Institute of Barcelona (ICMAB-CSIC)

January 2016

Universitat Autònoma de Barcelona

Prof. Xavier Obradors Berenguer, full professor of the Superconducting Materials and Large Scale Nanostructures of the Materials Sciences Institute of Barcelona (ICMAB-CSIC); **Dr. Mariona Coll Bau**, Ramon y Cajal Scientist of the Superconducting Materials and Large Scale Nanostructures of the Materials Sciences Institute of Barcelona (ICMAB-CSIC) and **Prof. Jordi Sort Viñas**, full professor of the Physics Department of the Autonomous University of Barcelona (UAB),

Certify

That the dissertation **Multifunctional nanostructured superconductors by chemical routes: towards high current conductors** submitted by Mr. Pablo Cayado Llosa to the Sciences Faculty in fulfillment of the requirements for the degree of Doctor of Philosophy in the Materials Science program has been performed under their supervision.

Prof. Xavier Obradors Berenguer	**Dr. Mariona Coll Bau**	**Prof. Jordi Sort Viñas**
Department of Superconducting Materials and Large Scale Nanostructures	*Department of Superconducting Materials and Large Scale Nanostructures*	*Physics Department*
Materials Sciences Institute of Barcelona (ICMAB-CSIC)	*Materials Sciences Institute of Barcelona (ICMAB-CSIC)*	*Autonomous University of Barcelona (UAB),*

Bellaterra, Barcelona (Spain). January, 2016

ACKNOWLEDGEMENTS

I would like to thank the people and institutions that have made this thesis possible.

In the first place, I would like to express my deep gratitude to Prof. Xavier Obradors and Prof. Teresa Puig for giving me the opportunity to come to Materials Science Institute of Barcelona (ICMAB) and for the confidence put in me to be part of the Superconducting Materials and Large Scale Nanostructures group.

Very special acknowledgments to my supervisors Prof. Xavier Obradors and Dr. Mariona Coll for their continuous support, collaboration and patient day by day. Their valuable guidance and advises have been essential to carry out this PhD thesis. Also, I would like make this acknowledgment extensive to Prof. Teresa Puig for the helpful discussions and knowledge shared.

I would like to thank the Spanish Government, the Generalitat de Catalunya and the European Union for the financial support with the research projects: Consolider NANOSELECT (CSD 2007-00041), SENY (MAT 2011-28874-C02-01), Pla de Recerca (2009-SGR-770) and European development of Superconducting Tapes (EUROTAPES, FP7-NMP-Large-2011-280432).

This work would have not been possible without the collaboration and interaction with a good number of scientific experts in various fields. So, I would like to say thanks:

To the members of "Inorganic nanoparticles and functional ligands" group at Autonomous University of Barcelona (UAB), particularly to Mrs. A. Garzón, and the members of "Sol-Gel Centre for Research on Inorganic Powders and Thin Films Synthesis (SCRiPTS)" at the Ghent University (UG), especially to Dr. K. De Keukeleere and Mr J. De Roo, for the NPs colloidal solutions supply and for everything that I have learned from them about chemistry and NPs synthesis.

To Dr. S. Ricart, for all her help and wise advises about all kind of chemical and NPs issues and for having always her office door opened when I needed.

To Dr. E. Bartolomé, for all the time invested in the research of the magnetic behavior of the NPs and for teaching me the basis of XMCD. Thank you very much also for count on me to perform the synchrotron measurements at ALBA.

To the transport measurements team of SUMAN group at ICMAB, Dr. A. Palau, Dr. V. Rouco and, most especially, Mr. F. Vallès, for the transport measurements and all the information provided that was vital for reaching some conclusions of this work.

To the TEM measurements team of the SUMAN group at ICMAB, Dr. J. Gázquez and, particularly, Mr. B. Mundet for TEM images employed in this thesis and the collaboration in the analysis of the results and image processing. Also, to Mr. A. Meledin from "Electron Microscopy for Materials Science (EMAT)" at Antwerp (Belgium) for the TEM images and EDAX maps of some of the films shown in this work.

To Mr. V. Rodríguez, Mr. X. Palmer and, especially, Dr. C.Pop for the support with the chemical solutions preparation and characterization. Thank you Mr. V. Rodríguez for guide me in the lab work in the first months.

To Dr. C. F. Sánchez-Valdés for teaching me all the tricks about the in-situ resistance measurements.

To the rest of the senior staff of the SUMAN group, Dr. X. Granados and Dr. N. Mestres, for the interesting conversations and wisdom advise they have given me about many issues.

Particular thanks must be given to all those who provided indispensable technical assistance at ICMAB-CSIC scientific-technical services. To Mr. A. Gómez and Mrs. M. Simón for the AFM measurements. To Dr. B. Bozzo for the SQUID measurements and the interesting discussions about the results and the training to know how to operate with the SQUID. To Dr. A. E. Carrillo and Mrs. J. Oró for the SEM images and the training to became an independent user of the SEM. To the Nanoquim clean room staff, Dr. N. Romà, Dr. E. León and Mr. E. Irisarri, for helping me with the different techniques employed during my thesis. To the members of the X-ray diffraction lab Mrs. A. Crespi, Mr. J. Esquius and Mr. F. J. Campos for their effort performing XRD measurements. Special thanks go to Mrs. A. Crespi for her motivation and efficiency performing 2D XRD measurements and for her dedication in teaching me all the basis of XRD.

To the administration personnel of ICMAB for their help with the bureaucratic issues.

To all the rest present and past members of the SUMAN group at ICMAB Mr. J.C. González, Dr. R. Ortega, Dr. M. de la Mata, Dr. A. Genç, Dr. M. Tristany, Dr. R. Guzman, Dr. R. Zamani, Mrs. P. Garcés, Mrs. S. de Arriba, Mrs. L. Soler, Mr. B. Villarejo, Mr. A. Stangl, Mr. J. Sintas, Mr. R. Ortigosa, Mrs. M. de Palau, Mrs. P. Álvarez and Mrs. C. Fu for their valuable help but also for their friendship during this time. I want to pay a special tribute to all my officemates Dr. R. Vlad, Mr. R. Ayala, Dr. M. Vilardell, Dr. A. Queraltó, Mr. Z. Li and Mrs. J. Jareño for their energy, promoting a good climate of work.

To my family, especially to my parents, for their help and support in every moment.

ABSTRACT

One of the hot topics in the field of superconductivity is the $YBa_2Cu_3O_{6+\delta}$ (YBCO) Coated Conductors (CCs) fabrication due to the excellent superconducting properties and promising application prospects. However, in order to spread worldwide the use of YBCO coated conductors, a low cost fabrication is required. Chemical Solution Deposition has emerged as a promising alternative that can accomplish this requirement.

Despite that YBCO CCs can satisfy the requirements in many different applications, the fact is that there are other uses that are out of it reach with its current status, especially those power applications in which high magnetic fields are applied. The vortex movement which takes place at such high magnetic fields makes YBCO CCs useless for these particular applications.

The aim of this work is to improve the properties of YBCO satisfying the demands of these power applications. For this, we studied, mainly, two different strategies: nanostructuration of the original YBCO matrix by adding NPs (superconducting nanocomposites) and optimization of the YBCO oxygenation process to enhance as much as possible the critical temperature and critical current density.

The preparation of YBCO nanocomposites was done following two different "Sequential deposition and growth" approaches: the in-situ approach in which the NPs are spontaneously segregated during the growth process; and the ex-situ approach, a new methodology developed in this thesis in which the NPs are firstly synthesized in a colloidal solution and then embedded in the YBCO matrix.

Using the in-situ approach we have made an extensive study of how different NPs ($BaZrO_3$, Y_2O_3, Ba_2YTaO_6 and mixtures of these) affect the microstructure of the YBCO creating defects that increase the pinning properties. We have also studied the influence of these defects, in particular, the stacking faults (double chains of Cu-O), on the final properties of the YBCO and GdBCO nanocomposites.

With the ex-situ approach we have started by synthesizing different colloidal solutions of both magnetic ($CoFe_2O_4$) and non-magnetic (CeO_2 and ZrO_2) NPs. The stability of YBCO+NPs solutions was checked using TEM and DLS analyses to ensure that the NPs are maintaining the initial size without forming agglomerates. The pyrolysis process was optimized for each type of NPs. We realized that the stabilization agents can critically influence the homogeneity of the pyrolyzed films. Finally, the growth process was also optimized for each type of NPs trying to solve different difficulties that appeared: coarsening, pushing or reactivity.

The study of the oxygen diffusion process in YBCO thin films was done using in-situ resistivity measurements that allow to monitor the evolution of the resistance in the thin films in different annealing conditions. We have studied how the temperature, the gas flow and the oxygen partial pressure affect the diffusion process. According to our results, we can conclude that the surface reactions that take place before the oxygen bulk diffusion is the limiting factor for the oxygen diffusion. The effect of the silver addition to the YBCO as oxygen catalyst was also tested. Finally, the first study about the oxygen diffusion process in nanocomposite films gave an idea of how the oxygen diffusion works in this kind of materials.

RESUMEN

Uno de los temas de mayor interés en el ámbito de la superconductividad es la fabricación de cintas superconductoras (CCs) de $YBa_2Cu_3O_{6+\delta}$ (YBCO) debido a las excelentes propiedades superconductoras que poseen y a las prometedoras perspectivas en cuanto a aplicaciones se refiere. Sin embargo, para poder generalizar el uso de dichas CCs, se requiere de un proceso de fabricación de bajo coste. En este contexto, la técnica de deposición por solución química se presenta como una alternativa muy prometedora.

Las CCs pueden cumplir los requisitos actuales exigidos en diferentes aplicaciones, pero hay otras que están fuera de sus capacidades, especialmente aquellas relacionadas con aplicaciones de potencia en las que están presentes campos magnéticos de gran intensidad. El movimiento de los vórtices que tienes lugar en presencia de tales campos magnéticos hace que el YBCO sea poco efectivo en estos casos.

El objetivo de este trabajo es mejorar las propiedades del YBCO de manera que se puedan satisfacer los requerimientos de estas aplicaciones de potencia. Para ello, hemos estudiado, principalmente, dos estrategias: la nanoestructuración de la matriz del YBCO añadiendo nanopartículas (NPs) obteniendo nanocomposites superconductores y la optimización del proceso de oxigenación del YBCO para conseguir aumentar todo lo posible la temperatura crítica y la densidad de corriente crítica.

La preparación de los nanocomposites de YBCO se llevó a cabo siguiendo dos métodos diferentes de "deposición y crecimiento secuencial": el método "in-situ" en el que las NPs se forman de manera espontánea durante el proceso de crecimiento, y el método "ex-situ", que es un novedoso procedimiento desarrollado durante esta tesis en el cual las NPs se sintetizan primeramente formando una solución coloidal para luego quedar atrapadas en la matriz del YBCO durante los procesos térmicos.

El uso del método "in-situ" se ha enfocado al estudio de como diferentes NPs ($BaZrO_3$, Y_2O_3, Ba_2YTaO_6 and mezclas de éstas) afectan la microestructura del YBCO creando defectos cristalinos que incrementan la fuerza de anclaje. Hemos estudiado también la influencia de estos defectos, en particular, de las dobles cadenas Cu-O, en las propiedades finales de los nanocomposites de YBCO y GdBCO.

En el caso del método "ex-situ", el primer paso fue sintetizar diferentes soluciones coloidales de NPs magnéticas ($MnFe_2O_4$ and $CoFe_2O_4$) y no magnéticas (CeO_2 and ZrO_2). Se comprobó la estabilidad de las soluciones YBCO+NPs mediante medidas de DLS y de TEM para asegurar que las NPs conservaban su tamaño inicial sin formar aglomerados. El proceso de pirólisis fue optimizado para cada tipo de NPs teniendo en cuenta que los ligandos usados para estabilizar las NPs pueden influenciar de manera drástica la homogeneidad de las capas pirolizadas. Por último, el proceso de crecimiento fue también investigado para cada tipo de NPs.

El estudio del proceso de oxigenación en la capas de YBCO se llevó a cabo usando medidas de resistencia "in-situ", que permiten monitorizar la evolución de la resistencia en las capas durante los distintos procesos térmicos. Hemos estudiado como la temperatura, el flujo de gas y la presión parcial de oxigeno afectaba al proceso de difusión. De acuerdo con nuestros resultados, las reacciones que tienen lugar en la superficie de la capa antes de que en oxígeno se difunda en el interior de la misma, son el factor que limita la cinética del proceso de oxigenación. Por último El efecto de la adición de plata como catalizador y la difusión en nanocomposites también se ha estudiado.

CONTENTS

MOTIVATION

Functional oxides are nowadays a hot topic in materials science and other disciplines such as physics, chemistry or engineering. The wide range of applications such as ionic and electronic conductivity, thermoelectricity, magnetoresistance, ferroelectricity or superconductivity makes them very attractive for research and also for industrial purposes.

Superconductivity is a particular functionality of some of these functional oxides. The main property of superconductors, which is the absence of electrical resistance below a certain temperature, makes them aspirants to the efficiency and capacity of electrical grid and other devices such as transformers, fault current limiters or generators.

REBCO (Rare-Earth Barium Copper Oxides) materials highlight among the superconductors, especially $YBa_2Cu_3O_{7-\delta}$ (YBCO) thanks to its excellent properties. Since its discovery in 1987 the research about its optimization in terms of crystallographic and physical properties and the search for new applications has not stopped growing. However, nowadays the use of YBCO as a candidate to substitute the conventional copper devices is far away due to two main issues: the performances and the cost.

Despite the advances during last years, there is still much work to do in order to achieve the optimal performances of YBCO. The use of YBCO in superconducting tapes requires excellent texture over the crystalline substrate (or buffer layers) which is tough labor. Also the performance of YBCO necessitates an improvement if it will be use in some applications such as generators, transformers or others in which high magnetic fields are applied.

Nowadays, most of commercial YBCO tapes are manufactured using vacuum techniques (in-situ techniques) especially PLD (Pulsed Laser Deposition). However, these methods imply a large investment in machinery and high cost of operation, since ultra-high vacuum is necessary, which makes the YBCO uncompetitive in cost with traditional copper wires.

More recently, CSD (Chemical Solution Deposition) it has been developed as a new method to prepare thin films of functional oxides and, in particular, of YBCO. This seems to be an attractive alternative to in-situ techniques since the cost of the manufactured tapes is drastically reduced maintaining excellent performances. CSD is a versatile and cost-effective method based on the use of an organometalic chemical solution which is deposited over a substrate and then subjected to different thermal treatments to finally obtain the YBCO. The use of chemical solutions, which can be synthesized in large quantities employing inexpensive raw materials, and the fact that it is not necessary the use of vacuum, makes this technique an adequate alternative to manufacture YBCO tapes that can compete in cost/performance ratio with copper wires.

The improvement of the YBCO tapes performances produced by CSD is a challenge for the coming years. This is a complicated issue and several alternatives are being studied. One option is to focusing on the YBCO processing parameters and tuning them to obtain the optimal YBCO properties. Another via, which is probably the most important nowadays, is the nanostructuration of the YBCO by introducing artificial defects in its matrix. The last choice is to change the rare-earth ion, in the case of YBCO the Y^{3+} ion, for a different one, for example Sm^{+3} or Gd^{3+}, since some of these alternative REBCO materials in some cases show improved properties as compared to YBCO.

The present work, performed in the framework of the "European Development of Superconducting Tapes (EUROTAPES)" project, one of the biggest ever funded in Europe about superconductivity, explores each of these alternatives in search for improved properties as compared to standard YBCO prepared by CSD. The nanostructuration of YBCO and GdBCO via has been also investigated in this work using two different approaches: in-situ and ex-situ. Each approach shows different characteristics and both of have been explored to reach a comprehension of all the involved phenomena. Finally, it has been performed a thorough investigation of a critical step in YBCO films processing: the oxygenation step.

1
Introduction

Functional oxides have attracted the attention of researchers from many different disciplines such as physics, chemistry, material science or even engineering due to their wide range of applications. Some of the functionalities most exploited are thermoelectricity, magnetoresistance, ferroelectricity and superconductivity.

Two main structural properties characterize functional oxides: cations with mixed valence state and anions with vacancies[1]. These properties make functional oxides the base for smart and functional devices. By varying one or both of these characteristics, the magnetic[2], optical[3], electrical[4, 5] or chemical properties can be tuned.

Most of the applications of the functional oxides involve the preparation of epitaxial thin films to achieve the optimal performances[6]. Therefore, the comprehension of how epitaxial growth is carried out over the substrate is mandatory prior to focusing on the optimization of the device.

Nowadays, most of the effort is devoted in the nanostructuration of these oxides in order to generate new or improved functionalities[7-9]. A nanostructure is a system in which at least one dimension is smaller or equal to 100 nm[10]. At this scale, quantum effects of different physical processes starts to occur as the size of the objects are comparable with the critical lengths of these processes (typically 1-10 nm).

Cuprates and, in particular REBCO compounds, are a particular case of functional oxides. Their properties offer the possibility to satisfy the increase of energy demand. The efficiency and capacity of electrical grid can be drastically improved by using superconductor wires and other superconductor devices such as transformers, fault current limiters or generators[11].

In particular, $YBa_2Cu_3O_{6+\delta}$ (YBCO) has attracted the attention of researchers since its discovery in 1987[12]. Its features make it a good candidate to fabricate wires and devices. It is also the base material for many studies of superconducting nanocomposites which show a large improvement of performances at high magnetic fields[13-15].

1.1 Superconductivity

Collins dictionary defines superconductivity as "the property of certain substances that have no electrical resistance", and certainly this definition summarizes properly the nature the phenomenon. Superconductors have other interesting properties but, the absence of electrical resistance below a certain temperature is, without doubt, their grand peculiarity.

1.1.1 Historical remarks

The discovery of superconductivity was one of the many events in science that seem to appear by chance. But nothing could be further from the truth. This phenomenon was first observed at exactly the right time since some preconditions were accomplished. Actually, the discovery of superconductivity is a consequence of the earlier achievement of helium liquefaction in 1908[16].

It was in 1911 when Heike Kamerlingh Onnes, who was studying the electrical conductivity of metals at temperatures approaching the absolute zero (taken advantage of liquid helium), realized that a sudden drop in the resistance of pure mercury took place at a temperature near 4 K. He had discovered the superconductivity[17].

During the first years of superconductivity, many researchers manifested interest in the new phenomenon but, apart from increasing the list of elements that exhibit superconductivity, no relevant advances were recorded. However, in 1933, Meissner and Ochsenfeld showed that in magnetic fields lower than a certain value the flux inside a superconductor was expelled[18]. This effect, called Meissner effect, is another important property of superconductivity. It demonstrates that a superconductor is not only a perfect conductor, but it defines a new thermodynamic state. Two years later, in 1935, Fritz and Heinz London proposed the London equations which relate current to electromagnetic fields in and around a superconductor. The major ability of these equations is to explain the Meissner effect[19]. In the same year, Rjabinin and Shubnikov experimentally discovered the Type-II superconductors[20].

The year 1957 has a great relevance in the history of superconductivity. The studies of Abrikosov about the magnetic properties of superconductors came to light[21, 22]. But the most remarkable event is the publication of BCS theory by Bardeen, Cooper and Schrieffer[23]. It was the first microscopic theory in superconductivity. It explains the superconductivity as an effect caused by the condensation of Cooper pairs (a pair of electrons bound together at low temperatures) into a boson-like state. This theory describes the behavior of type-I superconductors but can not explain the behavior of type-II superconductors.

Two years later, in 1959, Gor´kov could bind the Ginzburg-Landau theory[24], which is a phenomenological model published in 1950 that describes type-I superconductors

without taking into account the microscopic properties, with the BCS theory showing that the experiments and theory had a real link[25].

The 60s and 70s are marked by the discovery of Josephson effect in 1962[26], which opened the window for multiple applications of superconductor devices. However, it was in the 80s when the way in which scientist valued the superconductivity would change due to the discovery of High-Temperature Superconductors (HTS). In 1986, Bednorz and Müller published their work about a new class of ceramics for superconductivity, the cuprates, in which the transition from superconductor to normal state took place at 35 K[27]. This discovery started the race towards new applications for superconductors with excellent economic prospects. Many works were published in the following years in this topic. One of these works was the discovery of one of the most known and used superconductors nowadays, the $YBa_2Cu_3O_{6+\delta}$ (YBCO) reported by Wu in 1987[12].

In recent years, specifically in 2006, a new class of superconductors called Iron-Based Superconductors (FeSC) was discovered[28].

1.1.2 The phenomenon of superconductivity

The absence of resistance below a certain temperature in superconductors took several years to be explained microscopically. During more than 40 years only phenomenological explanations were reported. It was the BCS theory in 1957 which gave the first explanation to this phenomenon in the microscale[23].

This theory evidences that, below the critical temperature, the charge carriers in the superconductor bound together forming Cooper pairs. Cooper pairs are possible due to the weak interaction between electrons which is mediated by the phonons of the lattice (electron-phonon-electron interaction). Cooper pairs are coupled together, i.e., they are all in the same state, due to the formation of bosons (two fermions constitute a boson) which aggregates forming a Bose-Einstein condensate. The formation of Cooper pairs gives the system superfluid properties and, therefore, their movement is coherent and does not dissipate energy.

The wavefunction that describes the movement of the Cooper pairs is called ψ. This wavefunction changes in the proximity of a normal region (not superconducting region) in a distance given by the coherent length, ξ.

This theory gives a satisfactory explanation for many superconductors, called conventional superconductors. However, it can not explain the properties and the behavior of High Temperature Superconductors (HTS). There are several theories that try to explain this behavior. One example is the theory that affirms that the superconductivity in HTS comes from antiferromagnetic-spin fluctuations[29]. Another example is the interlayer coupling model, that explain the superconductivity in HTS considering that a layered structure consisted of BCS-type superconductors can enhance the superconductivity by itself[30]. However, these theories can not satisfactory explain the experimental phenomena in this kind of superconductors. This is still an open issue in the superconducting field.

1.1.3 Properties of superconductors

As it was mentioned previously, the cardinal feature of superconductors is the absence of resistance below the critical temperature (T_c). This behavior is not observed in normal metals (figure 1.1).

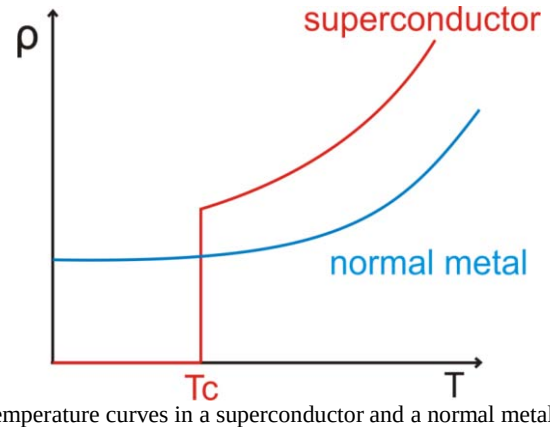

Figure 1.1. Resistivity vs. Temperature curves in a superconductor and a normal metal. It is observed that while for normal metals the resistivity decrease smoothly until zero, in the superconductor the resistivity becomes zero below T_c.

Apart from this, there are other properties that also define the superconductors. Among of them, probably, the most important one is the Meissner effect, discovered in 1933 by Meissner and Ochsenfeld[18].

This effect is based on the fact that when a magnetic field is applied to a superconductor in normal state and this is cooled below its T_c, the magnetic field is expelled from its interior, obtaining zero magnetic field inside the superconductor. This means that the superconductors behave as perfect diamagnetic (χ=-1) material below its T_c. On the other hand, if the magnetic field is applied when the superconductor is below its T_c, magnetic field can not penetrate inside the superconductor. The superconductor maintains the zero magnetic field inside it. This effect was the first evidence that showed that superconductors are not just perfect conductors. In a perfect conductor when a magnetic field is applied and then the temperature is decreased, the magnetic field is not expelled but it remains inside even when the magnetic field is removed to enforce the laws of classical electromagnetic theory (Faraday and Lenz´s laws).

In the case of superconductors in Meissner state, it is said that the magnetic field can not penetrate inside. But this is not completely correct. There is a tiny superficial region in which the magnetic field penetrates. The length of this penetration is given by the London equation (Eq 1-1)[19]:

$$\nabla^2 \mathbf{B} = \frac{1}{\lambda_L^2}\mathbf{B} \qquad \text{Eq. 1-1}$$

where $\lambda_L^2 = \left(\frac{m}{\mu_0 n e^2}\right)^{1/2}$ (for m= mass of charge carriers , μ_0= vacuum permeability, n= number density and e= charge)

Additionally, there are other two fundamental properties of superconductors: the isotope effect[31, 32], which establish a dependence of the T_c with the isotopic mass, and the energy bandgap[33], which described the abrupt discontinuity of the specific heat of a superconductor exhibited at T_c that suggests the existence of a gap in the energy.

1.1.4 Types of superconductors

The classification of superconductors is done according to two different criteria: the value of the T_c or the physical behavior that they have.

-Critical temperature

The values of the T_c allow the distintion between:

- *Low Temperature Superconductors (LTS)*. The value of T_c is below 20 K. Pure metals and metal alloys are in this group.
- *High Temperature Superconductors (HTS)*. The value of T_c is above 20 K. Usually the HTS are also known as cuprates or copper-based superconductors because, except for a few compounds (for example MgB_2 and Fe-based superconductors), all of them are formed by layers and planes of Cu-O which play a key role in the superconducting phenomenon.

-Physical behavior

The behavior of superconductors under magnetic fields allows their separation in two big groups:

- *Type I superconductors*. The magnetic field is expelled from the inside of the superconductor below T_c or below the critical field, H_c (maximum magnetic field that the superconductor admits before breaking the superconductivity). In this situation, the superconductor is in Meissner state. Above T_c (or H_c) the magnetic field can penetrate inside the superconductor changing from superconducting state to normal state (figure 1.2). Most of the pure metals that are superconductors at low temperatures are in this group.

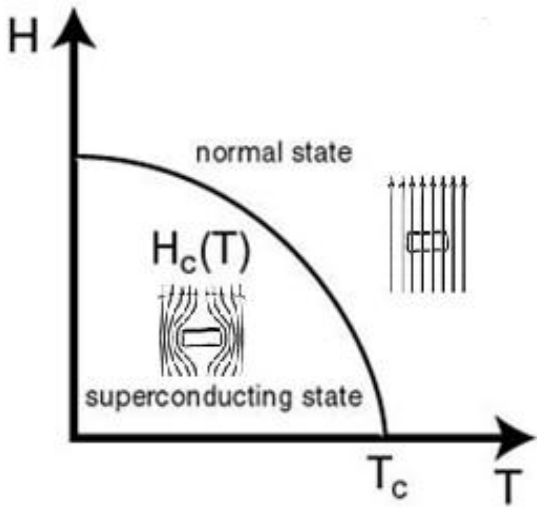

Figure 1.2. Magnetic field as a function of temperature in Type I superconductors. Two different states are identified: the Meissner state (superconducting state) and the normal state

- *Type II superconductors*. The behavior of this type of superconductors are the same as in the case of Type I at low temperatures (Meissner state, magnetic field is expelled from inside of superconductor) and in the normal state (magnetic field can penetrate inside the superconductor). The main difference, in this case, is that the magnetic field can penetrate inside the superconductor even below T_c without losing its superconducting state. These are the conditions that define the mixed state, a new region in the H-T diagram for Type II superconductors (figure 1.3). So,

in Type II superconductors, the lower critical field, H_{c_1}, define the transition to Meissner state to mixed state and the upper critical field, H_{c_2}, is defined as the magnetic field in which the transition from mixed state to normal state takes place (figure 1.3). In the mixed state (between H_{c_1} and H_{c_2}) the magnetic flux penetrates the material in a regular triangular or square array of flux tubes, called vortices, each one carrying a quantum of flux defined by: $\Phi_0=hc/2e=2{,}07.10^{-7}$ G.cm^2.

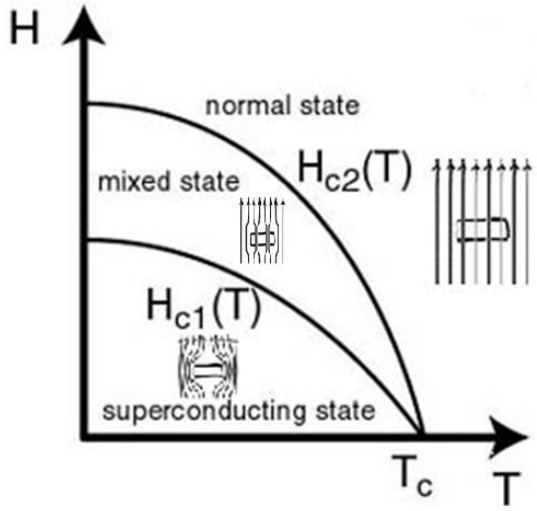

Figure 1.3. Magnetic field as a function of temperature in Type II superconductors. In this case, a new state appears with respect to the Type I superconductors: the mixed state which is situated in the middle of the Meissner state (superconducting state) and the normal state.

The value of κ is defined by the ratio of the London penetration depth λ (Ec. 1-4) to the superconducting coherence length ξ. It determines whether a superconductor is type-I or type-II. Type I are defined by $\kappa<1/\sqrt{2}$ and Type II by $\kappa>1/\sqrt{2}$.

1.1.5 Mixed state in Type II superconductors

The main feature that differentiates the Type I and Type II superconductors is that in Type II superconductors the magnetic field can penetrate inside the superconductor without losing the superconducting state. This new state is called the mixed state. Apart from the Meissner state, Type II superconductors can stay in the mixed state maintaining the superconducting properties.

The penetration of the magnetic field in the mixed state is through a network of vortices each one including a single quantum of flux[22]. Therefore, each vortex is called fluxon (figure 1.4)[34]. Mathematically, a vortex, in a neutral or charged superfluid, is a line-like topological defect in the order parameter phase. In the case of superconductors, a vortex is a normal region (non-superconducting region) surrounded by a supercurrent that circulates around the core of the vortex. They arrange defining an array due to the repulsive force between each other, behaving as if they were solenoids. In this array of vortices, the distance between each other is given by the lattice parameter of the Abrikosov vortex lattice (Eq. 1-2):

$$\mathbf{a = a_0 \sqrt{\frac{\Phi_0}{B}}} \qquad \text{Eq. 1-2}$$

where a_0= 1 for square lattice and $a_0=\sqrt[4]{4/3}$ for a hexagonal lattice (figure 1.4).

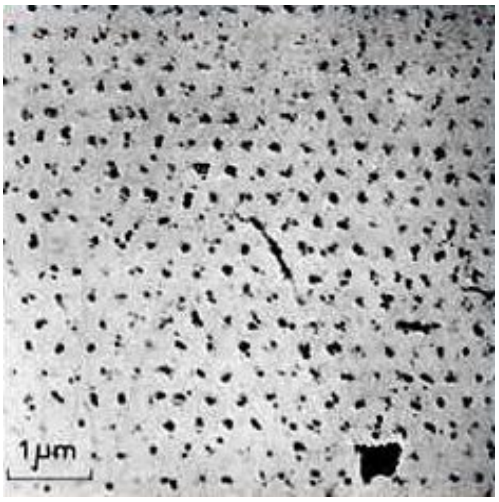

Figure 1.4. First experimental observation of the hexagonal Abrikosov lattice of vortices in a Pb-4%In rod at 1,1 K[34].

As it was referred before, the interior of the vortices is a non-superconducting region, so in that region the superconductivity is suppressed (which means that $\psi \rightarrow 0$) and the magnetic field has the maximum value (figure 1.5). The evolution of the magnetic field inside the vortices, assuming that $\kappa >> 1$ and $r > \xi$, is given by (Eq. 1-3):

$$\mathbf{B(r) = \frac{\Phi_0}{2\pi\lambda^2} K_0\left(\frac{r}{\lambda}\right)} \qquad \text{Eq. 1-3}$$

where $K_0\left(\frac{r}{\lambda}\right)$ is zero´th order Bessel function.

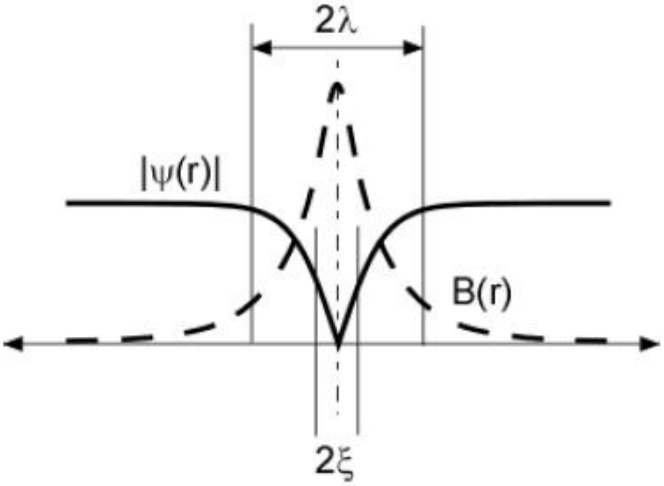

Figure 1.5. Structure of a single vortex centered in r = 0: ψ (r) and B(r) profiles, with length scales ξ and λ, respectively.

1.1.5.1 Critical current density

Understanding the physical phenomena that take place in the mixed state is crucial to comprehend the final properties of different Type II superconductors. One of the properties that is determined by these phenomena in the mixed state is the critical current, I_c, defined as the maximum current that can flows through the superconductor without losses of energy, i.e., maintaining the resistance equal to zero. In a Type II superconductor, if a current is flowing through it with an applied magnetic field, an increase of the resistance is due to the movement of vortices.

When a current is flowing through a superconductor in the mixed state while a magnetic field is applied, a driving force per unit length on each single vortex appears and tends to move them (Eq. 1-4):

$$\mathbf{f} = \mathbf{J} \times \mathbf{\Phi_0} \qquad \text{Eq. 1-4}$$

where Φ_0 is the quantum of flux and J is the current density (J=I/A where A is the area of superconductor´s cross section).

F becomes a volume force, F_L, dividing both sides by unit area (Eq. 1-5):

$$\mathbf{F_L} = \mathbf{J} \times \mathbf{B} \qquad \text{Eq. 1-5}$$

F_L in Eq. 1-5 is stated to be the Lorentz force on the vortex due to the interaction between the current density, J, and the vortex magnetic field. This force tends to move the vortices in the perpendicular direction of the current. If this force is high enough to move the vortices and they start to flow, work is done and there is energy dissipation. The consequence is that the vortex motion creates a finite resistance. The explanation for that was given by Bardeen and Stephen in 1965[35]. They considered a vortex core of radius ξ as if were in normal state. The motion of the flux lines generates an electric field in its surroundings and also in the vortex core that induce resistive currents and, therefore, a flux-flow resistivity which causes energy looses. Also, the movement of the vortex entails a transformation of Cooper pairs in electrons when the normal core touches the superconducting part, and also a transformation of electrons in Cooper pairs when the vortices left behind a region becoming again a superconducting region. In this case, the superconductor behaves essentially like a normal conducting material.

To stop or to prevent this motion, it is necessary to apply a pinning force, F_p, at least with the same value of F_L. The value of this F_p is determined by the potential wells that the vortices have to overcome to start their movement. These potential depends on the type of pinning center in which the vortices are pinned.

Considering the presence of F_p and assuming that $F_p>F_L$, the vortices are pinned and they can not move. However if $F_p<F_L$, the driving force is higher than the pinning force and the vortices start to move. The limit for non-movement of vortices is reached when $F_p=F_L$. In this case (considering only the modulus of the F_L vector) the F_p can be defined as (Eq. 1-6):

$$\mathbf{F_p} = \mathbf{F_L} \rightarrow \mathbf{F_p} = \mathbf{J_c B} \qquad \text{Eq. 1-6}$$

When the driving force density is equal to F_p the corresponding current density is defined as the critical current density, i.e., the maximum current density that can flows in

the superconductor without energy looses. According to Eq. 1-6, it is possible to define the critical current density, J_c, as (Eq. 1-7):

$$J_c = F_p/B \qquad \text{Eq. 1-7}$$

1.1.5.2 Irreversibility line

The phenomenon of flux motion in Type II superconductors does not start when the applied magnetic field is equal to H_{c_2} (figure 1.3), as one may think. The flux motion starts and, therefore, J_c becomes zero, for an applied magnetic field lower than H_{c_2}. Therefore, it is not possible to work with the maximum possible current density, J_c, in a range of applied magnetic field that would go from zero to the H_{c_2}, in which the transition to normal state would take place. This is due to the behavior of vortices in the mixed state which is not constant. The phase diagram shows two different regions: the solid phase and the liquid phase (figure 1.6)[36, 37].

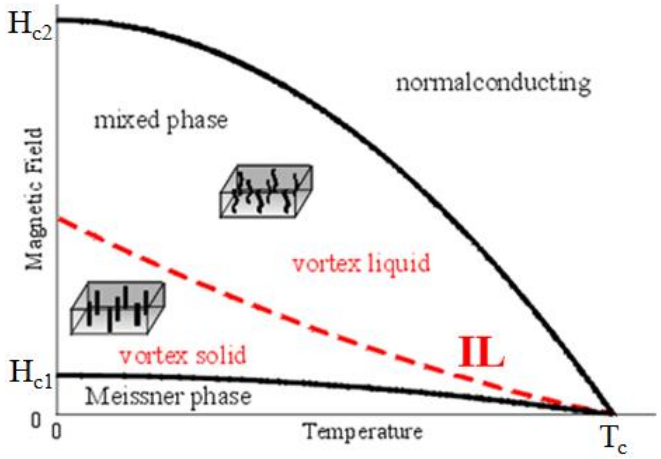

Figure 1.6. Magnetic phase diagram for Type II superconductors in which the different vortex phases can be observed.

The vortex solid phase is found at low temperatures and low magnetic fields. In this region F_p is higher than F_L and no motion of vortices is observed, so there are no looses of energy (R=0) and $J_c>0$. Vortices freeze into one of several possible solid phases, including a variety of "glasses"[36]. Vortices in this region are pinned in natural pinning centers (in the case of the pristine samples): oxygen vacancies, cation disorder, screw, edge dislocations, etc. These pinning centers are crystalline defects generated spontaneously during the film growth[38]. These defects locally change the electronic structure, reducing or cancelling the T_c. Therefore, in these small regions the Cooper pair formation is suppressed becoming normal regions embedded in the superconducting matrix. When a vortex finds one of these defects it will prefer to stay in this defect to minimize its energy (the vortex is also a normal core). If lots of vortices do the same, the total energy of the system decreases, so this phenomenon is energetically favorable. The effectiveness of this process depends on the competition between the condensation energy, which is gained by putting the core of the vortex in these normal regions, and the increase of elastic energy, which is necessary to

modify the shape of vortices in order to place them in these pinning centers. This is the basis for the collective pinning mechanism[39].

On the other hand, in the vortex liquid phase, found at higher temperatures and magnetic fields, the pinning potential wells that the vortices have when they are pinned are overcome by the thermal activation energy. This causes the melting of the solid phase to form a liquid phase describing a melting line in the H-T diagram. Therefore, in this region, the vortices can move ($F_L > F_p$) so, substantial electrical resistance is observed causing the disappearance of J_c.

Both regions in the phase diagram, the solid phase region and the liquid phase region, are separated by the irreversibility line (IL), which defines the transition from an irreversible system (solid phase) to a reversible system (liquid phase) (figure 1.6).

The IL is not the same for all the Type II superconductors[40, 41]. It depends on their different physical parameters and crystal structures. One parameter that has a great influence on the IL is the anisotropy. The higher the anisotropy is, the lower the IL than H_{c_2} (figure 1-7).

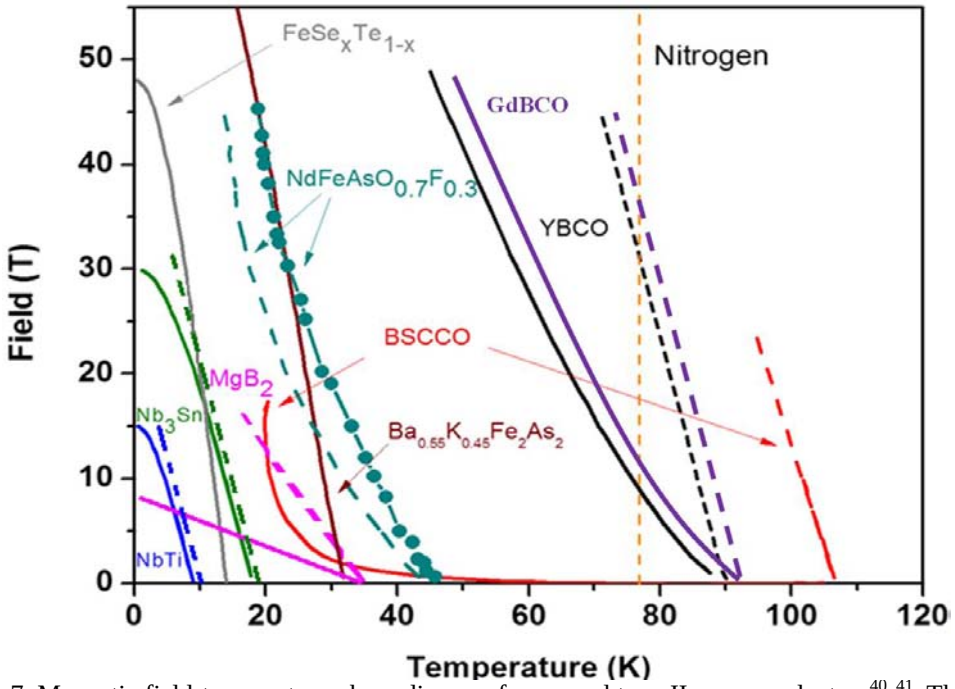

Figure 1.7. Magnetic field-temperature phase diagram for several type II superconductors[40, 41]. The upper critical field, H_{c_2}, is indicated as a dashed line, while the irreversibility line, IL, is indicated as a solid line. The IL marks the transition from vortex solid phase to vortex liquid phase.

1.1.5.3 Bean´s critical state model

The Bean´s critical-state model, introduced by C. P. Bean in 1962[42, 43], provides a phenomenological description for the hysteretic magnetization of type-II superconductors in a temporally varying external magnetic field.

The critical current density (J_c) in a superconductor depends, in general, on the position (r) and the applied magnetic field (B). However, as an approximation, Bean assumed that the J_c was constant and independent of B to construct his model that fits quite well with the experimental results obtained so far. Since the J_c is constant, the field

gradient within the sample is constant and thus, the magnetic field decreases linearly with the distance (Eq. 1-8):

$$\mathbf{J_c = \mu_0^{-1} \frac{dB}{dx} = cst \rightarrow \frac{dB}{dx} = cts} \qquad \text{Eq. 1-8}$$

Considering an infinite cylinder of diameter d, the behavior of magnetic field and J_c is shown in figure 1.8. As the magnetic field is increased (figure 1.8, a)), vortices starts to penetrate inside the superconductor from the external part with a constant field slope, J_c. In the area in which the magnetic field penetrates supercurrents appears so $J=J_c$. In the flux free regions (B=0), where no flux gradients are present, the current density is zero. When the internal field reaches the centre of the sample, the applied magnetic field is named full penetration field, B*. In these conditions the system arrives to the Bean´s critical state (situation (2) in figure 1.8, b)). For this particular value of the magnetic field, supercurrents are induced in the whole sample and J_c will be constant through the sample. Although the magnetic field continues to increase up to a maximum value B_m, the current density remains constant at the value of J_c.

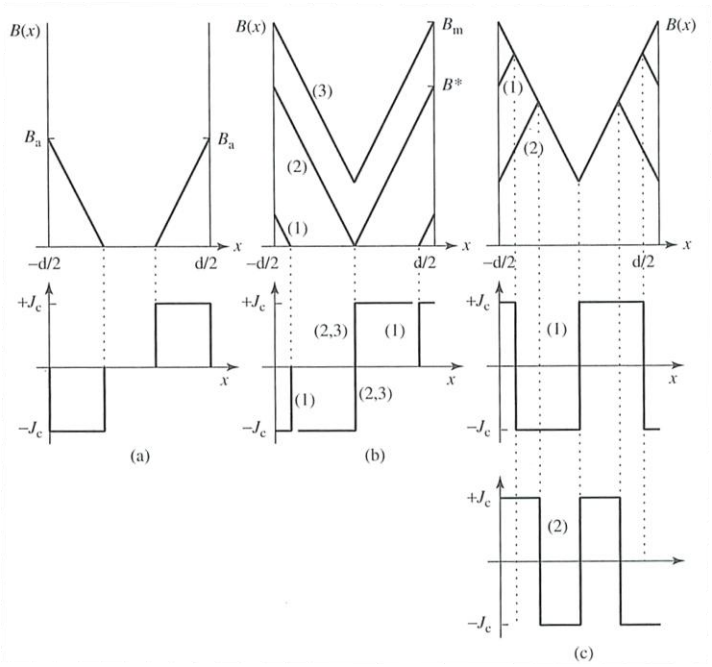

Figure 1.8. Magnetic field and J_c behavior in an infinite cylinder based on the Bean´s critical state model as the magnetic field is increased (a) and (b) and decreased (c)[44].

After reaching the maximum induced magnetic field B_m, if now the magnetic field is decreased (figure 1.8, c)), supercurrents appears circulating in the opposite direction. The currents will penetrate the sample from the external part (situations (1) and (2) in figure 1.8, c)). At this point, there is a flux trapped inside the superconductor since the internal magnetic field is higher than the applied magnetic field and there is a region in which the J becomes $-J_c$ since the supercurrents flow in the opposite direction. As the magnetic field is further decreased, the supercurrents flowing in opposite direction penetrate further inside the sample. This causes an increase of the J transformation into $-J_c$. In one moment, the supercurrents in the opposite direction will penetrate in the entire sample changing completely J into $-J_c$.

1.2 $REBa_2Cu_3O_{6+\delta}$ (REBCO) Compounds

Nowadays, the major interest in superconductivity is deposited in the HTS. Their properties, specially the high values of T_c, open the possibility to use them in technological applications at temperatures above liquid nitrogen and thus, reducing the cost of the cryogenics involved at working temperatures 65-77 K. Among them, $REBa_2Cu_3O_{6+\delta}$ (REBCO) compounds (RE=Rare Earths) have attracted the attention of scientific community due to their excellent current capabilities at high magnetic fields. REBCO compounds have a structure that can be described as a triple perovskite compound based on $BaCuO_3$ and $RECuO_2$ units. This is a highly anisotropic structure with Cu-O planes lying normal to the crystallographic c-direction (figure 1.9).

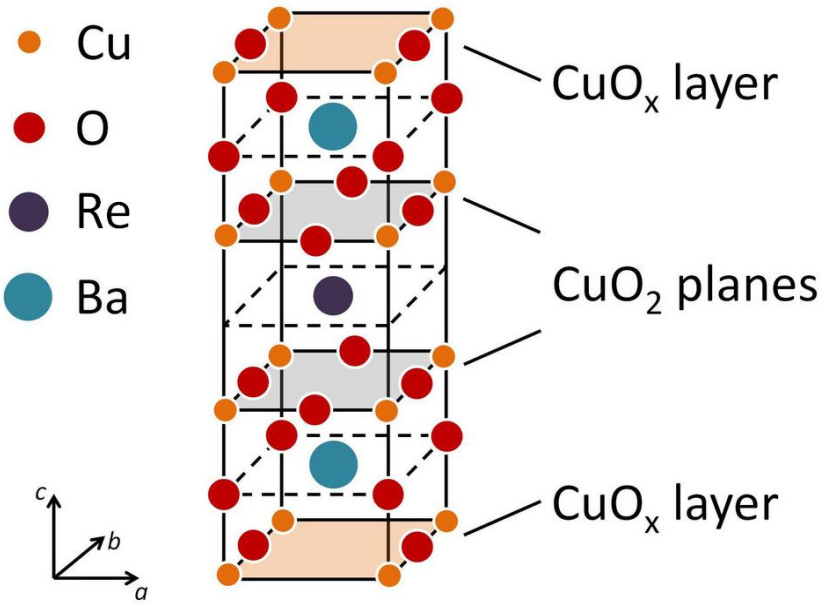

Figure 1.9. Unit cell of the orthorhombic phase of ReBCO compounds.

As it was mentioned before, this Cu-O planes and layers have a key role in the superconducting phenomenon. CuO_2 planes, formed by Cu atoms and O atoms, are parallel to a-b direction. They are called conducting planes because the transport of carriers is done in this planes. The holes in these planes somehow attract each other and form the Cooper pairs (there is still not a satisfactory explanation for this). CuO_x layers are formed by Cu atoms and O atoms. They are arranged in chains which act as charge reservoirs providing carriers to the CuO planes. This model works for the entire REBCO materials, but it can not explain the behavior of $PrBa_2Cu_3O_{6+\delta}$ which shows superconductivity even when it is assumed to be non-superconducting according to this model[45].

In the Cu-O chains the oxygen content is not fixed and, actually, the type of structure of the REBCO compounds is determined by the concentration of oxygen in these chains. They change from a tetragonal P4/mmm structure when there is no oxygen in the chains into an orthorhombic Pmmm structure when the chains are full of oxygen (figure 1.9). The transition between these two structures depends on the compound and processing conditions. This change in the oxygen content in the Cu-O chains defines the stoichiometry of the oxygen in the final REBCO compound, i.e., it defines the δ that appears in the unit

formula of these compounds. So, for δ=0 REBCO compounds have tetragonal P4/mmm structure and for δ=1 they have orthorhombic Pmmm structure.

These structural changes are crucial in REBCO compounds since they are superconducting materials only when they have the orthorhombic structure. When they have tetragonal structure, they are isolating materials. Therefore, it is essential to control the amount of oxygen present in the structure in order to ensure superconductivity properties. The process by which the oxygen goes in the YBCO structure is called oxygenation and, due to the above reasons, it is a critical process. For this reason, a whole chapter (chapter 5) of this thesis will be devoted to the study of this process.

The anisotropy of the REBCO compounds structure, due to their layered structure, is also remarkable. Since, as it was mentioned, the current flows only along the CuO_2 planes, the conductivity is confined in the a-b planes and a large anisotropy in transport properties is observed. Along the c-axis normal conductivity is much smaller than in the a-b plane (typically three orders of magnitude smaller). This anisotropy, obviously, is also observed in the vortices' structure. The coherence length (ξ) and the penetration depth (λ) depend on the magnetic field orientation relative to the crystallographic axis of the material. The anisotropy (γ) is defined in the framework of Ginzburg-Landau theory as (Eq. 1-9)[24]:

$$\gamma = \frac{\lambda_c}{\lambda_{ab}} = \frac{\xi_{ab}}{\xi_c} = \frac{H_{c_1}^{c}}{H_{c_1}^{ab}} = \frac{H_{c_2}^{ab}}{H_{c_2}^{c}} \qquad \text{Eq. 1-9}$$

where the subscripts or superscripts ab and c indicate the direction in which this parameter is measured.

Taking this into account, in order to allow the current to flow freely, it is important that all the grains show perfect c-axis orientation. Any deviation from perfect c-axis orientation, no matter how small, will hinder the current flow and the physical properties will not be the best. Thus, perfect biaxial texture is needed (out-of-plane and in-plane grain orientations).

This thesis is mostly focused on YBCO and also a particular study of GdBCO is also presented.

1.2.1 YBCO features

Within the REBCO compounds YBCO is probable the most well-known and the most studied material due to its high T_c ≈92 K and its high field current carrying capacity. It was the first discovered superconductor with the T_c above 77 K[12].

From the point of view of the crystallographic structure, it has, as all the REBCO compounds, a tetragonal structure for low values of oxygen content which changes to an orthorhombic structure for high values of oxygen doping. The values of different cell parameters are listed in the following table (Table 1.1):

Structure	a (nm)	b (nm)	c (nm)
Tetragonal[46]	0,3870	0,3870	1,1801
Orthorhombic[12]	0,3886	0,3821	1,1687

Table 1.1. Unit cell parameters of YBCO tetragonal ($YBa_2Cu_3O_6$) and orthorhombic ($YBa_2Cu_3O_7$) structures

The anisotropic nature of YBCO and, in general, of all REBCO compounds, is essential to understand its behavior. The values of ξ and λ for YBCO are collected in the following table (Table 1.2):

Direction	λ (nm)	ξ (nm)
c-axis	890	0,24
a-b plane	135	1,60

Table 1.2. Values of coherence length (ξ) and penetration length (λ) for YBCO in the c-axis direction and a-b plane direction[47].

Considering the previous values of ξ and λ, a γ=6,6 is obtained. In general for YBCO it is reported that the γ varies from 5 to 7[48]. This value is the lowest within the HTS and this is the main reason why the IL of YBCO is much higher that others HTS as, for example, $Bi_2Sr_2Ca_{n-1}Cu_nO_{2n+4+x}$, (BSCCO) which γ is approximately 30 (figure 1.7)[49]. This makes the YBCO a good candidate for power applications in which high magnetic fields are applied since the pinning performances will be maintained until higher magnetic field values.

1.2.2 GdBCO potential

Nowadays, there is much interest in other REBCO compounds created as a result of the change of the Y^{+3} ions in the YBCO structure by other RE ions (e.g. Nd^{+3}, Sm^{+3}, Eu^{+3} or Gd^{+3})[50-52]. The interest of these other REBCO compounds is due to the fact that, for some of them, better properties than in YBCO were observed (table 1.3).

Ion	Effective ionic radius (Å)	T_c (K)	J_c (MA/cm^2) (77 K)	References
Lu^{+3}	0,97	88	0,5	[53]
Yb^{+3}	0,98	90	0,1	[54]
Y^{+3}	1,01	92	2-3	[55]
Gd^{+3}	1,05	94	3-4	[56]
Eu^{+3}	1,07	93	1-2	[57]
Nd^{+3}	1,11	96	2-4	[58]
La^{+3}	1,16	93	1	[59]

Table 1.3. Values of the ionic radius of some rare earths, critical temperature (T_c) and critical current density (J_c) of the REBCO superconductors made with these ions.

The differences in the physical properties are determined by variations in electronic structure, valence state and, largely, in the ionic radius of the rare earth atom[60]. The RE ions have to fit in the structure. Their size influences the distances between different planes in the structure and, therefore, the interaction between the orbitals of different atoms which leads to a change in properties of the different compounds.

In the case of small rare-earth ions such as Yb^{3+} and Lu^{3+}, the formation of single-phase REBCO is impeded because the ions do not fit in the lattice site and it is likely to exist RE ion vacancies. On the other hand, it was demonstrated that bigger cations show a

greater tendency to partially substitute the Ba^{2+} hindering the formation of stable and single phase REBCO[61,62]. Among them, one can observe that GdBCO shows remarkable properties, even better than YBCO. So, it appears to be a good candidate to compete with YBCO.

As it was mentioned, the first challenge that one finds trying to prepare a REBCO with a RE ion size bigger than Y^{+3}, is the Ba^{2+} ion substitution. This difficulty is also present in the GdBCO preparation, but the Gd^{+3} shows the lowest tendency (apart from Y^{3+}) to substitute the Ba^{2+} ions among the REBCO compounds (figure 1.10).

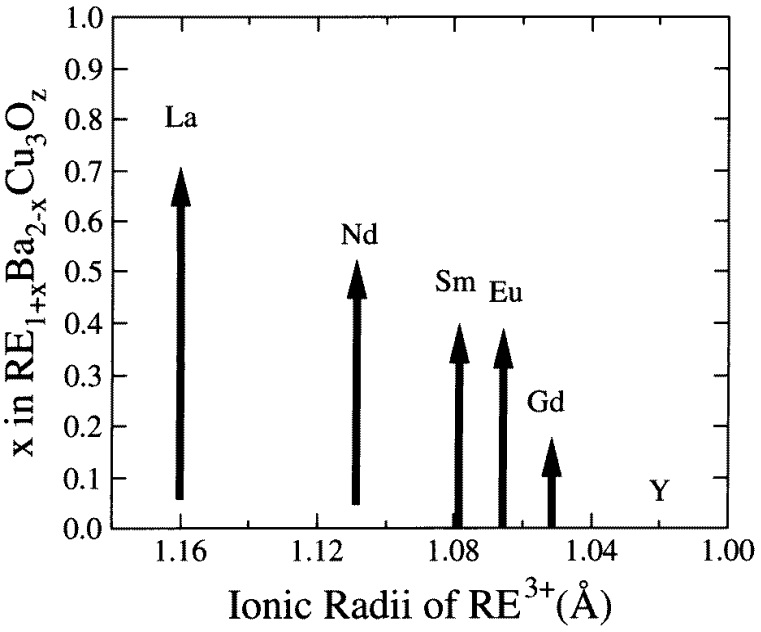

Figure 1.10. RE–Ba substitution for the different ReBCO systems in air[50]

From the applications point of view, the great interest in other REBCO compounds is due to the fact that the IL (see section 1.1.5.2) of some of them is higher than in the case of YBCO. And this enhancement of the IL is generated by the increase of T_c. Observing the table 1.3, it is noticeable that there are several compounds with T_c higher than in the case of YBCO: GdBCO, EuBCO, NdBCO and LaBCO. However, due to all the difficulties in the preparation that were mentioned before, the focus will be on GdBCO. GdBCO has a T_c of 94K which is 2K higher than the YBCO´s T_c. This means that the H_{c_2}, limited by the T_c in the H-T phase diagram, is higher in the case of GdBCO. Therefore, as the H_{c_2} is displaced to higher T, the IL is also displaced to higher T, resulting in the possibility to obtain high values of J_c until higher magnetic field values (figure 1.7).

1.2.3 REBCO superconducting wires

One of the main goals in the field of superconductivity is the manufacture of long, robust and flexible conductor to be used in several power applications, for example as magnet coils. However, this is rather difficult when dealing with ceramic superconductors as the cuprates.

Nowadays, the technology to fabricate superconducting wires using LTS is well established. Most of this LTS are metallic compounds, which facilitate the mechanical treatment to obtain the final wires. NbTi or Nb_3Sn wires are mass produced using different techniques as co-extrusion or bronze route[44]. However, the need to refrigerate these wires with liquid helium due to their low T_c and their low performances at high magnetic fields, have made that the interest nowadays were more focused in the HTS wires. These wires allow the refrigeration with liquid nitrogen, which is cheaper, and offer better performances when magnetic fields are applied.

The fabrication of HTS wires is very challenging for two main reasons: the ceramic nature of almost all the HTS (cuprates included) that makes the handling of these compounds extremely difficult due to their brittleness and the need to obtain biaxial texture (as it was mention before) in these compounds to achieve good properties. Nowadays, there are several techniques which can overcome these issues.

The first approach to assess the manufacturing of superconducting HTS tapes resulted in the so-called first generation tapes. These tapes are prepared with BSCCO using the so called "Powder-In-Tube (PIT) method". This process is performed introducing the sintered BSCCO in a sealed silver tube. From this tube, a very thin wire is obtained which is rolled and subjected to a thermal process. The rolling and the thermal processing are performed several times until the final tape has the desired texture and properties. The first generation tapes show great properties at liquid nitrogen temperature (77 K). They can carry up to 100 A/mm^2 with no applied magnetic field. However, due to the high anisotropy of BSCCO the IL is really low .Therefore, in the moment that a small magnetic field is applied, the properties decrease drastically[63-65].

To solve the problem of low performances in high magnetic fields observed in the first generation tapes, the use of REBCO compounds was proposed as superconductor materials to fabricate the tapes. This led to the appearance of the so called "second generation tapes" or "Coated Conductors (CCs)", first demonstrated in 1991[66]. The fabrication of CCs presents the same difficulties that in the case of first generation tapes: the fragility of REBCO compounds and the perfect biaxial texture that is needed in order to obtain the best possible properties. But, in this case, is even more complicated because the REBCO compounds are more difficult to machine than BSCCO, so it is not possible to use the PIT process.

The general architecture of CCs consist of a multilayered structure formed by a metallic substrate, intermediate buffer layers, the REBCO superconducting film and protective metallic cap layers (figure 1.12). Metallic substrates are used due to their excellent mechanical properties. The buffer layers provide a continuous, smooth, and chemically inert surface (avoiding metallic ions diffusion from the substrate) for the growth of the REBCO films while transferring the biaxial texture from the substrate to the superconducting layer. They are indispensable since, if the REBCO films are deposited directly on the metallic substrate, the texture will be not the right one (not epitaxial orientation of grains, but polycrystalline). This is due to the high mismatch between the unit cell of REBCO compounds and the unit cell of metals used to fabricate the substrates (stainless steel (SS), cooper, etc). The most commonly used materials as buffer layers are CeO_2, MgO, $Y:ZrO_2$, $SrTiO_3$ and $La_2Zr_2O_7$. Finally, the protective caps layers fulfill the function of protecting the superconducting layer from the environment.

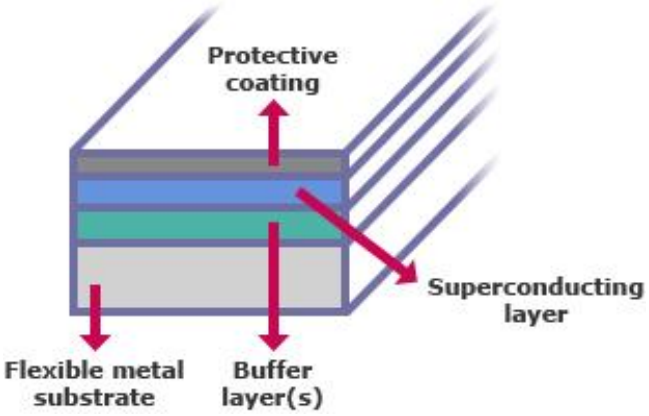

Figure 1.12. General architecture of the Coated Conductors.

As it was mention before, the most important issue when the CCs are fabricated is procuring the biaxial texture of the superconducting film. There are two different strategies to obtain this texture: the Ion Beam Assisted Deposition (IBAD) and Rolling-Assisted Biaxial Texture Substrate (RABiTS)[67].

In the IBAD process a buffer layer (commonly YSZ) with the appropriate texture is situated over the metallic substrate (usually SS). The deposition of this buffer layer is performed by evaporating the buffer´s material using a high power electron beam. The components are placed in the vapor state, and individual coating atoms or molecules condense and stick on the surface of the component to form the coating. Simultaneously, highly energetic ions (100-2000 eV) are produced and directed to the surface. It significantly improves adhesion and allows the control of the film properties such as morphology, density, stress level, crystallinity, chemical composition and, the most important, the texture of the buffer layer. However, the texture of the first buffer layer, usually, do not allow the REBCO epitaxial growth so, it is necessary to deposit more buffer layers on the top of this first layer to transfer the correct texture to REBCO film. Finally, the complete IBAD CC will be formed by the metallic substrate, a first textured buffer layer, a group of buffer layer to transfer the texture to the REBCO film, the REBCO layer and then the cap layer[67].

The other strategy is the RABiTS approach. The process is very similar to the IBAD approach but, in this case, is the metallic substrate what is directly textured. This is achieved by performing multiple rolling and annealing steps on an untextured metallic substrate to produce a particular texture. After that, epitaxial buffer layers (usually a seed layer, a barrier layer, and a cap layer) are deposited on the textured substrate. The REBCO film is deposited onto these buffer layers and finally the cap layer to protect the superconductor[67, 68].

1.2.4 Preparation of REBCO thin films

The preparation of REBCO thin films is not easy. First attempts showed polycrystalline orientations of REBCO grains which resulted in a very low critical current densities due to the fact that the grain boundaries act as connectivity barrier for the current flow[69]. In addition, the high anisotropy in the transport properties (J_c//a−b planes >>> J_c//c - axis) requires that the YBCO a-b planes (i.e. the superconducting CuO_2 planes)

were aligned parallel to the substrate surface to allow the current flow without impediments. This means that perfect epitaxially oriented (c-axis oriented) grains are required to obtain the highest performances. Methodologies to prepare REBCO thin films can be classified as in-situ and ex-situ growth techniques.

1.2.4.1 In-situ vs. Ex-situ growth techniques

The preparation of REBCO thin films with biaxial texture is really challenging because of the special conditions needed. However, there are several techniques that are usable for achieving this goal. These techniques can be separated in two groups.

The first one is the group of in-situ techniques. These techniques are characterized by the formation of the REBCO phase (or, in general, the desired phase) during the deposition of the material. Therefore, in this case, the deposition and the growth are simultaneous processes. The growth mode in the films prepared by in-situ growth techniques is more or less a layer-by-layer process which implies a non-equilibrium process where the surface diffusion is particularly important. By using different in-situ growth techniques such as Pulsed Laser Deposition (PLD)[70-72], Pulsed Electron Deposition (PED)[73], Chemical Vapor Deposition (CVD)[74], Physical Vapor Deposition (PVD)[75, 76], Liquid Phase Epitaxy (LPE)[77] or Sputtering[78], extremely high quality REBCO thin films can be grown.

The mayor drawback of the in-situ growth techniques is the high cost. In recent years, there have been huge developments in engineering that have led to the deposition of large areas using a continuous in-situ techniques process[79-81]. However, these techniques require ultra-high vacuum in the deposition chamber which greatly increases the cost of growing long lengths REBCO films.

On the other hand, the ex-situ growth techniques are characterized by the fact that after the deposition there is no REBCO formation and a subsequent annealing process at high temperatures is required. Therefore, the deposition and the growth of the REBCO phase are sequential processes. Most of the ex-situ growth techniques are solution-based and, therefore, they enable the continuous deposition over large areas at atmospheric pressure (no vacuum in any step of the process) that dramatically reduce costs. However, there other ex-situ growth techniques that also uses vacuum during the deposition as the BaF_2 method[82, 83] (amorphous film is deposited through PVD) Solution based ex-situ growth technique is called Chemical Solution Deposition (CSD).

In this thesis, the REBCO thin films were prepared by CSD method where SUNAM group is a world-recognize leader.

1.3 Nanostructured superconductors: Nanocomposites

In our days, the use of REBCO CCs is possible in some applications in which low external fields are applied, as in the case of transmission power cables or Fault Current Limiters (FCL). However, those applications in which high magnetic fields are applied, as generators, motors or magnets, require an improvement of the CCs properties in order to enhance the performances of these devices (figure 1.13).

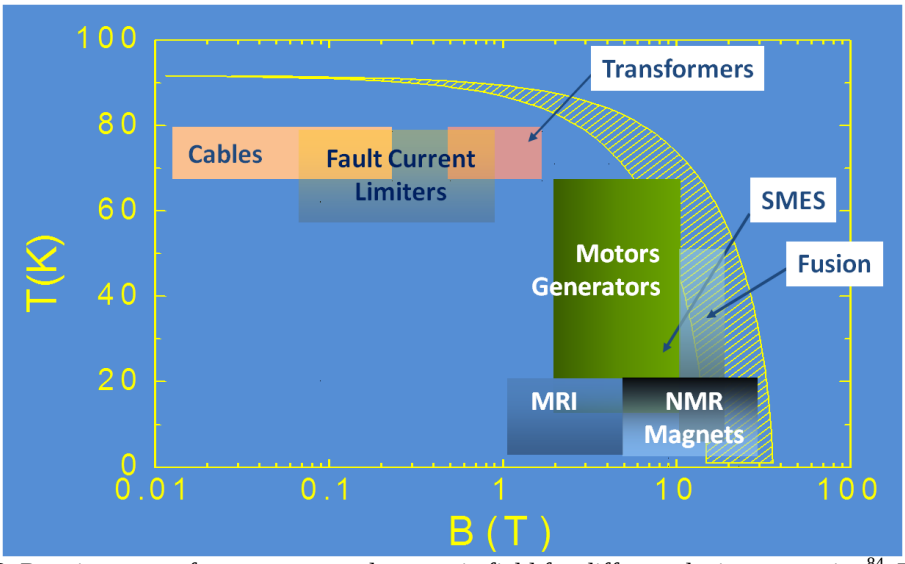

Figure 1.13. Requirements of temperature and magnetic field for different devices operation[84]. The yellow line is the H_{c_2} line of a typical REBCO compound (transition to normal state).

Generators or motors are electrical machines that need to work with high values of J_c at high applied magnetic fields. This is not possible using conventional REBCO compounds because, as it was discussed in section 1.1.5, a drop in J_c as the magnetic field increases (figure 1.13) is inevitable due to change from vortex solid to vortex liquid state.

As it was mentioned in section 1.1.5 vortex solid region size is determined by the amount of natural crystalline defects that appears during the processing of REBCO. This will determine the value of the pinning force. These natural defects are created in higher densities in thin films than in single crystals due to the different growth processes. This is why the J_c in thin films is much higher (1 or 2 order of magnitude) than in single crystals[38].

The goal is to develop a strategy to enlarge the vortex solid region in which the vortices are pinned and no losses of energy occur. This means that the objective is to increase the pinning force and displace the irreversibility line to higher fields enlarging the vortex solid region and reducing the vortex liquid region (from red dashed line to blue dashed line in figure 1.14). This can be done by nanostructuration of REBCO matrix introducing artificial defects in its matrix forming superconducting nanocomposites.

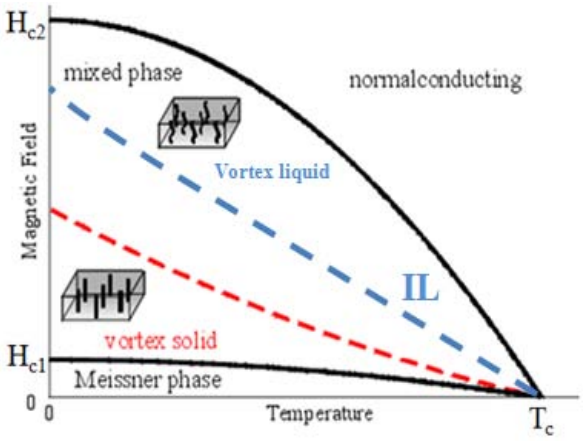

Figure 1.14. H-T phase diagram with two different irreversibility lines (red and blue dashed lines). The wider the vortex solid region, the higher the magnetic field at which J_c is still obtained. Therefore, blue irreversibility line is preferable than red one.

1.3.1 Superconducting nanocomposites

A composite material is formed by two or more different phases. The properties of this new integrated material are different than the properties of each individual one making the total greater than the sum of each one.

The nanocomposites are nothing more but composites in which, at least, one of the compounds has a dimension of less than 100 nm. In the particular case of superconducting nanocomposites, they are formed by a matrix of a superconductor and nanoinclusions of non-superconducting secondary phases.

First investigations about the nanostructuration of superconductors were done by bombarding superconductor's single crystals with heavy ions, neutrons, electrons or protons. With this procedure it is possible to generate 0D and 1D defects (columnar defects)[85-87]. However, adding irradiation defects to superconductor´s thin films resulted in a marginal J_c improvement, since the natural defects in thin films is already high, and also in T_c reduction if the irradiation is not perfectly controlled.

Another approach to nanostructure the superconductor's matrix was the surface decoration. In this procedure, NPs of non-superconducting phases are deposited in the substrate prior to the superconductor. These NPs act as initial points for dislocations in the c-axis direction which act as pinning centers. Different NPs (mostly metals as Au or Ag and oxides) was used to test this procedure. Physical and chemical methods were used to deposit these NPs in crystalline substrates or buffer layers but, as in the case of irradiation, the improvement in the performances is not enough for some in-field applications[88-91].

The last evolution in the nanocomposites preparation was to embed the NPs in the superconductor´s matrix. The best performances of the resulting nanocomposites samples are obtained in this way because if the NPs are homogeneously distributed in the superconductor´s matrix the benefits of these NPs will not be restricted only to interface superconductor-substrate but it will also have a volumetric effect in the whole film.

The choice of the NPs phase must consider several requirements: i) high stability at the YBCO growth temperatures, ii) no chemical reactivity neither with YBCO nor with intermediate phases of YBCO which would led to off‐stoichiometries, and iii) no cationic substitution into the YBCO lattice which would diminish T_c. Some examples of suitable phases are: barium perovskites ($BaBO_3$) where B=Zr, Sn and Hf[13, 92-97], binary rare earth oxides (RE_xO_y) and their solid solutions with RE= Y, Gd, Ho, Er, Dy[98, 99], intermediate phases of YBCO like YBa_2CuO_5[100] and rare earth tantalates and niobiates (double perovskite $Ba_2RE(Ta,Nb)O_6$ and pyrochlore RE_3TaO_7 with RE= Y, Yb, Gd, Er,)[101, 102].

1.3.2 Vortex pinning in REBCO compounds

The vortex pinning properties in REBCO compounds are determined by the amount and type of crystalline defects that are present in the superconductor matrix. These crystalline defects act as pinning centers increasing the pinning force that maintain the vortices motionless. The defects change the electronic structure in their surroundings preventing the formation of Cooper pairs and transforming these small areas into normal regions (non-superconducting regions) in which the vortices are placed to diminish their energy (vortices have a normal core).

These defects can be induced naturally during the pristine REBCO thin film growth. Typically, these natural defects are: oxygen vacancies, cation disorder, threading, screw or edge dislocations, in-plane dislocations, twin boundaries, antiphase boundaries,

stacking faults, intergrowths, etc (figure 1.15). All these defects create strain fields in their surroundings that can also act as pinning centers.

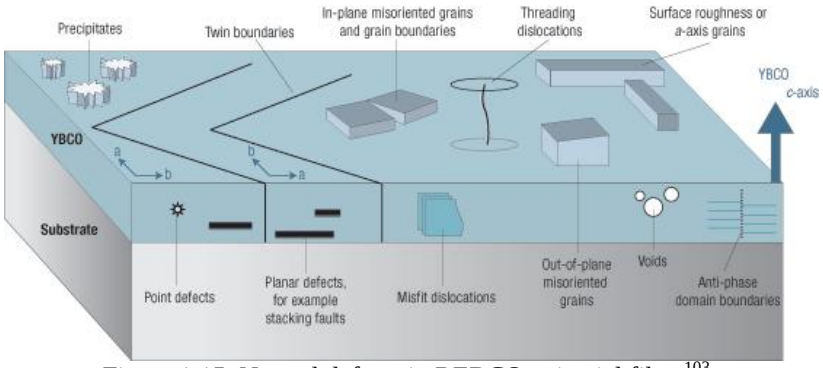

Figure 1.15. Natural defects in REBCO epitaxial films[103].

These defects can be classified according to their dimensions in 0D, 1D, 2D or 3D defects (figure 1.16). Cation disorder or oxygen vacancies are included in the group of 0D defects (figure 1.16 a)). These are natural defects whose dimensions are so small (in the range of Å) that are considered as punctual defects. In the group of 1D defects are included the dislocations and other columnar defects (figure 1.16 b)). Planar defects as twin boundaries, grain boundaries, stacking faults or misfit dislocations belong to the 2D defects group (figure 1.16 c)). And finally, in the group of 3D defects are included the precipitates, the secondary phases or the voids (figure 1.16 d)).

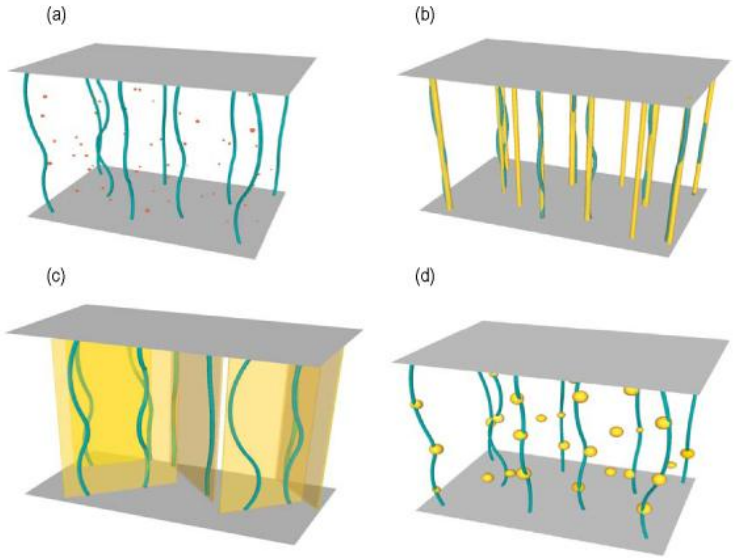

Figure 1.16. Picture of the dimensionality of different pinning centers: (a) 0D, (b) 1D, (c) 2D and (d) 3D[104].

However, these natural defects are not effective enough to pin the vortices at high magnetic fields. So, in order to increase the REBCO thin films performances at high magnetic fields, it is necessary to introduce Artificial Pinning Centers (APC) which can be either additional defects in the matrix or secondary non-superconducting phases creating what is called superconducting nanocomposites. In the case of this work, YBCO and GdBCO nanocomposites are created by embedded NPs (3D defects) in the superconducting matrix which create additional defects in the superconductingmatrix.

1.3.3 Growth approaches to superconducting nanocomposites

In REBCO and, in particular, in YBCO and GdBCO thin films, the amount of natural defects created during the growth process is quite high. However, as it was mentioned before, the effectiveness of the natural defects as pinning centers is still too low. So, by developing nanocomposites, the aim is to increase the amount of these normal regions by adding non-superconducting phases to the superconducting matrix. The introduction of NPs in the superconducting matrix can be done using in-situ or ex-situ growth techniques. The pinning mechanism depends on the features of the embedded NPs and growth technique will determine the NPs features.

1.3.3.1 Simultaneous deposition and growth case

First experiments in the preparation of superconducting nanocomposite films were performed using in-situ growth techniques which are characterized, as it was mentioned before, by a simultaneous deposition and growth of the, in this case, REBCO phase and the NPs, processes. One of the most used in-situ growth techniques is the Pulsed Laser Deposition (PLD). Nanocomposites with PLD are achieved by adding a fine dispersion of the dopant phase (mixed single target) or by switching two targets (YBCO target + dopant target). The resulting thin films demonstrated enhanced in-field performances and J_c values compared to pristine YBCO films. However, a decrease in T_c is observed for the most of the dopants used, probably due to stress induced in the YBCO lattice by the highly lattice mismatched interfaces[105].

Most common feature of all nanocomposite thin films grown with in-situ growth techniques is the epitaxial relationship of the embedded nanoparticles with the superconductor matrix leading to coherent interfaces. This is inherent to the in-situ techniques in which the heterogeneous nucleation is promoted (see details about nucleation issues in chapter 2). It is also extensively observed that the NPs suffer a self−assembling process leading to homogeneously dispersed vertical nanostructures or nanorods with small width of less than 5 nm that can pin the vortices by itself as the width is similar to the vortex sizes (figure 1.17 a) and b))[15, 106, 107]. There are, however, other cases in which homogeneously distributed NPs were observed (figure 1.17 c)[14, 108].

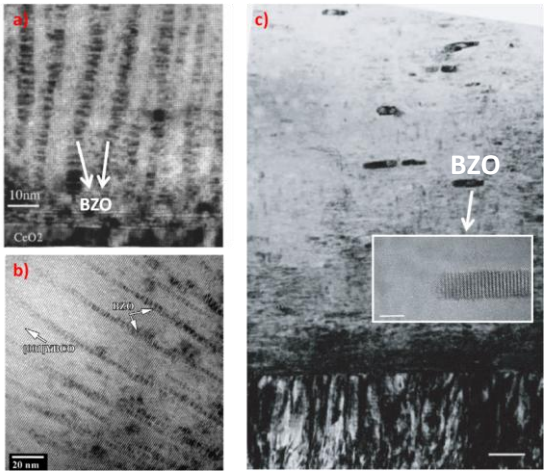

Figure 1.17. TEM images that show different distributions of BZO NPs in YBCO-PLD nanocomposites. Columnar arrangement of BZO NPs are shown in a) and b)[106,107] and homogeneously distribution of epitaxial BZO NPs in c)[14].

The NPs can act as pinning center themselves only in the case that their sizes are similar to the coherence length of YBCO: 2-5 nm (size of vortex core). If their size exceeds the coherent length size, the pinning properties will not improve because the vortices only need normal regions of this size. The extra normal region does not give any advantage. Actually, the opposite effect is observed. Bigger secondary phases will contribute to enhance the total energy of the system as they are normal regions embedded in the matrix that is not energetically favorable and causes a decrease in the condensation energy. This scenario could be achieved[109-112], but a very fine control of YBCO processing parameters is required.

1.3.3.2 Sequential deposition and growth case

The ex-situ growth techniques are characterized, as it was explained before, by a sequential deposition and growth processes. In the case of the nanocomposites, the growth process is also sequential since the growth of the REBCO phase and the growth of the NPs are not simultaneous but occurs at different times. Within the ex-situ techniques or sequential deposition and growth techniques, it is possible to distinguish two different approaches to prepare nanocomposite films. The first one, which will be extensively explained in chapter 3, is called "in-situ nanocomposites" and its typical feature is the formation of the NPs during the growth thermal treatment (one of the steps of the CSD method as it will be explained in chapter 2). The other one is called "ex-situ nanocomposites" and it is characterized by the fact that the NPs are firstly synthesized and, then, a colloidal solution with the NPs and the YBCO precursor solution is formed. This last approach is a novel technique mostly developed in this thesis and will be widely treated in chapter 4.

To achieve NPs with sizes in the range of 2-5 nm is very difficult when ex-situ growth techniques are used. In the majority of cases, the sizes of the NPs that are embedded exceed 10 nm. These sizes of the NPs are higher than the optimum size for single vortex pinning. However, these oversize NPs can create additional pinning centers as it was demonstrated for the first time by Llordes et al[97]. The key point here is that these nanostructures can induce nanostrained regions in which Cooper pair formation is suppressed[113].

Figure 1.18 outlines why these oversize nanostructures originate nanostrained regions that act as pinning centers. When one of these NPs is embedded in the superconducting matrix, it distort the matrix due to the mismatch in the lattice parameters between the NPs and the REBCO (barium perovskites, binary rare earth oxides or rare earth tantalates and niobiates have a much different lattice parameter than REBCO) generating interfacial energy in the interface of the two compounds (figure 1.18 a)). This interfacial energy is release by the system creating extra Cu-O chains (indicated in the figure 1.18 b) with red arrows) which are called stacking faults or 248 intergrowths and which are planar defects (figure 1.18 b)). In the perimeter of the SF very strained regions appear due to the presence of local partial dislocations. These cause a nanodeformation of the surrounding unit cells which lead to an increment of the strain in this nanoarea. These strained nanoregions, that create nanostrain, behave as normal regions avoiding the formation of Cooper pairs and, therefore, they act as pinning centers for the vortices with sizes in the range of the vortices core[113, 97].

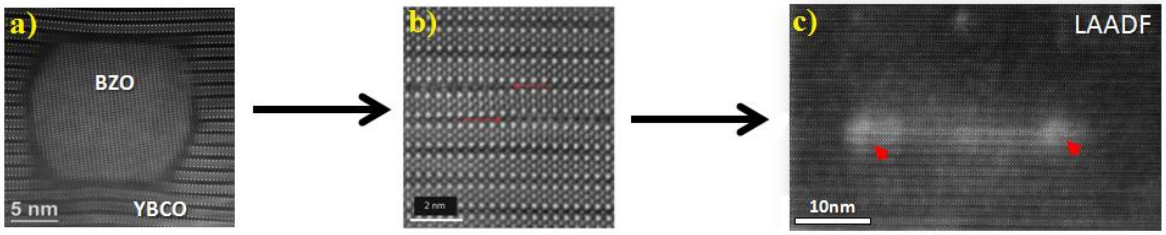

Figure 1.18. TEM images that show the pinning mechanism in CSD YBCO nanocomposites with big nanoparticles. a) The embedded NPs create a distortion in the YBCO matrix which causes an interfacial energy. b) This energy is released by adding extra Cu-O chains (stacking faults or 248 intergrowths). c) At the perimeter of these intergrowths very strained regions appear (LAADF TEM image) that acts as normal regions which pin the vortices.

This explanation is supported by experimental measurements. Llordés et al found that nanostrain values are directly proportional to the total incoherent interface (figure 1.19 a))[97]. This means that, by increasing the number of NPs, the interfacial energy raise (more incoherent interfaces). Therefore, to release this interfacial energy, more SFs are created and, consequently, more strained nanoregions appears resulting in an enhacement of the nanostrain. This enhancement of nanostrain results in an increase of pinning force (figure 1.19 b)).

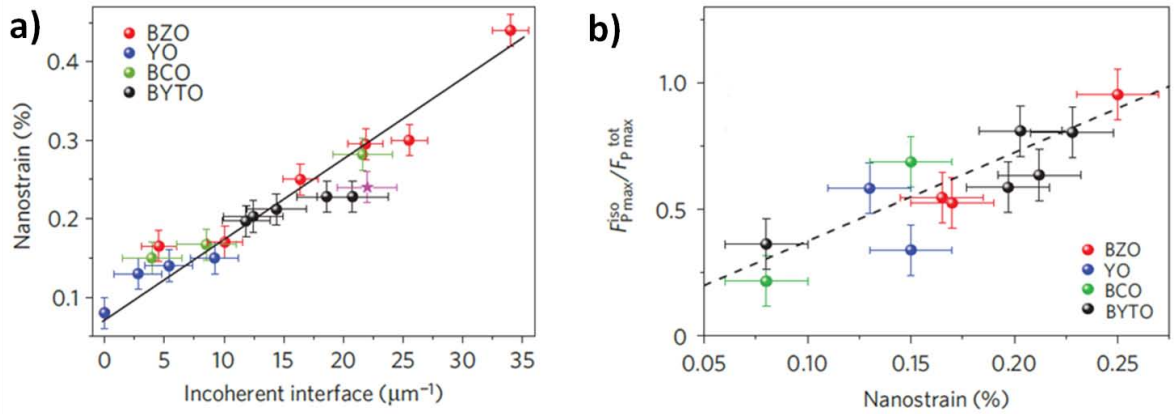

Figure 1.19. Different features in YBCO nanocomposites with oversize NPs: a) evolution of nanostrain with incoherent interface and b) pinning force dependence with nanostrain[97].

The presence of SFs leads to a great enhancement of the pinning force in this kind of systems resulting in excellent YBCO performances[97]. It is remarkable that, in recent years, SFs were also detected in nanocomposite films synthesized by in-situ techniques such as PLD when the NPs have larger sizes than the 2-5 nm[108].

This proposal of pinning mechanism based on the apparition on SF associated to the presence of NPs is supported with several reports in which the SF where found[13, 101, 97, 114, 108, 115]. However, there are different works in which the REBCO thin films, with excellent performances at high magnetic fields, do not show the presence of SFs despite that ex-situ growth techniques were also used[116-118]. In these cases, the pinning mechanism based on the SFs is not valid and it has to be explained in a different way. This opens the possibility to other possible pinning mechanism that had higher influence in certain conditions.

1.4 Thesis content

The content of this thesis is divided in two main blocks: the first one, which comprise chapter 3 and 4 is devoted to CSD YBCO and GdBCO nanocomposites and the second one, which include chapter 5, deals with the oxygenation and oxygen diffusion processes in CSD YBCO films. It is also included the explanation of the experimental procedures and characterization techniques in chapter 2 and the general conclusions in chapter 6. Finally, the appendices, the references and the nomenclature will be presented in the last pages.

In chapter 2 the experimental procedures and the film characterization techniques will be explained. The experimental part includes a detail description of the CSD methodology and also the procedure to prepare the different precursor solutions used in this thesis. Regarding the characterization techniques, both the solution and the films characterization (structural, morphological and physical) techniques will be exposed.

In chapter 3 all the work related with the CSD YBCO and GdBCO nanocomposites prepared by the in-situ approach will be described. Structural properties of the films obtained with different compositions are analyzed. Then, the microstructure of these films and how the microstructure affects the final properties of the films is studied. CSD GdBCO and GdBCO nanocomposites thin films using low-fluorine content solution are also studied in this chapter.

Chapter 4 is also related with nanocomposites but, in this case, it is the turn of the ex-situ approach. This is a new approach, mostly developed during this thesis, for the preparation of CSD YBCO nanocomposites by using NPs colloidal solutions. First part of this chapter is about the characterization of the NPs used to prepare the colloidal solutions. Then, NPs stability in the YBCO precursor solution and how this stability affects the quality of the films after the pyrolysis is studied. Finally, all the problems that have appeared during growth process (coarsening, pushing or reactivity) are analyzed and a solution is proposed for each one.

In chapter 5 the study of the oxygenation and the oxygen diffusion processes in the YBCO is explained. A deep study of the diffusion process using in-situ resistivity measurements varying different parameters is performed, in order to clarify which is the real role of the surface reactions in the diffusion process.

Final chapter, chapter 6, is devoted to the general conclusions achieved in this thesis.

2
Experimental Methodologies

In this second chapter, the experimental procedures and characterization techniques used in this work will be explained in detail. First part of the chapter is devoted to explain in depth the Chemical solution deposition (CSD) methodology. The used thermal processes applied in each step of the process and the basis of the thin film crystallization is included in this part. The synthesis of the different precursor solutions that were used is also exposed.

The second part deals with the different characterization techniques employed to study the properties of the precursor solutions and the structural, morphological, compositional and physical properties of the obtained thin films.

2.1 Experimental procedures

2.1.1 Chemical Solution Deposition method

CSD method has appeared in last years as an attractive alternative to in-situ growth techniques since it is a scalable, versatile and low-cost process. This process has been applied to the preparation of thin films of functional oxides in many different fields. In particular, in the field of superconductivity, it has been used to prepare long lengths CCs with reduced cost and similar performances than those prepared using in-situ techniques.

2.1.1.1 Processing steps

CSD process consists of four steps that can be observed in figure 2.1 that are explained in the works of Lange and Schwartz et at[119, 120]. These steps are: the preparation of the chemical precursor solution, the solution deposition on an adequate substrate, the pyrolysis process and the growth process. All these steps will be explained in detail for the particular case of this thesis.

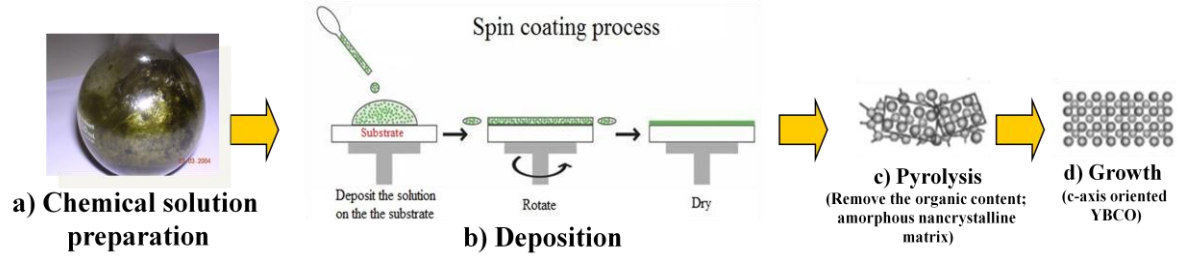

Figure 2.1. CSD process divided in its four steps: a) Chemical solution preparation, b) Solution deposition (spin-coating in this particular case), c) pyrolysis process and d) growth process.

2.1.1.1.1 Chemical solution preparation

The first step is the preparation of the chemical solution using the metalorganic precursors that contains the metals of the final material. These precursors are dissolved in adequate solvents and then mixed in a stoichiometric ratio that yields the desired composition of the final oxides film (figure 2.1 a)).

In this thesis different precursor solution were used both for the preparation of pristine films or superconducting nanocomposites. These solutions are: YBCO-TFA solution, GdBCO-LF solution, YBCO and GdBCO in-situ nanocomposites solutions and YBCO ex-situ nanocomposites solutions. The synthesis of all of them is detailed below.

<u>Synthesis of YBCO-TFA solution</u>

From the discovery of the TFA route, the synthesis of the TFA precursor solution was extensively studied. In the case of the TFA solutions used for this work, the synthesis process proposed by Roma et al at ICMAB was followed[121]. The procces is summarized in figure 2.2

YBCO powder ($YBa_2Cu_3O_x$, Solvay) is used as raw material. The synthesis process starts by mixing the YBCO powder in an excess of trifluoroacetic anhydride (trifluoroacetic anhydride (TFAA), Sigma-Aldrich ≥ 99%), a small amount of trifluoroacetic acid (trifluoroacetic acid (TFAH), Sigma-Aldrich 99%) as a catalyst and acetone (HPLC acetone, Scharlab 99,98%) as solvent. This mixture is stirred during 60 h maintaining a constant temperature of 55ºC. Using this procedure it is possible to obtain a solution with Y-TFA ($Y(CF_3COO)_3$), Ba-TFA ($Y(CF_3COO)_3$) and Cu-TFA ($Cu(CF_3COO)_2$) precursors as a result of the reaction between the YBCO powder with the TFAA and TFAH. Afterwards, the as-obtained solution is filtered to eliminate the possible remaining precipitates.

The filtered solution is placed in a rotary evaporator with vacuum at 60ºC during 6 h to remove the solvent and, to finally obtain a gel. To further remove any trace of the

solvent, the gel is submitted to a drying process under vacuum. After that, the solid is dissolved in methanol (Sharlab 99,9%) under Ar atmosphere and the volume is adjusted using methanol (MeOH) to the desired concentration.

The final step is the titration of the solution to check if the stoichiometry is correct. If the stoichiometry is not respected by one of the elements (Y, Ba or Cu), it is necessary to add the corresponding TFA salt (Y-TFA, Ba-TFA or Cu-TFA). Finally, the volume is again adjusted and the solution, which is already ready to use, is kept in sealed vials under Ar atmosphere.

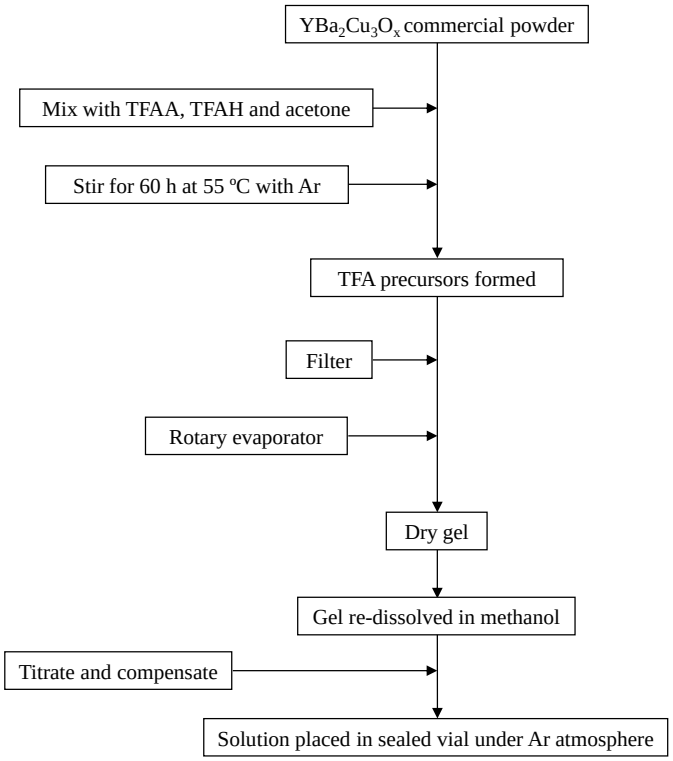

Figure 2.2 Chart flow to prepare the YBCO-TFA precursor solution

Synthesis of GdBCO-LF solution

The GdBCO Low-Fluorine solution (GdBCO-LFS) is similar both in the formulation and in the synthesis procedure to solution 4 reported in the work of Palmer et al[123]. The solution is prepared using three different salts: gadolinium trifluoroacetate (Gd-TFA), barium acetate (Ba-OAc) and cooper acetate (Cu-OAc). The preparation of this kind of solutions is much easier and faster than the TFA solutions as it was also shown in some other reported works[124, 125]. All this process is summarized in figure 2.3.

The first step in the synthesis is to dissolve the Ba-OAc ($Ba(CH_3COO)_2$, Sigma-Aldrich ≥99,5%). For this, the calculated amount of BA-OAc is added to a vial containing methanol. The mixture is maintained under continuous stirring during 15 min to get the dispersion of BA-OAc in methanol. Afterwards, propionic acid (CH_3CH_2COOH, Sigma-Aldrich ≥99,5%) is added. The amount of propionic acid added to the mixture is 26% of the final volume of the solution that is being prepared. This mixture is maintained under stirring approximately 2 hours to completely dissolve the Ba-OAc. Once the BA-OAc is dissolved , TriEthanolAmine (TEA, Sigma-Aldrich 98%) in an amount of 5% of the total volume of the final solution is added and homogenized during 10 minutes.

After the homogenization is done, the Cu-OAc ($Cu(CH_3COO)_2$, Alfa-Aesar ≥98%) is added. After 15-20 minutes, the Cu-OAc is completely dissolved and, finally, the Gd-TFA is added to complete the solution. The solution is adjusted to the desired concentration with methanol and then placed in sealed vials under Ar atmosphere. In this case there is no need to titrate and compensate because the stoichiometry is fixed in the beginning by weighting the calculated amount of salts.

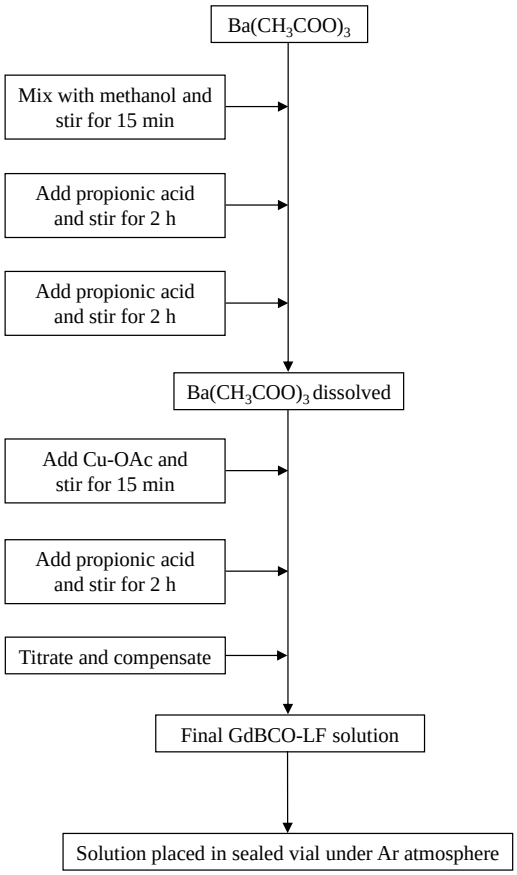

Figure 2.3 Chart flow to prepare the GdBCO-LF precursor solution

The Eq. 2-1 shows how the weights for the different salts are calculated. In this particular example, it is calculated the amount of Gd-TFA which is needed to obtain a 5 ml solution of 0,25M Gd-LF solution:

$$\mathbf{5ml\ of\ GdBCO\ x}\frac{\mathbf{1\ l}}{\mathbf{1000\ ml}}\ \mathbf{x}\ \frac{\mathbf{0{,}25\ mol\ Gd}}{\mathbf{1\ l}}\ \mathbf{x}\ \frac{\mathbf{1\ mol\ Gd-TFA}}{\mathbf{1\ mol\ Gd}}\ \mathbf{x}\frac{\mathbf{496{,}27\frac{g}{mol}\ Gd-TFA}}{\mathbf{1\ mol\ Gd-TFA}} = \mathbf{0{,}6203\ g\ Gd-TFA} \quad \text{Eq. 2-1}$$

The amount of different salts that are used for different volumes and different molarities of the solution are shown in table 2.1:

Molarity of the solution	**0,125M**			**0,25M**		
Solution volume (ml)	**5**	**10**	**20**	**5**	**10**	**20**
Amount of Gd-TFA (g)	0,3102	0,6204	1,2408	0,6203	1,2406	2,4812
Amount of Ba-OAc (g)	0,3193	0,6386	1,2772	0,6386	1,2772	2,5544
Amount of Cu-OAc (g)	0,3406	0,6812	1,3624	0,6811	1,3622	2,7244

Table 2.1. Amount of different salts needed to prepare GdBCO-LF solutions

Synthesis of YBCO and GdBCO in-situ nanocomposites solutions

The precursor solutions of the in-situ nanocomposites are based in the YBCO-TFA or GdBCO-LF precursor solutions. The preparation is simple. The procedure is to calculate the amount of each precursor salt needed to form the desired NPs with the adequate molar concentration. These salts are added to the YBCO-TFA or GdBCO-LF solution and the mixture is stirred during 20 min until the complete dissolution of the NPs precursor salts. The solution is filtered over a 0,2 µm membrane filter (Teflon) to remove dust and insoluble impurities and, the in-situ nanocomposite solution is ready for deposition.

The addition of NPs salts is made in excess. In this way the NPs formation will not change the stoichiometry of the YBCO or GdBCO. During this thesis different kind of NPs were used: $BaZrO_3$ (BZO), Y_2O_3 (YO), Ba_2YTaO_6 (BYTO), Gd_2O_3 (GdO) and also different combinations of them.

In the case of the BZO NPs it is necessary to add Ba-TFA and zirconium acetylacetonate (Zr-acac, Zirconium(IV) 2,4-pentanedionate, Alfa Aesar). But also it is required to add some Y-TFA because there is a certain tendency to replace the Zr by Y in the BZO structure forming compounds with a certain amount of Y. It was estimated that 20% of Zr is replaced by Y, forming $BaZr_{0,8}Y_{0,2}O_3$ compound[97].

For BYTO NPs synthesis, Y-TFA, Ba-TFA and Tantalum ethoxide (Ta-etox, Tantalum(V) ethoxide, Sigma-Aldrich 99,98%) are added to the YBCO-TFA solution. Here is has to be taken into account for the calculation of the needed amount of Ta that the Ta-etox is a liquid.

Finally, in the case of Y_2O_3 or Gd_2O_3 only Y-TFA or Gd-TFA is added to the YBCO-TFA or GdBCO-LF solution.

The Eq. 2-2 shows how the calculations for the different NPs precursor salts are done. In this particular case, the calculations are done for the amount of Zr-Acac necessary to prepare 1 ml of YBCO+10%M BZO solution starting from 0,25M (with respect to the Y) YBCO-TFA solution. During this thesis, the concentrations of the NPs in the solutions will be measured in molar concentration with respect to the YBCO molar concentration (YBCO+10%M BZO means a 10% of BZO with respect to the molarity of the YBCO).

$$\mathbf{0,25}\,\frac{\text{mol YBCO}}{\text{l}}\ \mathbf{x}\ \frac{\text{0,1 mol BZO}}{\text{1 mol YBCO}}\ \mathbf{x}\ \frac{\text{1 mol Zr-Acac}}{\text{1 mol BZO}}\ \mathbf{x}\ \frac{\text{487,66}\,\frac{\text{g}}{\text{mol}}\,\text{Zr-Acac}}{\text{1 mol Zr-Acac}}\ \mathbf{x}\ \frac{\text{1 l}}{\text{1000 ml}} = \mathbf{0,0122\ g\ Zr-Acac} \qquad \text{Eq. 2-2}$$

The table 2.2 shows the amount of the different salts needed to prepare 1 ml of the different in-situ nanocomposites precursor solutions used in this thesis. The YBCO-TFA solution is 0,25M. If a combination of different NPs is used, it is necessary to add the amount of salts required for each one.

Solution	YBCO+BZO		YBCO+YO	YBCO+BYTO
NPs molar concentration	5%M	10%M	5%M	6%M
Amount of Y-TFA (g)	0,0011	0,0021	0,0053	0,0064
Amount of Ba-TFA (g)	0,0045	0,0091	-	0,0109
Amount of Zr-Acac (g)	0,0061	0,0122	-	-
Amount of Ta-etox (ml)	-	-	-	0,0039

Table 2.2. Amount of different salts needed to prepare the in-situ YBCO nanocomposites

Synthesis of YBCO ex-situ nanocomposites solutions

As in the case of the in-situ nanocomposites precursor solutions, ex-situ nanocomposites precursor solutions are also based on YBCO-TFA solution. The preparation of this kind of solutions is again quite simple. Once the NPs colloidal solution is prepared, it is mixed with the YBCO-TFA solution. If this YBCO+NPs solution is stable (no NPs precipitation) and the features of NPs in the solution (NPs size, presence of aggregates etc) are within the established limits, the solution is ready for deposition (the preparation of the NPs colloidal solution and the requirements of the final solution will be extensively explained and discussed in chapter 5).
The most difficult step in this case is to calculate the volume of the NPs solution needed in YBCO-TFA solution in order to obtain the desired concentration of NPs in the final film. To do this, it is necessary to take into account the molarity of the initial colloidal solution and the molarity of the YBCO-TFA solution. It has to be considered that when the colloidal solution is added to the YBCO-TFA solution, the molarity of the YBCO is changed due to the presence of methanol in the colloidal solution. So, depending on the volume of the colloidal solution used, the molarity of the YBCO in the final solution will be different. The Eq 2-3 is an example of the calculations required to obtain 2 ml of a final YBCO+10%M NPs solution with a 0.125M YBCO starting with 25mM NPs colloidal solution. As in the case of the in-situ nanocomposites solutions, the concentration of the NPs in the ex-situ nanocomposites solutions will be measured in molar concentration with respect to the YBCO molar concentration.

$$\frac{\mathbf{1\ ml\ NPs\ solution\ x\ 25\ mM\ solution} \times \mathbf{100}}{\mathbf{1ml\ YBCO\ solution\ x\ 0{,}25\ M\ YBCO\ solution}} = \mathbf{YBCO + 10\%M\ NPs\ solution} \qquad \text{Eq. 2-3}$$

2.1.1.1.2 Deposition of the metalorganic precursor solutions

Once the different precursor solutions are prepared, the deposition of this solution over an adequate substrate is carried out. The solution deposition can be executed using different techniques. Spin-coating, bar coating or the spray-coating are very common deposition techniques at lab scale. In order to deposit the solutions in a scalable way, it is necessary to introduce alternative techniques such as ink-jet printing or dip-coating. However, most of the thin films that were prepared in this thesis were deposited by spin-coating.

The spin-coating deposition technique is a widespread deposition technique used to deposit uniform thin films in flat substrates. The solution is deposited on the substrate and then submitted to a rotary movement under a certain controlled angular velocity and acceleration. It is commonly used at the lab scale, but it is also used in some fields, as in microelectronics, as an industrial procedure.

The different steps of the spin coating process are presented in figure 2.4. The first step is the deposition of the solution covering the entire substrate surface. Then, the second step is the spin-up, in which the substrate is accelerated up to its final rotation speed and it is characterized by an aggressive fluid expulsion from the substrate surface by the rotational motion. The third step is the spin-off, when the substrate is spinning at a constant rate and fluid viscous forces dominate the fluid behavior causing a gradual fluid thinning. Finally, the last step is the evaporation, that starts at the end of the spin-off and it is distinguished by a shrinkage due to the solvent loss[122].

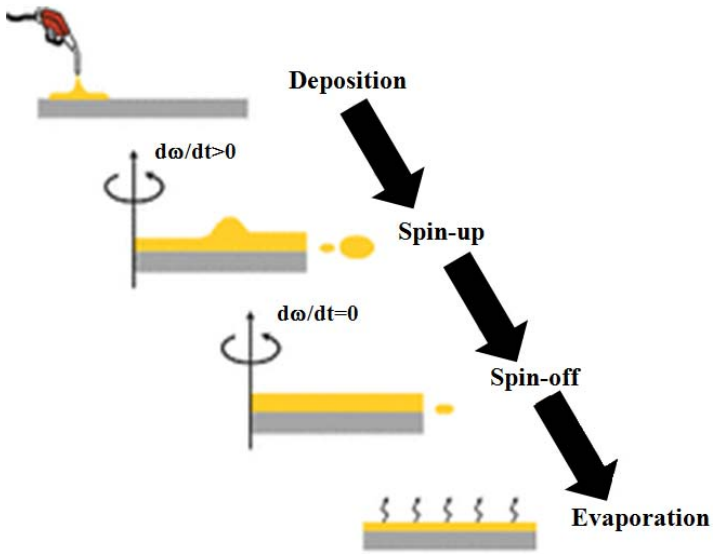

Figure 2.4. Evolution of the precursor solution during the spin-coating process.

All the synthesized solutions were deposited over lanthanum aluminate ($LaAlO_3$, LAO) single crystals ($LaAlO_3$, CrysTec). The choice of this type of substrates was done considering the low mismatch between the superconducting cuprates and LAO. For the $YBa_2Cu_3O_7$ the mismatch is -2,41% (<0→compressive) in the a-axis and -0,76% (<0→compressive) in the b-axis. In the case of $GdBa_2Cu_3O_7$ the mismatch is -1,26% (<0→compressive) in the a-axis and -2,67% (<0→compressive) in the b-axis.

Before using the substrates for the deposition, it is necessary to clean them in successive ultrasonic baths of acetone and methanol (5 min each) in order to remove impurities from the surface and, then, dry them using compressed N_2. After that, the substrates are exposed to a thermal process in order to remove all possible remaining organic content and induce a surface reorganization that creates terraces, favoring the nucleation of new phases[123, 124]. The thermal process used for the LAO treatment is presented in figure 2.5.

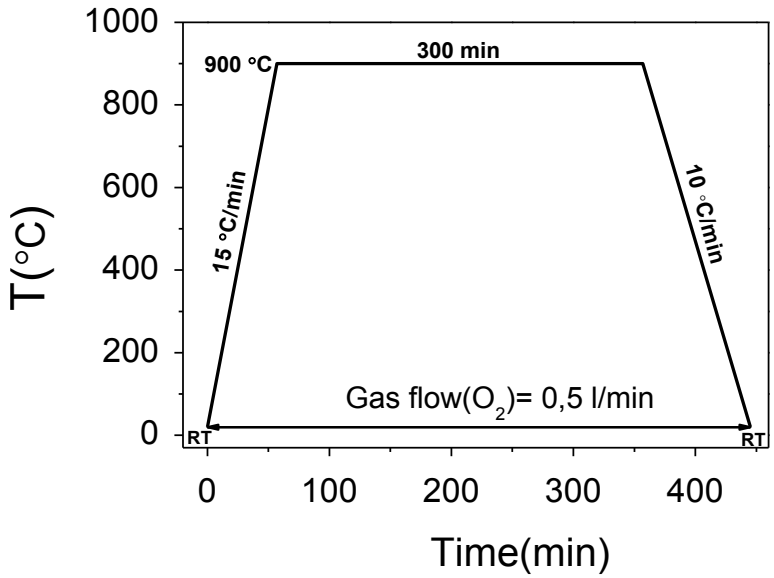

Figure 2.5. Thermal profile used in this thesis for the LAO single crystals treatment.

It consists of three steps. First a heating ramp of 15 ºC/min until 900 ºC is performed. Then, this temperature is maintained constant during 300 min. Finally, the temperature is decreased until room temperature using a 10 ºC/min ramp. All this process is performed in a quartz tube under continuous oxygen flow of 0,5 l/min.

2.1.1.1.3 Pyrolysis process

Once the deposition is done, the films are exposed to a pyrolysis process in order to remove all the organic content from the precursor salts that are present in the as-deposited films.

The so called "standard pyrolysis process" for the TFA solution is showed in figure 2.6. This thermal process is very similar to the one reported in the work of Roma et al that was optimized by members of the SUMAN group[121]. It consists on a first heating ramp of 5 ºC/min up to 230 ºC where the ramp is changed to 3 ºC/min up to 310 ºC. At this point the temperature is maintained constant during 30 min. After that, the temperature is decreased at a rate of 5 ºC/min to the room temperature. The process is performed in a quartz tube with an oxygen flow of 0,07 l/min. From 110 ºC, the oxygen passes through a group of bubblers to get humid oxygen. This is necessary to avoid the Cu-TFA sublimation[125, 126].

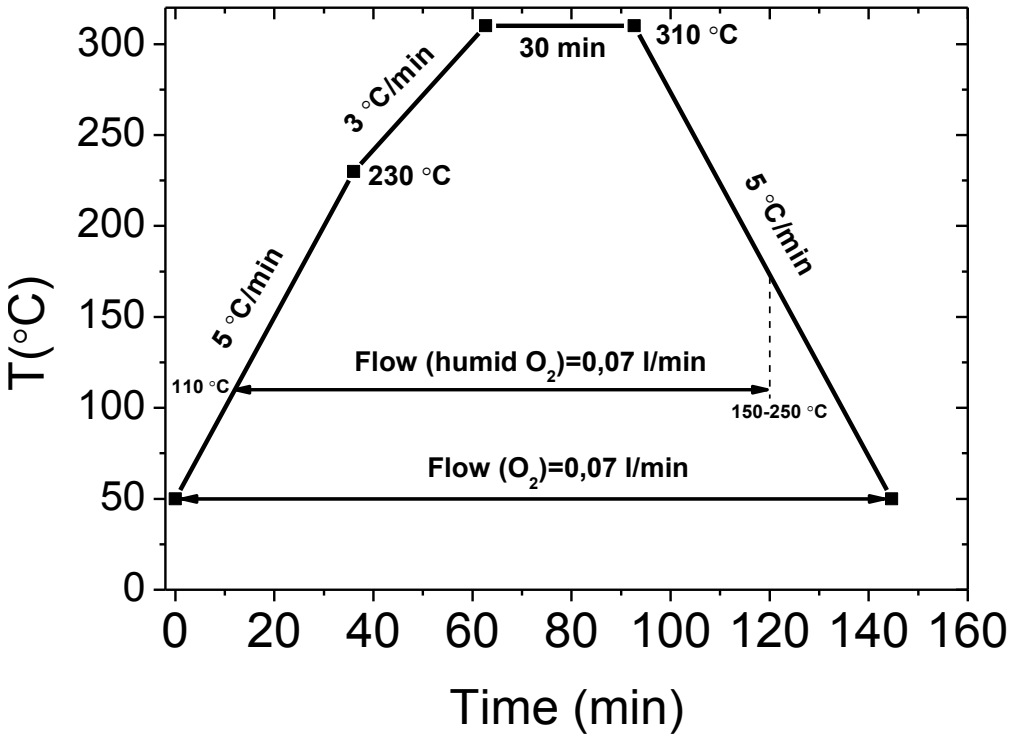

Figure 2.6. Standard pyrolysis process for the TFA-solution.

In the case of the GdBCO-LFS, the pyrolysis process used is very similar to the one shown in figure 2.6 but with the difference that the dwell is performed at 500 ºC instead of 310 ºC. This change is based in the proposed process in the work of Palmer et al[127].

2.1.1.1.4 Growth process

After the pyrolysis, in order to convert the achieved nanocrystalline film into epitaxial superconducting YBCO or GdBCO films, a growth process is necessary.

Figure 2.7 shows the "standard growth process" for the TFA solution[128]. This is a very common process, also optimized by members of the SUMAN group, used to crystallize thin films starting from TFA precursor solutions and also in-situ nanocomposites also from TFA solutions[97, 129-131].

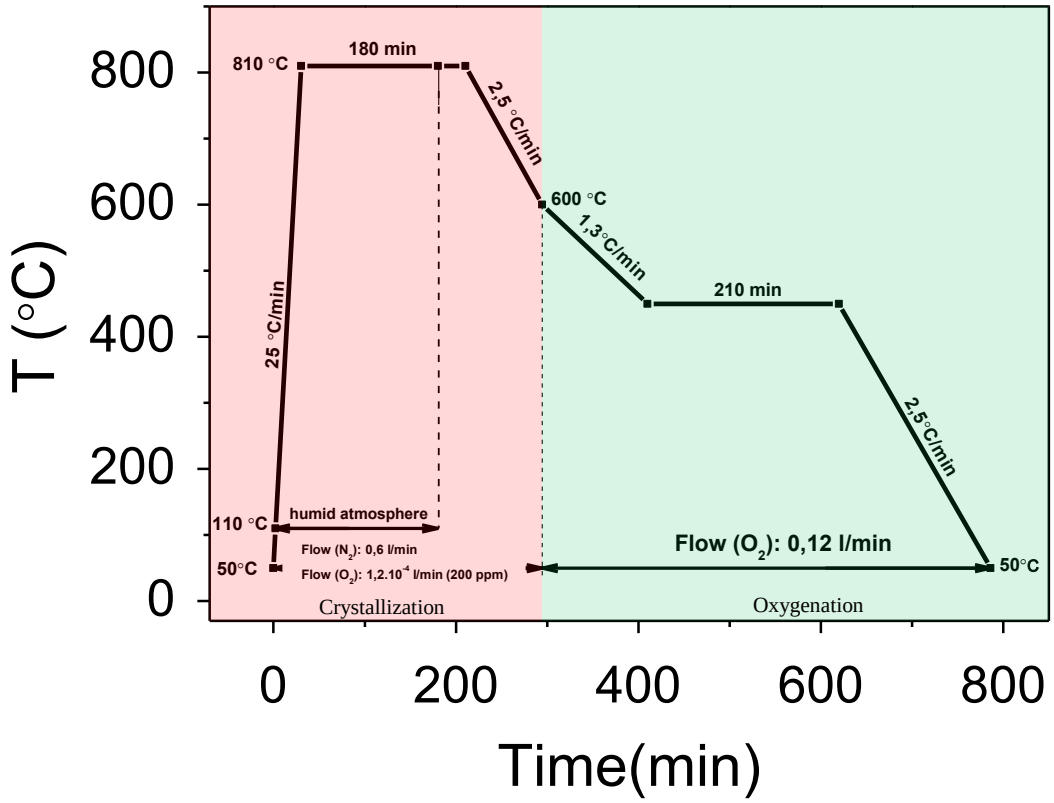

Figure 2.7. Standard growth process for the TFA-solution.

This growth process contains actually two different steps: the crystallization step (red background), in which the epitaxial YBCO is achieved and the oxygenation step (green background) which is required to insert oxygen in the YBCO structure and transform the structure from the tetragonal to the orthorhombic phase (the superconducting one).

The crystallization process takes place in the first part of the thermal profile shown in figure 2.7. First, the temperature is increased up to 810 ºC at a rate of 25 ºC/min. In this stage the epitaxial or c-axis YBCO nucleates and starts to grow. Then, the temperature is maintained constant during 180 min. This dwell is necessary to finish the YBCO growth and sinter the thin film (connect the YBCO grain in order to avoid the porosity in the thin film). The whole process is carried out under humid nitrogen and oxygen flow (see the values in figure 2.7). The water is needed to achieve the YBCO transformation (chapter 1).

The oxygenation process occurs in the second part of this thermal treatment. After the dwell at 810 ºC, the YBCO has finished the growth and sintering processes, but it has a tetragonal structure. So, it is necessary to insert some oxygen in the structure in order to

change it to orthorhombic structure. Therefore, after the dwell, the temperature is decreased until 600 ºC using a ramp of 2,5 ºC/min and here the flow is changed to a 0,12 l/min of dry oxygen. Then the temperature is decreased again to 450 ºC where it is maintained during 210 min in the same O_2 atmosphere. Finally, the film is brought to room temperature with a ramp of 2,5 ºC/min maintaining the same O_2 atmosphere. In chapter 5 the oxygenation process will be studied in detail.

In the case of the GdBCO thin films, this process has to be accommodated to their optimal conditions. In chapter 3, the required changes and the final growth process for the GdBCO thin films will be presented.

2.1.2 Metal-Organic Decomposition (MOD) route

In order to apply the CSD method with success, the chemical precursors must be selected by taking into consideration the following factors: an adequate solubility in the solvent to obtain stable coating solutions, admissible wetting of the substrate, removal of undesired residues after decomposition and elimination of cracks or other inhomogeneities during thermal processing. These requirements can be accomplish by metal-organic compounds since their solubility in either polar or non-polar solvents can be tuned through modification of the organic part of the molecule, and due to the fact that the decomposition of the organic fraction in oxidizing atmosphere does not leave residue[132]. In particular, short−chain carboxylates (e.g. acetates) or strongly chelating β−diketonates (acetylacetonate-type) precursors are usually selected in the so called Metal−Organic Decomposition (MOD) route.

CSD-MOD route is a widespread and straightforward process for the preparation of functional oxide films despite of some limitations that have to be overcome: i) possible film cracking during films drying and pyrolysis processes due to films weight loss and shrinkage during precursor decomposition, ii) film porosity and iii) the limited control of structural evolution and film microstructure. These limitations have been overcome in some cases, as in the case of using acetates and trifluoroacetates (TFA) as chemical precursors.

2.1.2.1 MOD route using trifluoroacetates

MOD route was used shortly after the discovery of YBCO since the potentiality of this approach was promptly notice. However, first results showed low performances of the thin films. These low performances were related to the use of Y,Ba and Cu carboxylate salts (e.g. acetates) which cause carbon contamination in the thin films due to the formation of $BaCO_3$ during growth process, a very stable compound[133, 134].

A solution to this difficulty was first proposed by Gupta et al[135]. They prepared an amorphous precursor film after pyrolysis, very similar to that used for the BaF_2 process[82], by a low-cost non-vacuum chemical route using metal trifluoroacetates as chemical precursors for the preparation of the initial solution. For this reason, TFA-MOD process had been regarded as a kind of the "BaF_2 process". However, the precursor film produced by TFA-MOD is slightly different. In the case of TFA-MOD, it consists of CuO nanocrystallites and an amorphous matrix of $Ba_{1-x}Y_xF_{2+x}$ (BYF) instead of the pure BaF_2 that is found in the case of "BaF_2 process". Thus, this TFA-MOD process is called "fluoride process" instead of "BaF_2 process".

These changes in the composition of the amorphous film allow the decomposition of these metal fluorides in humid atmosphere via HF removal, ending with a total conversion to metal oxides and ultimately to YBCO. The intermediate reactions that take place until final YBCO conversion were deeply studied by Zalamova et al[136] and they are summarize in figure 2.8.

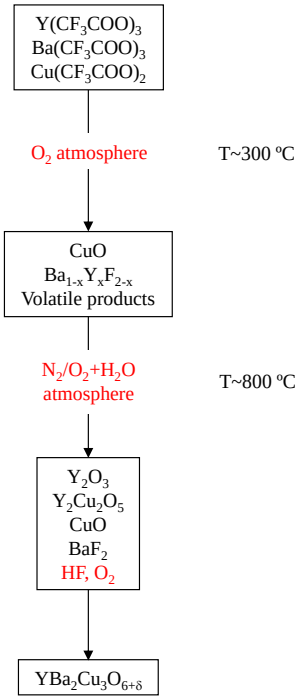

Figure 2.8. YBCO formation pathway from the precursors of chemical solution to the final YBCO thin film for TFA route. Gaseous compounds are written in red.

According to figure 2.8, the initial trifluoroacetates are transformed into CuO and $Ba_{1-x}Y_xF_{2+x}$ (BYF) under oxygen atmosphere during the pyrolysis process performed at temperatures around 300 ºC. This is the amorphous precursor film for the growth process. During the growth process two competing reactions can take place. First one, the main one, starts when BYF decomposes between 500-550 ºC forming $Ba(O, F)_2$ (taking some oxygen) and leaving free Y atoms that reacts forming Y_2O_3. At higher temperatures than 700 ºC, Y_2O_3 reacts with CuO, $Ba(O, F)_2$ in presence of water to form the final $YBa_2Cu_3O_{6+\delta}$ (Eq 2-4). The other competing reaction starts again when BYF decompose leaving free Y atoms that forms Y_2O_3. But, in this case, the Y_2O_3 react with some of the CuO present in system forming $Y_2Cu_2O_5$. (Eq. 2-5). Finally, at temperatures higher than 700 ºC, $Y_2Cu_2O_5$ reacts with $Ba(O, F)_2$ and with CuO in presence of water to form $YBa_2Cu_3O_{6+\delta}$ (Eq. 2-6)[136, 131].

$$Ba(O_x F_y)_2 + 1/4Y_2O_3 + 3/2CuO + yH_2O \rightarrow 1/2YBa_2Cu_3O_{6+\delta} + 2yHF \quad \text{Eq. 2-4}$$

$$2CuO + Y_2O_3 \rightarrow Y_2Cu_2O_5 \quad \text{Eq. 2-5}$$

$$Y_2Cu_2O_5 + 4Ba(O_x F_y)_2 + 4CuO + 4yH_2O \rightarrow 2YBa_2Cu_3O_{6+\delta} + 8yHF \quad \text{Eq. 2-6}$$

Using the TFA-MOD route it is possible to prepare thin films with similar performances as those prepared using in-situ techniques. This shows the potential of this route to fabricate long length CCs with reduced cost[132].

2.1.2.2 MOD route using Low-Fluorine Solutions

Nowadays the science community is increasingly aware of the atmosphere pollution. Mitigate fluorinated compounds emissions, which are highly reactive and toxic, is one of the targets in many industrial processes. In the case of the preparation of long length coated conductors, HF formation and its release to the atmosphere is one of the major drawbacks of the MOD process via TFA from the point of view of environmental contamination.

For this reason, in the last years, alternative routes to the TFA were explored, maintaining the same YBCO performances. One of the most promising alternatives is the use of the so called "Low Fluorine Solutions (LFS)", in which it is possible to reduce the amount of fluorine in the initial precursor solution by an 80%, resulting in an important reduction of HF during the YBCO conversion.

This LFS is a modified TFA solution in which two of the precursor salts are changed from TFA to acetates (no fluorine content). In this way, only one of the three initial salts has fluorine content. The most common solution is prepared using acetates salts of Ba and Cu and maintaining the TFA salt of Y, but it is possible to maintain the TFA salt for any other metal.

One could think that, if the aim is to reduce the HF production during YBCO conversion, the best option is to used fluorine-free precursor salts and completely avoid HF formation. And this is true. However, in this case, the problem is that the reactions that take place to convert the amorphous film after the pyrolysis into final epitaxial YBCO are completely different and much more complicated[127, 137]. For this reason, by maintaining this tiny amount of fluorine in the solution the growth mechanism is the same as in the case of TFA route since the decomposition of these metal fluorides remains through HF removal in humid atmosphere. So, this is still a fluoride process[127, 138]. Figure 2.9 summarizes the YBCO formation pathway starting from LFS. The intermediate reactions that take place are the same than in TFA route, so equations 2-4, 2-5 and 2-6 are also valid in this case.

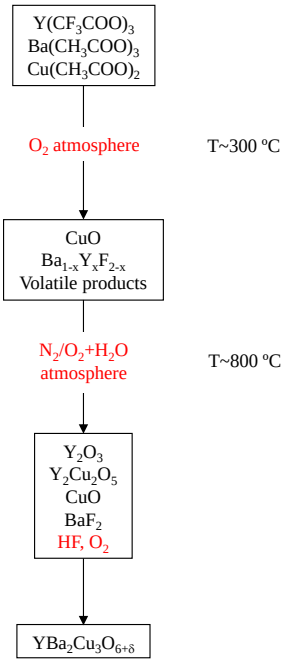

Figure 2.9. YBCO formation pathway from the precursors of chemical solution to the final YBCO thin film starting from LFS solution. Gaseous compounds are written in red.

By using this fluoride process it is possible to obtain excellent YBCO performances reaching the same level of TFA route and in-situ techniques[127, 138, 139].

2.1.3 Basis of thin films crystallization

The transformation of the amorphous films into fully epitaxial YBCO in the CSD method is a complex process which is determine by the nucleation of the desired phase and the heteroepitaxial growth of this phase. The nucleation of the new phase can be analyzed using the Classical Nucleation Theory (CNT). Basically, the CNT states that small clusters of a new phase stabilize if they are able to surpass a thermodynamic barrier G*, which occurs after they grow beyond a critical size r*.

The general approach to calculate this energy barrier considers the formation of a solid nucleus in a supercooled liquid or glass, which has associated a change in the Gibbs free energy ΔG. In CSD-derived heterostructures, the driving force to convert the amorphous films into a crystalline phase is the decrease of Gibbs free energy difference (ΔG_v) between both states[120, 140]. This change can be generally written as (Eq. 2-7):

$$\mathbf{\Delta G = -V\Delta G_v + \Phi} \qquad \text{Eq. 2-7}$$

where the first term takes into account the volume contribution with V= volume of the nucleus and $\Delta G_v = \Delta\mu/v$ is the Gibbs free energy difference per unit volume which depends on the change in chemical potential (Δμ) and the volume of the smallest unit v, e. g., unit cell volume; and the second term accounts for the change in surface energy due to the formation of a nucleus, as well as its surface area.

The difference in the chemical potential between both phases, Δμ, determines the energy barrier to the phase transition. It is, therefore, the driving force to the nucleation. The higher the driving force is, the higher the tendency to carry out the nucleation. It works in this way because the higher the energy barrier is, the higher the accumulated energy in the system and the higher the instability. So, the system tends to remove this stored energy by creating the first nuclei of the crystal and reach a lower energy state. In these conditions, Δμ is called supersaturation.

Figure 2.10 shows the Gibbs free energy (y axis) as a function of the temperature for the different states in a CSD process starting with the amorphous film (blue curve) after pyrolysis and ending with a perovskite crystalline phase (black curve)[120]. It can be observed that these phases are separate by an energy barrier, ΔG_v, which is decreasing as it approaches the melting poing (T_{mp}). In the middle of both phases the equilibrium liquid state is found. The nucleation process is determined by the value of the driving force Δμ which will be defined as: $\Delta\mu = \mu_{crystal} - \mu_{amorphous}$. This value is always negative because the value of the chemical potential of the crystal should be lower than the chemical potential of the amorphous film in order to favor the nucleation. Otherwise, the nucleation would not happen as it would not be energetically favorable.

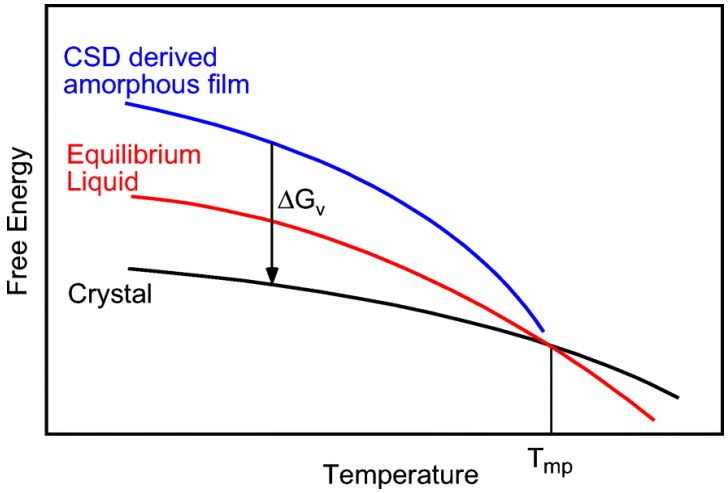

Figure 2.10. Gibbs´s free energy for an amorphous film (blue curve) and the crystalline final phase (black curve). This difference has to be interpreted as the driving force to the nucleation process. The higher the ΔG_v is the more favorable nucleation process. In the middle of both phases it is found the equilibrium liquid (red curve)[120].

The nucleation is the first stage of the phase change, when the first nuclei of the new phase are formed. This phenomenon can occur in a homogeneous or in a heterogeneous way. In the heterogeneous nucleation the nuclei are more likely to form in specific parts of the system such as inhomogeneities, interfaces or on substrate surfaces. On the other hand, if the nucleation is homogeneous, there will be no preferential region for forming the first nuclei and it will happens through the whole volume of the amorphous film. Depending on the type of nucleation, the energy barrier is different. Considering that for homogeneous nucleation the equilibrium shape is often assumed to be a spherical droplet with radius r, the Gibbs free energy barriers is given by (Eq. 2-8):

$$\Delta G^*_{hom} = \frac{16\pi\gamma_i^3}{3(\Delta G_v)^2} \qquad \text{Eq. 2-8}$$

In the case of the heterogeneous nucleation, considering the equilibrium shape as a spherical cap of the same radium r, the energy barrier is given by (Eq. 2-9):

$$\Delta G^*_{het} = \frac{16\pi\gamma_i^3}{3(\Delta G_v)^2} f(\theta) \qquad \text{Eq. 2-9}$$

where γ_i is the interface energy, ΔG_v is the driving force for crystallization and $f(\theta)$ is a function related to the contact angle θ with the substrate that takes a value of $f(\theta)=(2-3\cos\theta+\cos^3\theta)/4$ for the case of an hemispherical nucleus.

The critical size that a nucleus has to overcome in order to be stable is, for both cases (Eq. 2-10):

$$r^* = \frac{2\gamma_i}{\Delta G_v} \qquad \text{Eq. 2-10}$$

Since $0 \leq f(\theta) \leq 1$, the probability to form a nucleus with a size r* is higher in the heterogeneous nucleation case because the barrier is lower.

In the case of YBCO thin films, the goal is the epitaxial growth of the crystalline phase. So, in this case or, in general, in all the systems that require a particular orientation of the crystal, it is necessary to find the conditions which enhance the heterogeneous nucleation against homogeneous nucleation. If the nucleation is heterogeneous, the first nuclei are more likely to appear in the interface substrate-amorphous film and they will grow along the interface and through the film consuming the randomly oriented grains and thus, minimizing the grain boundary energy.

If the driving force is high enough (high values of $\Delta\mu$), the probability of the homogenous and heterogeneous nucleation will be similar as the value of ΔG^* becomes almost equal because, in these conditions, the $f(\theta)$ term becomes less important because there is more than sufficient energy to surmount the energy barriers for all (including less energetically favorable) nucleation events. Hence, there is a mixture of homogeneous and heterogeneous nucleation, emerging nuclei at numerous sites in the entire volume of the amorphous film with identical surroundings and activation energies. This will lead to a large number of very small crystallites thorough the film.

As it can be notice in figure 2.10, the driving force depends on the temperature. This allows the variation of the driving force, determining the nucleation events, by tuning the growth thermal process. The thermal process will determine the total thermal energy present in the system useful to form the nuclei. Film crystallization starts when the temperature is high enough to form the first nuclei. As the temperature increases, more energy is present in the system to overcome the barriers for nucleation events and more nuclei are added. When the temperature is very high, accordingly with figure 2.10, the driving force is smaller. This results in a lower energy barrier for the heterogeneous nucleation due to $f(\theta)$ term and therefore epitaxial growth is achieved.

2.1.3.1 YBCO epitaxial growth from CSD fluoride process: role of the processing parameters

Shortly after the discovery of YBCO, it became clear that there are specific regions in the oxygen pressure (P_{O_2})-temperature (T) phase diagram where c-axis (epitaxial) nucleation is optimal, whatever the in-situ or ex-situ technique is used. The presence of these specific epitaxial growth regions is related with energy barriers for different nuclei inside the heterogeneous nucleation region.

Heterogeneous nucleation in CSD YBCO follows a Volmer-Weber mode. First of all, single islands are formed in random positions on the interface amorphous film-substrate. Then, they grow along all directions to finally coalesce forming a continuous film[141-143]. If the final YBCO film is c-axis epitaxial or not will depend on the direction in which the nuclei appear. In this way, YBCO can nucleate with the c-axis perpendicular to the substrate or with the c-axis parallel to it (a-axis nuclei). The nucleation in either direction depends on the processing parameters used in growth process. The presence of a-axis nuclei in the films is very detrimental for their final properties. Therefore, in the YBCO and, in general, in all the REBCO, it is not enough to find the conditions for the heterogeneous nucleation but it is also required to find the conditions that promoted the c-axis heterogeneous nucleation.

It is possible to define the heterogeneous energy barrier for cylindrical shape of the interfacial epitaxial grains as (Eq. 2-11)[131, 144, 145]:

$$\Delta G^* = \frac{\pi(h\gamma_{lat})^2}{-\left(\frac{h}{v}\right)\Delta\mu-(\gamma_{up}+\gamma_{int}-\gamma_{sub})} \quad \text{Eq. 2-11}$$

where h is the height of the grains, v is the unit cell volume, γ is the surface free energy per unit area (lat= lateral surface, up= upper surface, int= interface and sub= substrate) and Δμ is the chemical potential change per molecule between epitaxial YBCO phase and the precursor random nanocrystalline state (supersaturation).

For different orientations of the grains, the energy barrier is different because the chemical potential is different for each orientation of the grains. When the energy barrier is too low, i.e., the driving force to the nucleation (Δμ) is large, there is a mixture between the nucleation of c-axis and a-axis oriented grains because the probability of both events becomes very similar. Therefore, the c-axis oriented grains nucleation will be favorable at higher energy barriers which mean low values of the driving force (low values of Δμ).

Looking at Eq. 2-11, it is observed that the only way to increase the value of the ΔG^* is to decrease the absolute value of Δμ. (as the Δμ is always negative, the minus is put outside). In this way, it is possible to create a phase diagram ΔG^*-|Δμ|, according to Eq. 2.11, in which there are different regions depending on the grain orientation (figure 2.11).

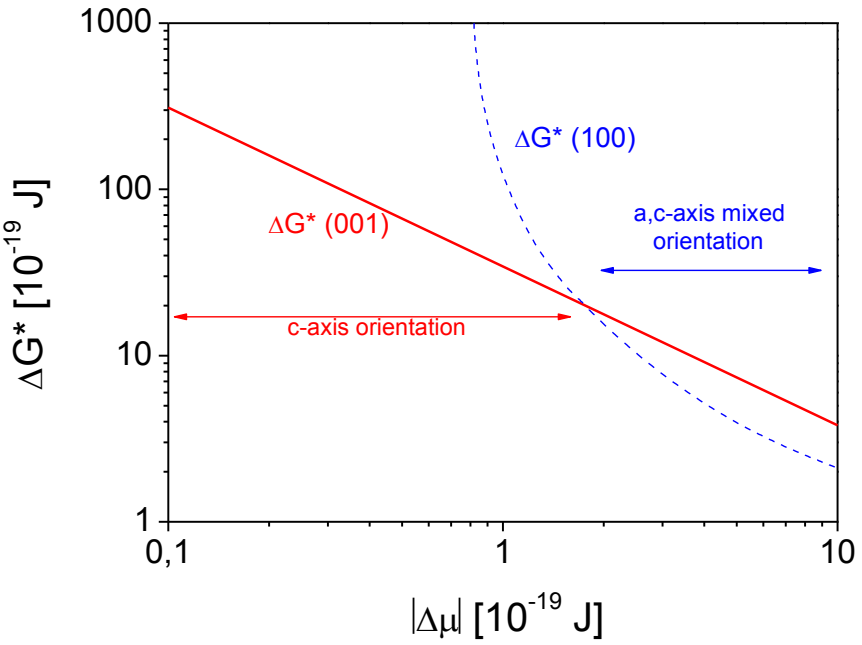

Figure 2.11. $\Delta G^* - |\Delta\mu|$ phase diagram in which the regions for the nucleation of YBCO grains with different are showed[146].

In accordance with figure 2.11, it is predicted that c-axis grains nucleate under low supersaturation conditions while a mixture of a-axis and c-axis nucleation is found under high supersaturation conditions (considering the absolute value). This happens because under high supersaturation conditions the energy barrier for both orientations is very similar[146-148].

Now considering the fluoride CSD process, it was mention that the main reaction to form the YBCO is Eq. 2-4. So, it is possible to define the chemical potential change of this

process, i.e., supersaturation for the change from the amorphous film to the YBCO crystalline film, using processing parameters as follows (Eq. 2-12)[149, 150]:

$$\Delta\mu = \Delta\mu_0 + yK_BTln(\frac{P_{HF}^2}{P_{H_2O}}) \quad \text{Eq. 2-12}$$

where P_{HF} and P_{H_2O} are the partial pressures of HF and H_2O respectively in the vicinity of YBCO nucleus sites, y comes from Eq. 2-4, K_B is the Boltzmann´s constant, T is the temperature and $\Delta\mu_0=\Delta h_0-T\Delta s_0$ with Δh_0=enthalpy (heat of sublimation) and Δs_0=entropy change between the amorphous film and the crystalline YBCO (note that this equation is only valid for ex-situ growth because in the in-situ growth parameters as P_{HF} and P_{H_2O} are not present so, only the first term would be taken into account).

Both terms of the right side of Eq. 2-12 are negative so, in order to find the optimum processing conditions for c-axis nucleation, i.e., the conditions which minimize the supersaturation, it is necessary to analyze each term separately.

The first term in Eq. 2-12 is $\Delta\mu_0$. This value depends on Δh_0, which typically has negative values; Δs_0 which is also negative (the change from an amorphous film to a crystalline film cause an increase in the system "order" resulting in a decrease in entropy) and T. The evolution of $\Delta\mu_0$ with the temperature is presented in figure 2.12. As the temperature is increased, $\Delta\mu_0$ also increases (Δh_0 is the intercept of the resulting straight line), i.e., $|\Delta\mu_0|$ decreases.

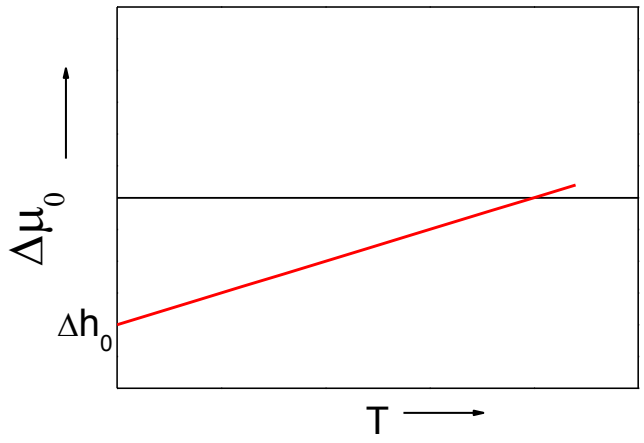

Figure 2.12. Evolution of $\Delta\mu_0$ with the temperature.

The second term is $ykTln(\frac{P_{HF}^2}{P_{H_2O}})$ which depends on $ln(\frac{P_{HF}^2}{P_{H_2O}})$ and T. The value of the $ln(\frac{P_{HF}^2}{P_{H_2O}})$ is negative for the typical experimental values of P_{HF} andP_{H_2O} found in the YBCO reactions (P_{HF} <P_{H_2O})[151, 152]. Therefore, the term $ykTln(\frac{P_{HF}^2}{P_{H_2O}})$ is negative. The evolution of this term with T is shown in figure 2.13. It is observed that, as the temperature is increased, the value of this term decreases linearly. But, the slope of the straight lines depend on the values of the P_{HF} and P_{H_2O}, in such a way that if P_{HF} decreases or P_{H_2O}, increases or both conditions at the same time, the slope of this lines will be higher (more

negative) because the value of $ln(\frac{P_{HF}^2}{P_{H_2O}})$ will be lower (more negative). This is represented with the green and orange curves in figure 2.13.

However, it was found experimentally that both pressures, P_{HF} and P_{H_2O}, are correlated, in such a way that the increase of P_{H_2O} causes an increase of P_{HF}. Both variables are connected by the following equilibrium relationship (Eq. 2-13)[153]:

$$\frac{P_{HF}}{\left(P_{H_2O}\right)^{1/2}} = K_e \rightarrow \delta P_{H_2O} = \frac{2P_{HF}\delta P_{HF}}{K_e^2} \qquad \text{Eq. 2-13}$$

where K_e is the equilibrium constant. It takes a value of 3.10^{-2} $(atm)^{1/2}$ when P_{H_2O}= $3{,}2.10^{-2}$ atm, P_{O_2}=$1{,}3.10^{-3}$ atm and T=740 ºC.

Eq. 2-13 indicates that small changes on P_{HF} cause larger variations on P_{H_2O} and viceversa. In this way, although both variables change at the same time increasing their values, the raise of P_{H_2O} will be always larger than the increase of P_{HF}. This means that the raise of P_{H_2O} will always cause an increase of the slope of the straight lines represented in figure 2.13, no matter the change of P_{HF}.

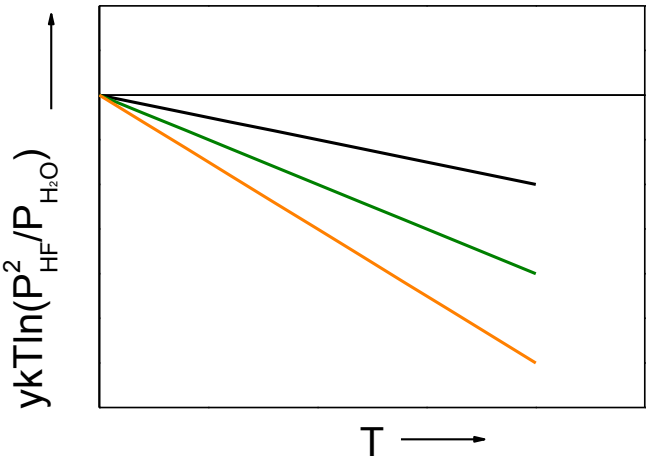

Figure 2.13. Evolution of $ykTln(\frac{P_{HF}^2}{P_{H_2O}})$ with the temperature. Orange and green lines, which have higher slope, represent different conditions of P_{H_2O} and P_{HF} (lower values of P_{HF} or higher values of P_{H_2O} or both at the same time).

Considering this behavior for both terms of the expression of Δμ, it is possible to extract the behavior of supersaturation as a function of T by adding both terms. To extract the sum curve of both terms, it is necessary to analyze the complete expression of Δμ which is shown in Eq. 2-14.

$$\Delta\mu = \Delta h_0 - T\Delta s_0 + yK_BTln(\frac{P_{HF}^2}{P_{H_2O}}) \qquad \text{Eq. 2-14}$$

Reorganizing the terms, the following expression is obtained (Eq. 2-15):

$$\Delta\mu = \Delta h_0 + T[-\Delta s_0 + yK_B ln\left(\frac{P_{HF}^2}{P_{H_2O}}\right)] \quad \text{Eq. 2-15}$$

Looking at Eq.2-15, one realizes that it corresponds to the equation of a straight line with Δh_0 as intercept and $-\Delta s_0 + yk ln\left(\frac{P_{HF}^2}{P_{H_2O}}\right)$ as slope. Knowing that Δh_0 is negative, Δs_0 is also negative and $ln(\frac{P_{HF}^2}{P_{H_2O}})$ is negative too, one concludes that the intercept will be negative and the slope can be positive, zero or negative depending on the values of Δs_0 and $ln(\frac{P_{HF}^2}{P_{H_2O}})$. There is a competition between two different terms: one which is positive ($-\Delta s_0$) against one which is negative ($ln(\frac{P_{HF}^2}{P_{H_2O}})$). Therefore, the slope of $\Delta\mu$ vs. T line (blue lines in figure 2.14) can be positive (case 1 in figure 2.14) if the value of $-\Delta s_0$ is higher than the value of $ln(\frac{P_{HF}^2}{P_{H_2O}})$, zero (case 2 in figure 2.14) if the value of $-\Delta s_0$ is the same as the value of $ln(\frac{P_{HF}^2}{P_{H_2O}})$ or negative (case 3 in figure 2.14) if the value of $ln(\frac{P_{HF}^2}{P_{H_2O}})$ is higher than the value of $-\Delta s_0$. This three cases are represented in figure 2.14 a) using a unique value of Δs_0 (red curve) and three different values of $ln(\frac{P_{HF}^2}{P_{H_2O}})$ (black curves, different slope of the lines). Figure 2.14 b) shows this evolution of the absolute value of the supersaturation to see the three cases more clearly.

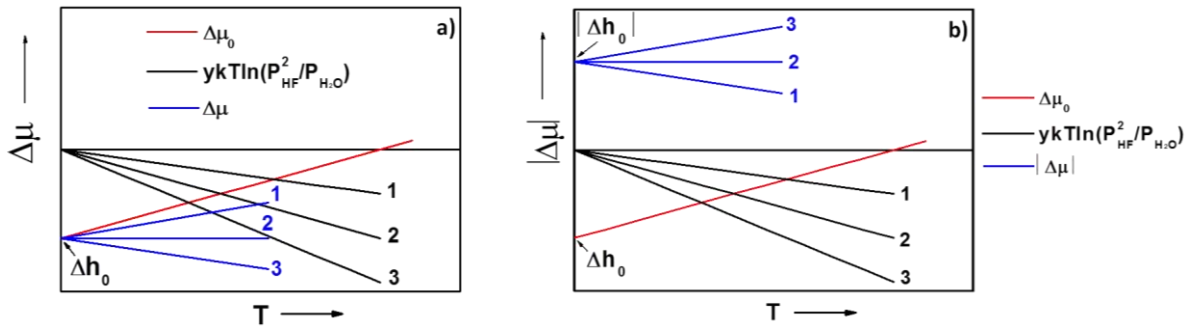

Figure 2.14. Evolution of the a) chemical potential value, $\Delta\mu$, and b) absolute value of supersaturation, $|\Delta\mu|$, as a function of temperature (blue curves) showing the three different cases in which the supersaturation can evolve with the temperature.

Analyzing the blue curves in figure 2.14, one realizes that as the temperature increases, the supersaturation decreases only in case 1, i.e., only when $-\Delta s_0$ is higher than $\left| ln\left(\frac{P_{HF}^2}{P_{H_2O}}\right) \right|$. The optimum conditions would be those which make the $ln(\frac{P_{HF}^2}{P_{H_2O}})$ zero or near zero and this would imply to work with values as similar as possible of P_{H_2O} and P_{HF} (to make the division similar to 1). In case 2 and 3 as the temperature increases the supersaturation either remains stable or increases. For ex-situ techniques, at atmospheric pressure (P_T=1 atm), it was experimentally found that as the temperature is increased, supersaturation is reduced and, therefore, more c-axis nucleation is promoted[154]. This means that, in these conditions, the system is in case 1.

On the other hand, it was also found experimentally that when YBCO conversion reaction takes place at total lower pressures (P_T=0,05 atm) the reduction of the T leads to

greater tendency of c-axis oriented grains nucleation[150]. This implies that, at low pressures, the system evolves as in case 3 of figure 2.14, i.e., the lower the T is, the lower the supersaturation and, therefore, the higher the probability of c-axis oriented grain nucleation. The change from case 1 to case 3 at low pressures is due to the drastic reduction of P_{HF} that the total pressure reduction causes. At low total pressures the mean free path of the HF molecules is enhanced which causes a reduction of the local pressure in the surroundings of the nuclei. The decrease of P_{HF} (and also, to a lesser extent, of P_{H_2O}) cause an increase of $\left| ln\left(\frac{P_{HF}^2}{P_{H_2O}}\right) \right|$ that can surpass the value of $-\Delta s_0$. It is noted, however, that in all the cases the supersaturation at reduced P_T will be higher than at P_T=1 atm.

The supersaturation not only changes due to the variation of the processing parameters, but also it can be due to the geometry or the thickness of the YBCO films. In particular, the increase of the thickness modify the P_{HF} because as the thickness increases, the H_2O, O_2 and HF find more difficulties to diffuse (the impedance of the diffusion increase) creating a pressure gradient. As a result of this, the P_{HF} and probably the P_{H_2O} and the P_{O_2} decrease at the interface, moving away from the optimal values for a perfect c-axis YBCO growth[153, 155]. In general, it was observed that the raise of the thickness cause an increase of the a-axis and randomly oriented grains nucleation[151, 152]. This means that the supersaturation increases with the thickness.

It should be noted that, in all the previous analysis, the effect of P_{O_2} has not been considered. However, there are some works which suggest that P_{O_2} is also an important variable playing an important role when the optimal nucleation conditions are pursued[149].

Most of these variations of the supersaturation values are not observed in the case of the in-situ growth techniques, in which only the first term exists (red curve) making the analysis much easier. The supersaturation decrease with the temperature until of $\Delta\mu_0$ becomes zero (when the temperature is high enough, the product of $T\Delta s_0$ can compensate Δh_0). If T continues to increase, then the supersaturation will start to increase too.

2.1.3.1.1 Nucleation rate

The previous thermodynamic analysis is very useful to distinguish which are the best conditions to achieve c-axis orientation of the grains. However, it is also interesting to determine the rate of nucleation, $\dot{N} = \frac{dN}{dt}$, which is a way to quantify the amount of nuclei that are able to form after overcoming a nucleation barrier ΔG^*. In general, the nucleation rate is a thermally activated process that can be written (obviating the atomic mobility dependence) as (Eq. 2-16):

$$\dot{\mathbf{N}} \propto \mathbf{exp}\left(-\frac{\Delta \mathbf{G}^*}{\mathbf{K_B T}}\right) \qquad \text{Eq. 2-16}$$

where ΔG^* is the nucleation barrier, K_B is the Boltzmann´s constant and T is the temperature.

Eq. 2-16 quantifies the nuclei growth when the nucleation barrier is overcome. The nucleation rate depends strongly with temperature, but it also, depends on other parameters such as P_{HF}, P_{H_2O} or P_{O_2} which determine, as it was shown in Eq. 2-11, the value of ΔG^*.

Figure 2.15 depicts two different typical regimes that can be observed by varying the temperature:

1) The energy barrier to form a nucleus has a dominant role and $\Delta G^* = \frac{1}{(\Delta T^2)}$. ΔG^* rises with temperature faster than $K_B T$, and thus, the nucleation rate decreases with temperature.
2) The energy barrier ΔG^* is too high ($\Delta G^* >> K_B T$) and nucleation is practically suppressed at a critical temperature (T_{cr}) below the melting point (T_{mp}). The driving force ΔG_v is too small as depicted in figure 2.10.

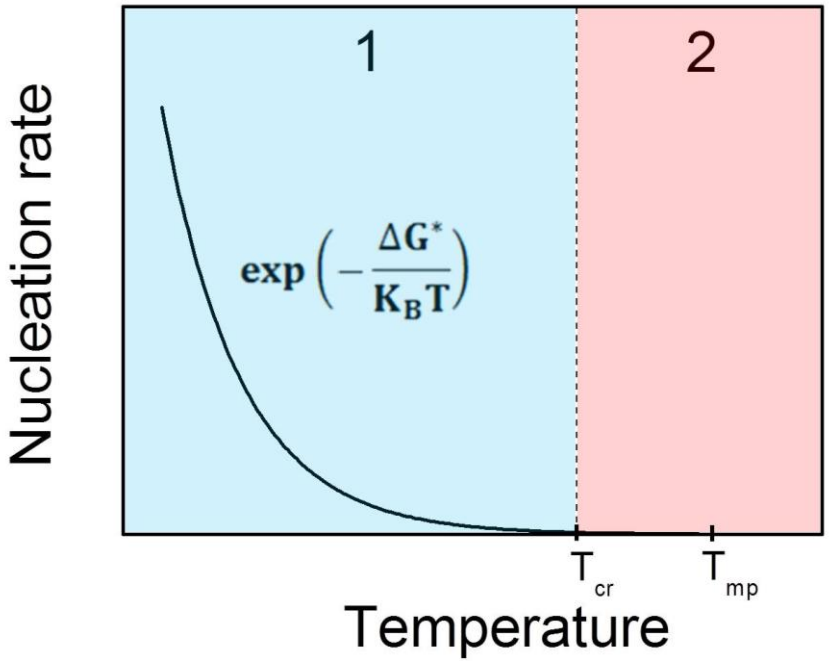

Figure 2.15. Nucleation rate dependence with temperature without considering the effect of atomic diffusion. The energy barrier dominates in the blue region (1) while in the red region (2) the nucleation is practically suppressed as the energy barrier is too high.

Eq. 2-16 is very useful in situations where the formation energies of distinct crystalline orientations are substantially close, allowing the determination of the degree of coexistence between them. In figure 2.16, it is plotted the nucleation rate dependence with temperature of homogeneous ($\dot{N}_{hom}$) and heterogeneous nucleation for the (100) direction ($\dot{N}_{het}^{(100)}$) and (001) direction ($\dot{N}_{het}^{(001)}$) using logarithmic scales and calculating ΔG^* with Eq. 2-8 and Eq. 2-9. The factor $f(\theta)$ was taken as 0,7 for (100) direction and 0,5 for (001) direction.

Since the energy barrier for heterogeneous nucleation is lower than the homogeneous one[156, 157], its rate will be always larger and the difference will increase with temperature as shown in figure 2.16. Moreover, figure 2.16 shows that the regions described in figure 2.15 are shifted towards higher temperatures for heterogeneous nucleation (note in figure 2.16 that the red dashed line that indicates the critical temperature for the homogeneous nucleation is in the left side of the green and blue that mark the critical temperature for the heterogeneous nucleation in the (100) direction and (001) direction respectively). Thus, $\dot{N}_{hom}$ is depressed at lower temperatures as compared to $\dot{N}_{het}^{(100)}$ or $\dot{N}_{het}^{(001)}$ and, therefore, there is a temperature window (between red and blue or

green dashed lines in figure 2.16) in which the heterogeneous nucleation rate is orders of magnitude higher than the homogenous nucleation rate, thus favoring the heteroepitaxial growth. Moreover, it exists a remarkable difference between the critical temperatures of the nucleation rate of the heterogeneous nucleation in (100) and (001) directions as can be observed by the difference between green and blue dashed lines in figure 2.16. This means that, as above with the homogenous and heterogeneous nucleation, there is a temperature window (between green and blue dashed lines in figure 2.16) in which the c-axis (or (001)) nucleation is much favored with respect to the a-axis (or (100)) nucleation.

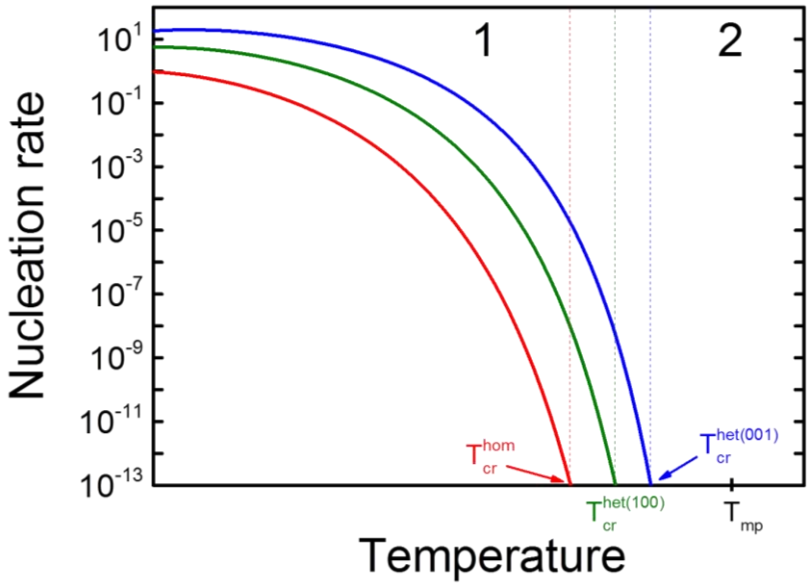

Figure 2.16. Nucleation rate dependence with temperature without considering the effect of atomic diffusion. It is contemplated the homogeneous and heterogeneous nucleation rates in the logarithmic scale. The heterogeneous barrier has been calculated from Eq.2-9 with f(θ)=0,7 for (100) direction and f(θ)=0,5 for (001) direction.

2.1.3.2 Homogeneous and heterogeneous nucleation of NPs in the YBCO matrix

As it was previously alluded, ex-situ techniques and, in particular, CSD-MOD route, allows the modification of the nucleation conditions by changing the processing parameters. In the case of the preparation of YBCO nanocomposites the aim will be to have homogeneous nucleation of the NPs within the YBCO matrix to enhance the vortex pinning properties.

When a new phase is formed within another, its nuclei have to overcome what is called the critical radius, r*, to form the first stable nuclei (Eq. 2.17)[158]:

$$\mathbf{r^* = \frac{2\sigma T_M V}{\Delta H \Delta T}} \qquad \text{Eq. 2-17}$$

where σ is the surface energy, T_M is the melting point, V is the molar volume, ΔH is the molar change in enthalpy and ΔT is the undercooling defined as: $\Delta T=T_M-T$.

To form these first stable nuclei, clusters of atoms have to overcome an energy barrier that, for a spherical clusters, take a value of (Eq. 2-18)[158]:

$$\Delta G^* = \frac{16\pi\sigma^3 T_M{}^3 V^3}{3\Delta H^2 \Delta T^2} \quad \text{Eq. 2-18}$$

According to Eq. 2-18, the energy barrier to form the first stable nuclei is proportional to the inverse square of the undercooling and, therefore, of the temperature. This means that the homogeneous nucleation is favorable at low temperatures. Also, the heterogeneous nucleation is propitious at the same conditions since, in accordance with Eq. 2-9, $\Delta G^*_{hetero} = \Delta G^*_{homo} f(\theta)$. However, at low temperatures, the contact angle which determines the value of f(θ) is higher, and the difference between the two energy barrier is reduced. So, it is at low temperatures where there are more chances to enhance the homogeneous nucleation against the heterogeneous. This strategy has been carried out in some works as in Coll et al[101] in which by performing a nucleation step prior to the YBCO nucleation, they have achieved a homogeneous distribution of small size NPs within the YBCO matrix.

2.2 Characterization techniques

The second part of this chapter explains in detail how the different precursor solutions are characterized and which kind of measurement should be performed in order to obtain the information about the structural, morphological, compositional and physical properties of the synthesized thin films.

2.2.1 Precursor solution characterization

In order to obtain stable and reproducible solutions, both the chemical and physical properties of the different solutions have to be tested. A chemical analysis of the solution is needed to obtain information about the stoichiometry (metal ions concentration), the water content and the pH of the solution. The physicochemical parameters as viscosity or the contact angle are also measured. DLS measurements are needed to check the features of the colloidal solutions used in the ex-situ process.

2.2.1.1 Metal ions concentration

The analysis of the metal ions concentration in the different solutions is crucial in order to verify that the stoichiometry is the desired one. Eventual non−stoichiometries have to be readjusted by addition of the required metallic precursor salts.

The Y^{+3} concentration is analyzed by complexometric titration. When a certain volume of YBCO solution is mixed with deionized water, dimethylurea ($C_3H_8N_2O$) and xylenol orange ($C_{31}H_{32}N_2O_{13}S$), maintaining the pH fixed at 5 (using a buffer solution pH=5), the mixture becomes violet. Then, EDTA (ethylendiaminetetraacetic acid) is added drop by drop until the dissolution changes its color from violet to a yellow-orange. The volume of EDTA used until the color change indicates the concentration of Y^{3+}.

The procedure to determine the Cu^{+2} concentration is very similar to the Y^{3+} one. In this case, iodimetry titration is used. When the YBCO precursor solution is mixed with deionized water, glacial acetic acid ($C_2H_4O_2$), potassium iodide (KI), starch and sodium thiocyanate (NaSCN) the mixture takes a violet-brown color. Then, if a certain volume of sodium thiosulfate ($Na_2S_2O_3$) is added, the mixture changes its color from violet-brown color to a white-yellow. Again, the amount of the sodium thiosulfate used to cause the color change is related with the Cu^{+2} concentration in the YBCO solution.

Finally, the Ba^{+2} concentration is established using a different procedure. In this case is not a titrate methodology but a gravimetric one. In this process potassium chromate (K_2CrO_4 (aq)) acts as precipitation agent. It reacts with the Ba present in the YBCO solution forming $BaCrO_4$ which precipitate. This solid is dried and weighted with an analytical balance. From its mass it is possible to extract the Ba^{+2} concentration.

2.2.1.2 Water content

The water content in the YBCO or GdBCO solution is an important parameter that can decide (as will be seen later) the homogeneity of the films after the pyrolysis. So, it is crucial to control it and maintain it within the acceptable values.

The water content is measured by a Karl Fisher titration. It uses a coulometric or volumetric titration (the water is detected by an electric circuit between an anode and a cathode that works only while water is present in the solution) to determine traces of water in a sample[159]. The measurements were done with a Crison Tritomatic 1S (Karl-Fisher).

2.2.1.3 pH value

The pH value of a solution is an important parameter that determines the compatibility with certain materials. It is measured using a pH-meter Crison GLP 22. The pH determination consists in measuring the potential which develops through a fine glass membrane separating two solutions with different concentrations of protons.

2.2.1.4 Viscosity

The viscosity of a solution is a parameter that has a great influence on the wettability over a certain substrate and the final thickness of the films. It is also a determining factor for choosing the suitable solutions in some deposition techniques as Ink-Jet printing.

The viscosity is measured with a rheometer HAAKE RheoStress RS600 (Thermo Electro, GmbH). The rheometer is a device used to measure the way in which a liquid flows in response to applied forces. In this case, the solution is placed between two cylinders: one is fixed and the other one is rotating at a set speed. The angular velocity causes a shear rate in the sensor system filled with the sample. The torque (shear stress) that the equipment has to apply to maintain this shear rate is related with the viscosity. With the values of the shear rate, shear stress and other geometrical parameters of the system, the value of the viscosity can be obtained.

2.2.1.5 Contact angle

The contact angle is an important parameter that determines the wettability properties of a solution in a certain substrate. The contact angle of the different solutions were extracted from the analysis of images of 2 μl digitized sessile drops photographs taken by a DSA100 equipment (KRÜSS, GmbH) by using the Axysimmetric Drop Shape Analysis (ADSA) technique[160].

The ADSA technique finds the best fitting of the theoretical drop profile to the real one. Theory says that the equilibrium shape of a liquid drop can be numerically determined by solving the Laplace equation of capillarity together with proper boundary conditions. The ADSA software creates an objective function, which represents the discrepancy between the theoretical calculated Laplacian curve and the physical observed drop profile[161, 162].

2.2.1.5 Dynamic Light Scattering (DLS)

The DLS equipment is a technique that is used to determine the behavior of the NPs in colloidal solutions. DLS measurements give valuable information about the size distribution of the NPs in colloidal solutions which can be used to extract conclusions about the degree of agglomeration of the NPs. DLS measurements were done with a Zetasizer Nano ZS (Malvern Instruments) equipment.

DLS measures Brownian motion and relates this to the size of the particles. Brownian motion is the random movement of particles due to the bombardment by the solvent molecules that surround them. Therefore, the larger the particle, the slower the Brownian motion will be. The speed of the Brownian motion is defined by a property known as the translational diffusion coefficient (D) and it is the parameter that is used to measure the size of the particles.

The size of a particle is obtained by calculating the hydrodynamic diameter (d(H)) which is defined as the diameter of a sphere that has the same translational diffusion coefficient as the particle. The d(H) is calculated by using the Stokes- Einstein equation(Eq. 2-19):

$$\boldsymbol{d(H) = k_B T / 3\pi\eta D} \qquad \text{Eq. 2-19}$$

where K_B is the Boltzman´s constant, T is the temperature, η is the viscosity and D is the translational diffusion coefficient.

According to Eq. 2-19 the diameter is dependent on translational diffusion coefficient (D). And this parameter depends not only on the size of the particles core, but also on any surface structure (any structure in the surface will modify the velocity of the particles movement), as well as the concentration and type of ions of the media. For this reason DLS do not measure the core diameter of the particles but the sum of the core and the surface structures.

The measurements are carried out by illuminate with a certain wavelength light the recipient containing the particles in particular liquid medium and measuring the speed at which the particles are diffusing due to the Brownian motion. This is done by measuring the rate at which the intensity of the scattered light fluctuates when it is detected using a suitable optical arrangement.

2.2.2 Thin films characterization

2.2.2.1 Structural characterization

The structural characterization, as it name suggests, is utilized to determine the internal structure of the synthesized thin films. Within this group of characterization techniques, in this thesis, two different techniques were used: the X-Ray Diffraction (XRD) measurements and Transmission Electron Microscopy (TEM)

2.2.2.1.1 X-Ray Diffraction (XRD)

The XRD is a powerful tool for the structural characterization of materials. The fact that the wavelength of the X-rays radiation is of the same order of magnitude as of the atoms size and interatomic distances (Å) allows the study of the internal structure of the matter up to an atomic scale.

The theoretical basis of the XRD measurements is the Bragg law[163]. According to Bragg´s formulation, a given crystal can be decomposed into any number of different plane configurations separated by a constant parameter d (interplanar distance), due to the periodicity of the crystal lattice (figure 2.17). It was found that in these crystals, as a response of X-ray radiation for certain incident angles, intense peaks of reflected radiation will be produced if these reflections interfered constructively. The consequence of that is the Bragg´s law, which describes the condition on θ for the constructive interference appearance (Eq. 2-20):

$$\mathbf{2dsin\theta = n\lambda} \qquad \text{Eq. 2-20}$$

where d is the interplanar distance, θ is the angle of the incident and reflected wave, n is a positive integer and λ is the wavelength of the X-ray radiation.

The Eq 2-20 entails that the constructive interference (which only occurs when the phase shift is a multiple of 2π) only occurs when the path difference between two waves undergoing interference (2dsinθ) is an integer multiple of the wavelength (figure 2.17). This condition is fulfilled, an increment in the diffracted wave is found (constructive interferences) that can be easily detected with an adequate equipment.

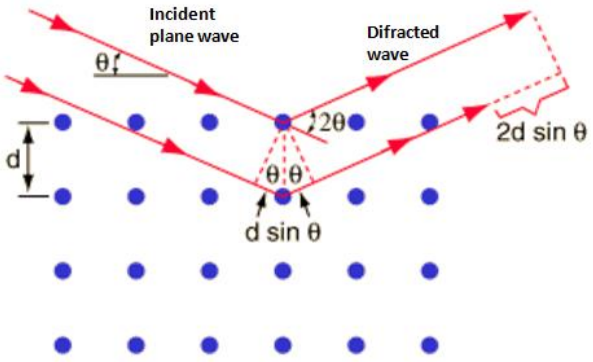

Figure 2.17. Schematic view of how the diffracted wave is formed according to the Bragg´s formulation. Blue points indicate the atoms in the lattice and the red lines are the incident and diffracted waves.

The usual configuration for X-rays diffraction is shown in figure 2.18. The sample is placed in a holder and then X-ray source sends the X-ray radiation to the sample. At the lab scale, the X-rays are generated in the anode of an X-rays tube by bombarding it with electrons. This causes an excite state in the anode material that emits X-ray radiation when restoring the equilibrium state. Depending on the anode material, the emitted wavelength is different. The diffracted wave is collected by a detector. In order to vary the incidence angles, both the source and the detector rotate at the same time obtaining the intensities at each angle.

The pattern obtained when the Bragg law is fulfilled can be identified by comparing it with an internationally recognized data base powder diffraction file (PDF) reference patterns.

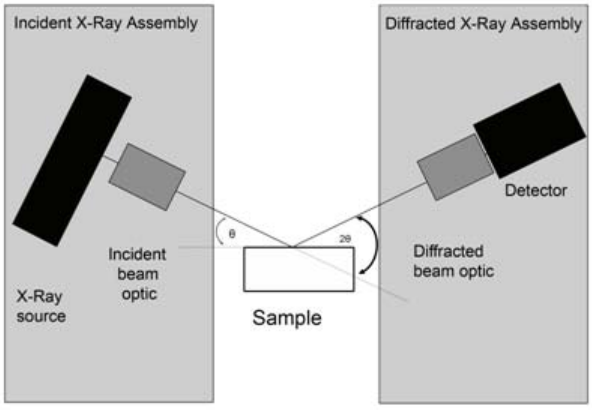

Figure 2.18. X-ray measurements common configuration (Bragg-Brentano configuration).

The intensities of the diffracted peaks depend on the orientation and distribution of the coherent diffracting domains within the sample. This orientation and distribution is different depending on the kind of sample that is being analyzed. A difractogram of a powder sample is different from one of a single crystal or textured sample.

For a powder sample, in which the domains are randomly oriented, the same volume fraction of the sample will accomplish the Bragg´s law (Eq 2-20) whatever the incident beam angle. Therefore, for powder samples, diffraction from different set of planes will always occur. Therefore, the diffracted peaks are clearly observed.

Texture effects are recognized in the difractogram by the enhancement of certain peaks and reduction or even absence of others when compared with a powder pattern of the same material. In particular, in highly oriented samples like single crystals or epitaxial films the Bragg´s law will only be fulfilled for a certain family of planes, those which lie parallel to the surface. In the case of perfect epitaxial thin films with the c-axis perpendicular to the substrate (the ideal case of the YBCO or GdBCO), there are only planes lying perpendicular to the substrate, so only the (00l) reflections will be obtained (the Miller indices h, k and l are used to univocally identified a family of crystallographic planes being h the index for the x direction, k for the y direction and l for the z direction).

For this thesis, three different diffractometers located at ICMAB and a fourth one at the UAB have been used. A Siemens model D-5000, a Rigaku model “Rotaflex” RU-200B and also a diffractometer with a bidimensional detector Hi-Star (GADDS-General Detector Diffraction System) Bruker-AXS model D8 Advance are located at ICMAB while the Phillips XPert equipped with two goniometers and Cu tube is located at the UAB. Each

one can operate at different operation mode and, therefore, give different information about the thin films.

- *Siemens diffractometer*. This difractometer works in the usual configuration showed in figure 2.18. It has a punctual detector that recovers the diffracted radiation intensity to construct the patterns. This equipment is useful for four different kind of measurements:
  1) θ-2θ scans. This scans are carried out in order to identify the main peaks of thin films materials. The 2θ angle of each diffraction peak of the XRD pattern is a characteristic of the interplanar distance, d, in the material. Therefore, the diffraction pattern generated allows the determination of the chemical compound or phase composition of the film. This kind of measurement are performed using the configuration showed in figure 2.18 by moving the source and the detector (varying 2θ) and also the sample (varying θ) maintaining always the relationship θ=2θ/2.
  2) Rocking curves. This type of measurements is made to determine the out-of-plane orientation of the thin films (figure 2.19). To do so, one particular reflection is selected (usually for the epitaxial YBCO and GdBCO thin films the (005) is the most adequate reflection) and the source and the detector are placed at this particular position. Then, the θ of the sample is varied in the selected range. This allows the procurement of information about the width of the selected peak. In particular, the Full Width at Half Maximum (FWHM) is measured and this value gives information about the out-of-plane orientation of the films. The smaller is the FWHM, the better is the out-of-plane orientation.
  3) Nanostrain (ε) measurements. The ε is a measure of the degree of deformation (compression or tension) to which a material is subjected relative to the same object in an undeformed state. These values are given in percentage. To obtain the nanostrain values, usual θ-2θ scans are carried out but using longer acquisition time per point and higher density of measured points to increase the accuracy of the difractograms. It is necessary to avoid the region in 2θ in which the substrate peaks appear in order to not saturate the detector. Once the difractograms are obtained, one can use the Williamson-Hall method to extract the ε along the c-axis (procedure in Appendix A.1)[164].
  4) c-parameter determination. To determine c-parameter of the thin films, it is necessary to perform usual θ-2θ scans but decreasing the step between two consecutive measured points. In the standard θ-2θ scans the step is 0,02º. In this case, the step is decreased to 0,01º. In that way it is possible to obtain very accurate and define difractograms. These difractograms are used to apply the Nelson-Riley method and finally extract the c-parameter value (procedure in Appendix A.2)[165, 166].

a) Out-of- and in-plane disorientation: Polycrystalline film

b) Out-of- and in-plane perfect orientation: Biaxially textured film

Figure 2.19. Sketch of out-of- plane and in-plane orientation concept.

- *Rigaku diffractometer*. This difractometer works in the same configuration as the Siemens one, but it also has a rotating anode that allows increasing the power by approximately 10 times. As both of them are really similar, the same types of measurements are carried out in both: θ-2θ scans, rocking curves, nanostrain measurements and c-parameter measurements.

- *Bruker diffractometer (GADDS)*. This difractometer works in a completely different configuration that the ones presented before (figure 2.20). In this case the film is glued in a vertical position while the detector and source are moving in the horizontal plane (2θ movement).

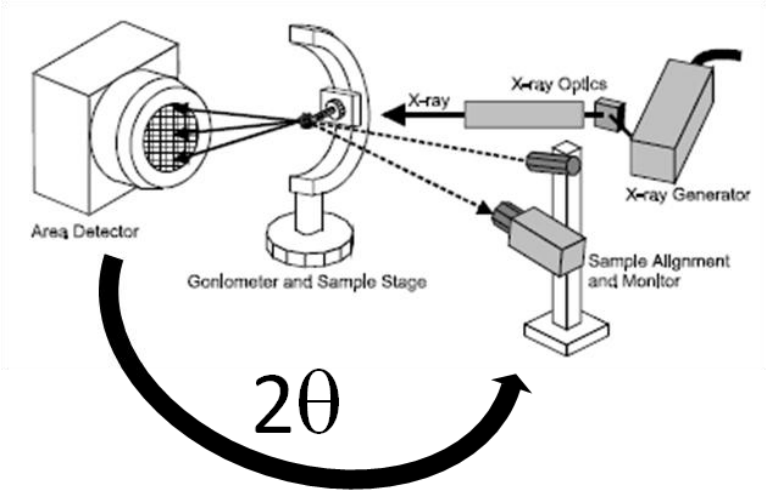

Figure 2.20. Bruker difractometer work configuration.

Another important feature of this difractometer is the freedom of movement of the films. It is possible to move the film in any direction while the measurements are running. This allows the obtaining of much more structural features of the studied films.
In figure 2.21 the different degrees of freedom of the film are shown. It is possible to change the ω position of the films (this is equivalent to varying the θ due to the particular disposition of this difractometer (figure 2.20)), the ϕ which means rotating the film around the z-axis and the χ or ψ (is the same direction so $\chi=90-\psi$).

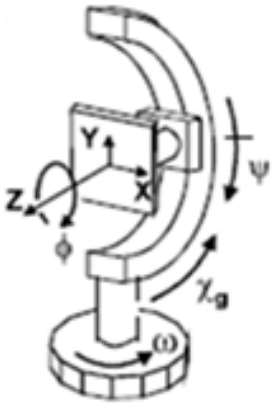

Figure 2.21. Different degrees of freedom of the films on the Bruker difractometer configuration.

Finally the most important feature of this difractometer is its bidimensional detector. This detector is capable of detecting the diffracted photons and also can determine the position in which these photons arrive. Therefore, it is possible to create a 2D diffraction pattern of the thin films (figure 2.22). The x-axis in figure 2.22 is the 2θ position (increasing from the right to the left) and the y-axis is the χ (or ψ) position. These patterns are later integrated using the GADDS software and transformed to a conventional "powder pattern".

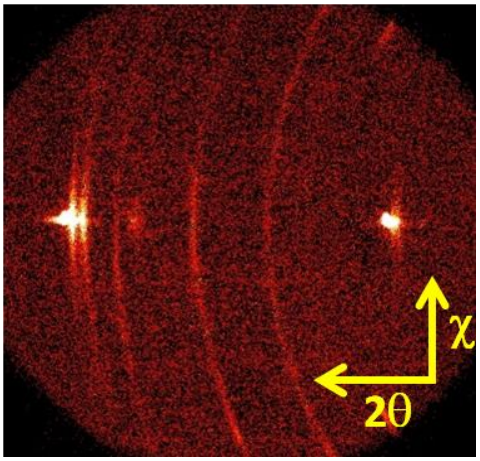

Figure 2.22. 2D XRD typical pattern obtained with GADDS difractometer.

For all this reasons, this difractomenter is much more versatile that the other ones. For this work it was used to perform the following measurements:

1) θ-2θ scans. In the GADDS this scans are made following the same philosophy than in the others difractometers. But here it is not necessary to vary the position of the detector (the 2θ position) since the detector can detect the photons coming from a window of 30º in 2θ. For the usual scans performed in this difractometer (from 20º to 50º) the detector is motionless. So, the movement in ω will be the only movement in this type of scans. The final result is shown in figure 2.22. With this kind of measurement it is possible to know whether a film is epitaxial or polycrystalline and, therefore, its texture. The polycrystallinity is represented by rings because in this case the films are diffracting in all different χ. This means that there are many different planes parallel to the substrate surface and not only those parallel to c-axis. If the films are epitaxial, the rings are replaced by spots in the central line of the image. In this only the planes parallel to c-axis are parallel to the substrate surface.
2) θ-2θ scans for amorphous films. In the case of amorphous films (before the crystallization of the superconducting phase) it is necessary to perform longer measurement times as the amorphous or semi-amorphous diffracted X-rays have very low intensity. The problem is that this operation must be done taking into consideration that the substrate reflections have to be eliminated in order to not saturate and broke the detector. For this reason, it possible to increase the measurement time by reducing the movement range in ω to explore the region without substrate reflections.
3) Random fraction determination. The value of the random fraction of a certain phase is defined as the amount of this phase which is polycrystalline. For example,

if the random fraction is 90% means that the 90% of this phase is polycrystalline or randomly oriented and the other 10% is epitaxial. This value is very important in the particular case of the nanocomposites. As it was mention in the introduction, if the NPs within the matrix are randomly oriented, they will create more incoherent interface between them and the superconductor and therefore more defects that will result in better pinning properties. So it is very important to know the amount of random NPs. To do so, a θ-2θ scan is carried out. Then, the image is analyzed and if NPs are polycrystalline (presence of rings in some reflections) one of the reflections is chosen. The source and the detector are placed in the 2θ of this particular reflection. Then, the film is rotated in ψ to look for the particular ψ of the chosen reflection (for example for the (110)BZO, ψ is 45º). At these conditions, the diffraction pattern is measured. By obtaining the intensity of the ring and the epitaxial part of the studied reflection one can extract the value of the random fraction (see Appendix A.3 to see the procedure more in detail).

- *Phillips XPert difractometer*. This difractometer has been used for powder measurements. It works in the usual configuration Bragg-Brentano configuration, but it counts with a special holder for powders. The θ-2θ scans for the NPs powders have been acquired with this equipment.

2.2.2.1.2 Transmission Electron Microscopy (TEM)

Transmission Electron Microscopy is a structural characterization technique which allows the obtaining of information at the atomic scale. It can use different diffraction and compositional techniques to finally obtain a complete scenario of the materials structural properties at the atomic scale.

TEM uses the same principle as the common optical microscopes in which a beam of photons (in the visible wavelength) is reflected (reflection mode) or transmitted through the sample (transmission mode). However, in the case of TEM, the beam is not of photons but of electrons. The resolution of any microscopy technique is limited by the wavelength. The smaller the wavelength, the smaller the accessible sizes. Since the electrons, behaving as a wave (by the de Broglie principle), have a smaller wavelength than the photons in the visible range (in the order of picometers at the usual working conditions in TEM), it is possible to obtain images of the samples at the atomic scale.

When an electron beam interacts with matter not only the reflected and the transmitted beams are present. An electron beam can cause many other phenomena which are summarized in figure 2.23. Some electrons are reflected as a result of the collision with the atoms in the specimen, the BackScattered Electrons (BSE). Other part of the beam is absorbed by the specimen causing an excitation of the atoms that cause the apparition of Secondary Electrons (SE), Auger electrons (Auger e^-) and X-rays when the atoms come back to the equilibrium state. The SE, BSE and X-rays are used in the Scanning Electron Microscopy (SEM) and in Energy Dispersive X-ray (EDX) analysis. The remaining electrons cross the specimen and become transmitted electrons. These transmitted electrons can be elastic scattered electrons, if they suffer elastic collision with the atoms in the specimen, or inelastic scattered electron, if the collisions are inelastic. To extract the structural composition of the specimen, the elastic electrons are used in TEM and High-Resolution TEM (HRTEM). However, if the required information is compositional, the

inelastic electrons are used in techniques such as Electron Energy Loss Spectroscopy (EELS) or Energy Filtered Transmission Electron Microscopy (EFTEM).

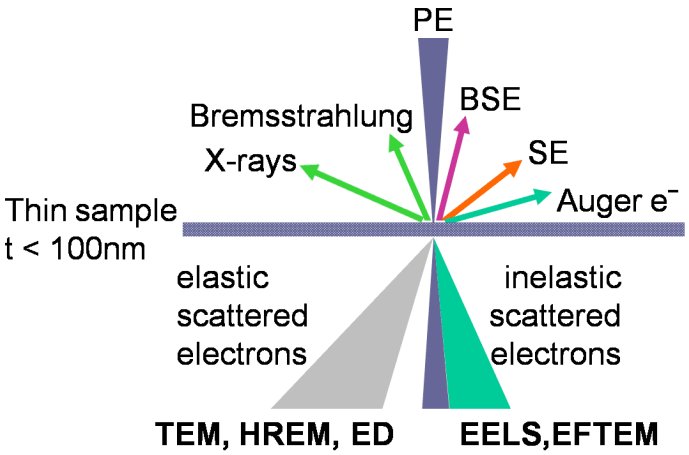

Figure 2.23. Different products resulting from the electron-matter interaction.

The operation scheme of a Transmission Electron Microscope is shown in figure 2.24. A narrow and collimated electron beam is created in an electron gun with a define kinetic energy. This electron beam passes through several condenser lenses that focus or defocus the electron beam depending on the special measurement conditions and several apertures to collimate the beam. The electron beam crosses the specimen and the transmitted beam, after the interaction with the specimen, traverses different kind of lenses (objective, intermediate and projector lenses) that create the final image. All this system is inside a column in which a high vacuum is created.

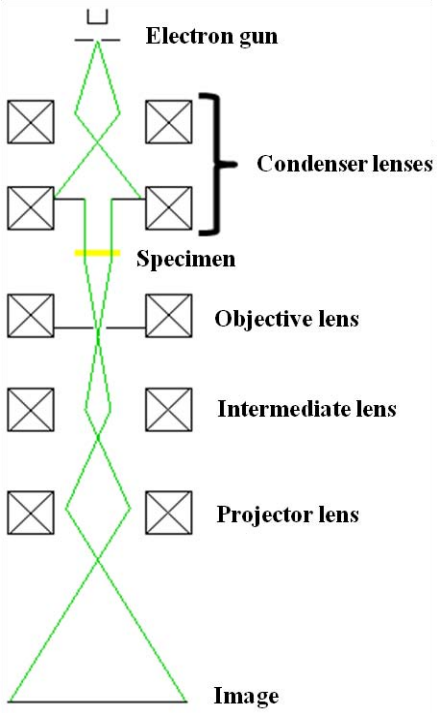

Figure 2.24. Transmission Electron Microscope operation scheme.

An aspect that it is necessary to take into consideration is the width of the specimen. As this technique uses the transmitted electrons beam, the width of the specimen can not exceed the mean free path of electrons in certain conditions, usually in the order of tens of nanometers. So, in order to make the specimens as transparent as possible to the electrons their width have to be in the range of 15-30 nm for the HRTEM measurements.

In this thesis, the TEM analyses were carried out by members of the SUMAN group at ICMAB. They used different TEM equipment depending on the resolution needed for each analysis. Low magnification TEM images and EELS analysis were performed with a FEI Tecnai F20 S/TEM located at Catalan Institute of Nanoscience and Nanotechnology (ICN2). High resolution TEM images and also EELS analysis were performed using Titan low-base (FEI Company) placed at Zaragoza in the "Advanced Microscopy Laboratory (LMA)". It was also used the FEI X-Ant-EM located in the "Electron Microscopy for Materials Science (EMAT)" at Antwerp (Belgium) for high and low resolution TEM images and, specially, for EDAX analysis of the films.

2.2.2.2 Morphological characterization

Morphological characterization in the framework of this thesis is referred to all of those techniques that give information about the surface morphology of the thin films. Therefore, they can be named also surface characterization techniques. Different techniques belonging to this group were used: Optical Microscopy, Scanning Electron Microscopy (SEM), Atomic Force Microscopy (AFM) and the atomic force profilometry.

2.2.2.2.1 Optical Microscopy

In the section about TEM, it was said that both the Optical and the Electron microscopy use the same principle. They use the diffraction, reflection or refraction of electromagnetic radiation/electron beams interacting with the specimen to create an image. In the case of the optical microscopy visible light is used.

The wavelength of the visible light is in the range of 390-700 nm. This implies that the resolution can not be smaller than hundreds of nanometers in the conventional optical system (it is possible to have more resolution in some new systems[167]). Also the penetration depth of the visible light is smaller than the electrons one, only few nanometers in the surface being accessible. For these reasons, for this work, the optical microscope was used only to check the film´s surface, especially after the pyrolysis process.

The homogeneity of the films after the pyrolysis process is very important. It determines if the sample is suitable for the growth process or not. An inhomogeneous film after pyrolysis is not used for the growth process because the final properties are seriously affected. In this thesis, films morphology was characterized using the Leica DM 1750 M optical microscope located at the ICMAB.

2.2.2.2.2 Scanning Electron Microscopy (SEM)

The SEM technique uses the same principle as the TEM but in the case of the SEM, only the reflected (backscattered) and the secondary electrons are taking into consideration to make the analysis.

This is a technique that gives information about the surface morphology of the films. The penetration depth of the electrons in a solid compound is very low, about 100 nm in the usual working conditions. So, the information that it is possible to obtain corresponds only to this first nanometers of film. That is why this technique is in the group of morphological characterization.

The structure of a scanning electron microscope is presented in figure 2.25. The structure is very similar to the one of the transmission electron microscope. It has also the electron gun that generates the electron beam, some condenser lenses to focus and defocus the electron beam and apertures to collimate the beam. Then, the beam passes through a set of plates (the scan coils) that can deflect the electron by varying the potential between them. If these plates are attached to a scan generator, the beam can be made to scan lines across the sample (this system is similar to the one attached to Scanning Transmission Electron Microscope (STEM)). By reducing the size of the area scanned by the scan coils, the SEM changes the magnification of the image. Finally, the objective lenses focus the beam in the desired area.

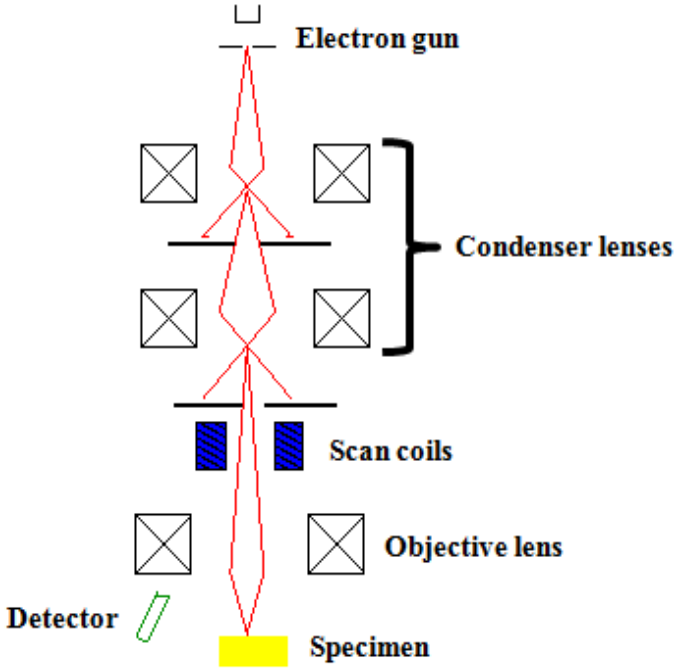

Figure 2.25. Scanning Electron Microscope schematic structure.

The scanning electron microscope has two different detection systems. One is devoted to the detection of Secondary Electrons (SE). The SE (figure 2.23) are low energy electrons resulting from the emission of atoms from the film due to collision of the incident beam. They are ejected from the k-shell of the specimen atoms by inelastic scattering interactions with beam electrons. As they are low energy electrons, they can only come from the first few nanometers of the film. They give an image of three-dimensional appearance of the sample while the beam is scanning a defined area. The contrast that appears in the secondary electron images are produced by the different heights between the different regions in the film. The incident beam scans across the sample's surface topography. If the beam travels into a depression or hole in the film, the amount of secondary electrons that can escape from sample´s surface is reduced and then darker image will be obtained. On the other hand, if the incident beam scans across a projection or

hill on the film, more secondary electrons can escape from the film´s surface and, therefore, the image gets a bright contrast.

The other detection system is devoted to the BackScattered Electrons (BSE). The BSE (figure 2.23) are reflected high energy electrons due to the collision of the incident electrons with the atoms nucleus. These BSE are used to create compositional images of the films. This is possible due to the fact that a material with a higher density will reflect more electrons than a material with less density. A low atomic weight area of the films will not emit as many backscattered electrons as a high atomic weight area of the films. So, in reality, the image is mapping out the density of the sample surface but it is not possible to precise which one of the materials are present in the films.

In this work a SEM Quanta 200 ESEM FEG located at ICMAB was used. SEM images of the fully grown films were taken to study the presence of precipitates, porosity and grain disorientation degree.

2.2.2.2.3 Atomic Force Microscopy (AFM)

AFM is a surface characterization technique that provides precise information about the samples topography. It is based on the detection of nanometric scale forces between the atoms present in certain surface and a sharp tip that is used as probe. Depending on the situation, the forces that are measured in AFM include mechanical contact force, Van der Waals forces, capillary forces, chemical bonding, electrostatic forces, magnetic forces, etc.

The AFM configuration is shown in figure 2.26. It consists of a sharp tip attached to a spring, the cantilever. When the tip approaches a surface, the force between it and the surface leads to a deflection of the cantilever according to Hooke´s law. The degree of deflection of the tip is proportional to the intensity of the force tip-surface. The cantilever deflection is measured using a four quadrant photodiode which is able to detect a laser beam reflected on its back side. When the cantilever is not deflected, the laser beam strikes in the center of the photodiode, but any movement of it will cause a displacement of the reflected laser beam arriving to any of the four quadrants. The four quadrant photodiode allows the quantification of the bending and the torsion of the cantilever and, therefore, measure both the normal and the friction forces between the tip and surface. By moving the tip in a certain region using a scanner with piezoelectric components, it is possible to create a 2D map of the forces present in this area. With an adequate feedback system one can transform the information about the forces into a topographic map of the surface.

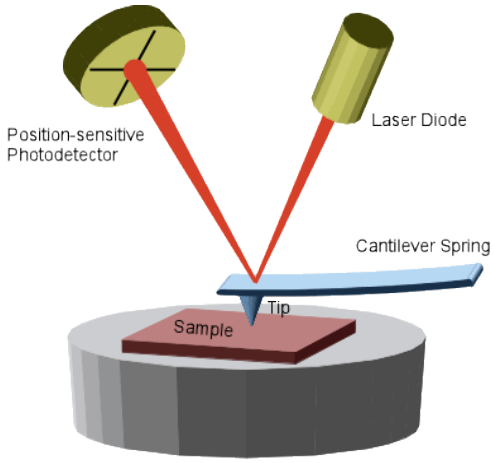

Figure 2.26. Scanning Electron Microscope schematic structure.

An atomic force microscope can operate in three different measure modes depending on the purposes and the environmental conditions:

- *Contact mode*. In this mode the tip is brought close to the surface (<5Å) and the force tip-surface is maintained constant. At these distances the last atoms of the tip feel a weak repulsive force due to the overlap of the electron orbital with the atoms of the surface of the sample causing a deflection of the cantilever. If the tip finds a depression or a hill in the surface, the force will change decreasing or increasing respectively, and the feedback system will move the cantilever up or down in order to maintain the force constant. Recording these movements a topographic map of the surface can be plotted.
- *Non-contact mode*. In this mode, called also modulated frequency mode, the tip hangs 50-150 Å above the sample's surface, thus mainly sensing Van der Waals forces. In this mode, the cantilever is vibrating at its resonance frequency and this frequency is maintained constant during all the measurement. When the tip reaches a hole or a bump in the surface, the frequency changes. So, to maintain the frequency constant, the feedback system displaces the cantilever up or down registering the topography of the sample.
- *Tapping mode*. This mode is a mixture of the other two modes. Here the tip is vibrating with defined amplitude and the tip is in contact with the sample´s surface instantaneously in each vibration. Here the amplitude is maintained constant and, as in previous modes, the feedback system moves the tip to maintain is constant. In this mode problems related to friction, adhesion, electrostatic forces or other difficulties are drastically reduced.

In this work, AFM was used to measure the topography of pyrolyzed samples to extract some quantitave values about the homogeneity of the films. Also it was used to measure the thickness of the pyrolyzed and growth samples.

Thickness measurements require a special preparation of the films. It is necessary to etch part of the film obtaining a "step" between the film and the etched part (the substrate). A standard photoresist is deposit onto the film to protect a define region from the acid. The, the etching is done with orthophosphoric acid diluted 1:10 in deionized water. Finally, the remaining photoresist is removed with acetone.

The AFM analysis presented in this work was done with an Agilent 5100 AFM system from Agilent Technologies installed at ICMAB. The AFM images were processed with Mountains Map software from Digital Surf.

2.2.2.2.4 Atomic force profilometry

The atomic force profilometry uses the same operation principle than the AFM. In this case the measurements are done in contact mode.

The main advantage of profilometry respect to the AFM is the higher analysis area that can reach up to hundreds of μm while the AFM is limited to 80 μm. So, it is possible to analyze a higher area of the films. However, the resolution with the profilometry is much smaller. For this reason the profilometer use is restricted to thickness measurements.

The profilometry measurements were done in a P16 profilometer from KLA Tencor located at ICMAB. The images were processed with Mountains Map software from Digital Surf.

2.2.2.3 Compositional characterization

The compositional characterization is used to identify the different elements present in certain samples. It is also very common that, although the different elements of the sample are known, one wants to find the distribution of these elements in the sample (surface, interface, etc). And this is precisely the role of the XPS and EDAX analysis in this thesis.

2.2.2.3.1 X-ray Photo-electron Spectroscopy (XPS)

The XPS is a surface-sensitive quantitative compositional technique that measures the elemental composition with a great resolution (parts per thousand). This technique uses an X-ray source to excite the atoms and measures the kinetic energy and number of electrons that escape from the analyzed material (figure 2.27).

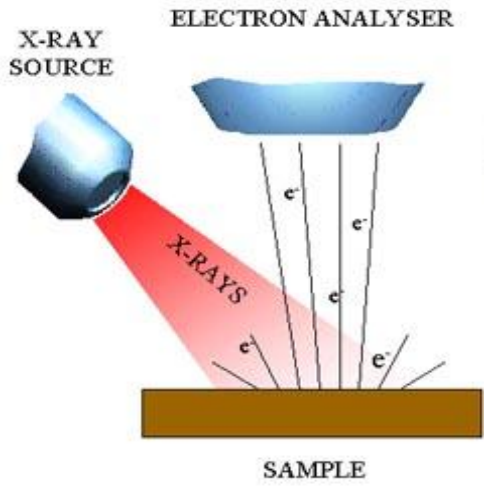

Figure 2.27. XPS operation basis: X-rays excite the surface atoms emitting electron when they come back to the equilibrium state.

When the X-rays arrive to the surface, the photons transfer their energy to the atoms causing an excited state in the atoms. In order to come to the equilibrium state, the atoms emit from their electronic shells. As the used X-rays have a fixed wavelength and, therefore, a fixed energy, each element will behave in a different way emitting electrons of certain energies. The detector can measure the kinetic energy of the emitted electrons so it is possible to extract the binding energy one particular electron as follows (Eq-2-21):

$$\mathbf{E_{binding} = E_{photon} - (E_{kinetic} - \Phi)} \qquad \text{Eq. 2-21}$$

where Φ is the work function depending on both the spectrometer and the material.

Each element emits electrons at characteristic binding energy values. So, by scanning a wide range of binding energies, it is possible to identify all the elements present in the surface. This is done by representing the number of electrons emitted versus the binding energies and looking at the position that different peaks appears. The intensities of the peaks (the number of detected electrons in each of the characteristic peaks) are directly related to the amount of element within the XPS sampling volume. So, by quantifying the peaks it is possible to obtain percentage of each element in the studied area.

In this thesis the XPS was used combined with the sputtering. The sputtering uses a similar concept to the FIB: bombards a material with energetic ions in order to remove material from a target. The sputtering is commonly used to deposit thin films if the removed atoms are deposited over a substrate creating a film.

But in this case the sputtering is only used to remove the atoms that immediately are measured by an XPS. In this way, it is possible to know the composition in the entire volume of the film and not only in the surface. While the sputtering is removing atoms and, therefore, going deeper in the film, the XPS is analyzing the removed material obtaining a compositional map of the cross section.

In this thesis two different XPS equipments were used. The XPS-AES model Kratos AXIS UltraDLD placed at Zaragoza in the "Laboratorio de Microscopias Avanzadas (LMA)" and PHI VersaProbe II Scanning XPS Microprobe placed at the University of Ghent (UG).

2.2.2.3.2 Energy-Dispersive X-ray spectroscopy (EDX)

As it was mentioned previously and shown in figure 2.23, when the electrons interact with the materials´ atoms, X-rays appear coming from ionization of these atoms. The electron beam causes the emission of electrons (secondary electrons). They leave holes in some of the electronic shells. These holes are filled with electrons of the outer shells that emit X-ray radiation to release the energy difference between the higher-energy shell and the lower energy shell.

The number and energy of the X-rays emitted from a specimen can be measured by an energy-dispersive spectrometer. As the energies of the X-rays are characteristic of the difference in energy between the two shells and of the atomic structure of the emitting element, EDX allows the elemental composition of the specimen to be measured.

Usually the EDX spectrometer is coupled with a SEM or TEM system in such a way that they create the electron beam and then the emitted X-rays are measured with the EDX spectrometer. In this way it is possible to obtain compositional information of the surface of a specimen if a SEM system is used or of the cross section if a TEM system is used.

In this work EDX analysis were performed using SEM Quanta 200 ESEM FEG located at ICMAB that has coupled a EDX spectrometer and with FEI X-Ant-EM TEM located in the "Electron Microscopy for Materials Science (EMAT)" at Antwerp (Belgium).

2.2.2.4 Physical characterization

In the field of superconductivity, the physical characterization is carried out in order to obtain the superconductivity properties of the thin films or, in general, of the

superconductor materials. For this purpose, there are two main tools: the Superconducting QUantum Interference Device (SQUID) and the electrical transport measurements. Both of them were used to characterize the thin film synthesized in this thesis.

However, this work also deals with NPs and, in particular, with magnetic NPs. And they require other kind of physical characterization. A deep study of the magnetic properties of these NPs is essential to understand their subsequent behavior when they are mixed with the superconductor material. This magnetic characterization is also done with the SQUID but also synchrotron radiation was used to make an X-ray Magnetic Circular Dichroism (XMCD) study on these NPs and the thin films with these magnetic NPs incorporated to their matrices.

2.2.2.4.1 Superconducting QUantum Interference Device (SQUID)

The SQUID is a magnetometer used to measure the magnetic moment of a sample in a non-destructive and accurate way. The evolution of the magnetic moment can give interesting information about some superconducting properties of the sample as the T_c, the J_c or the behavior of these materials when an external magnetic field is applied.

The SQUID operation is based on the Josephson effect which postulates the appearance of a electric current between two separated superconductors[26]. The Cooper pairs in the first superconductor can cross the insulating gap between the two superconductors by tunneling effect (a quantum effect at the nanoscale by which a particle can penetrate through a potential barrier higher than the kinetic energy of the particle itself) creating a current in the second superconductor. Although, the Cooper pairs can not exist in an insulator or non-superconducting metal, when the layer that separates the two superconductors is sufficiently narrow, they can cross and save the consistency of phase. It is the persistence of this phase coherence that leads to the Josephson effect.

A DC SQUID consists of two Josephson junctions connected in parallel on a closed superconducting loop. Applying current to the SQUID sends Cooper pairs of electrons tunneling through the junctions causing a magnetic field enclosed in the superconducting rings that can take values only in multiples of a universal constant called the flux quantum ($h/2e=2.07\times10^{-15}$ Wb). The sample is placed in a detection system composed by a set of pick-up coils where it is submitted to repetitive movements. With each movement, the electromotive induced force in the coils changes. These coils are inductively coupled with SQUID sensor causing changes in the current that is flowing in the superconducting loop. This will cause a change in the enclosed magnetic field which results in a change in the measure output voltage. So, actually the SQUID works as magnetic flux-to-voltage transducers where the sensitivity is set by the magnetic flux quantum. The output voltage, after a correct calibration of the system, is proportional to the magnetic moment of the sample.

Superconducting properties of thin films such as T_c and J_c are obtained from magnetic moment measurements performed with the SQUID. Also the magnetic features of the magnetic NPs are obtained using the SQUID (details about how the measurements are performed in Appendix B).

In this thesis the SQUID was used to measure field and temperature dependent magnetization curves of thin films and also NPs using Quantum design MPMS XL-7T SQUID.

2.2.2.4.2 Electric transport measurements

Electric transport measurements have been performed in order to obtain the critical current densities of the thin films and, specially, to deeply study the vortex pinning behavior on in-situ and ex-situ nanocomposites.

Superconductor materials can support high electrical currents without dissipation. The main consequence of this is the need to confine the electrical current in bridges with relative low cross-section to be able to perform transport measurements. By doing so, critical current density ($J_c = I_c/A$, where I_c is the critical current, and A the cross-section of the bridge) can be reached at these bridges with relatively low applied currents.

The preparation of the bridges is done with a pholithography process[168]. A 4-point bridges configuration is chosen in order to avoid the measurement of the contact resistance (figure 2.28), but this configuration can be changed if it is required. The typical dimensions of the bridges can vary as a function of the desired study but generally, they are between 100−200 μm length, and 5−50 μm width. Prior to the preparation of the bridges, silver contact pads were deposited by thermal evaporation at 10^{-6} mbar on the thin films and, then annealed under oxygen atmosphere at 450°C for 1 h to ensure good electrical contacts with resistances below 10 μΩ.

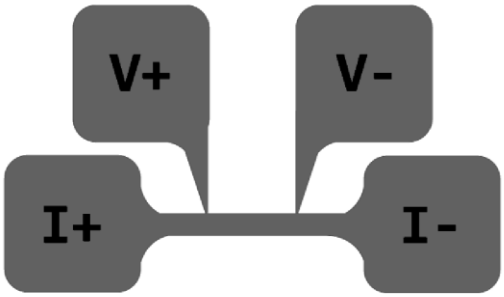

Figure 2.28. 4-point bridge configuration used in the transport measurements[169].

Electrical transport measurements were carried out in collaboration with expert members of the SUMAN group out with a Physical Properties Measurement System (PPMS) from Quantum Design at ICMAB. The system essentially consists of a 9 T superconducting magnet and a helium cryostat. Precise control of temperature within the range 1,8-400K can be achieved. The samples were mounted in a single-axis rotor with a total angular range of 370° with a precision of 0.1°. The system also has a nanovoltimeter and a dc/ac current source which can provide currents from 1 μA to 2 A with a resolution of 0.1 μA.

Two different kinds of measurements have been performed in order to analyze the superconducting performances of our samples: resistivity measurements to determine the critical temperature and irreversibility line, and V(I) curves for J_c analysis (see Appendix C for more details).

2.2.2.4.3 Synchrotron measurements: X-ray Magnetic Circular Dichroism (XMCD)

The synchrotron radiation can be used for structural, morphological, compositional or physical characterization. But it was included in this latter group because in this thesis it

was used to measure the magnetic properties of NPs and YBCO ex-situ nanocomposites made with magnetic NPs. In particular, X-ray Magnetic Circular Dichroism (XMCD) measurements were carried out.

The synchrotron radiation is generated in large scale scientific facilities. It is produced when charged particles moving at relativistic speed are accelerated radially. In order to do this, groups or charged particles (that usually are electrons) are deflected by bending magnets, undulators or wigglers.

In the synchrotron facility the electrons are generated in an electron gun and then they are accelerated in discrete packets up to certain energy in a linear accelerator (linac) that uses a series of RF (radiofrequency) cavities operating at certain frequency. After that, they are travel to the booster synchrotron in which the electrons are further accelerated up to energies in the range of GeV. Finally, the electron packets are introduced in the storage ring. The storage ring has the bending magnets, undulators and wigglers where the electrons generate the synchrotron radiation perpendicular to their direction. The beamlines are located in the places where the radiation is generated. Here the generated radiation is exploited for different purposes (figure 2.29).

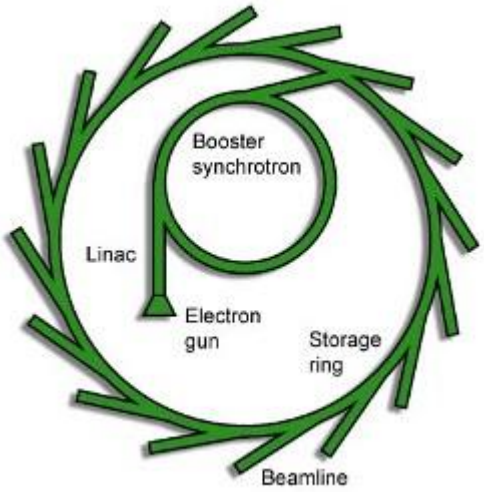

Figure 2.29. Basic scheme of a synchrotron facility

In this work the synchrotron radiation was used to carry out XMCD measurements in NPs and in YBCO thin films with the same NPs embedded in its matrix. XMCD, which is based on X-ray Absorption Spectroscopy (XAS), is a characterization technique that studies the composition and magnetic behavior of, principally, magnetic samples.

A dichroic material is one that presents different light absorption depending on the light polarization. The dichroic absorption in magnetic atoms depends also on the magnetization intensity and orientation caused by an external magnetic field. Therefore, by measuring the XAS spectra for both circular polarization senses (right-handed (RCP) & left-handed (LCP)), and subtracting one respect to the other, the XMCD spectrum is obtained. XMCD occurs only in magnetic samples because it is only caused by the magnetic atoms of the sample.

XMCD is a technique which uses circular polarized light to produce transitions between different electronic levels (especially from 2p to 3d) to study the magnetic behavior of a specific magnetic atom. RCP and LCP XAS spectrum are measured separately as a function of the photon energy (in the range of KeV) and under the same

magnetic field. XMCD spectrum results from the subtraction of RCP and LCP spectra (figure 2.30).

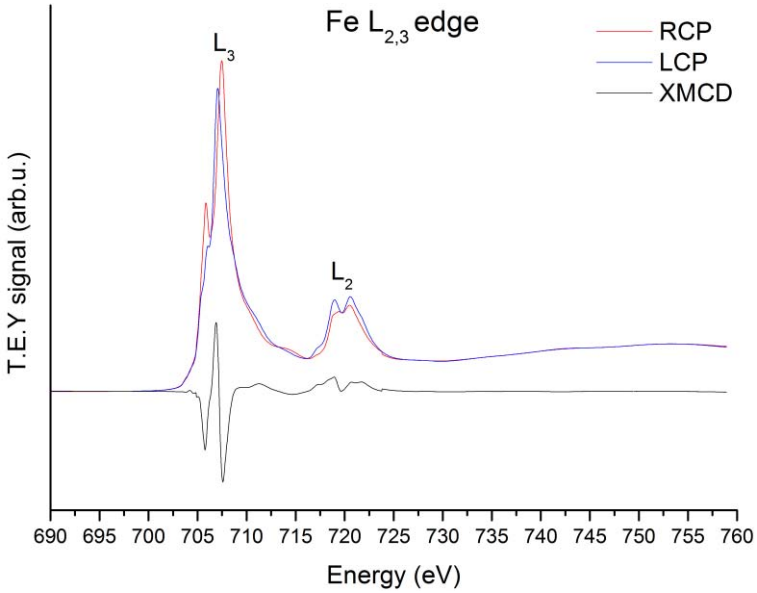

Figure 2.30. Figure showing the L_2 and L_3 absorption edge of Fe, the XMCD signal and their integration [170].

Both the XAS and XMCD spectra depend on the photon energy, which is related to the energy gap between the electronic levels. The maximum absorption and the shape of the peak depend on the atom (chemical specificity) and, more precisely, on the oxidation state. With the adequate tools and analyses, structural and chemical information can be extracted from the XAS spectrum. XMCD shows, by its part, the magnetic behavior of the studied atom. A null signal indicates a non magnetic atom, while peaks demonstrate a deviation between the RCP and LCP absorption, providing the existence of a magnetic moment in the atom. XMCD signal is sensitive to detect even a 0.001 μ_B.

The XAS/XMCD measurements have been carried out in the BOREAS beamline at the ALBA synchrotron (Cerdanyola del Valles, Barcelona) in collaboration with Dr. Elena Bartolomé and Dr. Eduardo Solano. Nanoparticle samples (0,1 g or less) were fixed on a gold coated sample holder with double-side carbon adhesive tape as support. This sample holder was introduced into the HECTOR UHV (Ultra High Vacuum) chamber, where the sample was magnetized in a magnetic field up to 5 T parallel to the beam direction at room temperature. The almost incident circular polarised light was produced by an APPLE II undulator that allows the control of the polarisation handedness between the right circular polarisation (RCP) and left circular polarisation (LCP). The measurements were performed by monochromating the soft X-ray beam with a low-energy grating monochromator (<1200 eV) and passing through entrance and exit slits, typically using 15 micron vertical openings for high resolution and flux, and much wider in horizontal opening (1000 microns).

2.2.2.4.4 In-situ resistance measurements

The in-situ resistance measurements are used to monitor “in-situ” the growth rates and the oxygen diffusion kinetics of the YBCO thin films. In this work the in-situ

resistance measurements were employed to investigate the oxygen diffusion process in YBCO and YBCO nanocomposites thin films.

Figure 2.31 shows the experimental setup used to perform the measurements. The system was designed and built by members of the SUMAN group. It consists on a silver holder in which the samples are connected by joints between silver threads (figure 2.31 d)), which are introduced in alumina tubes, to a current source and a nanovoltimeter (figure 2.31 b) and e)). The current is the input and the voltage is the output. With both values one can find the resistance. Both the current source and the nonovoltimeter are connected to a computer to register the data (figure 2.31 e).

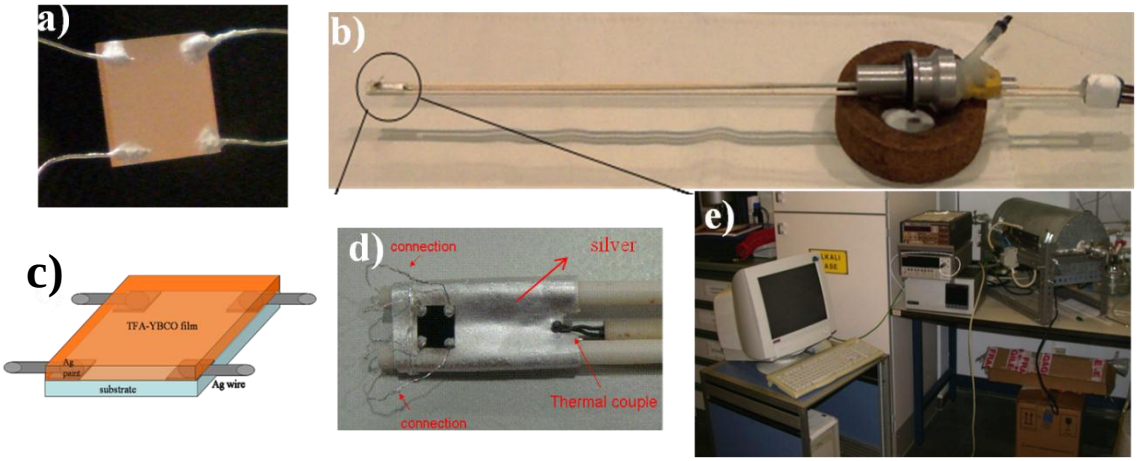

Figure 2.31. In-situ resistance measurements experimental setup.

The preparation of the samples involves more steps than in the usual YBCO films due to the presence of the silver threads. The preparation of the samples can be summarize in the following steps**:**

- Placing Ag contacts on the corners of a clean LAO substrate using 10 mm and 0,1 mm of diameter silver wire.
- Curing Ag contacts through high temperature annealing (900 ºC during 6 min using a heating rate of 3 ºC/min to heat up and cool) to attach them firmly to the LAO surface.
- Depositing the metalorganic YBCO solution by spin-coating and pyrolyze the organic material (standard pyrolysis process).
- In-situ resistance measurements.

3
CSD In-Situ Nanocomposite Thin Films

This is the first of two chapters that are focused on nanocomposite thin films and it is devoted to the CSD in-situ nanocomposites (in this chapter the expression "in-situ nanocomposites" is referred to the approach that is choose to prepare the nanocomposites using the CSD methodology, it has nothing to do with the "in-situ growth techniques" mentioned in the introduction). As it was mentioned in the introduction chapter, the development of the nanostructuration of REBCO matrix started very early after its discovery with the aim to improve the superconducting performances of the pristine REBCO samples. The evolution of this process has resulted in the introduction of NPs embedded in the REBCO matrix. This has opened the possibility to increase the REBCO performances by enhancing the vortex pinning properties of these nanostructured materials when the size of the NPs or the defects introduced by them approaches the superconducting coherence length (~2-4 nm). In particular, with the use of ex-situ growth techniques, with CSD as clear reference, one can tune the NPs features which allow to nanoengineer the material and, consequently, alter its microstructure looking for the best possible performances. This chapter will be devoted to study the microstructure and the properties–derived for YBCO and GdBCO in-situ nanocomposites films.

Apart from the nanostructuration of the pristine REBCO films, another important objective, from the industrial point of view, is to increase the thickness of the films. The increase of the films thickness using ex-situ growth techniques poses particular difficulties which differ from those appearing when in-situ growth techniques are being used. In this chapter, a preliminary study of the difficulties that appear when the thickness of the CSD-derived YBCO in-situ nanocomposites films increases will be exposed.

3.1 Introduction

The "in-situ nanocomposites" is one of the approaches to prepare nanocomposite thin films using sequential deposition and growth techniques. This is characterized by the fact that the NPs are spontaneously segregated during the thermal growth process. Using the CSD method, it is possible to modify the features of the NPs by varying its nucleation process. The nucleation of the NPs, which usually precedes the REBCO nucleation, can be tuned by changing the processing parameters in the growth process (heating ramps, P_{O_2}, P_{H_2O}, etc). This is something that it is not possible to carry out with the use of in-situ growth techniques due to the simultaneous nucleation of NPs and the REBCO which leads to epitaxial NPs embedded in its matrix[106, 14, 107].

The features of the NPs clearly determine the microstructure of the final thin films and, therefore, its final properties. The pinning efficiency of the solution derived YBCO nanocomposites is very dependent on the type of NPs nucleation and, therefore, the heterogeneous or homogeneous nucleation of the NPs will define the performances of the synthesized films[13, 97].

When the NPs are trapped within the matrix of REBCO, incoherent interfaces are very often formed depending on the mismatch between the NPs and the REBCO. This leads to the generation of an interfacial energy in the interface region. This effect is further increased when the NPs are randomly oriented (greater amount of incoherent interfaces) and, therefore, the amount of accumulated interfacial energy is larger. When the accumulated energy is too large, the system releases it by creating Stacking Faults (SFs), which are the responsible for the pinning effect[101, 97, 108]. The partial dislocations that are generated in the perimeter of the SFs create strained regions that prevent the Cooper-pair formation. Therefore, these regions behave as normal areas in which the vortices will be pinned[97, 113].

The pinning efficiency has been recently correlated with the nanostrain (ε) generated within the REBCO matrix due to the partial dislocations associated with the SFs, in the particular case of the YBCO[97, 101]. The presence of the SFs is related with the incoherent interfaces between the NPs and the YBCO which mainly arises from the percentage of randomly oriented NPs in the matrix and their size (see figure 1.21 in chapter 1)[97]. This is simply explained knowing that if the random fraction is higher, more NPs are randomly oriented, leading to a higher incoherent interface value and, consequently, more accumulated interfacial energy. To release this energy, more SFs are generated resulting in an increase of the nanostrain which is proportional to the pinning force.

Considering all the previous statements, it is possible to say that the features of the SFs, i.e., the SFs scenario, will affect the films properties. However, its relationship with the properties of the films is poorly understood and, therefore, a thorough study in this sense is needed in order to further increase the nanocomposite thin films performances. For this purpose, several "mixt compositions" of NPs were added to the YBCO creating different kind of nanocomposites. The study of the superconducting properties of these mixt composition nanocomposite films with different SFs scenarios and, consequently, different microstructure, will provide additional information about the role of the SFs on the vortex pinning properties.

3.1.1 CSD YBCO nanocomposites with NPs mixt secondary phases

The mixt nanocomposites are prepared by using two different kinds of NPs in such a way that the whole system is formed by the YBCO as superconducting matrix and two different nanosized secondary phases. The aim of the mixt nanocomposites is to better understand the effect of the NPs compositions and the generated structural defects on the nanostrain and, therefore, on the pinning properties.

In the mixt nanocomposites the purpose is to combine NPs that nucleate in a different way in the YBCO matrix. It is well known that, using CSD, the $BaZrO_3$ (BZO) and Ba_2YTaO_6 (BYTO) NPs tend to nucleate homogeneously giving high percentages of random fraction (> 90% in both cases) and, consequently, high values of nanostrain (> 0,2%)[97, 101, 114, 171, 172]. However, in the case of Y_2O_3 (YO), the NPs have a greater tendency to be epitaxial in the YBCO matrix due its low mismatch with the YBCO (-2,7%) resulting in low values of random fraction (< 50%) and also low values of nanostrain (< 0,15%)[97]. The effect of each NPs separately is known but there are no studies up to now about the effect of the combination of epitaxial NPs with polycrystalline NPs (BZO+YO or BYTO+YO) in CSD-derived YBCO in-situ nanocomposites. It is also unknown the result of combining two different kinds of NPs that tend to nucleate homogeneously (BZO+BYTO).

In this chapter, four different mixed compositions are studied: (i)YBCO+10%M BZO+5%M YO (YBCO+BYTO+YO), (ii) YBCO+6%M BYTO+5%M YO (YBCO+BYTO+YO), (iii) YBCO+6%M BYTO+10%M CuO (YBCO+BYTO+CuO) and (iv) YBCO+5%M BZO+6%M BYTO (YBCO+BZO+BYTO).

3.1.2 YBCO nanocomposite thick films

The transition to thick YBCO films is viewed as one of the key ingredients of the commercial success for the YBCO wire technology. The higher the thickness is, the larger the amount of current that the CC can carry and the lower the length of the CC that is needed for a certain application. In the lab scale, thin films that do not exceed the 500 nm are usually investigated. However, for their use in real applications, the superconducting films have to overcome, at least, the barrier of the 1 μm.

To achieve > 1 μm thick superconducting films with good performances is not an easy task, especially when ex-situ growth techniques are used. Several works, in which the BaF_2 process is used, show the difficulties of increasing the thickness. When YBCO thick films are being synthesized, the growth conditions used for thinner films have to be changed in order to achieve c-axis oriented grains[173, 174, 142, 153, 155]. This results in a drop of the J_c values as the thickness increases[155, 175-177]. The use of the CSD method adds another difficulty: the defects (cracks and buckling) that appear in the films during the pyrolysis process. These defects are due to the stress generated during the process caused by the shrinkage of the films and they limit the superconducting performances of the films[178].

Until now, most of the work related with the thickness increase was done in pristine YBCO films. Only few reports about this issue in REBCO nanocomposite films were published using PLD and CSD[179, 180]. However, these works demonstrate the potential of this kind of films for applications since a critical current of 717 A/cmW at 77 K self-field were achieved in a 3,6 μm PLD EuBCO+BHO film[179]. In this thesis, YBCO+10%M BZO nanocomposites films, with thicknesses varying from 200 to 700 nm, are studied. The

structural and physical properties have been analyzed in order to find the parameters that determine the conditions for obtaining epitaxial nanocomposites films.

3.1.3 CSD GdBCO nanocomposites

The main interest for the use of GdBCO is the possibility to increase the YBCO performances at high temperature due to an upward shift of its irreversibility line. This is a consequence of the higher T_c that GdBCO films show with respect to YBCO films.

The strategies that have been employed to synthesize the GdBCO samples are similar than in the case of the YBCO. Different research groups started to prepare bulk samples but, nowadays, most of people are interested in preparing thin films due to the requirements of most of the applications. CSD methodology, due to its low cost and scalability, is one of the most extended techniques in the preparation of GdBCO films.

The application of the CSD methodology to the preparation of GdBCO films is more difficult than in the case of the YBCO. The conditions in which the solutions can work properly and also the optimum conditions to achieve epitaxial GdBCO films are narrower than in the YBCO case. So, the degree of accuracy and refinement that the synthesis of GdBCO films requires is higher.

In this chapter, the focus will be in the preparation of CSD-derived GdBCO nanocomposites thin films using Low-Fluorine Solutions (LFS). The tradition within the SUMAN group is to use TFA solution. However, in this case, it was necessary to change to LFS solution due to some reasons that will be later detailed. The development of this new solution forced to optimize the pyrolysis process and the growth process, first, for pristine GdBCO films. The optimization of the growth process in order to obtained epitaxial films, resulted in the new "Flash-Heating" treatment. By using this new process, epitaxial GdBCO nanocomposite films could be obtained. The properties of the obtained CSD-derived GdBCO nanocomposite films have been analyzed in detail.

3.2 Pyrolysis process in mixt nanocomposites

The YBCO mixt nanocomposite thin films are deposited by spin-coating 15 μl of precursor solution of 0,17M respect to Y, on LAO substrate, leading to a final thickness of 200 nm (after the growth process). After the deposition, the films are exposed first to a low-temperature thermal treatment, the pyrolysis, to remove the organic content of the as-deposited films.

The pyrolysis process chosen for all the compositions is the so called "standard pyrolysis process" (see chapter 2, figure 2.6). The choice of this particular process is based in the reproducible results obtained for the pristine YBCO-TFA solution. Since the nanocomposite precursor solutions are TFA based, the results should be similar as in the case of pristine YBCO thin films. This process leads to homogeneous and continuous pyrolyzed thin films, as it is shown in the optical microscope image in figure 3.1.

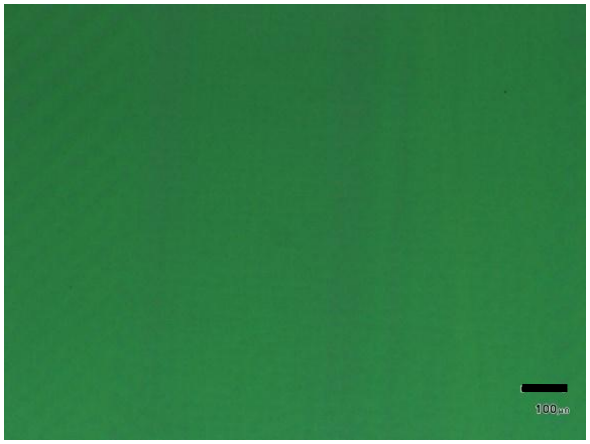

Figure 3.1. Optical microscope image of a YBCO+10%M BZO+5%M YO film after the pyrolysis showing a homogeneous and continuous film.

The phase composition of the mixt nanocomposites after the pyrolysis has been investigated by 2D XRD θ-2θ scans. Representative XRD patterns are shown in figure 3.2. The bright and well defined spots correspond to the LAO single crystal substrate whereas the low intensity rings are identified for CuO and BYF intermediate phases. The presence of the rings is due to polycrystalline nature of the intermediate phases at 310 ºC. In order to better identify the presence of these intermediate phases, integration of the 2D spectrum is performed, resulting in the θ-2θ scan shown in figure 3.2 b).

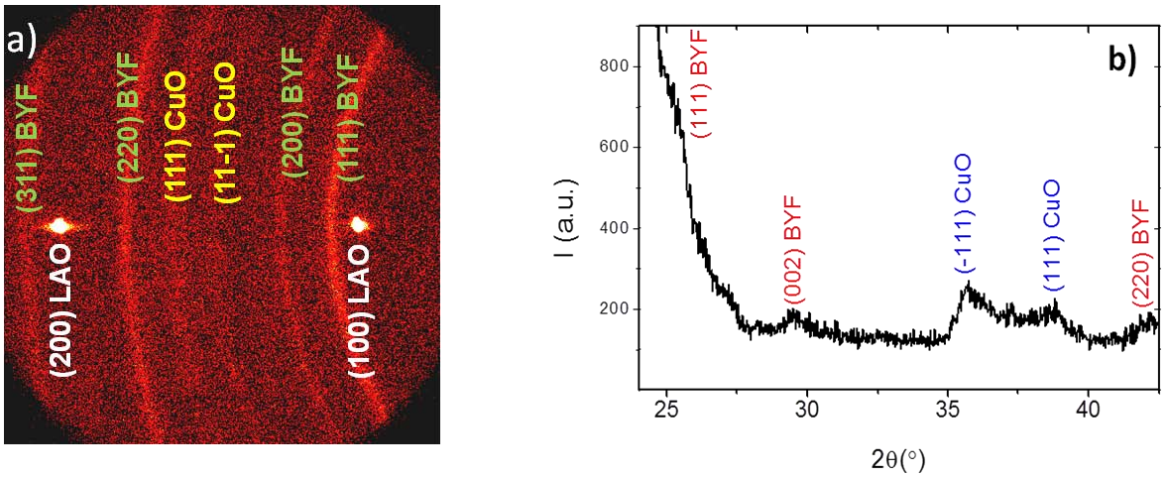

Figure 3.2. 2D XRD θ-2θ a) frame and b) integrated patterns of YBCO+6%M BYTO+5%M YO thin film. In the frame a) the rings of the polycrystalline phases are observed while in the integrated spectrum from the image b) the peaks of these phases are clearly identified.

In view of the composition of the film after the pyrolysis, it is concluded that, for all the studied compositions, the secondary phases NPs are still not formed due to the low temperatures of the process. The XRD patterns shows the same composition as in a pristine YBCO film after pyrolysis.

3.3 Growth process in mixt nanocomposites

After the pyrolysis, the films grown by using, for all the different compositions, the so called "standard TFA growth process" (described in chapter 2, figure 2.7). This process has been previously well established in the group for pristine and CSD in-situ nanocomposite films giving excellent results[97, 101]. Having this in mind, it was decided not to modify this process

After the growth process, the phase composition, microstructure, surface morphology and superconducting properties were evaluated using the experimental techniques described in chapter 2.

3.3.1 Film thickness

By using the profilometer and the AFM, it was possible to establish that the final thickness of the films was 200 nm. The films obtained with the 0,25M YBCO-TFA solution, have a thickness of 250 nm[121]. The use of 0,17M solution causes a reduction of 50 nm with respect to the 0,25M solution. Therefore, the in-situ nanocomposite thin films studied in this work have a thickness of 200±20 nm considering the error of the measurements equipments (figure 3.3). This thickness is independent of the particular composition of each solution.

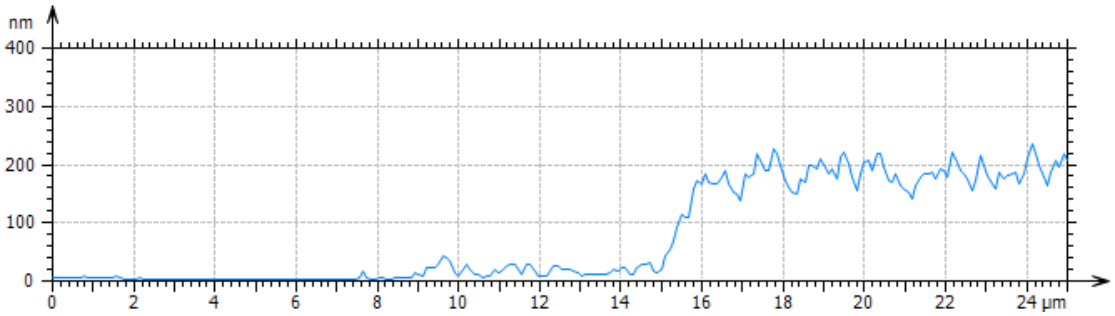

Figure 3.3. AFM measurement of an YBCO+6%M BYTO+5%M YO thin film showing that the thickness is approximately 200 nm after the complete film processing.

3.3.2 Structural properties

3.3.2.1 XRD analysis

XRD measurements have been used to study the phase composition, the epitaxial and random fractions and the nanostrain of the mixt nanocomposites.

3.3.2.1.1 Nanocomposites texture and random fractions

Figure 3.4 shows the 2D XRD θ-2θ frames for the studied mixt nanocomposite films after the growth process. Highly epitaxial (00l) YBCO films are obtained for all compositions. The presence of a ring at ~30º can be attributed to the (110)BZO and/or

(220)BYTO reflections identifying randomly oriented secondary phases. Both phases have almost coincident peaks (30,116º for (110)BZO and 29,923º for (220)BYTO and also 43,103º for (200)BZO and 42,823º for (400)BYTO according to ICDD 06-0399 and 04-005-7521, respectively), therefore, it is not possible to differentiate both with the resolution of the used equipment. For this reason, in the YBCO+5%M BZO+6%M BYTO case, both phases are indexed in the same angular position.

Finally, a low intensity single spot can also be identified at 2θ~43º corresponding to (200)BZO and/or (400)BYTO Bragg peaks which usually are associated to a epitaxial contribution (a ϕ–scan would be needed to secure it).

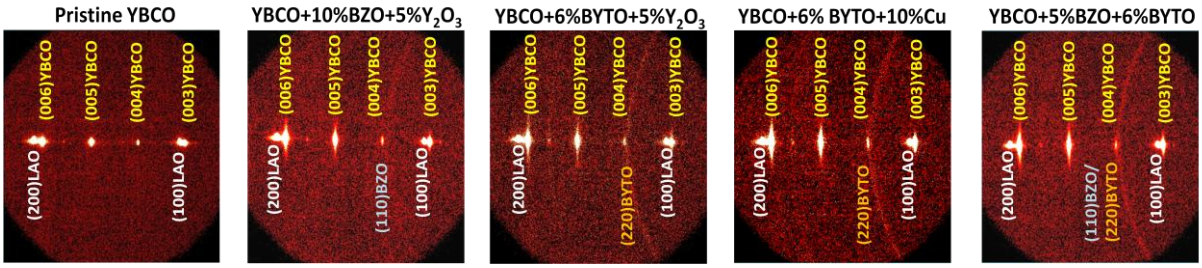

Figure 3.4. 2D XRD θ-2θ frames of the different mixed composition nanocomposites. It is remarkable that all of them presents epitaxial YBCO and polycrystalline BZO and BYTO NPs.

Figure 3.5 presents the integration of the previous 2D frames that allow a more clear identification of the phases present in these nanocomposites.

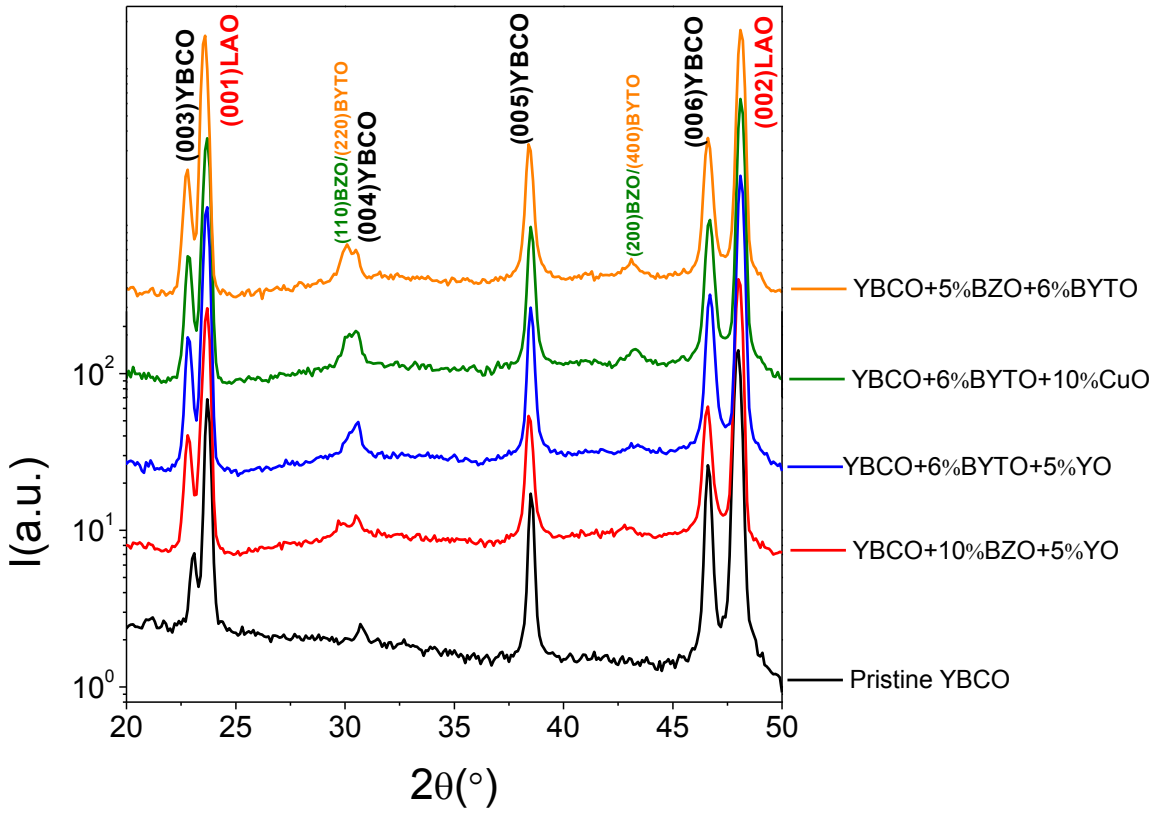

Figure 3.5. Integrated spectra of the figure 3.4 2D XRD θ-2θ frames for the YBCO mixt nanocomposites and pristine YBCO film.

The intensity of the polycrystalline contribution (ring at 2θ~30º) is different depending on the composition. This intensity is related to the amount of NPs that nucleate randomly. Only those NPs which are randomly oriented will contribute to the intensity of this ring. The intensity of the peak at 2θ~30º for YBCO+5%M BZO+6%M BYTO composition is the most intense one suggesting that it presents the highest percentage of randomly oriented NPs, i.e., the highest percentage of random fraction. The percentage of random fraction can be estimated from XRD measurements (see Appendix A.3 for details about the calculation of the random fraction).

Figure 3.6 shows the random fraction calculated for mixt nanocomposites compared with pristine YBCO and single phase nanocomposites (thickness of the single phase nanocomposites ~250-300nm)[97, 101]. It is observed that the lowest random fraction of the mixt nanocomposites corresponds to the YBCO+10%M BZO+5%M YO nanocomposites which are also the nanocomposites with the less intense ring (figure 3.4). The other mixt nanocomposites present high values of random fraction, all above 90%. The highest value (96%) is achieved for the YBCO+5%M BZO+6%M BYTO.

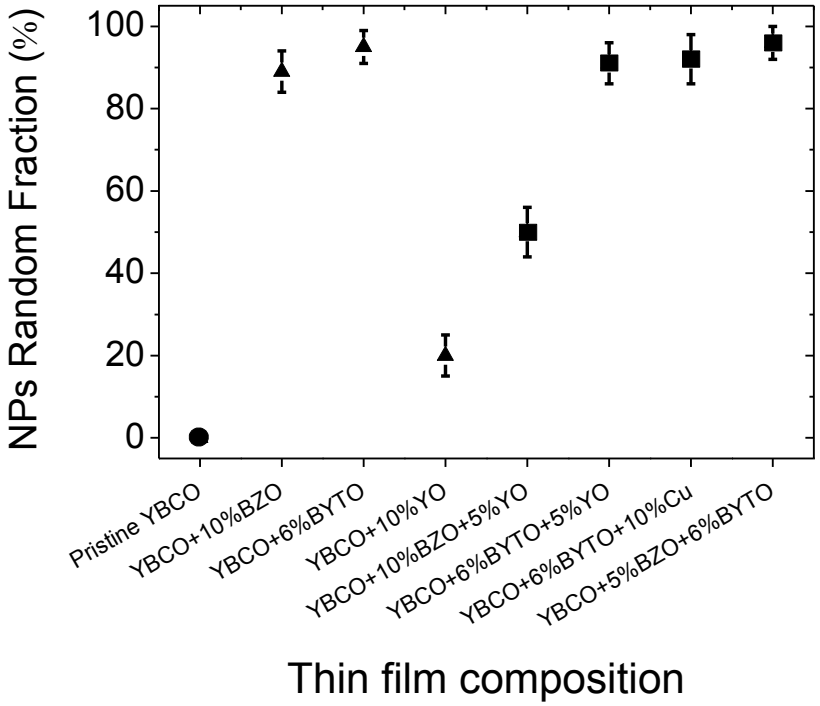

Figure 3.6. Random fraction values for the different mixt nanocomposites (squares) compared with the pristine YBCO film (circle) and the single phase nanocomposites (triangles)[97, 101].

The nanocomposites that contain BYTO show the highest percentage of random fraction, similar to analogous YBCO+BYTO simple nanocomposites[97, 101], suggesting that the random fraction is mainly dictated by the BYTO contribution.

However, the situation with the YBCO+10%M BZO+5%M YO is different. For the YBCO+10%M BZO nanocomposite films, the reported values are also in the range of 90%[97] but, in this case, the values do not go above 50%. The explanation for this is that the nucleation is not as homogeneous as in the reported cases and quite a lot of the NPs are epitaxial with no contribution to the random fraction (reasons for that will be discussed in section 3.4.).

In the case of the YBCO+5%M BZO+6%M BYTO nanocomposites, since the Bragg peaks of BZO and BYTO are almost coincident, it is not possible to separate the random contribution of each NP. However, it is very probable that the high value of the random fraction was due to, mostly, the BYTO NPs because a great part of the BZO NPs do not give random contribution (as can be seen from de low random fraction values of YBCO+10%M BZO+5%M YO).

Note that the included random fraction values of the single phase nanocomposites correspond to 250-300 nm films while in the case of the mixt composition nanocomposites the thickness of the films is 200 nm

3.3.2.1.2 Nanostrain and NPs size measurements

Nanostrain and NP size values are obtained using the Siemens diffractometer (Chapter 2) and then applying the Williamson-Hall method and the Scherrer formula, respectively (Appendix A.1).

In figure 3.7, it is shown the nanostrain value for the mixt nanocomposites, again compared with the pristine YBCO and single phase nanocomposite films (thickness of the single phase nanocomposites ~250-300nm)[97, 101]. The values are in the range 0,21-0,24% which is approximately the double of the value obtained for the 200 nm pristine YBCO film.

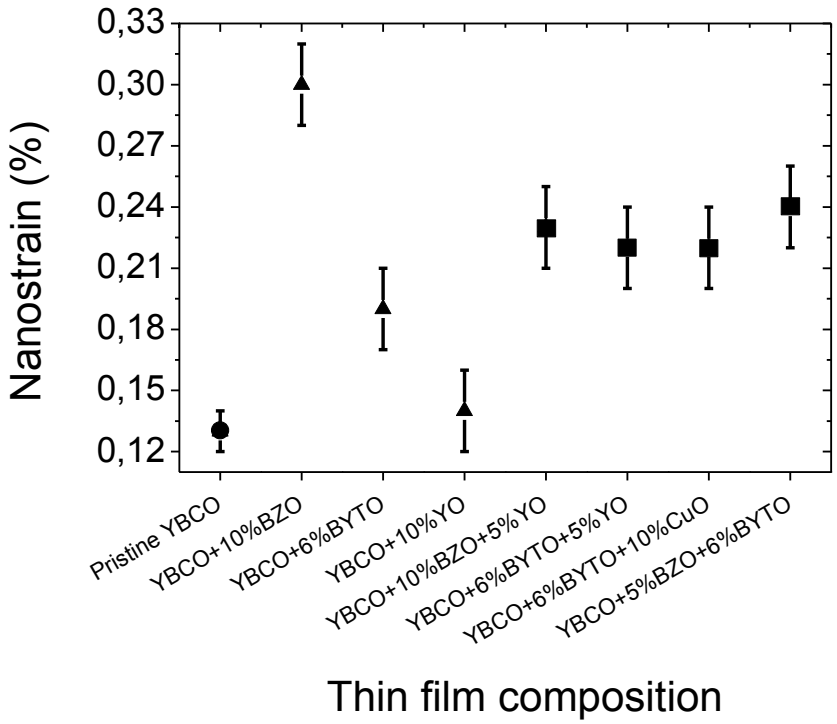

Figure 3.7. Nanostrain values for the different mixt nanocomposite films (squares) compared with the values of the 200 nm YBCO pristine film (circle) and the 300 nm single phase nanocomposite films (triangles)[107, 96].

The NP size has been calculated from the (200) and (400) BZO and BYTO reflections, respectively. The obtained sizes are 11-12 nm for all the mixt nanocomposites (figure 3.8). For the YBCO+5%M BZO+6%M BYTO films, the NP size is an average of both NPs since both contribute to the same peak.

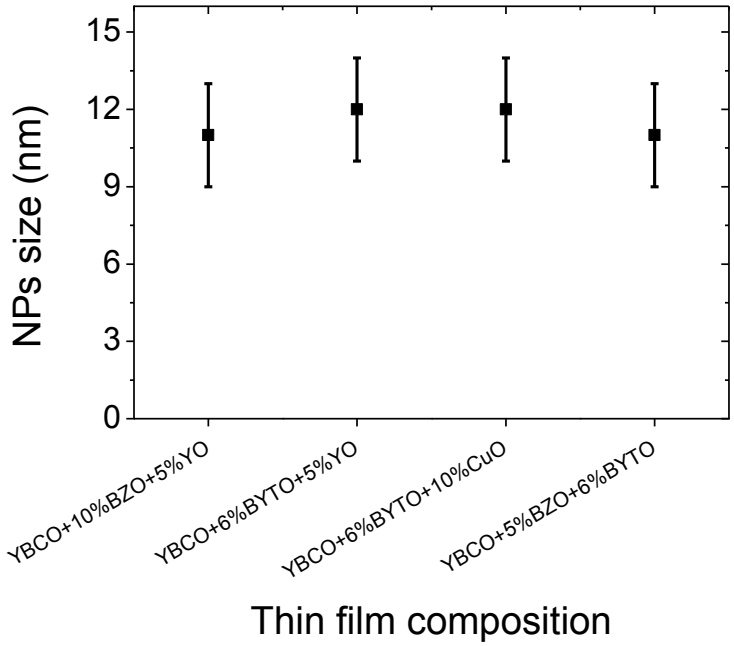

Figure 3.8 NPs size values for the different mixt nanocomposites calculated from Scherrer formula using (200) and/or (400) Bragg peaks for BZO and BYTO respectively.

It is important to take into account that the Scherrer formula only gives the size of the NPs in the perpendicular direction to the plane that originates the peak. As the calculations are made with the (200) and/or (400) Bragg peaks for BZO and BYTO respectively, the obtained sizes are the dimensions of the NPs in the (00l) direction (figure 3.9). So the obtained NP size obtained with Scherrer formula is not representative of the randomly oriented NPs size (usually their size is higher), but it can be used to observe the tendencies. The sizes of the random NPs have to be extracted from TEM images.

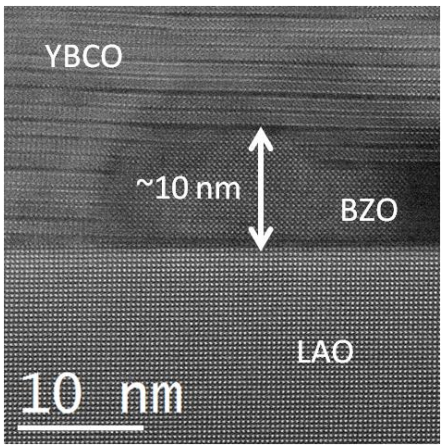

Figure 3.9 TEM image showing an epitaxial BZO NP at the interface. The size that can be extracted applying Scherrer formula is indicated with white arrows.

3.3.2.1.3 Incoherent interface calculation

Knowing the particle size and the random fraction values, it is possible to calculate the incoherent interface present in the nanocomposites. As it was mentioned before, the

incoherent interface plays a key role in the stacking fault formation; therefore its quantification is of a great importance.

The incoherent interface (measured in μm^{-1}) is calculated using the following expression (Eq 3-1)[97, 101]:

$$\boldsymbol{I.I.} = \frac{\boldsymbol{3.RF.[NPs]}}{\boldsymbol{r}} \qquad \text{Eq 3-1}$$

where RF is the random fraction expressed as decimal, [NPs] is the total concentration of the NPs in the nanocomposite film, also expressed as a decimal, and r is the radius of the NPs (in μm).

Figure 3.10 shows the evolution of the nanostrain as a function of the incoherent interface. As it was commented previously, the effect of having a high value of incoherent interface is to generate a high amount of SFs that contribute to the increase of the nanostrain. Previous work in the group demonstrated the existence of a linear dependence between the nanostrain and the incoherent interface[97]. This linear trend is valid for BZO, BYTO and YO nanocomposites. The mixt compositions studied in this thesis (pink points in figure 3.10) were compared with the simple BZO, BYTO and YO nanocomposites and it was observed that all of them follow the same trend: by increasing the incoherent interface, the nanostrain increases too.

For the calculations of the incoherent interface in the mixt nanocomposites, the r values was taken as an average between the reported r from TEM images: BZO (~15 nm), BYTO (7-20 nm) and YO (~15 nm) NPs[97].

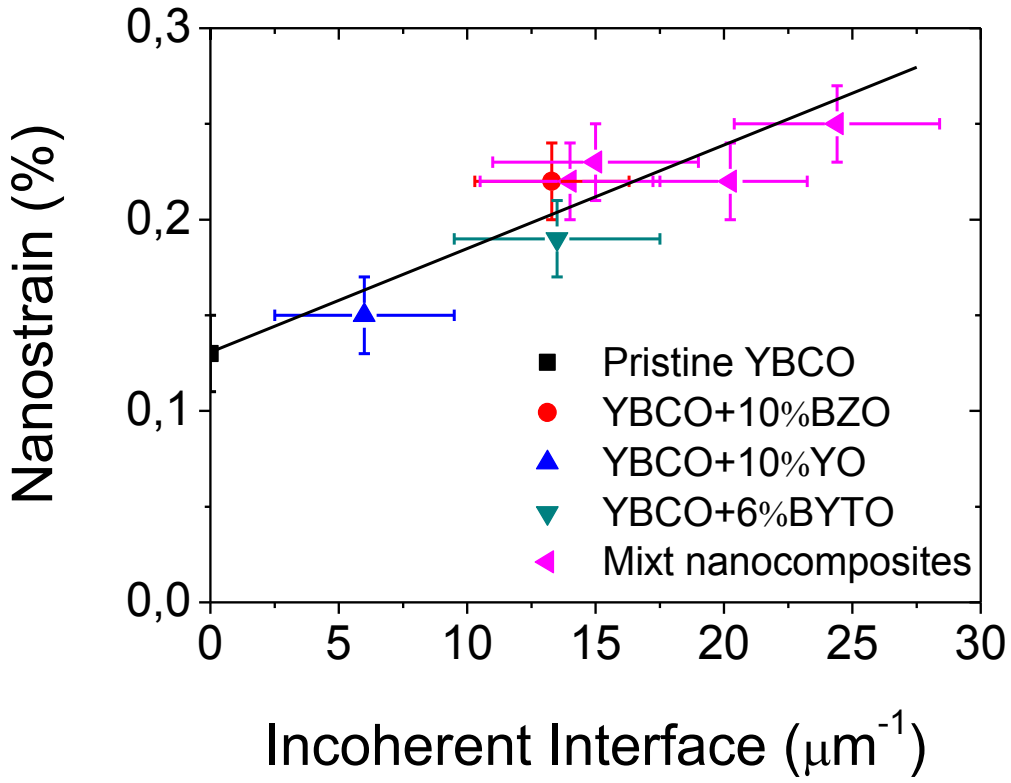

Figure 3.10 Dependence of the YBCO vertical nanostrain on the incoherent interface of NPs in the different nanocomposites (BZO, YO, BYTO and mixt).

3.3.2.2 Atomic scale structural analysis

Further insight into the microstructure of the mixt nanocomposite films is possibly by performing TEM measurements. In the case of the mixt nanocomposites, the focus has been on the NP distribution and the SF scenario, especially in the length, density and distribution of the SFs.

A cross-section Low-Angle Annular Dark Field (LAADF) TEM image of the YBCO+10%M BZO+5%M YO nanocomposite is presented in figure 3.11. It can be observed that the NPs are homogenously distributed within the YBCO matrix and their sizes vary in the range of 10-30 nm. This particular example is extensible to the rest of compositions in which similar results were found (without the BZO layer which is only observed in the case of the BZO doping nanocomposites). This demonstrates that, by using mixt compositions, it is possible to increase the concentration of NPs in the YBCO matrix up to 15%M, minimizing the coarsening effects which were a major issue in simple nanocomposites[101]. In the case of simple BZO and BYTO, it was found that the maximum concentration with no NP coarsening was 10%M and 6%M, respectively[13, 97, 114]. The BYTO concentration can be pushed to 10%M with no coarsening by careful control of the nucleation and growth process[101]. A similar strategy may be employed in mixt nanocomposite films to further increase the NP concentration.

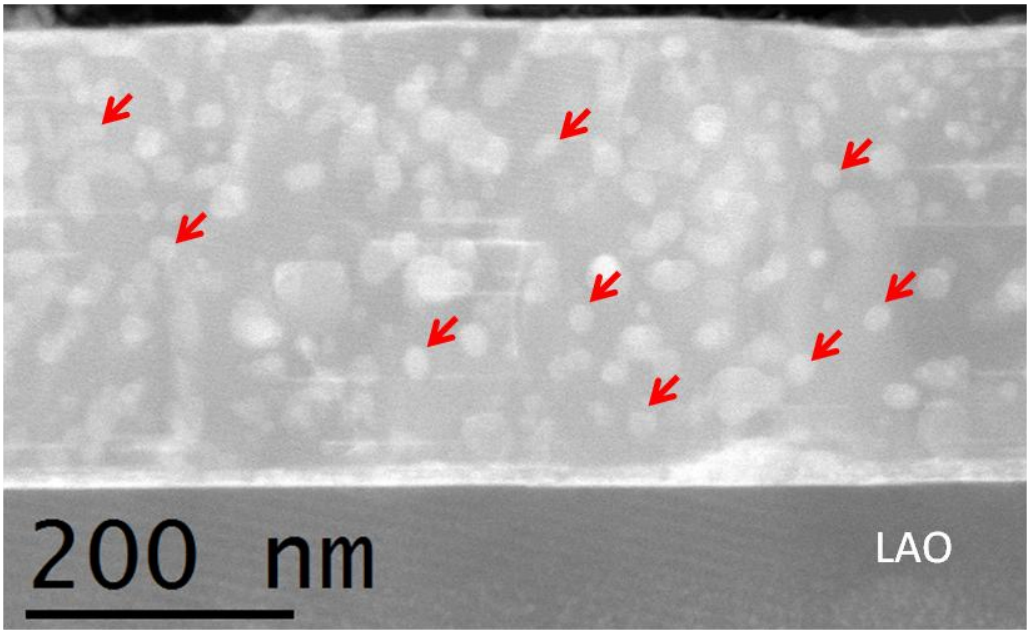

Figure 3.11 LAADF TEM image of YBCO+10%M BZO+5%M YO film showing the homogenous distribution of NPs within the YBCO matrix (red arrows mark NPs). Similar results were found for the rest of compositions (without the BZO layer).

Figure 3.12 presents the cross-section High-Angle Annular Dark Field (HAADF) TEM images of some of the studied mixt nanocomposite films in comparison with a cross-section of a pristine YBCO thin film and YBCO+10%M BZO film. Looking at these images, the most remarkable feature is the large number of SFs present in the mixt nanocomposites. Also, it is noticeable that the length of these SFs, especially in the case of the YBCO+10%M BZO+5%M YO film, is much smaller than those observed in the pristine YBCO and the YBCO+10%M BZO films processed in the same conditions as the mixed nanocomposites.

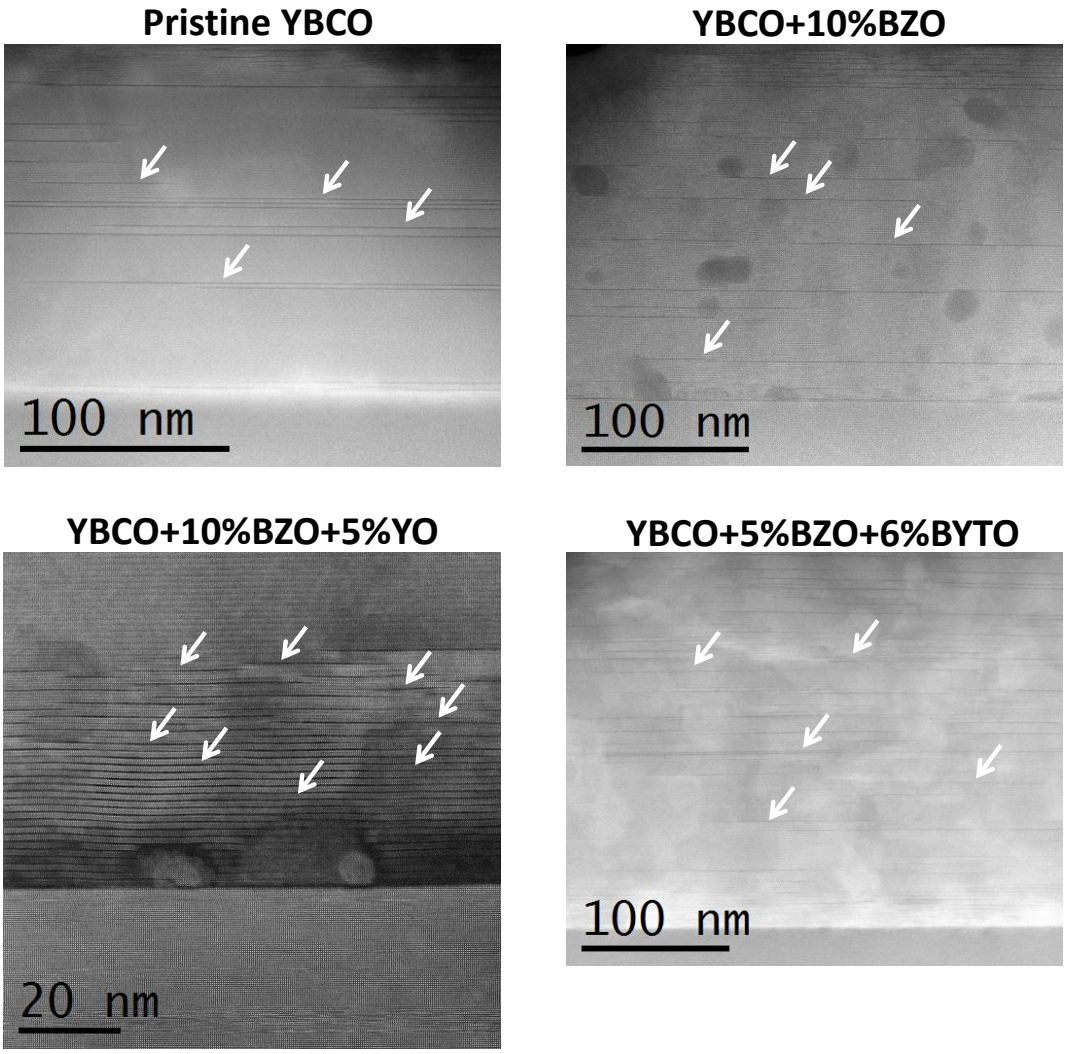

Figure 3.12 HAADF TEM images of the different mixt nanocomposite films showing the presence of SFs (indicated with white arrows) in all of them.

In order to quantify the qualitative change observed in the stacking fault scenario, TEM images have been processed using the software Digital Micrograph software. The results are presented in figure 3.13. This analysis confirms that the density of the SFs, whatever the length, is much higher, in general, for the mixt nanocomposites than in the case of pristine YBCO and even YBCO+10%M BZO films. Therefore, the mixt compositions clearly favor the formation of SFs. This is in agreement with the relationship found previously between the incoherent interface and the nanostrain. The amount of NPs was increased maintaining the size of the NPs. The higher the amount of NPs is, the higher the incoherent interface and the higher the stacking fault formation.

The highest density of SFs is reached in the YBCO+5%M BZO+6%M BYTO nanocomposites. In this case, both phases tend to nucleate randomly in the YBCO matrix adding efforts to generate more incoherent interface and hence, causing the formation of more SFs. This nanocomposite is the one that displays the largest value of incoherent interface in the linear trend shown in figure 3.10.

The lowest density of SFs is obtained in the YBCO+10%M BZO+5%M YO films. This composition has the lowest random fraction value. This means that there are many BZO NPs heterogeneously nucleated in the interface (it is well known that the YO NPs

tend to be epitaxial in the YBCO matrix due to their low mismatch with the YBCO) or that suffered a re-crystallization process (phenomenon observed in Melt-Textured YBCO by which the NPs rotate or re-crystallize to accommodate the YBCO structure during the YBCO growth[181]) which results in a coherent interface between both (the explanation for that will be discussed later in more detail in section 3.3.4). Under these conditions, the formation of SFs is not favored.

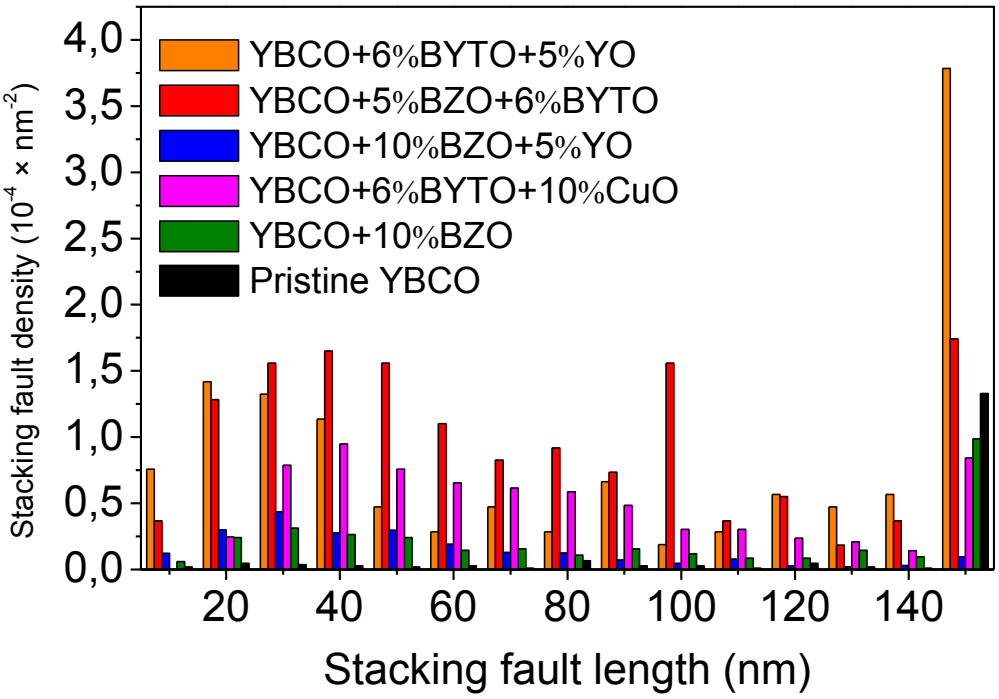

Figure 3.13 Stacking fault density and length of different mixt nanocomposite film compare with the pristine YBCO and YBCO+10%M BZO films.

Another interesting result is that the length of the SFs in the mixt compositions is much smaller than in the case of the pristine YBCO or YBCO+10%M BZO films. Even in the case of YBCO+10%M BZO+5%M YO in which the density of the SFs is low, their length is small. The reason why the length of the SFs is reduced is still unclear, but one possibility is related with an effect of the NPs concentration increase. An increase in the amount of nanoparticles involves a reduction of the separation between them. When the stacking fault is generated, it can extend only between NPs because the NPs act as barriers to the diffusion of the defects. Therefore, if the space between them is smaller, the length of the SFs is also smaller (figure 3.14 a)).

However, this argument is not valid to explain why there are other short SFs that are not cut by the presence of any NPs (figure 3.14 b)). In this case the fact that the SFs were short can be attributed to the strain accumulated in the matrix of the YBCO due to the presence of the NPs. The SFs propagation is limited by the strained regions present in the matrix. It is assumed that a greater number of NPs will cause more strained regions in the matrix that limit the SFs propagation. But, as it was mention, the mechanism is still uncertain and a more in detailed analysis of this issue is needed.

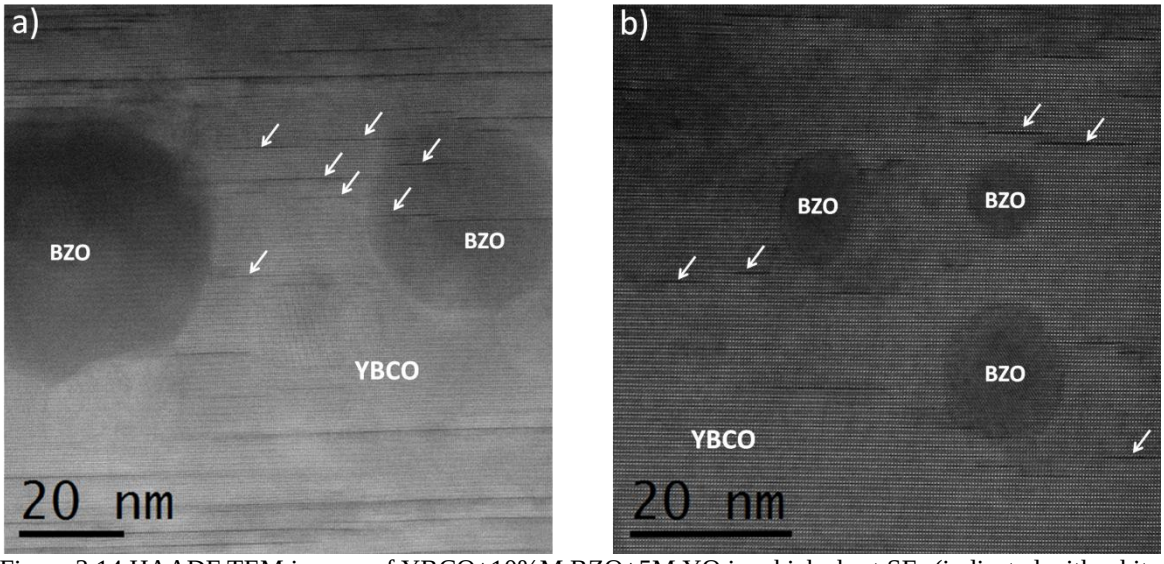

Figure 3.14 HAADF TEM images of YBCO+10%M BZO+5M YO in which short SFs (indicated with white arrows) are present. The increase in the concentration of NPs causes a reduction in the length of the SFs.

The SFs length reduction is something general in the mixt nanocomposite films, but it is particularly noteworthy in the case of YBCO+10%M BZO+5%M YO films. In this case, the concentration of short SFs is really high, much higher than in rest of compositions. This will have important consequences in the physical properties of the films, as it will be discussed in the next section.

3.3.3 Physical properties

Once the microstructure is completely characterized, it is time to study the physical properties of the nanocomposite thin films and try to correlate them to the microstructure.

The critical temperature and the critical current density of the mixt nanocomposites have been measured both by SQUID and transport measurements. The obtained results are similar in both cases, for all the different compositions: T_c~90 K and J_c^{sf} (J_c self-field) at 77 K~2,5-3,5 MA/cm^2 at 77 K These values are similar to those obtained for the pristine YBCO films processed in the same conditions and with the same solution concentration (T_c~91 K, J_c~3-4 MA/cm^2).

After that, it is important to check the behavior of the critical current density with respect to the magnetic field. Figure 3.15 shows the normalized J_c dependence with the magnetic field, obtained from transport measurements, for the different mixt nanocomposites and, for comparison, with pristine YBCO, YBCO+10%M BZO and YBCO+6%M BYTO films processed in the same conditions. It is possible to conclude that the mixt nanocomposites have a very similar behavior to single phase nanocomposites, showing the typical "rounded" form at intermediate fields.

To understand the nanocomposite films behavior, J_c(H) curves for H//c have been analyzed. It is well established that the J_c(H) dependence of YBCO thin films in a log-log plot shows three different regions[182, 103]. The first one is observed at low fields and, here, there is a plateau of J_c associated with a single vortex pinning regime. In this first region vortex-defect interactions are dominant. As the field is increased, the concentration of vortices is higher and the vortex-vortex interactions become relevant as the distances

between them are smaller. In this region, which is found at intermediate field values, the collective vortex motion is governed by a power law regime. At high field values, once the irreversibility field is approached, J_c drops very fast. In this third region, the pinning properties are usually mainly dominated by anisotropic defects such as twin boundaries which play an important role. At lower fields, the effect of the twin boundaries is not so relevant because the isotropic defects dominate[183, 184].

In the case of the nanocomposites, the three different regions are also found. But there are differences with respect to the pristine YBCO samples. The first region is extended to much larger magnetic fields. This is possible due to the additional defects that are artificially introduced and which allows the maintenance of the single vortex pinning regime up to higher fields. At intermediate fields, the decay of the J_c in nanocomposites is not so pronounced as in the pristine YBCO, as it is observed in figure 3.15. It causes smoothed field dependence in this region in the case of nanocomposite films. This happens because the collective vortex motion, that takes place in this region, is more difficult than in pristine YBCO due to the presence of defects. Finally, at high fields, it is observed that for the nanocomposite films studied in this thesis, in general, the J_c drop occurs faster than in the pristine YBCO (figure 3.15). At high fields, the twin boundaries are the most relevant defects at H//c because of their anisotropic nature. The SFs break the coherence of the twin boundaries and decrease the anisotropic pinning of these defects causing a faster drop of the J_c(H) curve than in pristine films when H//c[183, 184].

The fact that, in the case of the nanocomposite films studied in this thesis, the J_c drop occurs faster than in the pristine YBCO is not a general phenomenon. Other authors have found that CSD (Y,Gd)BCO films processed under slightly different conditions than in this thesis keep the coherence of straight twin boundaries and, then, J_c drop do not occurs faster that in pristine films but even takes place at higher magnetic fields[118].

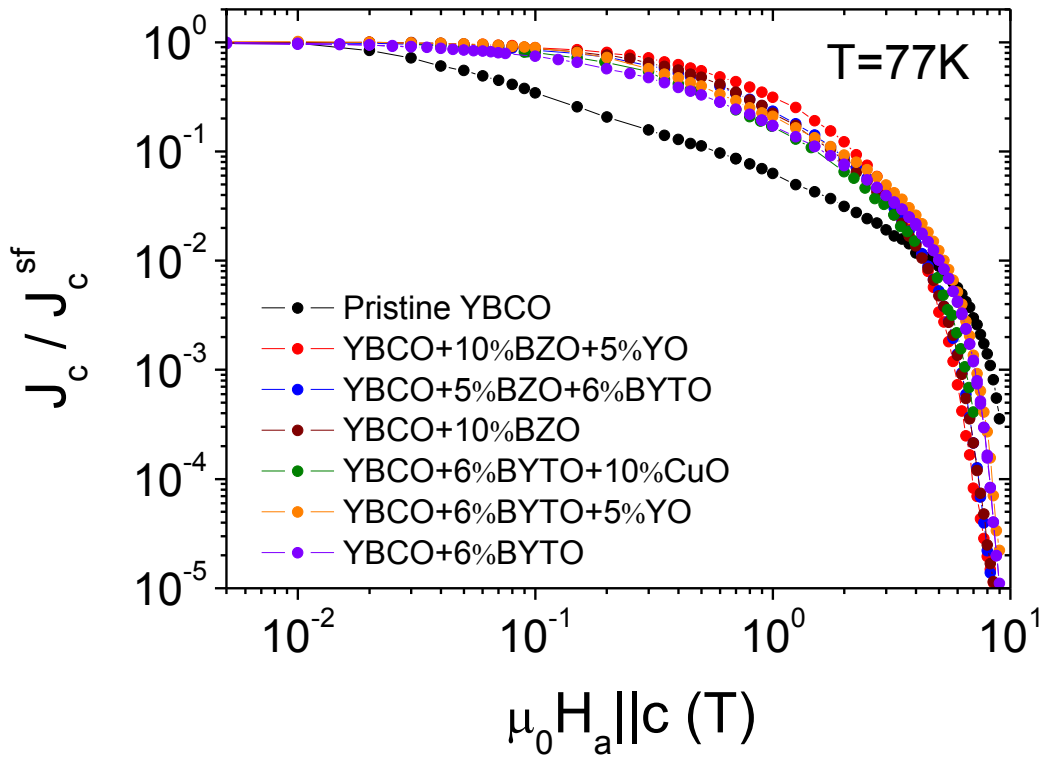

Figure 3.15 Normalized J_c(H) dependence with the magnetic field at 77 K for mixt nanocomposites obtained with transport measurements. Pristine YBCO, YBCO+10%M BZO and YBCO+6%M BYTO curves are also included for comparison.

In view of the previous results, it seems that the use of mixt nanocomposites, that cause the presence of shorter SFs in the films, do not introduce any advantage in terms of physical properties as compared to nanocomposites based on a single type of NPs. To find something different, it is necessary to analyze figure 3.15 in more detail.

3.3.3.1 Changes in H*

As it was mentioned in the previous section, the most remarkable change in the $J_c(H)$ curves of nanocomposite thin films with respect to pristine YBCO thin films is the expansion of J_c plateau, i.e., the extension of the single vortex pinning regime up to higher fields. This is related to the increase of the defect concentration in which the vortices can be pinned. To quantify this enlargement, a new variable, called H*, is employed. H* is the crossover magnetic field from single vortex pinning to the collective pinning. Mathematically is defined as (Eq.3-2):

$$\boldsymbol{J_c(H^*) = 0,6 J_c(sf)} \qquad \text{Eq 3-2}$$

Applying this definition to the $J_c(H)$ curves that appear in figure 3.15, one can extract the values of H* and use them to create the following graph by representing the dependence of H* (at 77 K) with the SFs length (figure 3.16):

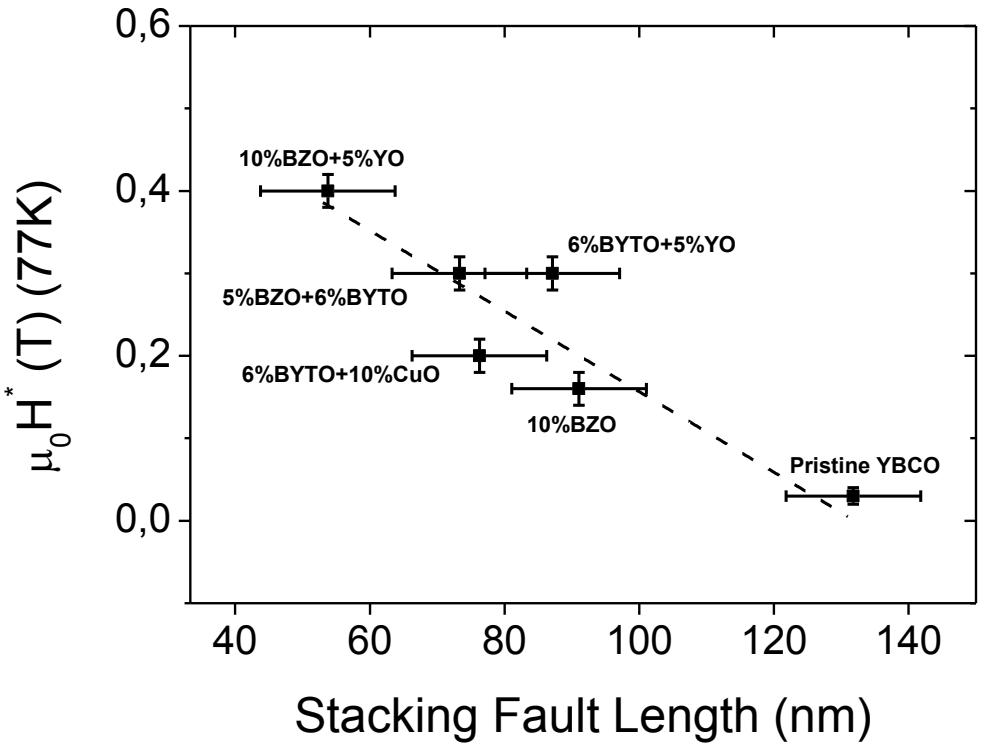

Figure 3.16 H* at 77 K dependence with the Stacking Fault length for different nanocomposites.

Figure 3.16 shows a linear dependence between the H* values and the SFs length. The shorter the SFs are, the larger the H*. This is clearly visible in the case of

YBCO+10%M BZO+5%M YO. In this case, it was found that the SFs they were very short and keeping a high concentration. As a result of this, the value of H* is the highest reaching 0,4 T.

As it was said before, a larger H* implies a wider region in which single vortex pinning regime is dominant. And, in view of the results, this is favored by the presence of shorter SFs. This is easy to understand knowing that the SFs are surrounded by partial dislocations which generate strained regions which are suggested to behave as pinning centers[97, 113]. So, shorter SFs mean more pinning centers (more perimeter of SFs). The results show that it is more relevant to have short SFs in low density than a high density of long SFs. This can be observed in the YBCO+10%M BZO+5%M YO films that exhibit high values of H* despite its low density of SFs.

3.4 Thickness effect in the structural and physical properties of YBCO+10%M BZO nanocomposites

As it was mentioned in the introduction of this chapter, the problem of the thickness increase in pristine YBCO films synthesized by ex-situ growth techniques has been widely investigated[142, 153, 155, 173-177, 185-187]. However, in the case of the CSD nanocomposites, most of the research has been done in 100-300 nm thin films (previous mixt nanocomposite films had 200 nm). Although some authors have already demonstrated that nanocomposite films up to 3 μm can be grown using multideposition of thin films[180, 188, 187], it is still unclear the effect of the increase of the thickness of these nanocomposite thin films. In this section YBCO+10%M BZO nanocomposites of different thicknesses were prepared in order to study their structural and physical properties.

Here, it has been studied films with three different thicknesses: 200, 450 and 700 nm. The 200 nm films are deposited by spin-coating, the 450 nm films by spin-coating multideposition (three cycles deposition/pyrolysis), and the 700 nm films by ink-jet printing, a well-known technique within the Superconducting Materials and Large Scale Nanostructures (SUMAN) department[189-191].

The films after pyrolysis are homogeneous and the used growth process was, for all the different thicknesses, the "standard growth process", already explained in section 3.3.

3.4.1 Effect of the thickness increase on the structural properties

The structural properties are studied by performing XRD measurements and TEM images.

3.4.1.1 XRD analysis

XRD 2D θ-2θ frames of the nanocomposite films reveal epitaxial YBCO and the presence of randomly oriented BZO for all the thicknesses here studied (figure 3.17). However, there are several differences between them.

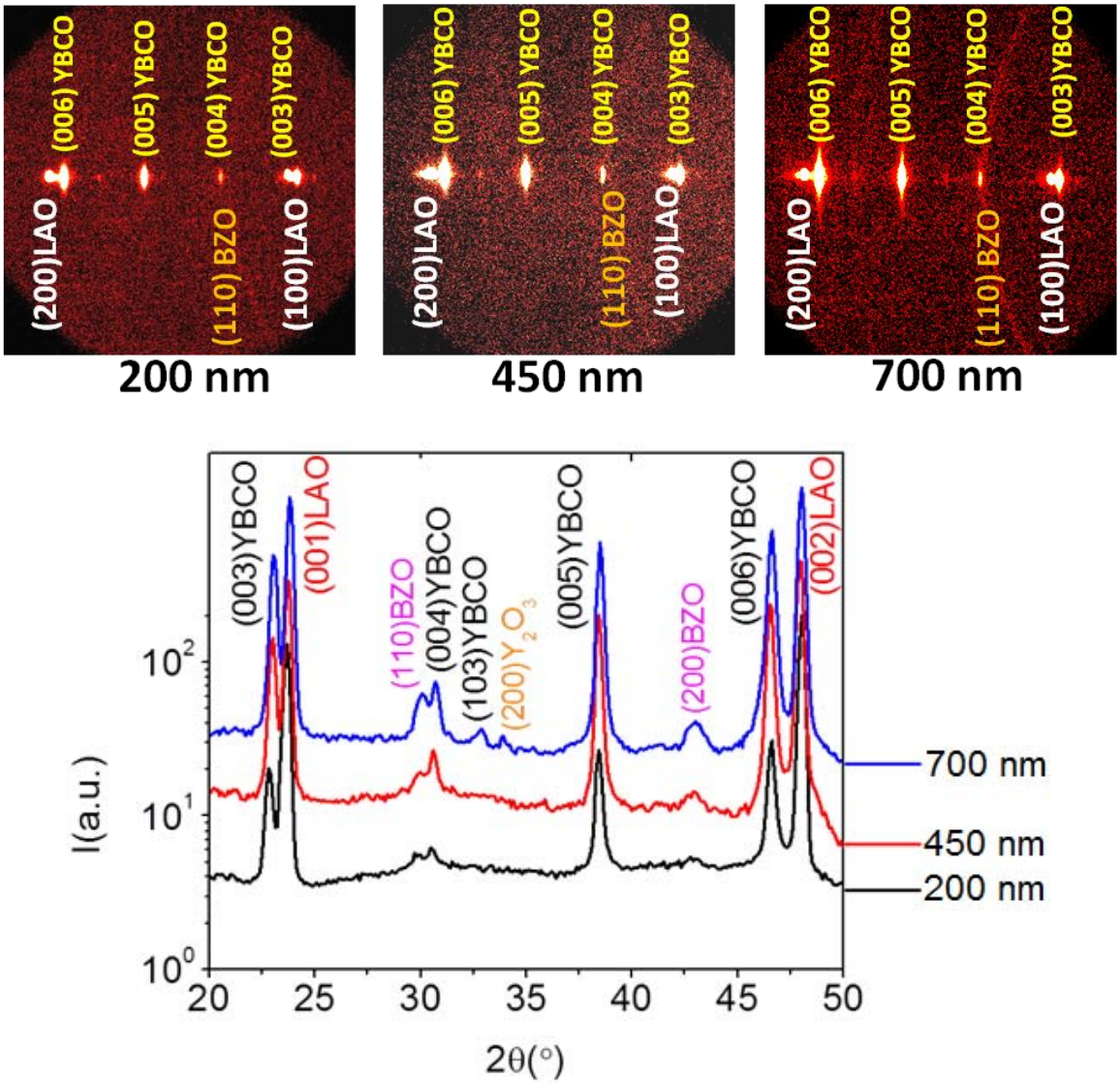

Figure 3.17. 2D XRD θ-2θ frames (above) and the corresponding integrated spectra (below) of the YBCO+10%M BZO films with different thickness in each case.

It can be observed that, as the thickness increases, the YBCO Bragg peak spots become wider. This means that the YBCO texture is progressively degraded as the thickness increases. This is something common when thin films are prepared and the thickness is increased, as it was demonstrated in pristine thick YBCO films[142, 153, 155, 173, 174]. In summary, what is happening is that the supersaturation changes with film thickness. And this occurs because, as the thickness increases, the P_{HF} decrease in the interface due to the pressure gradient that the thickness increase causes. The H_2O, the O_2 and the HF find more difficulties to diffuse through a big volume and, therefore, at the growing interface, the values of P_{H_2O}, P_{O_2} or P_{HF} could be very reduced as compared to the optimal values for a perfect c-axis YBCO growth[153, 155]. In the case of the nanocomposites this effect can be even worse due to the presence of NPs that can disturb the gas path or the epitaxial growth front. Therefore, the degradation of the texture is higher in the 700 nm films than in the 450 or 200 nm films (details on the supersaturation issues were explained in chapter 2, section 2.1.3.1).

It is also remarkable that thicker films present secondary phases visible in the XRD of the figure 3.17. The presence of Y_2O_3 is visible in the 700 nm film 2D XRD image and the integrated spectrum. These secondary phases correspond to unreacted phases (trapped intermediate phases) during the YBCO formation reaction indicating that the reaction to form YBCO is incomplete. This means that the growth process used in this study is not the optimum one for thick films and further optimization of the processing parameters is needed. In the 700 nm film it is also observed the Bragg peak corresponding to (103)YBCO. This shows that in this case random nucleation of the YBCO is also happening.

Another relevant information obtained from 2D XRD images and the corresponding integrated spectra is that the intensity of the (110)BZO ring is higher with the increase of the thickness. This fact has an important consequence: the random fraction of the 450 and 700 nm films is 90% while in the case of the 200 nm films is 50% (figure 3.18).

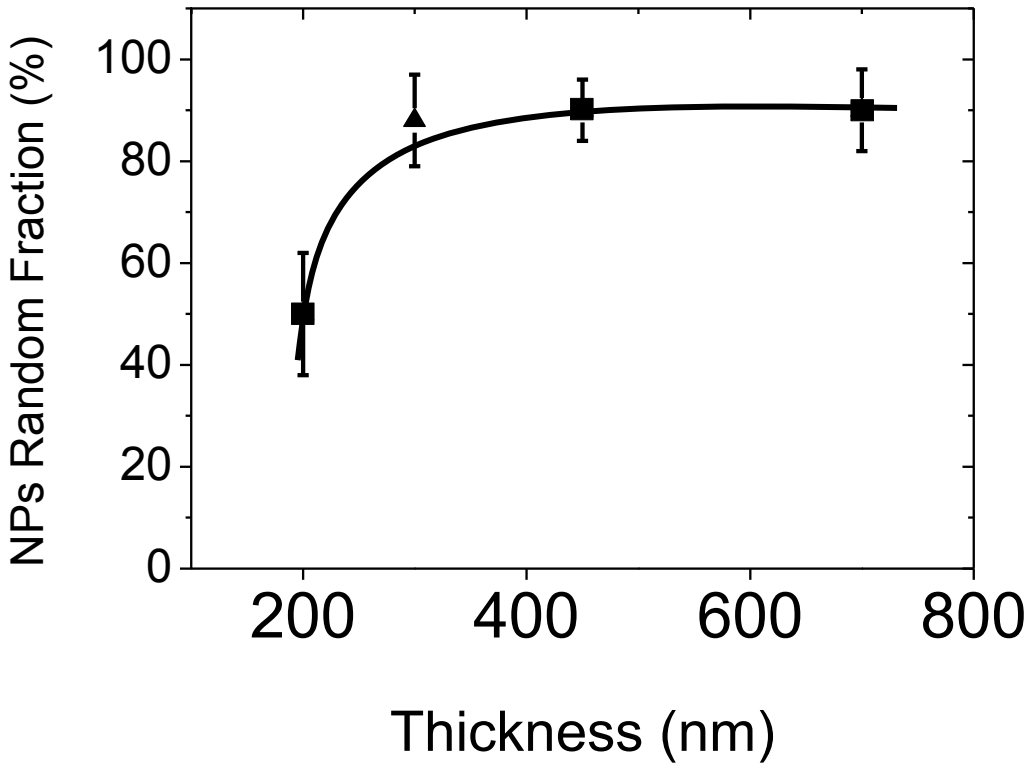

Figure 3.18. NPs Random fraction evolution of BZO with the thickness of the YBCO+10%M BZO films. Square symbols correspond to the values obtained in this thesis while the triangle correspond to the value of 300 nm YBCO+10%M BZO film from Llordes et al[97].

The random fraction of the 200 nm YBCO+10%M BZO film shown in figure 3.18 is similar to the value found for the YBCO+10%M BZO+5%M YO (figure 3.7). In both cases the BZO NPs tend to nucleate in a heterogeneous way on the substrate/YBCO interface resulting in an epitaxial orientation. Also, on the other hand, homogeneously nucleated BZO NPs can re-crystallize or rotate during the YBCO growth process accommodating to the YBCO matrix and leading to an additional epitaxial contribution. Therefore, the random fraction values can be reduced. However, this situation can change drastically when the thickness is increased.

The rise of the NPs random fraction when thickness increases could be attributed, in principle, to the important decrease in the ratio substrate surface/matrix volume that takes place going from 200 nm to 450 and 700 nm films. In this situation, the number of BZO NPs that suffer a re-crystallization or rotation during the YBCO growth decrease due to the changes in the nucleation conditions (the supersaturation changes affects the YBCO but also the NPs nucleation) that occur in thick films. On the other hand, the amount of BZO NPs that continue nucleating in a heterogeneous way in the substrate is maintained. To demonstrate if this hypothesis is correct, some simple estimations can be made.

It is possible to calculate the mass of the BZO present in the films (5x5 mm^2 LAO substrates): 1,3 μg for the 200 nm film, 2,9 μg for the 450 nm film and 4,6 μg for the 700 nm film. In the last two cases, the random fraction is ~90%. Assuming, as an extreme case, that the remaining 10% of epitaxial BZO place at the interface (epitaxial BZO because heterogeneous nucleation), there would be, in the case of the 700 nm film, 0,29 μg of BZO at the LAO interface. Considering that the amount of BZO that nucleate at the LAO is always the same, i.e., there are no changes in the heterogeneous nucleation of the BZO whatever the thickness (this is confirmed by TEM images in which the amount of BZO NPs at the LAO interface is maintained or, at least, do not increase, figure 3.19), in the case of the 200 nm the 0,29 μg at the LAO interface corresponds to ~22% of the total BZO. However, it was found experimentally (figure 3.18) that the epitaxial percentage is 50% (random fraction 50%), so the rest of the epitaxial BZO should come from the re-crystallization or rotation of BZO NPs in the matrix. These simple estimations suggest that the BZO NPs have an enhanced tendency to become epitaxial at small film thickness due to the re-crystallization or rotation during the YBCO growth.

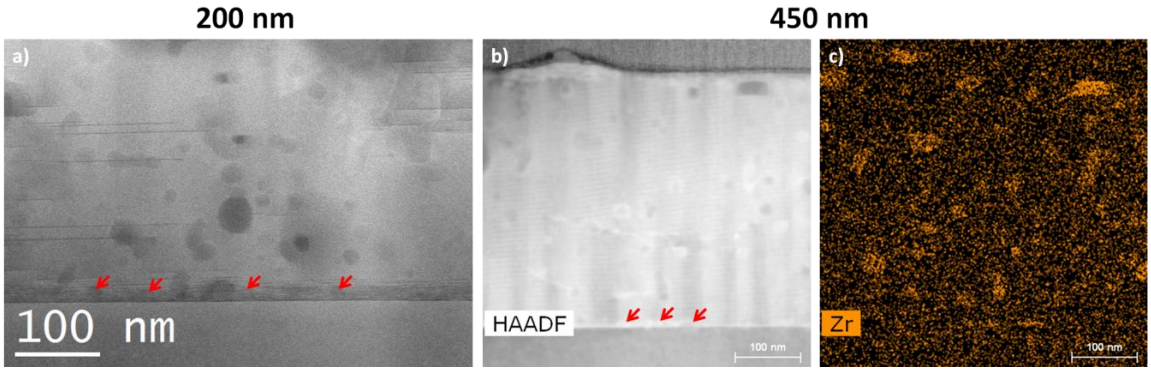

Figure 3.19 HAADF TEM images of YBCO+10%M BZO films of a) 200 nm and b) 450 nm. Picture c) corresponds to the EDX map image b). BZO NPs at the LAO interface are marked with red arrows. These images demonstrate that the amount of BZO at the LAO interface do not increase with the thickness.

The fact that in the case of the 200 nm films the random fraction was only 50% is due to the big tendency to BZO re-crystallization or rotation during the YBCO growth is well understood looking at figure 3.20. This figure shows several quench processes at different temperature. It is observed that the peaks corresponding to BZO appear at the same temperature (~770-780 ºC) as the peaks of the YBCO. This means that the heterogeneous nucleation of YBCO and the homogeneous and heterogeneous nucleation of BZO happen in the same range of temperatures and, therefore, they are competing. As a consequence of this, it is more probable that the BZO NPs re-crystallize or rotate within the YBCO matrix to accommodate to the YBCO structure since the YBCO front reaches the NPs just after the nucleation, especially considering that just after the nucleation the

size of the NPs is smaller (5-10 nm) than the sizes that TEM measurements is detecting (10-30 nm).

The nucleation of the BZO NPs at larger thickness changes in a similar way that in the case of the YBCO nucleation. The increase of the homogeneous nucleation of BZO at large thicknesses can be attributed to an enhanced supersaturation of thicker films as it was already explained.

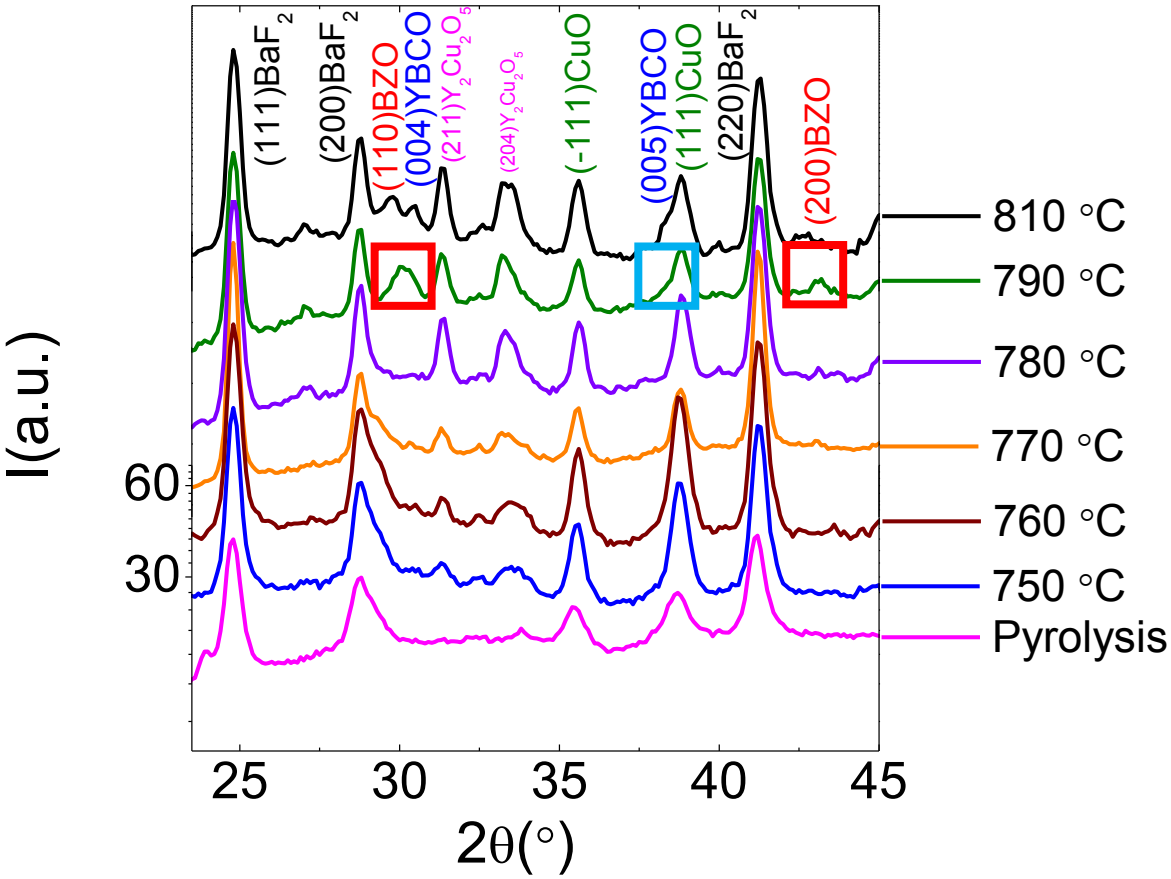

Figure 3.20. Quenches at different temperatures of 200 nm YBCO+10%M BZO films. First peaks of BZO are marked with a red square and the first peak of YBCO with a blue one.

Another important information that can be extracted from XRD measurements is the evolution of the nanostrain of the nanocomposites with the thickness. Figure 3.21 shows a comparison of the nanocomposites and the pristine YBCO films nanostrain values as a function of the film thickness.

It is observed in figure 3.21 that the nanostrain increases with the thickness for both pristine YBCO and YBCO+10%M BZO films. The values of nanostrain for the YBCO+10%M BZO films are always larger than in the case of the pristine YBCO films but, at higher thickness, the difference between these values decreases. Very likely, this is caused by the fact that at large thicknesses the nanostrain is not only affected by the defects created by the NPs, but also by other macroscopic defects associated to the texture degradation observed by XRD (figure 3.17). The texture degradation indicates that the link between different grains is not perfect. There is some misalignment between grains (small angle grain boundaries) that creates strain and defects at the grain boundaries. This strain is not locally homogeneous but act in the microscale, since the grain size is in the order of

μm. Therefore, when some texture degradation is observed in nanocomposite films, there are two different contributions to the strain that is being measured: the local scale, or the nanostrain, which is cause by the effect of NPs (the local distortions of the YBCO in the surroundings of the NPs and the nanostrain associated to the partial dislocations in the perimeter of the SFs are measured) and the mesostrain which is associated with the defects generated in the grain boundaries. It is not possible to distinguish between both contributions with the used XRD measurements, so the analysis of the measured strain has to take into account both contributions.

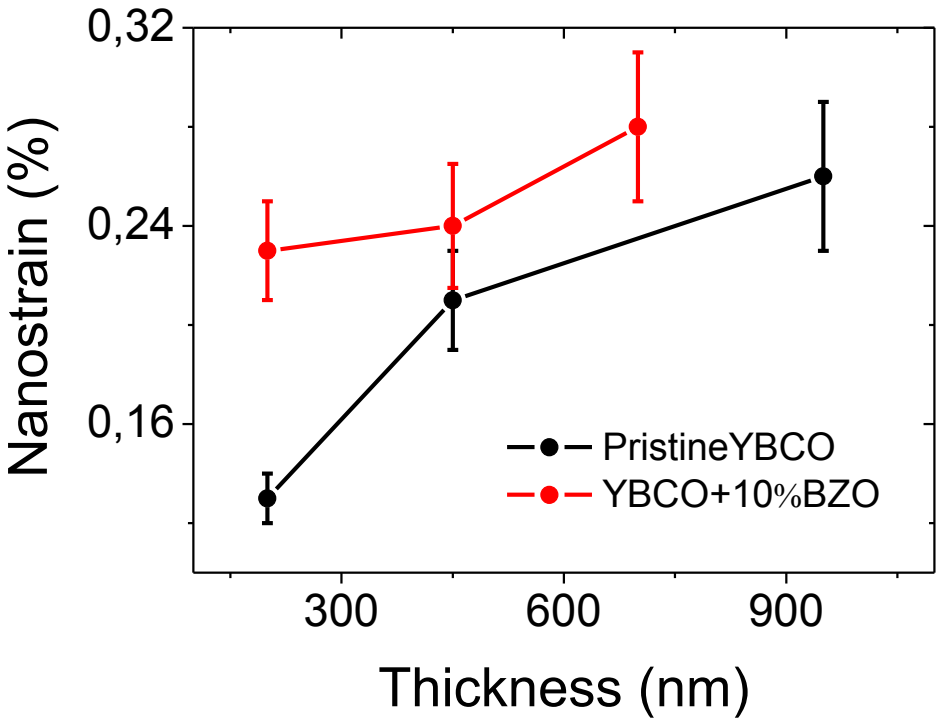

Figure 3.21. Nanostrain evolution with the thickness for pristine YBCO films and the YBCO+10%M BZO films.

By calculating the incoherent interface it is possible to add these values to figure 3.10 and see if thicker films follow the general linear trend that was found for the 250-300 nm nanocomposite films (figure 3.22). As the thickness increases, it is observed that the increase of the strain with the incoherent interface is, in any case, with a much lower slope than in the case of 200 nm films (the line of 700 nm takes into account a pristine film of 950 nm and a nanocomposite film of 700 nm because no pristine film of 700 nm were synthesized). This slope decreases as the thickness increases (slope for the 700 nm films is lower than the 450 nm). This effect can be explained taking into account the mesostrain contribution to the total measured strain. The increase of the strain measured in the pristine films (those with incoherent interface=0) can only be attributed to the increase of the mesostrain since no NPs are present. Therefore, in the case of the 450 and 700 nm nanocomposite films, the increase of the strain has one part associated to the mesostrain and another part associated to the presence of NPs (the difference between the strain of the pristine film and its strain value). The fact that the slope in the case of 450 and 700 nm decreases with respect to the 200 nm case, in which it is assumed that all the change in the strain is due to the presence of NPs (local strain or nanostrain), is indicating that the

presence of mesostrain is detrimental for the increase of the nanostrain when the NPs are added to the nanocomposite films.

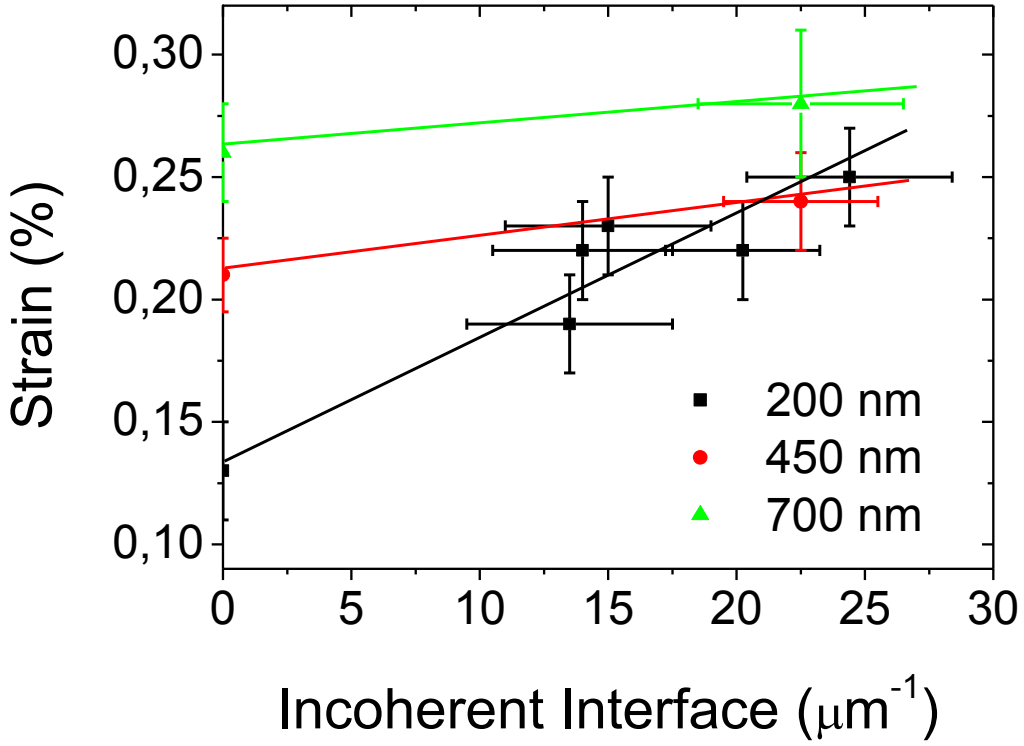

Figure 3.22. Dependence of the strain on the incoherent interface of NPs for different film thickness.

3.4.1.2 Atomic scale structural analysis

The structural characterization has been complemented with TEM images and EDX spectra. A general view and EDX map of the 450 nm YBCO+10%M BZO film is shown in figure 3.23.

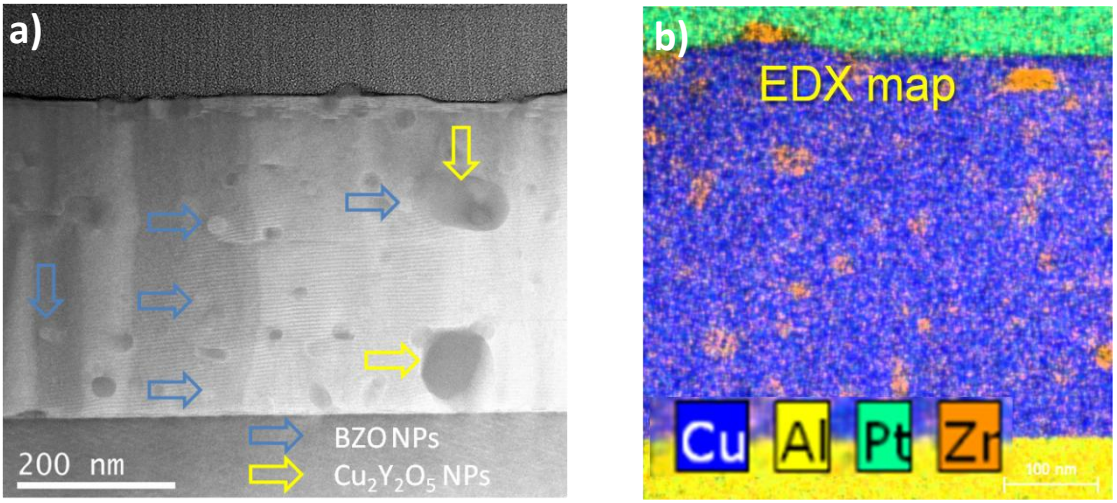

Figure 3.23. Cross-section HAADF TEM image of 450 nm YBCO+10%M BZO film a) showing the presence of BZO NPs and big unreacted phases. The EDX map b) demonstrates a fairly good homogeneous distribution of BZO NPs through the thickness of the film.

The most remarkable feature observed in these images is the presence of a great amount of secondary phases with large sizes (> 100 nm). This is also extensible to the 700 nm film and certainly differs from the 200 nm film, as it can be observed in figure 3.12 (YBCO+10%M BZO 200 nm film). This confirms what it has been observed by XRD measurements. It is also notorious, as it can be seen in the EDX spectrum of Zr, that the distribution of BZO NPs is quite homogeneous throughout the thickness of the film. So, it is possible to conclude that the homogeneous distribution of NPs is maintained despite the increase of thickness and, therefore, the increase of the NPs random fraction mentioned before probably asses from an enhanced supersaturation which increases the homogeneous BZO NPs nucleation

However, looking closely at TEM images, one important detail becomes obvious. There is a large amount of long SFs (> 100 nm) produced by the presence of the secondary phases (cuprates, in this particular case, that were not detected by XRD) and not by the presence of BZO NPs, as it can be observed in figure 3.24.

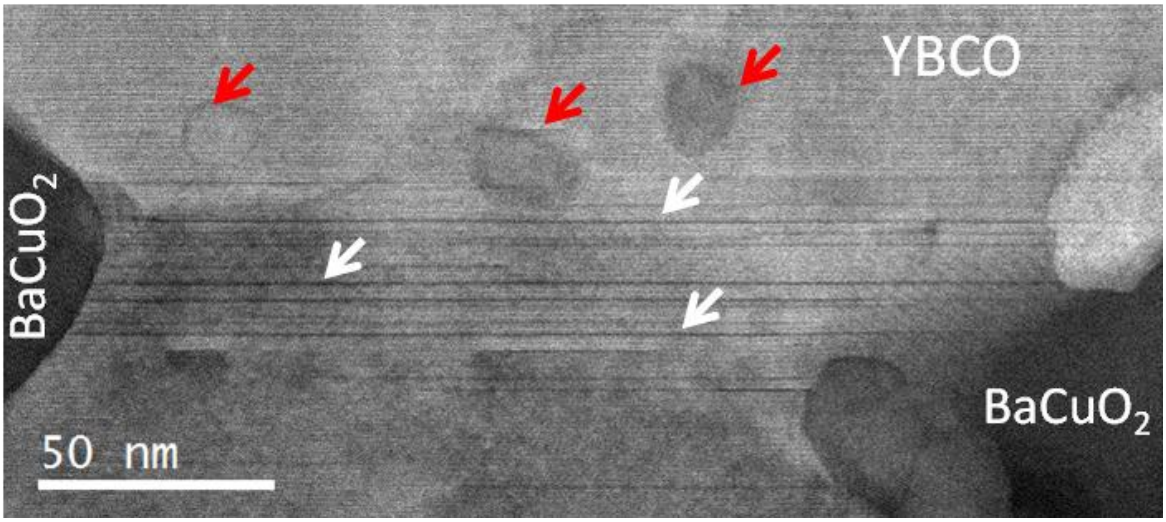

Figure 3.24. TEM image of 450 nm YBCO+10%M BZO film showing the presence long SFs (identified with white arrows) produced by the unreacted phases ($BaCuO_2$ NPs) and not by the BZO NPs (red arrows).

In summary, the interface stress that is created in the thicker films (450 and 700 nm) by the presence NPs and other secondary phases is released mostly forming long SFs in the surroundings of the unreacted phases. The long SFs do not create so much strained regions in the YBCO matrix as the short ones. This also makes that the strain values for 450 and 700 nm nanocomposite films were not as high as it should be from the incoherent interface values. If the secondary phases were not present, all the interface stress would be released by forming short SFs in the surrounding of the BZO NPs resulting then in an enhancement of the nanostrain values. Probably, even in this case, the difference between the nanocomposite and the pristine films would not be as large as in the case of the 200 nm film because of the presence of mesostrain, but it is sure that higher values would be reached.

Considering this scenario, it would be possible, in principle, to transform figure 3.23 into figure 3.25 in which the dashed line (lines parallel to the black one, the one for the 200 nm films) would be the hypothetic linear trend if the behavior of the thick films were the same as the thin films. In this case, if the mesostrain and the unreacted phases were not present, the behavior of the thick nanocomposites would be similar to the 200 nm

nanocomposite films in which all the interface stress is released by the short SFs created by the NPs and, therefore, they will follow the red and the green dashed lines. It could happen as well that the intercept of these lines decreases if the mesostrain is also reduced, but it is sure that the slope would be maintained in the optimum conditions. For these reasons, there is still room for improvement (which is symbolized by the two arrows in figure 3.25) by optimizing the growth conditions for the thick films.

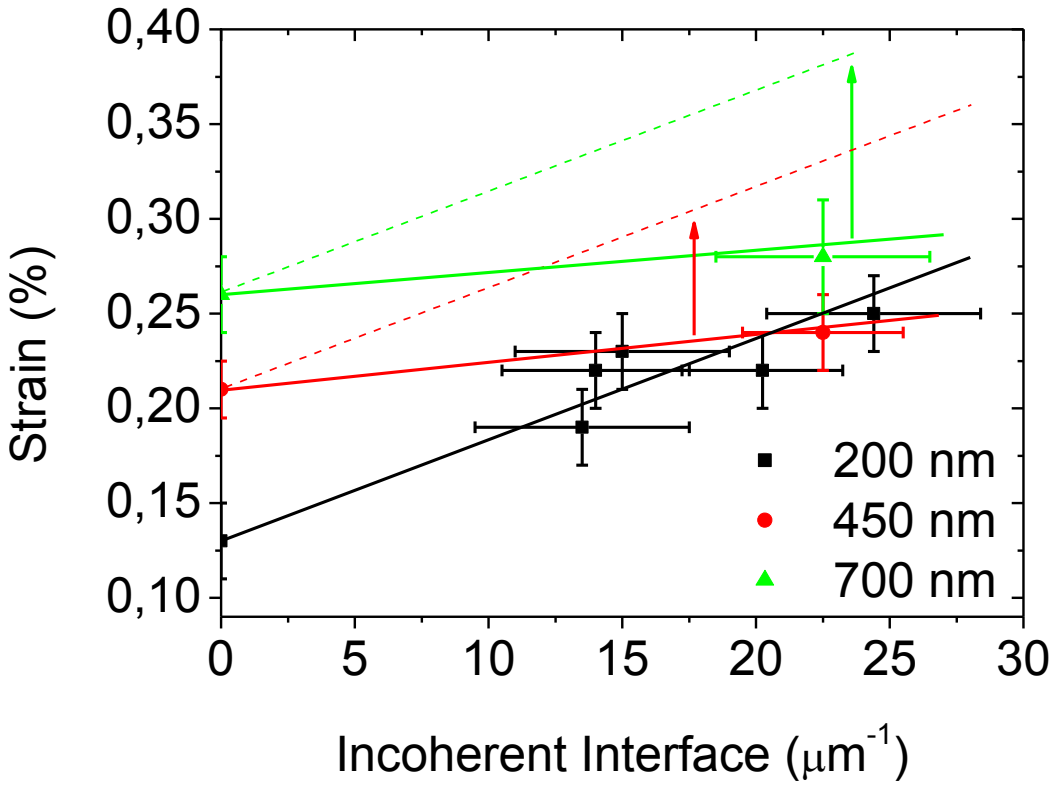

Figure 3.25. Dependence of the strain on the incoherent interface of NPs for different film thickness. The dashed lines mark the hypothetic linear trend in the case that the secondary phases were removed and all the contribution was caused by the BZO NPs.

3.4.1.3 Thickness effect on the physical properties

To study the effect of the thickness increase on the physical properties, SQUID measurements were performed. The T_c remains stable as the thickness increase. All the films present a T_c of 90-91 K. However, the values of the J_c values at 77 K are dramatically affected by the thickness increase as it can be observed in figure 3.26.

The decay in the J_c values is present in the pristine YBCO and YBCO+10%M BZO films, suggesting that the decay is not related to the presence of the NPs. Again this has to do with the presence of the unreacted phases and mesostrain. The presence of secondary phases or unreacted phases that act as "current blockers" reducing the effective area in which the current can flow freely can cause the drop of the J_c^{sf} at 77 K. The fact that the J_c^{sf} at 77 K values for the YBCO+10%M BZO are even lower is because here the NPs are added to the secondary phases so, if the process is not well controlled; the NPs will contribute to the drop of the critical current density

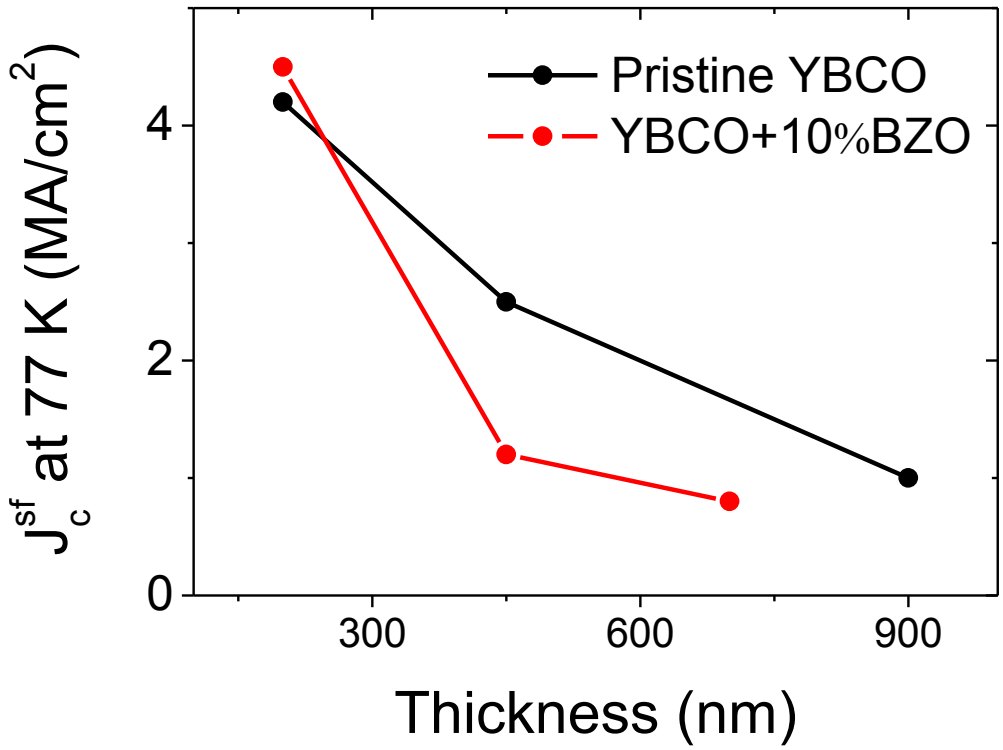

Figure 3.26. SQUID measurements showing J_c^{sf} at 77 K evolution with the thickness for pristine YBCO and YBCO+10%M BZO films.

On the other hand, it is well known that the mesostrain reduces J_c^{sf} values[104, 131], even when the grain misorientation is very low, due to weak-link behavior in the grain boundaries and the strain accumulated here similarly to the tensile strain generated by dislocations in low angle GBs[192]. It was shown that the increase of the thickness implies a degradation of the texture due to the change of the supersaturation conditions. But also, it was reported that the thickness increase involves the decrease of the grain density, the increase of the grain size and, therefore, the increase of the internucleus spacing[153, 155]. The consequence is that the intergranular connectivity among these large grains can become poor and granularity effects could start to appear thus decreasing the J_c^{sf} at 77 K values[193, 194]. The granularity can be detected by performing hysteresis loops at low temperatures and observing the displacement of the maximum of the magnetization at magnetic fields $\neq 0$[193, 194]. Figure 3.27 shows how the maximum (indicated with arrows) of the J_c at 5 K (proportional to the magnetization) is displaced to higher fields as the thickness of pristine YBCO films increases. This is an evidence of the increase of the granularity with the thickness for pristine YBCO films.

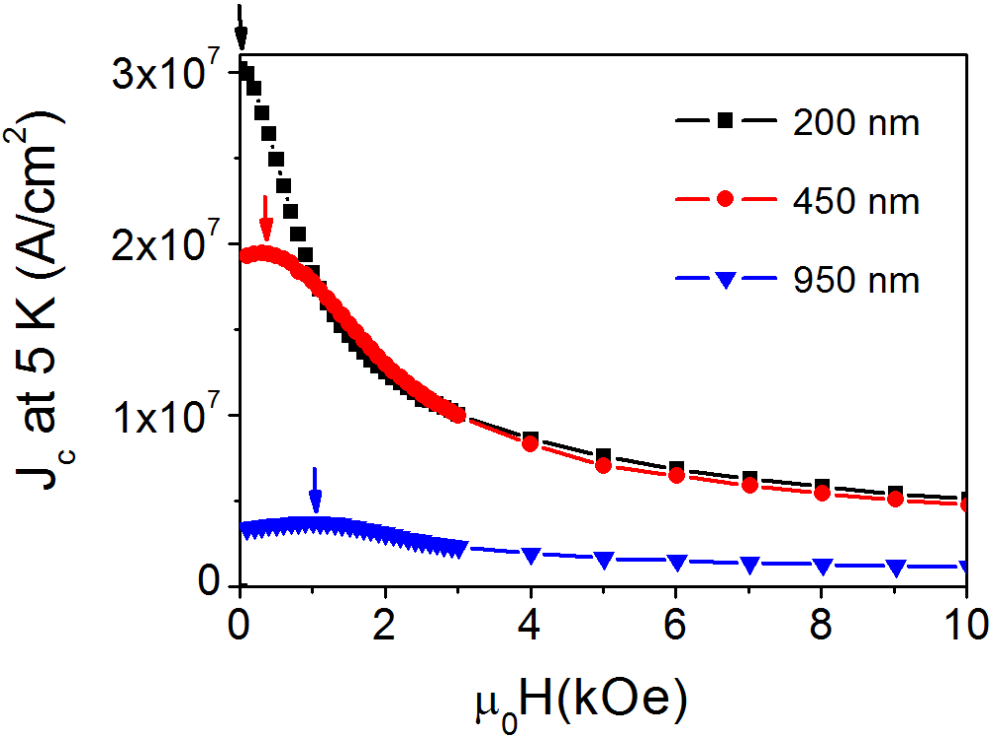

Figure 3.27. J_c at 5 K evolution with the magnetic field for pristine YBCO films of different thickness showing the displacement of the maximum (indicated with arrows) value of the J_c to magnetic fields ≠ 0.

Despite these limitations, the normalized J_c at 77 K dependence with the magnetic field for all the nanocomposites, whatever the thickness, shows the typical behavior of a nanocomposite film: an enlargement of the vortex pinning regime to higher fields obtaining smoothed J_c(H) curves (figure 3.28).

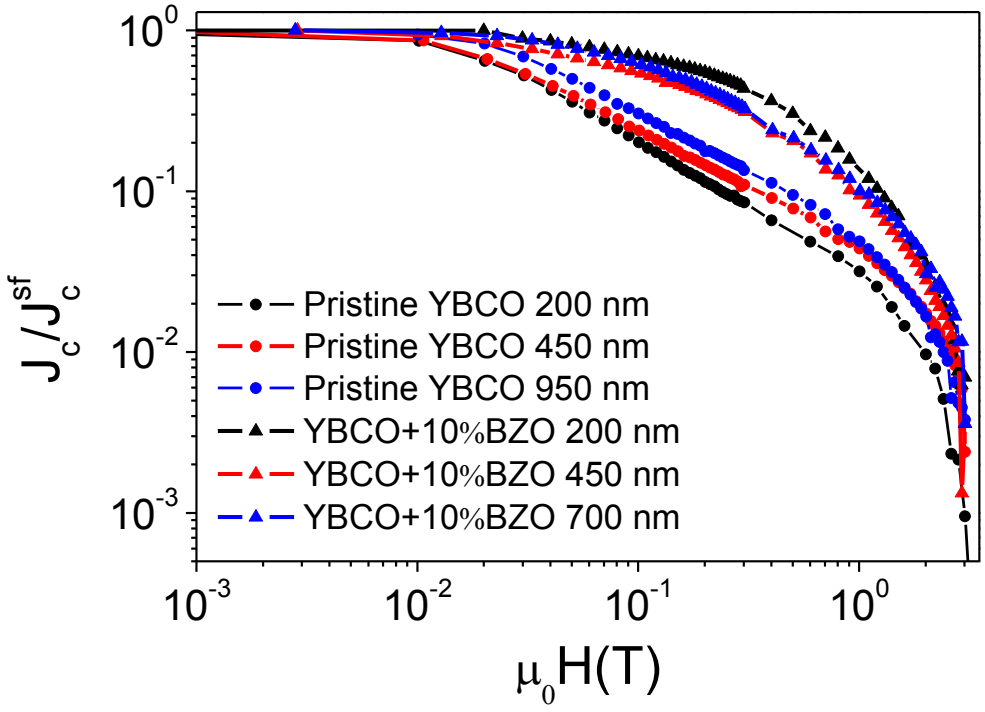

Figure 3.28. J_c at 77 K dependence with the magnetic field at 77 K for the 450 nm pristine YBCO and YBCO+10%M BZO films.

Looking carefully at figure 3.28, it is possible to understand the consequence of having a lower slope in the strain vs. incoherent interface plot (figures 3.22 and 3.25). In the case of the 200 nm nanocomposite films, it is assumed that the increase in the measured strain comes from the local strain (nanostrain), i.e., from the effect of the NPs and the SFs. This nanostrain is responsible of the enhancement of the pinning properties, as it was explained before, resulting in the black triangles curve. As the thickness is increased, more defects start to appear in the pristine films (unreacted phases that create long SFs) resulting in slightly smoothed curves as compared to the case of the 200 nm pristine films (read and blue circle curves for 450 and 950 pristine YBCO films respectively) Moreover, as it was explained before, the increase of the thickness implies the generation of mesostrain. The mesostrain in the thick nanocomposite films is detrimental for the nanostrain so the slope of the lines in figures 3.22 and 3.25 decreases for the thick films. The lower the nanostrain is, the lower the pinning performances. This is visible in figure 3.28 because the curves for the 450 and 700 nm nanocomposites films (red and blue triangles curves) less smooth than in the case of 200 nm nanocomposite film.

In view of these results, it is possible to conclude that the lower the slope of strain vs. incoherent interface plot is, the higher the influence of the mesostrain in detriment of the nanostrain and the lower the difference between the pristine and the nanocomposite films which means poorer pinning performances of the nanocomposite films.

However, and even with all these limitations, the nanocomposite films have higher J_c at high fields than pristine films, despite the low values of J_c^{sf}. In figure 3.29 the J_c values of the pristine YBCO and the YBCO+10%M BZO films of different thicknesses at 1T are shown. The decay in the J_c with the thickness is observed in both cases but the values of the nanocomposites are always higher than those of pristine YBCO films.

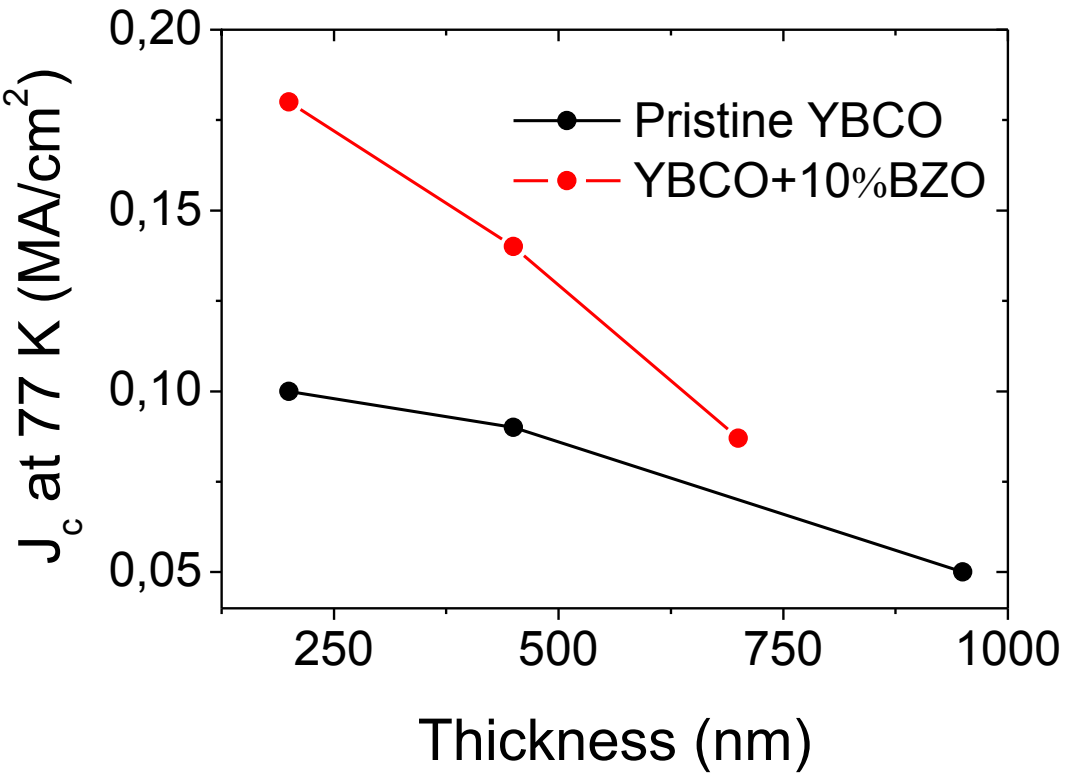

Figure 3.29. J_c at 77 K and at 1 T evolution with the thickness for the YBCO+10%M BZO and the pristine YBCO and the films.

In view of these results, it is clear that further optimization of the growth conditions of both pristine YBCO and the YBCO nanocomposite thick films is required in order to enhance the superconducting performances in both cases. To avoid the presence of unreacted phases and improve the intergranular connectivity, thus limiting the granularity effects, are mandatory issues to achieve this objective.

3.5 Synthesis of GdBCO-Gd_2O_3 nanocomposite films

In recent years it has been studied the replacement of Y^{3+} in $YBa_2Cu_3O_7$ by other rare earth elements such as Neodymium (Nd), Samarium (Sm), Europium (Eu) or Gadolinium (Gd) to form alternative $REBa_2Cu_3O_7$ (REBCO) and obtain improved superconducting properties. However, the change of the Y^{3+} ion results in different difficulties when the new REBCO compounds are synthesized. These difficulties are related with the partial substitution of the Ba^{2+} sites by large RE ions and the low stability of the 123 phase in some of the REBCO compounds.

Despite these difficulties, several REBCO compounds have been synthesized. Among them, the GdBCO highlights due to its excellent properties. In particular, the increase of the T_c that is observed in both the GdBCO bulk samples[195] and thin films[196] causes an upward shift of the irreversibility line which makes GdBCO a very promising material for some applications.

First, GdBCO samples were studied in form of single crystals[195] and melt-processed bulk samples[197, 198, 50]. These first samples already revealed the great properties of the GdBCO compared with other REBCO compounds. The GdBCO thin films have been prepared during many years by in-situ techniques. The properties of the thin films synthesized by sputtering[199-202], PLD[203] or MOCVD[204] have confirmed the results obtained in the case of the single crystals and bulk samples.

In recent years, a large group of researchers have opted for the ex-situ growth techniques to grow superconducting thin films at low cost and easy scalability. The case of the GdBCO is not an exception. In most of the works published in the preparation of GdBCO thin films by CSD, the well-known TFA route was chosen. The superconducting properties of GdBCO thin films obtained by TFA route are really interesting. They show values of J_c of 2-4 MA/cm^2 and values of T_c of 93-94 K which are similar than in the case of GdBCO thin films synthesized with in-situ methods and sometimes even better than in YBCO-TFA thin films[196, 205, 206].

Despite that the TFA route is an extended and well-controlled process, the fact that during the processing of the TFA-derived films HF is released to the ambient has made the researchers to look for alternative solutions to the TFA. In this sense, the logical path is the use of fluorine-free precursors leading to fluorine-free solutions. However, the fact that using this solutions the synthesis of the YBCO is more complicated and tricky (the reactions for YBCO formation are different)[207, 208], have determined scientists to look for an intermediate solution.

These middle-point solutions are the so called “Low-Fluorine Solutions” (LFS). The LFS solutions offer the possibility to reduce the F content and, therefore, the HF release, maintaining the same reaction mechanism for the YBCO formation than in the case of the TFA route which facilitates the procedure[127]. The LFS are quite extended for

the preparation of YBCO thin films, but minimal work is done in the case of GdBCO-LFS[139].

In this work, thin films of GdBCO will be prepared using LFS solutions. The advantages of the using LFS instead of TFA solutions will be explained in detail. The first results (structure and superconducting properties) of the GdBCO thin films using a new LFS never used before will also be presented. It will be explained also the new developed growth process called "Flash-Heating process" which is an alternative to the standard one used in the case of the TFA-derived films. Finally, the first results of the preparation of GdBCO-LFS nanocomposites will be reported. GdBCO+20%M Gd_2O_3 films were synthesized showing promising properties for the future use in power applications.

3.5.1 Features of Low-Fluorine Solutions

The formulation and the preparation of the GdBCO-LFS was explained in detail in chapter 2. As a brief summary, just remember that the formulation is equivalent to solution 4 reported in Palmer et al with a 26% of the total volume of propionic acid, a 5% of the total volume of trietanolamine (TEA) and methanol[127], but changing the Y-TFA salt for Gd-TFA salt. The typical molarity of the GdBCO-LFS is 0,25 M leading to a 250-300 nm films after all the processing steps.

The rheological features of the 0,25 M GdBCO-LFS are also very similar to those reported in Palmer et al (Solution 4), as it can be seen in table 3.1[127].

	YBCO-LFS	GdBCO-LFS
Viscosity (mPa.s)	9	10
Contact Angle	27	25
Water content (%wt)	<2	<2
pH (in water)	4,2	4,3

Table 3.1. Rheological features of the GdBCO-LFS compared to the YBCO-LFS (solution 4 from Palmer, X et al[127]).

3.5.2 Pyrolysis process: TFA vs. LFS

The pyrolysis process is used to remove the organic content present in the as-deposited metalorganic solution. The pyrolysis process is a critical step in the CSD method because the quality of the pyrolyzed films has a great influence on the final properties of the films. Any kind of inhomogeneity will cause a decrease of the final performances of the films, as it was demonstrated in the case of the YBCO films[178].

In general, to achieve smooth and defect-free films after the pyrolysis process is not an easy task. During this stage there is a strong film shrinkage due to the volatilization of organic solvents and the decomposition of the precursors. In the YBCO films derived from TFA solutions this shrinkage could be up to 50% of the initial thickness[178].

Apart from this issue, in the TFA solutions there is an additional limitation related with its chemical formulation. Due to its high Lewis acidity, the TFA salts are very hygroscopic[209]. The H_2O-trifluoroacetate bonds are stronger than methanol-trifluoroacetate bonds causing water absorption. This characteristic, joined to the fact that there is a big

difference between the values of vapor pressure ($P_{v\,H_2O}$=23,8 mmHg and $P_{v\,methanol}$=122 mmHg at 25 ºC) and surface tension (γ_{H_2O}=72,86 mN/m and $\gamma_{methanol}$=22,50 mN/m at 20 ºC) of methanol and H_2O, cause a distortion of the precursor species aggregation creating a stress in the film. This stress is likely to cause instabilities in the layer forming buckling[210].

This effect is quite important in the case of the YBCO films[178], and it is even more important in the case of the GdBCO-TFA films, as it was demonstrated in a previous work dealing with GdBCO-TFA films[211]. In this work, it was shown how the water content and the relative humidity affect the quality of the films. It was demonstrated that if the solution has a water content higher than 2% or the relative humidity is higher than 6-7% during the spin-coating process and higher than 40% during the pyrolysis, it is not possible to obtain homogenous GdBCO-TFA films. So, homogeneous GdBCO-TFA films after pyrolysis can be only achieved in a narrow window of conditions that lead to non-reproducible pyrolysis processes. The rate of success using the 0,25M GdBCO-TFA solutions is lower than 10% under the conventional conditions of the laboratory obtaining, mostly, films with buckling, as can be observed in a typical case presented in figure 3.30.

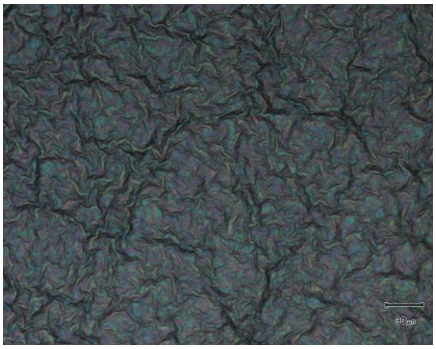

Figure 3.30. Optical microscope image of the typical GdBCO-TFA film after the pyrolysis process showing a buckled surface.

3.5.2.1 Use of Low-Fluorine Solutions

Apart from the environmental benefits related with the use of non-fluorinated compounds, most of the mentioned limitations associated to the TFA solutions can be overcome with the use of Low-Fluorine Solutions (LFS). The benefits of this kind of solutions comes from three different aspects related with its chemical formulation (experimental part, chapter 2): the reduction of the TFA-salts content in the solution, the use of Triethanolamine (TEA) as a ligand for the stabilization of the metal salts in the solution and the use of propionic acid as solvent.

First, the reduction of the TFA salts allows achieving solutions with a lower water absorption tendency. This will lead to a higher success ratio of homogenous films after pyrolysis. On the other hand, the use of TEA as ligand, apart from its role as coordination compound of the metal salts, helps to achieve a smooth release of the stress in the films during the pyrolysis due to its elastomeric properties.

Finally, the use of propionic acid also helps to reduce the water absorption of the solution. This fact has been demonstrated by a set of experiments carried out by Prof. Pere Roura and Dr. Hichem Eloussifi from Girona University. The experiments were performed by spreading the solution over a glass disk and then measuring the mass change due to the water absorption using a microbalance and leaving the sample in air. As it observed in

figure 3.31, the addition of propionic acid to both the GdBCO-TFA and GdBCO-LFS solutions leads to a decrease of the mass change due to the water absorption.

The reduction of the fluorine content and the presence of propionic acid in the solution cause much lower water absorption of the LFS solution than the TFA solution. Actually, the water content does not overcome the 2%. This fact can be observed in figure 3.31 in the case of GdBCO solutions and it was also observed in the case of the YBCO solutions[127]. These results can be explained by the presence of coordination compounds (TEA or propionic acid) to the metal atoms in the salts thus preventing their coordination with water molecules.

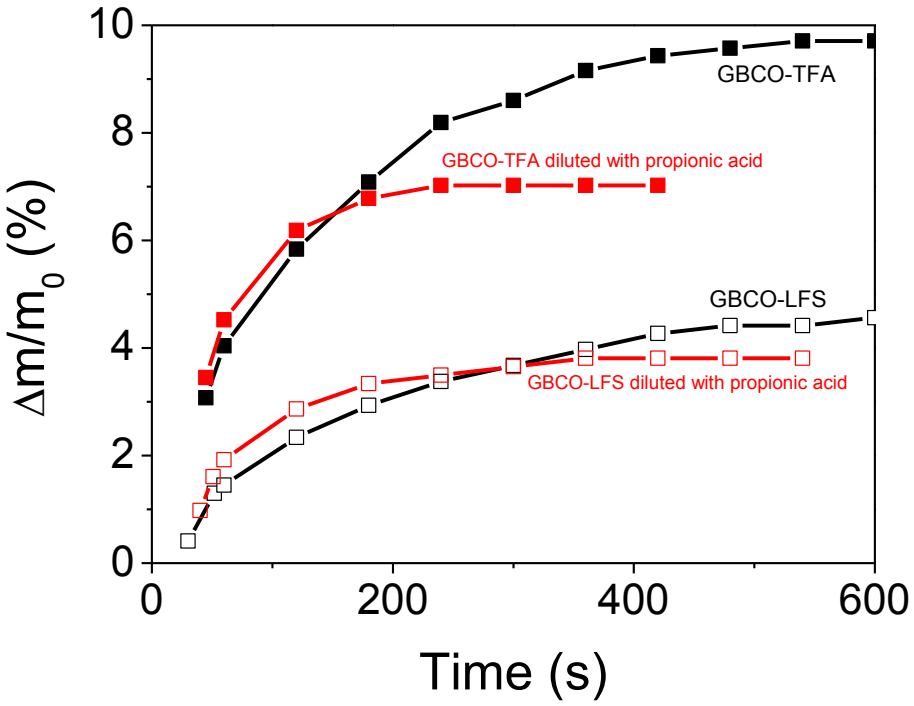

Figure 3.31. Mass change at room temperature in air due to the water absorption of GdBCO-TFA and GdBCO-LFS solutions and the same solutions with the addition of propionic acid.

The typical appearance of the GdBCO-LFS films over LAO after the pyrolysis is shown in figure 3.32. The fact that the GdBCO-LFS solutions absorb less water than GdBCO-TFA solution, together with the presence of the TEA that confer enhanced elastomeric properties to the system, makes that the rate of homogeneous films obtained after the pyrolysis increases from 10% to almost 95% in the case of 0,25M GdBCO-LFS.

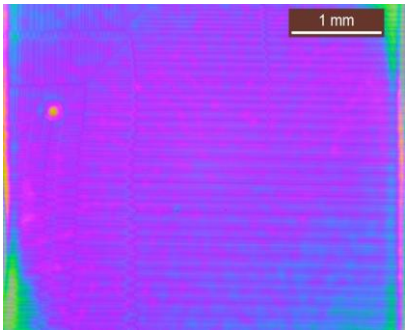

Figure 3.32. Optical microscope image of a typical GdBCO-LFS film after the pyrolysis process showing a homogeneous surface.

This fact reveals the convenience of changing from TFA solutions to LFS. The used thermal process is the same as in the case of YBCO-LFS which is nothing more than a modified "standard pyrolysis process" in which the dwell temperature is increased to 500 ºC with a higher gas flow (0,12 l/min)[127]. The rest of the parameters remain untouched..

3.5.3 Growth process: Flash-Heating process

Once the pyrolysis process leads to homogeneous films, the films are grown. In the case of the pyrolysis of GdBCO-LFS films, it was possible to use the same thermal profile than in the case of the YBCO-LFS. However, in the case of the growth process this is not possible because the crystallization conditions for achieving epitaxial GdBCO are different.

Looking at the phase diagram reported by Iguchi et al, one realizes that the stability line is shifted towards higher temperatures compared to YBCO[196, 212]. This suggests that the "standard growth process" described for the case of the YBCO has to be modified for GdBCO growth. In the "standard growth process", the crystallization temperature was set at 810 ºC, the P_{O_2} is 200 ppm ($1{,}2.10^{-4}$ l/min).

Most of the works related with the GdBCO synthesis by CSD use higher crystallization temperatures and also a lower values of P_{O_2} [196, 205, 206]. This was also confirmed in the previous author´s work for the case of the GdBCO-TFA films[211]. In this work, it was demonstrated that the use of modified process in which the crystallization temperature was increased to 820 ºC and the P_{O_2} was decreased to 100 ppm (6.10^{-5} l/min) leads to a perfect epitaxial GdBCO films from TFA solutions with excellent superconducting performances (T_c=91,1 K and a J_c=2,7 MA/cm^2). The oxygenation was maintained at 450 ºC.

However, the use of this modified standard process in the case of the GdBCO-LFS did not lead to satisfactory results. It is observed the presence of randomly oriented grains reflected by the intensity of the (103)GdBCO Bragg peak as well as the intensity of (200)GdBCO Bragg associated to the formation of a-b nucleated grains (figure 3.33).

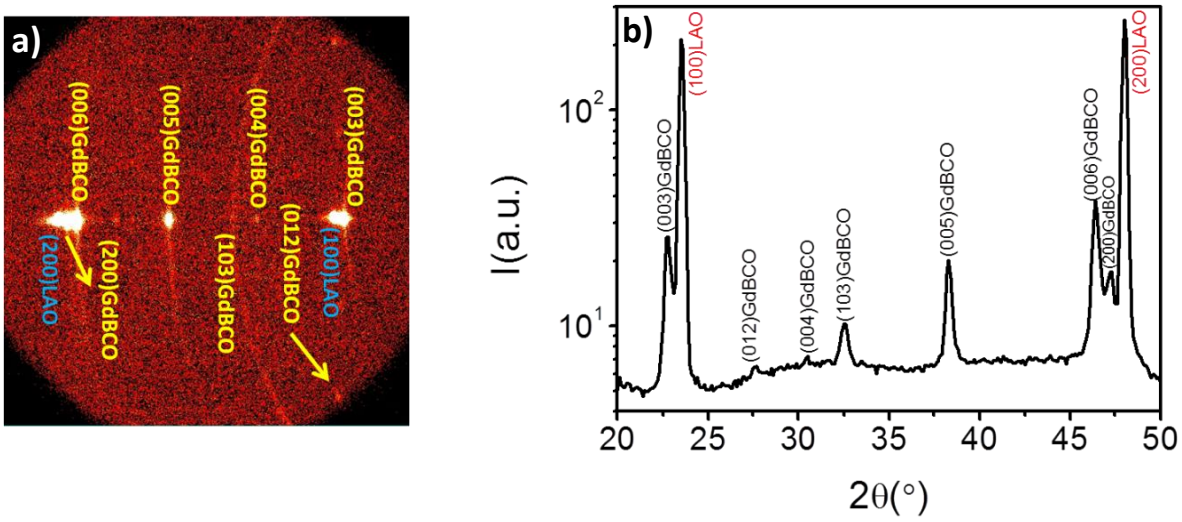

Figure 3.33. 2D XRD θ-2θ frame a) and integrated pattern b) of a GdBCO-LFS film grown using the modified standard process.

In order to encounter the reason why the films do not crystallize only with the c-axis epitaxial orientation, a quenching study was performed. The growth process is suddenly stopped at different temperatures during the heating process and the XRD patterns of the resulting films are analyzed. The results reported in figure 3.34 clearly show the origin of the problem. What happens is that the crystallization conditions of the modified standard process favors the nucleation of the randomly oriented grains (103)GdBCO prior to the c-axis oriented epitaxial grains. It is observed that between 710 and 725 ºC the (103)GdBCO Bragg peak starts to appear while the epitaxial Bragg peaks appears between 750 and 790 ºC. This means that GdBCO has, at these temperatures, an excessive supersaturation and homogeneous nucleation may be competitive enough with c-axis nucleation (see figure 2.11, chapter 2).

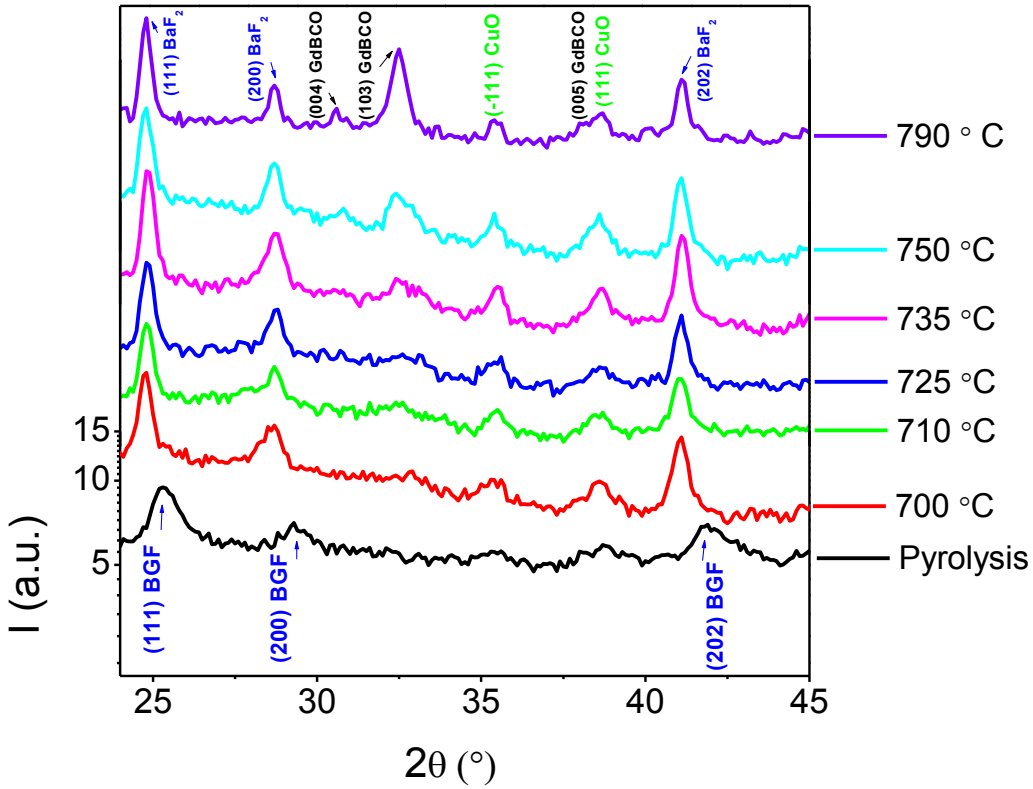

Figure 3.34. XRD patterns of quenched GdBCO-LFS films at different temperatures showing the nucleation of randomly grains before than the epitaxial grains.

3.5.3.1 Flash heating process

In view of the results from figure 3.34, it is clear that the conditions that are used in the modified standard process are not the optimum conditions for the epitaxial growth of the GdBCO-LFS films.

The GdBCO phase is being nucleated at temperatures in the order of 710-725 ºC. But, at these temperatures the nucleation of both a-b and randomly oriented grains is favored because, probably, the supersaturation in this range of temperatures is too high. The nucleation of c-axis oriented grains is more favorable at high temperatures. Therefore, it is interesting to accelerate, as much as possible, the transition through these intermediate temperatures, not allowing enough time to the nucleation of undesired GdBCO

orientations. The dwell temperature is reached faster in this way, favoring the nucleation of c-axis grains.

With this aim, the "flash heating process" was designed. This process is similar to the one reported by Erbe et al [213]. The furnace is first pre-heated at the dwell temperature (820 ºC in this case) and then the film is introduced directly at this temperature. With this procedure it is possible to reach heating ramps of ~400 ºC/min versus the 25 ºC/min of the original process. The XRD patterns of the films grown using this type of process are presented in figure 3.35. A perfectly epitaxial GdBCO films with no presence of other orientations or other phases are achieved. The calculated strain value for these films is 0,15±0,01%.

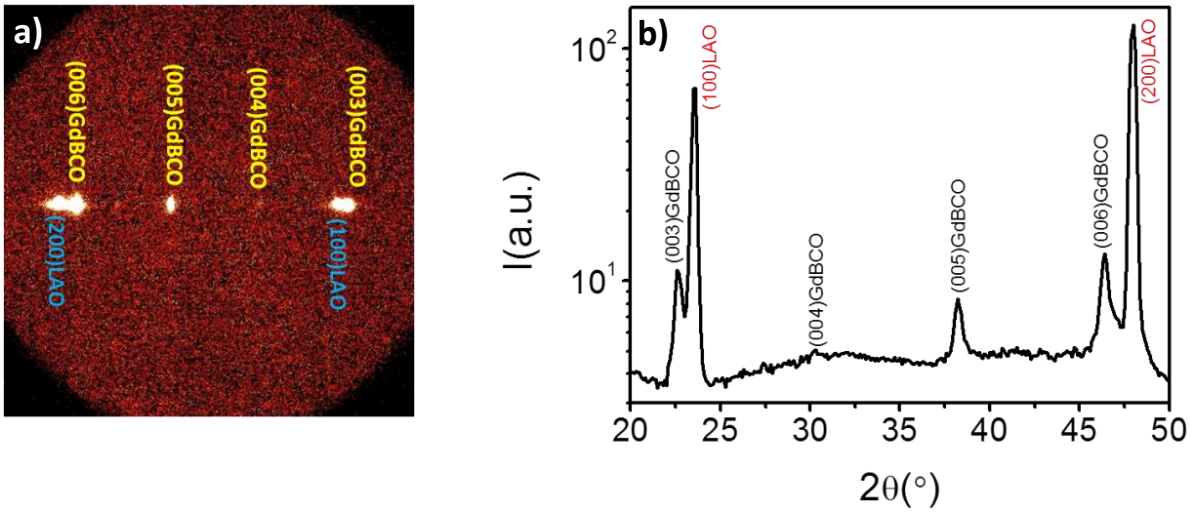

Figure 3.35. 2D XRD θ-2θ frame a) and integrated pattern b) of GdBCO-LFS films grown with the flash heating process.

Despite that the XRD patterns do not show the presence of other orientations, in the SEM images (figure 3.36) it is possible to still observe a small amount of a-b grains.

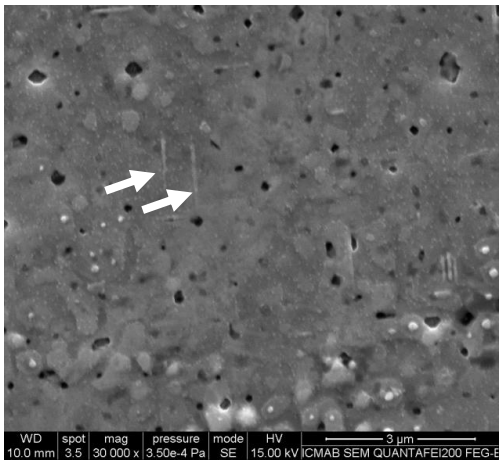

Figure 3.36. SEM image of a GdBCO film prepared by flash-heating process showing a small amount of a-b grains (indicated with white arrows).

This means that there is still room for improve the process. One possibility to improve the results and avoid a-b grain formation is to synthesize first an YBCO layer that

acts as buffer for the GdBCO top layer transferring the completely epitaxial orientation that is possible to achieve with the YBCO films. Another way to improve the quality of the GdBCO films would be to work at even higher temperatures and lower oxygen pressures because, according to the phase diagram of GdBCO, in this way it is possible to get closer to the stability line of the GdBCO which would improve the epitaxial growth of the films[212].

Despite that, as it was just mentioned, the growth process could be optimized; the superconducting properties of the obtained GdBCO films are fairly good. The critical temperature of these films reaches 92,8 K which is in accordance with the results of the reported GdBCO-TFA and GdBCO-LFS films[196, 213, 139]. However, the values of the J_c^{sf} at 77 K remain at ~1,5 MA/cm^2. It is likely that the presence of a small amount of a-b grains is still limiting the values of the J_c^{sf} acting as current blockers.

3.5.3.1.1 Granularity in GdBCO films grown with Flash-heating process

Apart from the presence of a-b grains, another problem has been identified in the GdBCO-LFS films that also restricts the J_c values: the granularity.

It was demonstrated that the granularity causes a decrease of the J_c^{sf}[193, 194]. The existence of granularity can be identified by performing hysteresis loops at different maximum applied fields. Figure 3.37 displays a set of such hysteresis loop measurements with a maximum magnetic field of 8 kOe. It is observed that the maximum value of the magnetization at the reverse branch appears approximately at an applied field of 500 Oe. For a single crystalline superconducting film this would be expected at 0 Oe. This displacement of the maximum value of the magnetization at higher fields is attributed to granularity effects[214].

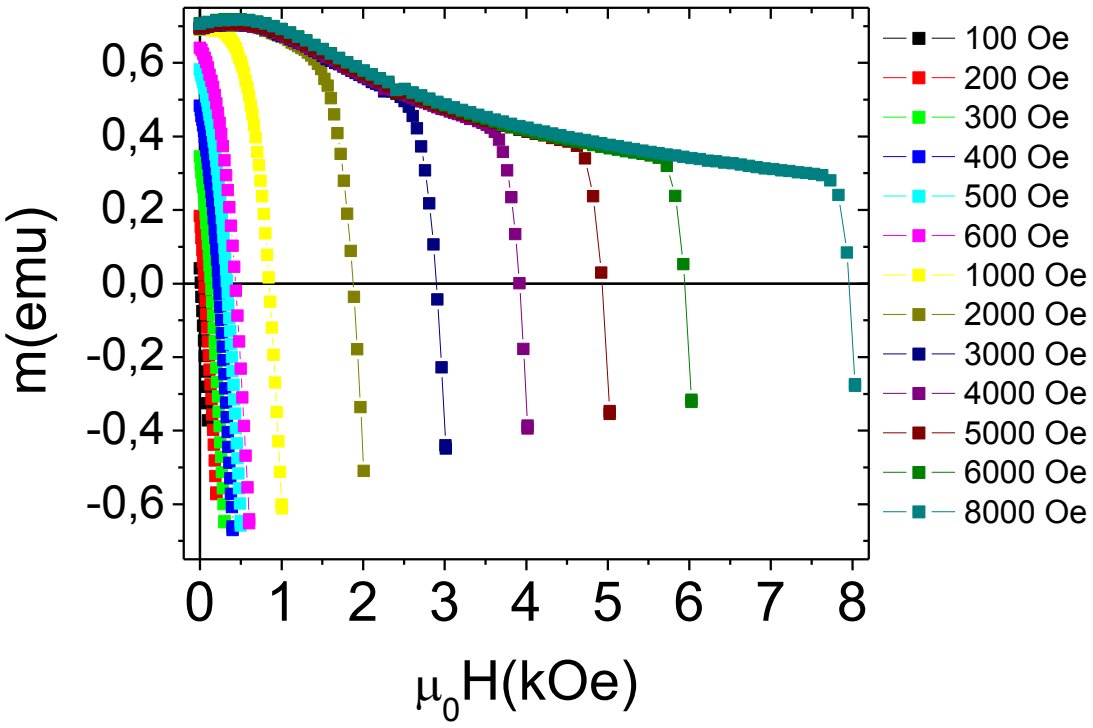

Figure 3.37. Hysteresis loops at different fields in a GdBCO-LFS film grown with the flash heating process showing a displacement of the maximum of the magnetization.

The granularity is characterized by the existence of two different critical current densities: one inside the grains (J_c^G) and another one associated with the grain boundary network (J_c^{GB}). It is possible to obtain J_c^G by applying the method reported by Palau et al[193]. The obtained J_c^G for the GdBCO film reported in figure 3.38 applying the method are: J_c^G(5 K)~40 MA/cm^2 and J_c^G(77 K)~5 MA/cm^2.

These results show that if the granularity is avoided by improved processing conditions, the performances of the GdBCO-LFS films might be largely enhanced.

3.5.4 GdBCO-Gd_2O_3 nanocomposites

The last part of the work with the GdBCO-LFS films was devoted to the preparation of GdBCO nanocomposites by using Low-Fluorine solutions. In this case, the chosen secondary phase was Gd_2O_3 NPs that it is expected to be the simplest alternative for the growth. The preparation of the solution was the same as in the case of the standard GdBCO-LFS but with an excess of Gd-TFA salt. During the growth process, the Gd_2O_3 NPs are spontaneously formed (in-situ nanocomposites). The excess of the Gd-TFA added leads to the formation of a GdBCO-LFS+20%M Gd_2O_3 films. The amount of NPs that is introduced is quite high, but it was chosen like this in order to detect clearly the real effect of the NPs.

The films were pyrolyzed using the same process as in the case of the pristine GdBCO-LFS and they were grown using the "flash heating process" which, as it was demonstrated before in the case of the pristine GdBCO films, leads to reasonably good results. The XRD patterns after the growth process are shown in figure 3.39.

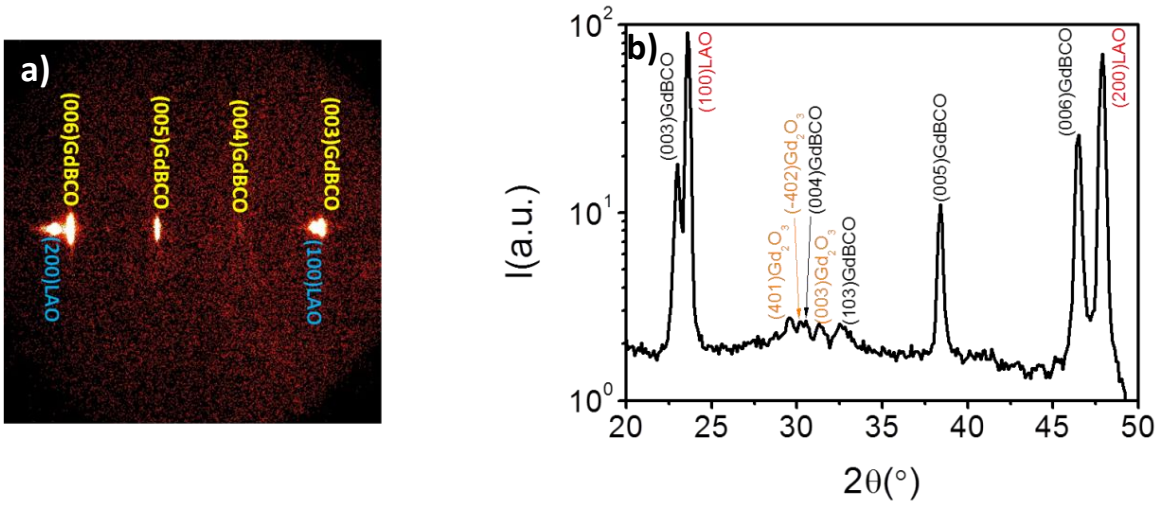

Figure 3.39. 2D XRD θ-2θ frame a) and integrated pattern b) of a GdBCO-LFS+20%M Gd_2O_3 film grown using the flash heating process.

The obtained films displayed a high degree of epitaxial structure. There is only a small amount of randomly oriented grains, as evidenced by the presence of a low intensity (103)GdBCO Bragg peak. The peaks corresponding to Gd_2O_3 can also be observed. This confirms the formation of the Gd_2O_3 phase during the growth process. The presence of the Gd_2O_3 NPs makes that the nanostrain of these films reach 0,24±0,01%, which is comparable with the mixt nanocomposites already explained in this chapter. It has to be

taken into account that this value of the strain has the contribution of the nanostrain and the mesostrain (if in the pristine GdBCO films there is granularity, in the GdBCO nanocomposites film even more).

The observed features in the XRD patterns are confirmed by TEM images. Figure 3.39 a) shows a perfect c-axis oriented GdBCO phase with the presence of SFs (white arrows). Figure 3.39 b) shows the presence of Gd_2O_3 NPs within the GdBCO matrix causing distortion in the surroundings and the formation of SFs justifying the high value of measured nanostrain.

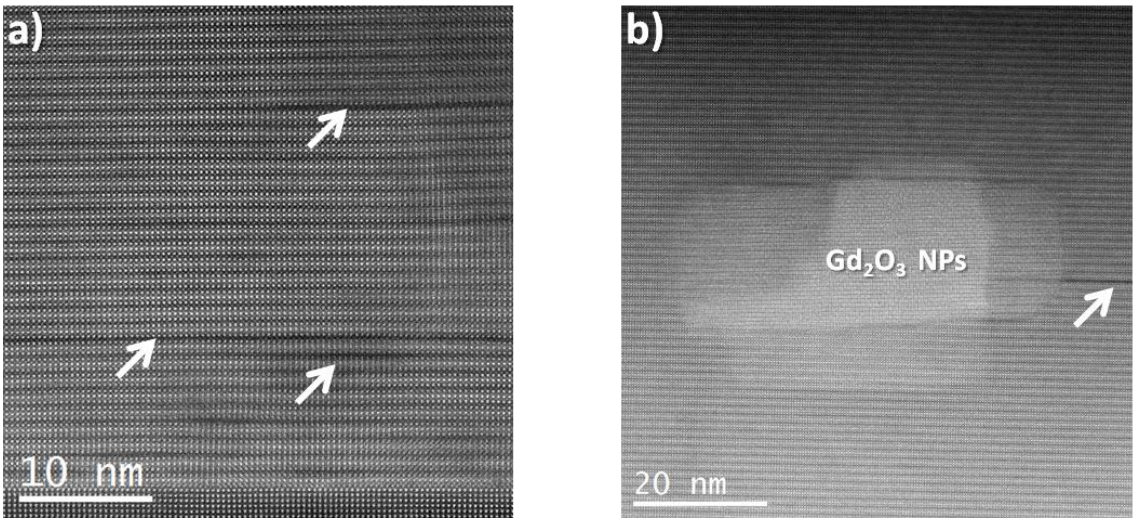

Figure 3.39. TEM images of a GdBCO-LFS+20%M Gd_2O_3 film. Picture b) shows two superimposed Gd_2O_3 NPs.

The superconducting properties of the GdBCO-LFS+20%M Gd_2O_3 nanocomposite films turned out to be enhanced as compared to those of the pristine GdBCO-LFS films and similar to the reported values on GdBCO+BHO nanocomposite films[95]. The T_c remains at the same value of the previous case, i.e., 92,7 K (this does not occur in the case of the YBCO nanocomposites in which the T_c usually decreases at least 1 K, as it was previously mentioned) but in this case the J_c^{sf} at 77 K reaches 3,2 MA/cm^2 which is the double of the pristine films.

The normalized J_c dependences with the magnetic field for the pristine GdBCO-LFS and for the GdBCO-LFS+20%M Gd_2O_3 are presented in figure 3.40 together with the pristine YBCO and some YBCO nanocomposites dependences for comparison. The GdBCO+20%M Gd_2O_3 curve shows the typical smoothed field dependence that is commonly observed in the best nanocomposites.

It is observed in figure 3.41 that the normalized J_c dependence with the magnetic field for the GdBCO+20%M Gd_2O_3 film is very similar to the YBCO+10%M BZO nanocomposite films and much smoother than in the case of the YBCO+10%M Y_2O_3 or the pristine GdBCO film. This demonstrates that the GdBCO+20%M Gd_2O_3 films enhance the pinning performances at least at the same level as the YBCO+10%M BZO nanocomposites. It is also noticed that the difference between the pristine GdBCO film and GdBCO+20%M Gd_2O_3 films dependences are smaller than in the case of the YBCO+10%M BZO film compared with the pristine YBCO films. This phenomenon can be attributed to the persistence of some granularity that can increase the mesostrain values causing a similar effect than in the case of the thick films previously commented. Further

characterization of the transport properties of these GdBCO nanocomposite films is expected to be carried out in the near future at ICMAB.

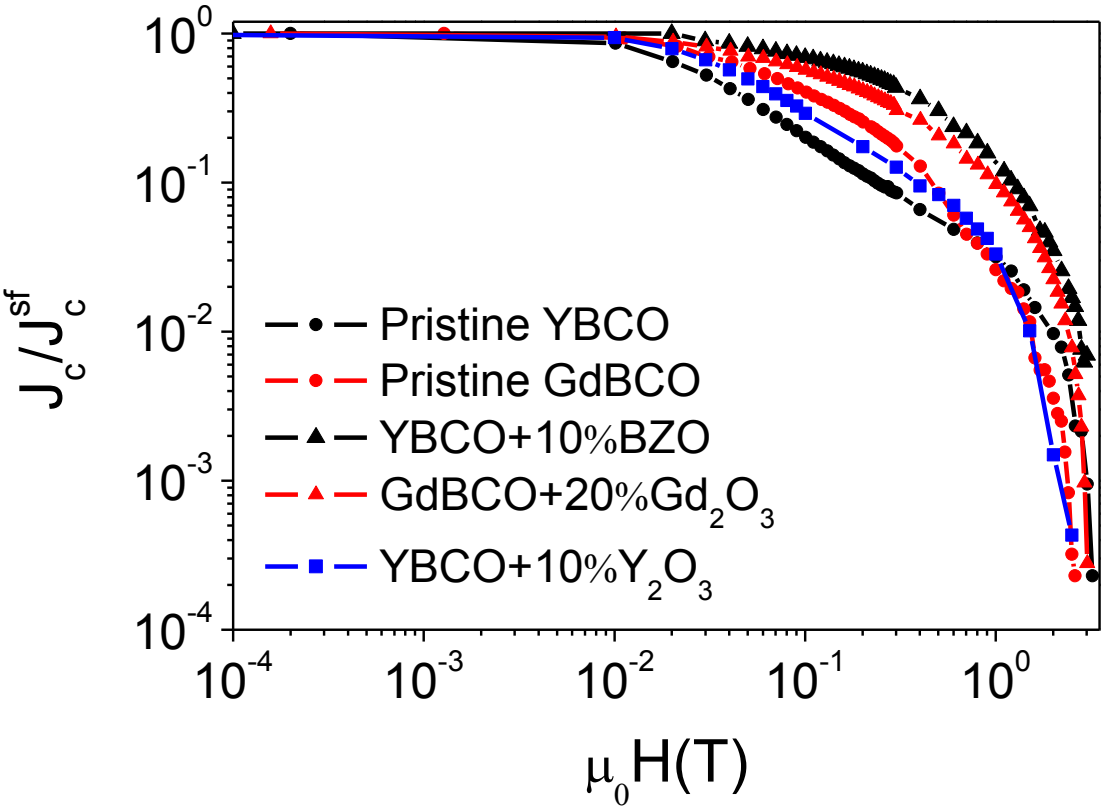

Figure 3.40. J_c dependence with the magnetic field curves for the pristine GdBCO-LFS and GdBCO-LFS+20%M Gd_2O_3 films. It have been also included

3.6 Conclusions

In this chapter the CSD in-situ approach was used to prepare nanocomposite films of different NPs compositions. It has been studied the effect of mixt compositions (BZO+YO, BZO+BYTO, BYTO+YO, BYTO+CuO) on the microstructural and physical properties. In particular, the focus was in the study of how the SFs scenario affects them. It was also analyzed the effect of the thickness increase, again, in the structural and physical properties. And, finally, the structure and the properties of GdBCO-Gd_2O_3 nanocomposite films from LF solutions were also investigated. Through this study the following conclusions were reached:

- It is possible to increase the NP concentration up to 15%M without coarsening and obtaining epitaxial YBCO nanocomposites by using mixt compositions of NPs (BZO+YO, BZO+BYTO, BYTO+YO, BYTO+CuO). This is not possible (with the same processing parameters) using only one kind of NPs because the coarsening effects start to be too strong when a certain limit of concentration is exceeded (10%M for BZO and 6%M for BYTO). The resulting films show high values of

random fraction (> 90%) and nanostrain (0,22-0,24%), which are comparable with the values obtained for the optimum concentration of the simple nanocomposites.

- By using mixed composition nanocomposites it is possible to reduce the length of the SFs with respect to the pristine YBCO, YBCO-BZO and YBCO-BYTO nanocomposites. Although the reasons for that are still unclear, one possibility that could explain this effect is that the increase of the NPs concentration maintaining small sizes prevents the SFs expansion to large areas. The NPs breaks the SFs in small pieces. The shortest SFs are found in the YBCO+10%M BZO+5%M YO nanocomposite.
- The physical properties of the films are influenced by the length of the SFs: the shorter the SFs are, the larger the vortex pinning effects, as reflected in larger H* values.
- Epitaxial YBCO+10%M BZO nanocomposites with thicknesses up to 700 nm were achieved by using the CSD methodology.
- It was found that the increase of the film thickness influences the superconducting properties. Despite that T_c is maintained, the J_c values showed a clear decrease at large thicknesses. This is attributed to the great amount of unreacted phases found in the films that act as current blockers itself and to the granularity effect that appears at high thickness probably due to the change in the supersaturation conditions during the growth of films with large thicknesses. Therefore, it is not related with the NPs introduction but with the growth process that needs to be further optimized to complete the formation reaction and to keep a highly textured structure with improved grain connection.
- In thick films, the pinning performances are limited by the presence of mesostrain associated to granularity and the presence of long SFs generated by the unreacted phases. In this way the nanostrain, linked to NPs effects and the associated defects (short SFs), have a minor contribution and the pinning properties are reduced.
- The preparation of GdBCO thin films has been revealed as a complicated task. The sensitivity of the GdBCO-TFA solutions to the ambient humidity has lead to the development of a new Low-Fluorine Solution with a formulation never used before in the preparation GdBCO thin films by CSD method.
- The developed Low-Fluorine GdBCO solution solves the problem of the homogeneity of the film after the pyrolysis process. It avoids using most of TFA precursor salts (highly hygroscopic compounds) and the presence of propionic acid and TEA (coordination agents) helps to prevent the water absorption that can derive in buckling formation and degradation of the texture quality. Also, the presence of TEA gives the system elastomeric properties that help to release the stress generated during the shrinkage without causing inhomogeneities.
- The rate of homogeneous films after the pyrolysis reaches 95% with the new GdBCO-LF solution while in the case of the GdBCO-TFA solutions the rate was below 10%.
- The growth of epitaxial GdBCO-LFS films requires redesigning the growth thermal profile because the use of the standard growth process leads to polycrystalline films. The new designed thermal profile called “flash heating process”, in which the heating ramp reaches ~400 ºC/min, allows the achievement of epitaxial films and it drastically decreases the amount of a-b grains.
- The superconducting properties of the GdBCO-LFS films are close to the best reported values. The T_c reaches 92,8 K while the J_c^{sf} at 77 K reaches values of 1,5 MA/cm^2. However, this J_c value is still limited by granularity effects and, therefore,

the flash-heating growth process should be further optimized. The value of the J_c^{sf} at 77 K inside the grains is ~5 MA/cm^2 which suggests that there is still a lot of room for improvement.

- The flash heating process was also used to grow successfully GdBCO-Gd_2O_3 nanocomposites. GdBCO-LF solutions were prepared with an excess of Gd-TFA precursor salt to generate a GdBCO-LF+20%M Gd_2O_3 solution. These nanocomposite films show the typical features already observed for the YBCO nanocomposite films and also improved properties than in the case of the pristine GdBCO-LFS films. The T_c is 92,7 K while the J_c goes up until 3,2 MA/cm^2, value that is still limited by granularity effects.

4

CSD Ex-Situ Nanocomposite Thin Films

This is the second chapter devoted to the CSD-YBCO nanocomposite thin films. Here, the novel "ex situ" CSD approach for YBCO epitaxial nanocomposite films growth is presented. The name "*ex-situ* nanocomposites" is related to the approach used to prepare the YBCO nanocomposite films following the CSD methodology. The used methodology relies on preparing colloidal solutions of preformed crystalline oxide nanoparticles through easily scalable and facile solvothermal or microwave-assisted solution methods. The combination of these colloidal solutions with the YBCO solutions will lead, after the deposition and the corresponding thermal processes, to embedded NPs in the YBCO matrix. This novel approach is as an attractive alternative to the conventional CSD *in-situ* approach to overcome some limitations found in the latter such as the poor control of NPs size or NPs reactivity. This approach has been developed for the first time in the Superconducting Materials and Large Scale Nanostructures (SUMAN) group at ICMAB within the framework of the European project "European Development of Superconducting Tapes (EUROTAPES)"

In the ex-situ approach there are many parameters than can influence the final performances of the YBCO nanocomposite films, from the NPs synthesis to the YBCO crystallization process, making this route very attractive to tune the nanocomposite properties but also very challenging. In this chapter, it is presented the basis and the general methodology of this route and three case examples. A sketch of general validity of the steps involved in this new approach and the relevant growth phenomena are provided.

4.1 Introduction

The preparation of REBCO and, in particular, YBCO nanocomposites films by CSD has been traditionally performed by the in-situ approach (described in chapter 3). The use of the in-situ nanocomposites approach has allowed the increase of the pinning performances. However, the use of this approach requires, in order to achieve the desired properties, a fine control of the processing parameters which makes it very challenging. It would be worthwhile, therefore, to define new synthetic routes where an extended compositional spread could be explored and modified nanostructure control paths could be defined. And the ex-situ approach is now appearing as an alternative potential path to prepare REBCO nanocomposite films.

4.1.1 In-situ vs. ex-situ approaches

As described in chapter 3, the name *"in-situ nanocomposites"* refers to the fact that the NPs are spontaneously segregated within the YBCO matrix from a complex metalorganic solution growth thermal process (figure 4.1). The processing parameters of the growth process determine the NPs nucleation and distribution within the YBCO matrix.

The superconducting properties and the pinning performances of these CSD in-situ YBCO nanocomposites thin films are excellent as it was shown in chapter 3 and different reported works[97, 101, 215]. However, the comprehension of the complex growth mechanisms, involving kinetic and thermodynamic effects, forced to use multi-step processing paths to achieve control of the separate nucleation and growth processes of the two crystalline phases forming the nanocomposite[101].

The use of the CSD ex-situ approach consists of synthesizing oxide NPs that are stabilized in alcoholic solution forming colloidal solutions. The NPs suspension is subsequently mixed and stabilized in the metal–organic TFA precursor solution, used for YBCO film growth, to form a stable colloidal solution with the desired nanoparticles concentration (figure 4.1). After the deposition and growth of the films, the NPs are embedded in the matrix. A key advantage of this novel approach is that a tight control of the composition, particle size, and concentration of the nanoparticles becomes possible.

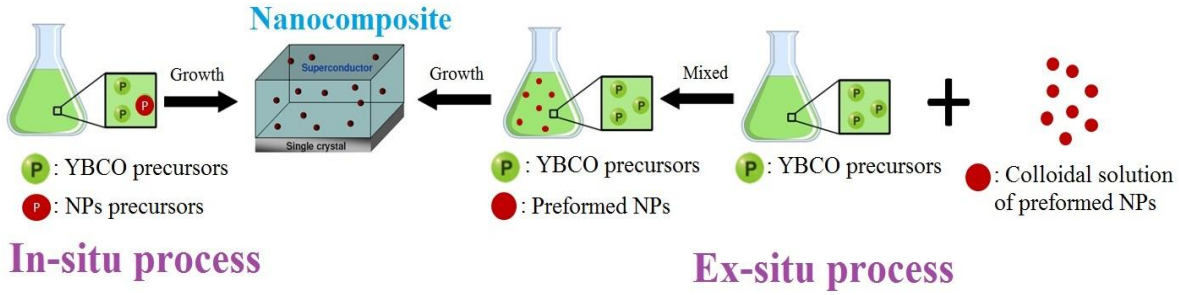

Figure 4.1. Scheme of the CSD in-situ and ex-situ approaches to prepare superconducting YBCO nanocomposites.

Previous work on YBCO nanocomposites using Au NPs colloidal solution was firstly reported within the SUMAN group[216]. However, the choice of Au NPs was not satisfactory due to their ability to locate on the top surface of the YBCO films and

sublimate at high temperatures. From this work and up to now, only limited progress has been made about YBCO nanocomposites grown via CSD-MOD ex-situ approach[115]. In this work, an extensive study using a wide variety of colloidal oxide nanoparticles (CeO_2, ZrO_2, $CoFe_2O_4$) which allowed the comprehension of the growth mechanisms to achieve epitaxial YBCO nanocomposites is presented.

4.1.2 Ex-situ approach challenges

Although the basis of the ex-situ approach seems very easy, there are many challenges to be faced. Most of them are related with the stability of the NPs when the colloidal solution is mixed with the YBCO precursor solution including aggregation and precipitation of NPs. In order to prepare competitive YBCO nanocomposites it is necessary to achieve colloidal solutions with: i) small NP size, ii) NPs stability in polar and acidic environments (like the TFA-YBCO solutions) and iii) avoid NPs aggregation.

After that, the pyrolyzed films have to be homogeneous. This is not an easy task due to the strong influence of the ligand (discussed in the following pages). Furthermore, during the growth process it is necessary to avoid some phenomena as NPs coarsening, NPs pushing to the surface or the possible reactivity that can take place at this stage.

In the next pages, the first study of the complete process associated with this novel growth route is exposed. Crystalline oxide magnetic ($MnFe_2O_4$ and $CoFe_2O_4$) and non-magnetic (CeO_2 and ZrO_2) NPs were used. For each kind of NP, the synthesis process will be detailed and also the properties of the obtained thin films. An explanation of the problems encountered in each step and the proposed solutions will be also shown.

4.2 NPs synthesis process

The first step in the ex-situ route is the synthesis of the NPs. This is a critical step because the final quality of the films will depend largely on the characteristics of the initial NPs. NPs synthesis is beyond the scope of this thesis and, therefore, they were provided by two different groups that have a wide experience in this topic: “Inorganic nanoparticles and functional ligands” within the Inorganic Chemistry Department of Autonomous University of Barcelona (UAB)[217-221] and “Sol-Gel Centre for Research on Inorganic Powders and Thin Films Synthesis (SCRiPTS) at the University of Ghent (UG)[222-224].

Both groups used the so called “solvothermal synthesis process” for the synthesis of NPs[225-227]. The advantages of the solvothermal method with respect to other methods (hydrolysis or the oxidation processes) are the versatility, the small sizes that can be obtained (< 2 nm) and the wide range of concentrations of the final colloidal solutions that can be achieved (13-256 mM) which matches de requirements for our YBCO nanocomopsites described above. The basic principles of the solvothermal process are shown in figure 4.2.

The NPs precursors are mixed with a solvent and a ligand (to act as stabilizing agent) and then the as-prepared solution is heated in a hot plate, a furnace or a microwave. If the solvents that are used are alcohols, the process is called polyol process[219]. During heating, the first NPs nuclei are formed by thermal activation. The formation of nuclei occurs until a certain supersaturation degree of the system. In this moment, the nuclei start to grow. The growth is limited by the temperature, the time and the ligand. By controlling

the concentration of the ligand one can achieve small steric stabilized NPs with no aggregates (figure 4.2). The NPs are stabilized due to the polymeric behavior of the ligand that prevents the contact between the NPs. This kind of stabilization is called steric.

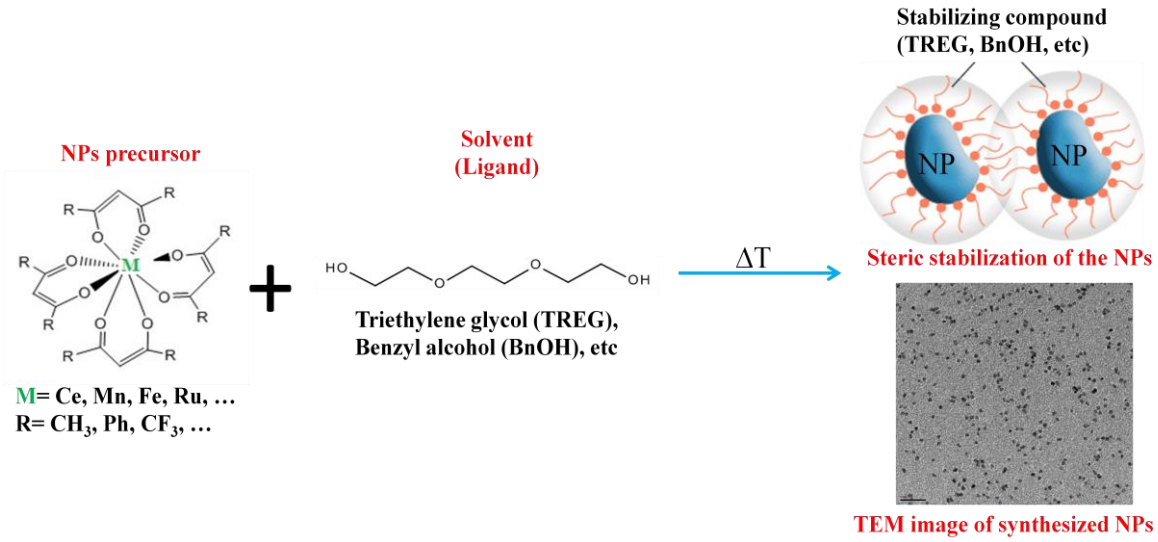

Figure 4.2. Scheme of the solvothermal synthesis process.

At this point the synthesis itself is over, but to be used in YBCO films, it is necessary to carry out more steps. First, the NPs are purified to separate them from the excess of ligand and then, optionally, a ligand exchange is performed. The ligand exchange is made sometimes because the compatibility of a certain ligand with a certain solution is not good or because the NPs stability with a certain ligand is really low. The complete process that used both groups is presented in figures 4.3 (CeO_2-UAB case) and 4.4 (ZrO_2-UG case).

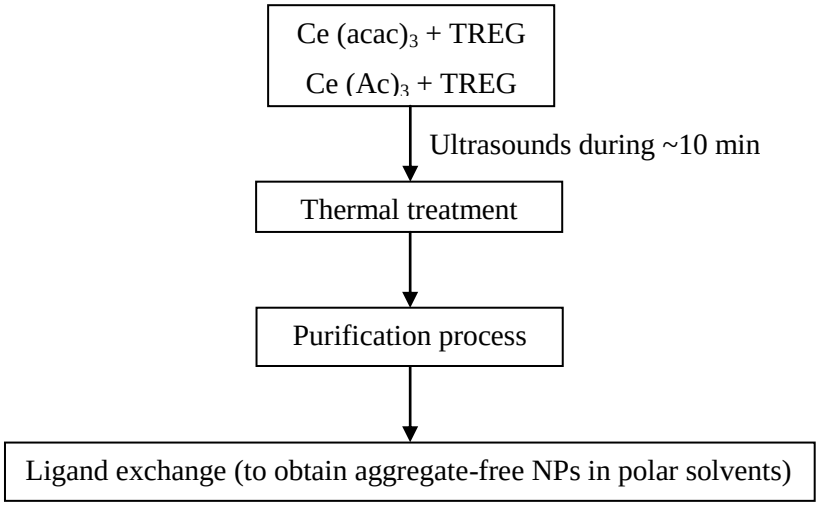

Figure 4.3. Sketch of synthesis process and ligand exchange of UAB group to obtain a colloidal solution of CeO_2 NPs in methanol using decanoic acid as ligand.

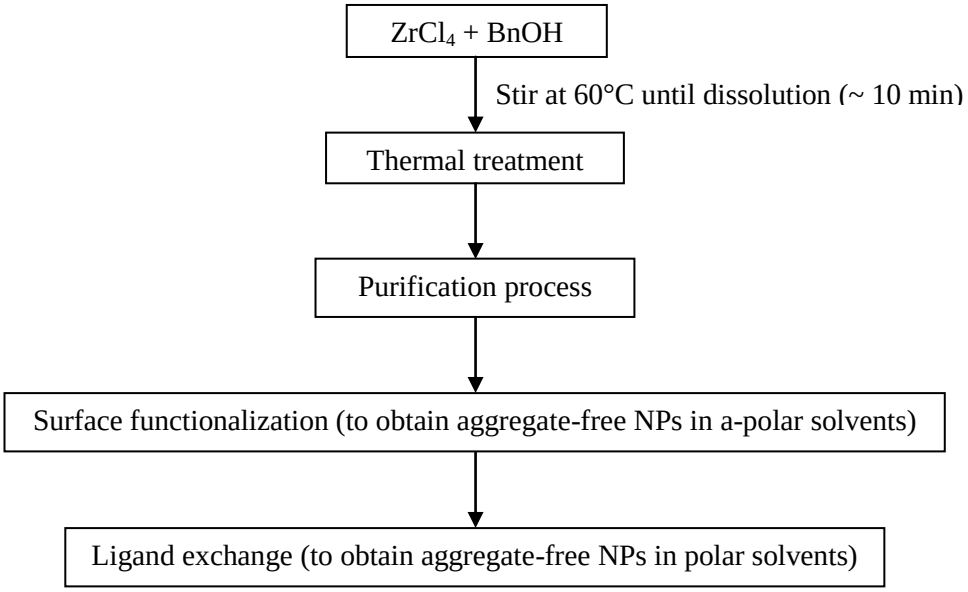

Figure 4.4. Sketch of synthesis process and ligand exchange of UG group to obtain a colloidal solution of charge stabilized ZrO_2 NPs in methanol.

In the UAB case, the complete process is shorter and easier than in the UG case. In figure 4.3 it is shown the particular example of the synthesis of CeO_2 NPs in triethylene glycol (TREG) ending with a colloidal solution of these NPs in decanoic acid (HDEC) after the ligand exchange, but it is extensible to any other kind of NPs. The main difference between TREG and HDEC is the viscosity as the value of the TREG is 47,8 cP at 20 ºC while the value of HDEC is 4,3 cP at 50 ºC. This difference has important implications as it will be explained later. Similar synthesis processes are used to prepare the rest of the UAB NPs. Following this procedure, the UAB synthesized the $MnFe_2O_4$ (MFO), the $CoFe_2O_4$ (CFO), the CeO_2 and some of the ZrO_2 (ZrO_2-UAB) NPs used in this thesis.

On the other hand, the UG process is a little bit more complicated as can be seen in figure 4.4. This figure shows the case of charge stabilize ZrO_2 NPs in methanol, but it is also applicable for any other kind of NP. In the particular case of figure 4.4, they produce charge stabilized NPs because of the use of $ZrCl_4$ as precursor which cause the presence of HCl during the reaction. This happens due to the fact that the steric stabilization occurs or not will depend on the NPs precursors that are used. If the precursors are chlorides and the solvent BnOH, the reaction causes the apparition of hydrochloric acid (HCl) which is adsorbed on the surface of the NPs causing charge stabilization. The charge stabilization is based on the repulsion between NPs due to the zeta potential that exists because of particle's surface charge in solution. The particular distribution of the ions in the NPs surface causes the apparition of an ultimate layer of positive or negative ions that cause the repulsion between NPs. However, these charge stabilized NPs, after the purification, are aggregated. To avoid this agglomeration, they perform a surface functionalization by adding dodecanoic acid, oleylamine (to make sure that the HCl is removed from the particles surface) and chloroform to the NPs. By re-dispersing the NPs, they achieve aggregate free sterically stabilized NPs in nonpolar solvents (chloroform). However, this solvent is not compatible with the YBCO-TFA solution in which the solvent is methanol, so they have to change the solvent from chloroform to methanol. To do that, they perform a ligand exchange by adding acetone (to remove the H_{dodec}), an amino acid and TFA

(trifluoroacetic acid) ending with a charge (electrostatic) stabilized NPs colloidal solution. With this procedure, the UG supplied another part of the used ZrO_2 (ZrO_2-UG) NPs.

4.2.1 NPs characterization

Once the synthesis, the ligand exchange (if necessary) and the change to polar solvents is completed, the characterization of the NPs is required both in powder and in colloidal solution to find out if they fulfill the requirements for preparing the YBCO nanocomposites.

4.2.1.1 XRD measurements

To perform the XRD measurements it has been used the solid precipitate obtained after the purification process. From figure 4.5 it is possible to conclude that all the synthesized NPs are crystalline. However, different crystal structures were found. The MFO, CFO and CeO_2 NPs have a cubic structure while in the case ZrO_2 NPs the structure is monoclinic (the spectrum shown in figure 4.5 is valid both for the UAB and UG NPs). The different intensities present in the different spectra are related with the different amount of NPs powder used to carry out the measurements.

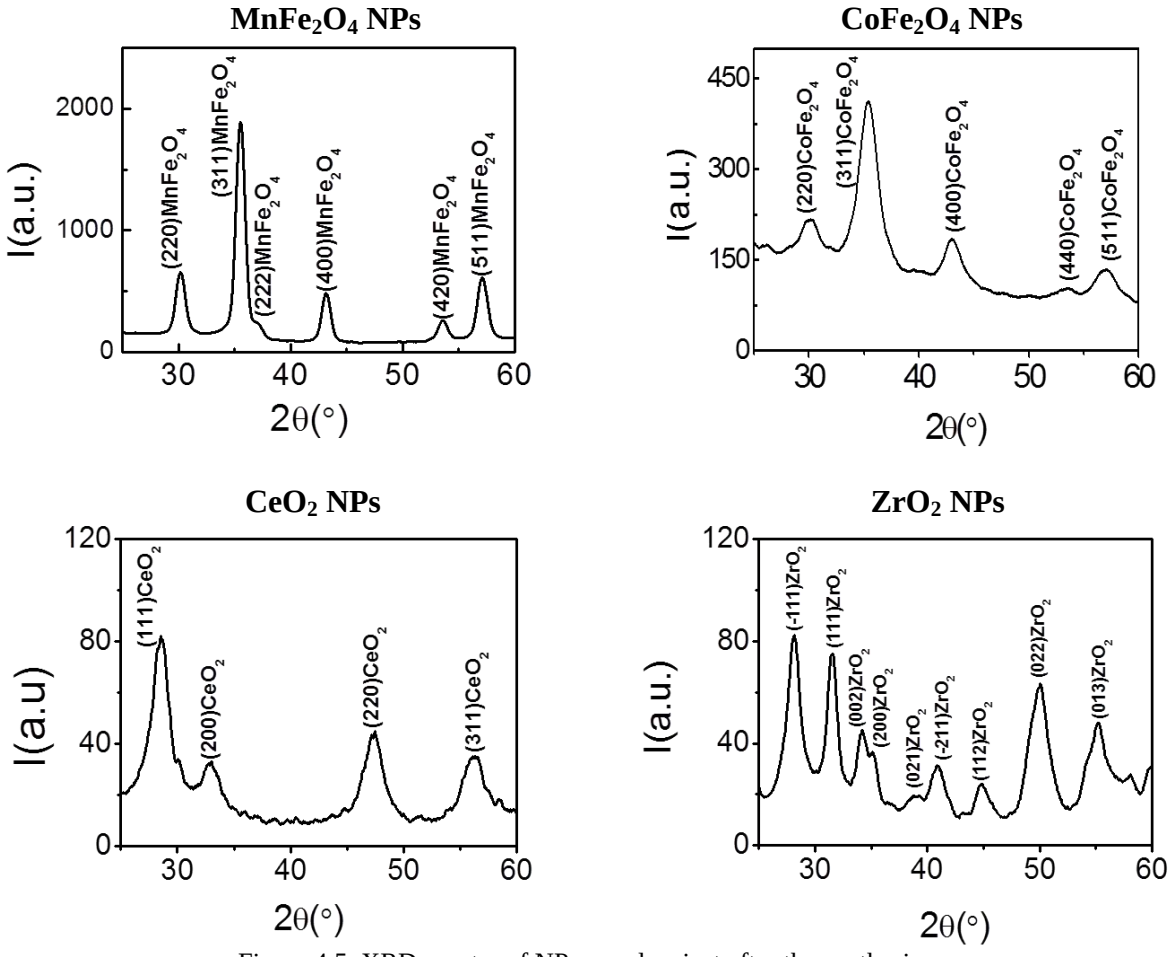

Figure 4.5. XRD spectra of NPs powders just after the synthesis.

These NPs are synthesized to be used in YBCO thin films. So, it is very important to check if they maintain the crystalline phase under the YBCO processing conditions or, conversely, they decompose and/or transform into other phases. To investigate that, the NPs powder are exposed to the "standard growth process" (which will be the growth process used to later prepare the ex-situ nanocomposite films) and then new XRD measurements are done on the resulting powder.

From the spectra shown in figure 4.6, it is concluded that CFO and ZrO_2 NPs maintain their structure after the thermal treatment at high temperature. The only change observed in the spectra is a narrowing of the peaks that is associated to a coarsening effect (the NPs aggregate forming bigger particles) and a better definition of the peaks as a consequence of the re-crystallization of the NPs. Same results are reported for the CeO_2 NPs[228]. However, it is observed that the MFO NPs decompose at high temperature forming mostly Fe_2O_3 phase. This means that they lose their structure at high temperature and also their magnetic properties. Therefore, the MFO are discarded for their use to prepare YBCO nanocomposites.

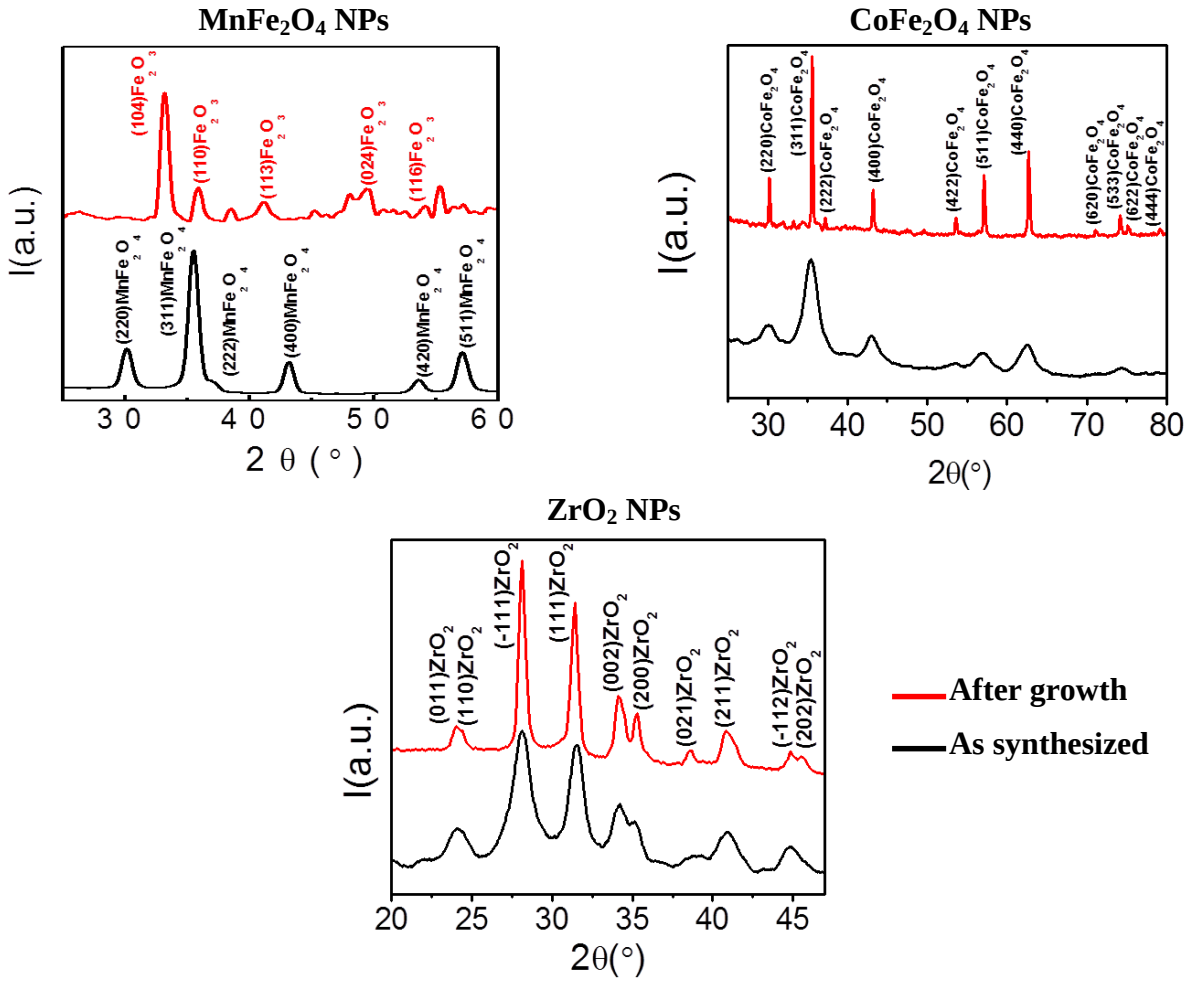

Figure 4.6. XRD spectra of NPs powders showing the comparison between the NPs just after the synthesis (black lines) and after being exposed to the "standard growth process" (red lines).

4.2.1.2 NPs stability

The NPs stability in the YBCO colloidal solution is critical. The stability is defined as the time that NPs takes to precipitate and it is checked by naked eye. The stability of the used NPs in the YBCO solution is shown in table 4.1. It is important to remark that, although one solution remains stable during a long time, this does not mean that the NPs do not suffer changes. Other effects, as aggregation, could occur before precipitation.

NPs	Stability
CeO_2 TREG	> 1 year
CeO_2 HDEC	3-4 hours
CFO-TREG	> 1 month
ZrO_2-UAB	3-4 hours
ZrO_2-UG	> 6 months

Table 4.1 Stability of the different YBCO+NPs colloidal solutions used in this work.

4.2.1.3 DLS measurements

In order to determine the NP size of these colloidal solutions, Dynamic Light Scattering (DLS) technique (described in chapter 2) is used. These measurements are very important as they give information about the degree of aggregation of the NPs which has direct consequences on the preparation of the YBCO nanocomposites films and on the final properties of the films. Figure 4.7 shows the DLS measurements performed on all YBCO-NPs solutions used to prepare YBCO nanocomposites films.

Important information can be extracted from figure 4.7. First of all, the NPs that used HDEC as ligand, i.e., the CeO_2 and ZrO_2 NPs from UAB, tend to agglomerate forming big cumulus of 100 nm in the case of CeO_2 NPs and 70 nm in the case of ZrO_2 NPs. This big agglomerates probably comes from an incomplete ligand exchange that prevents a fully NPs stabilization. This does not mean that all the NPs are forming the cumulus, they can be also individual, but most of them are part of the agglomerates.

On the other hand, the CeO_2 NPs in TREG, the CFO NPs in TREG and the ZrO_2 NPs from the UG do not form aggregates. Most of the NPs remain separate one from another. The hydrodynamic diameters of these NPs are 3 nm, 8 nm and 11 nm respectively. In the case of CeO_2 and CFO in TREG, no ligand exchange was performed and they maintain the same ligand that was used in the synthesis (TREG). In the case of the ZrO_2-UG, they are charge stabilized NPs and the difference between the ZrO_2-UAB NPs is that these NPs have suffered a surface functionalization that probably helps to complete the ligand exchange.

a) CeO_2-TREG

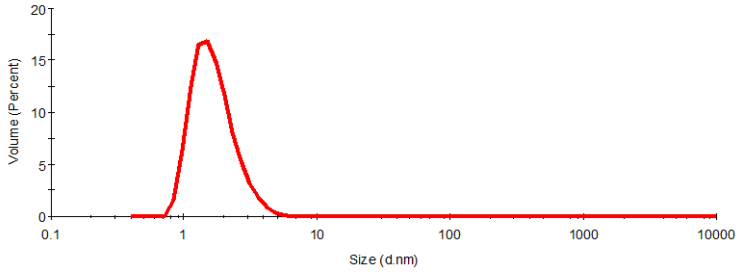

b) CeO_2-H_{dec}

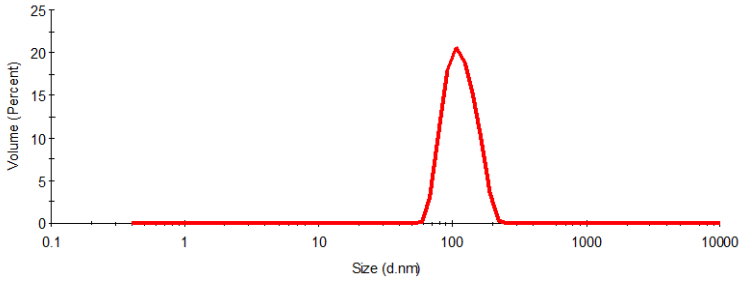

c) $CoFe_2O_4$-TREG

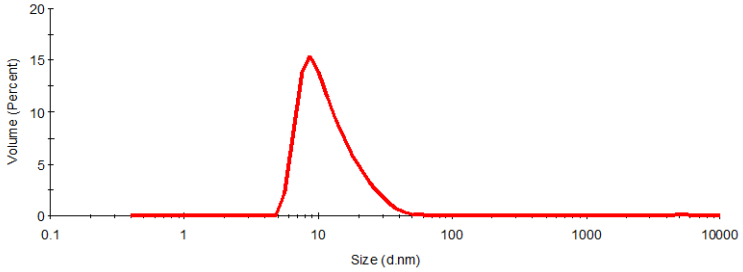

d) ZrO_2-UAB

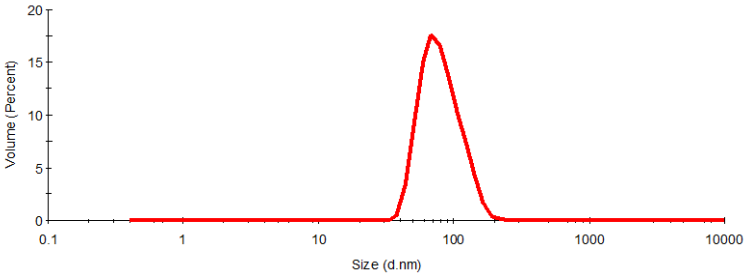

e) ZrO_2-UG

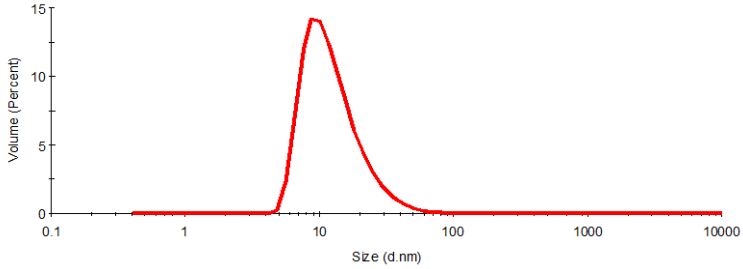

Figure 4.7. DLS measurements of the NPs present at all the YBCO+NPs colloidal solutions used.

In the case of ZrO_2-UG, a study of the NPs size evolution with time was carried out. Figure 4.8 demonstrate that the ZrO_2-UG NPs are stable in size during at least 2,5 months. After 4 months the NPs start to aggregate forming bigger clusters

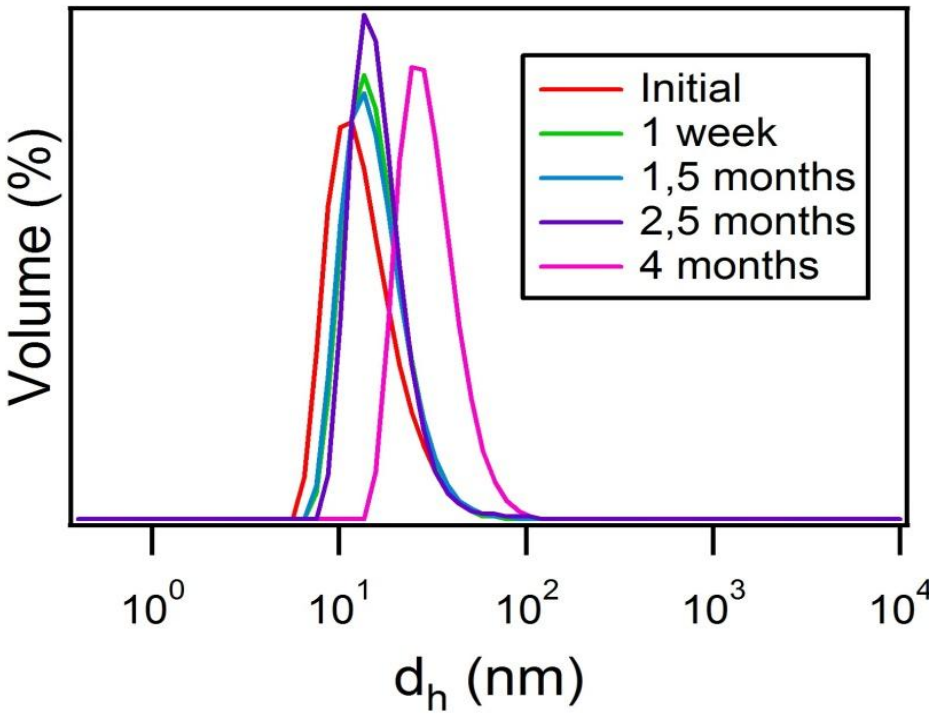

Figure 4.8. DLS measurements of the ZrO_2-UG NPs showing the evolution of the NPs size with the time.

4.2.1.4 TEM measurements of colloidal solutions

The last part of the NPs characterization is TEM observation of the NPs colloidal solution. TEM images give information about the core size of the NPs (not the hydrodynamic diameter as the DLS) and also the degree of agglomeration of the NPs. These measurements have to be related with the DLS results. TEM measurements of colloidal solution are performed by depositing a few drops of solution in a TEM´s grid. In this way the NPs remains in the grid while the liquid evaporates. The different TEM images of the NPs are presented in figure 4.9.

The TEM images confirm the information obtained previously with the DLS measurements. On one side, it is clear that both the CeO_2 and the ZrO_2 NPs that used HDEC as ligand have big agglomerates of sizes that are around the values obtained with the DLS (~100 and ~70 nm respectively). However, not all the NPs are in the cumulus, there are still some NPs that are individually dispersed. The size of these NPs is 2-3 nm in the case of CeO_2 in HDEC and 7-8 nm in the case of ZrO_2-UAB in HDEC. The shape of ZrO_2-UAB NPs is not spherical but is more rod-like being the 7-8 nm the size of the long axis. On the other hand the CeO_2 and the CFO in TREG and the ZrO_2-UG NPs do not form agglomerates and the sizes are in the range of the DLS results: 2 nm for the CeO_2 TREG NPs, 4-5 nm in the case of CFO TREG NPs and 8-10 nm for the ZrO_2-UG NPs.

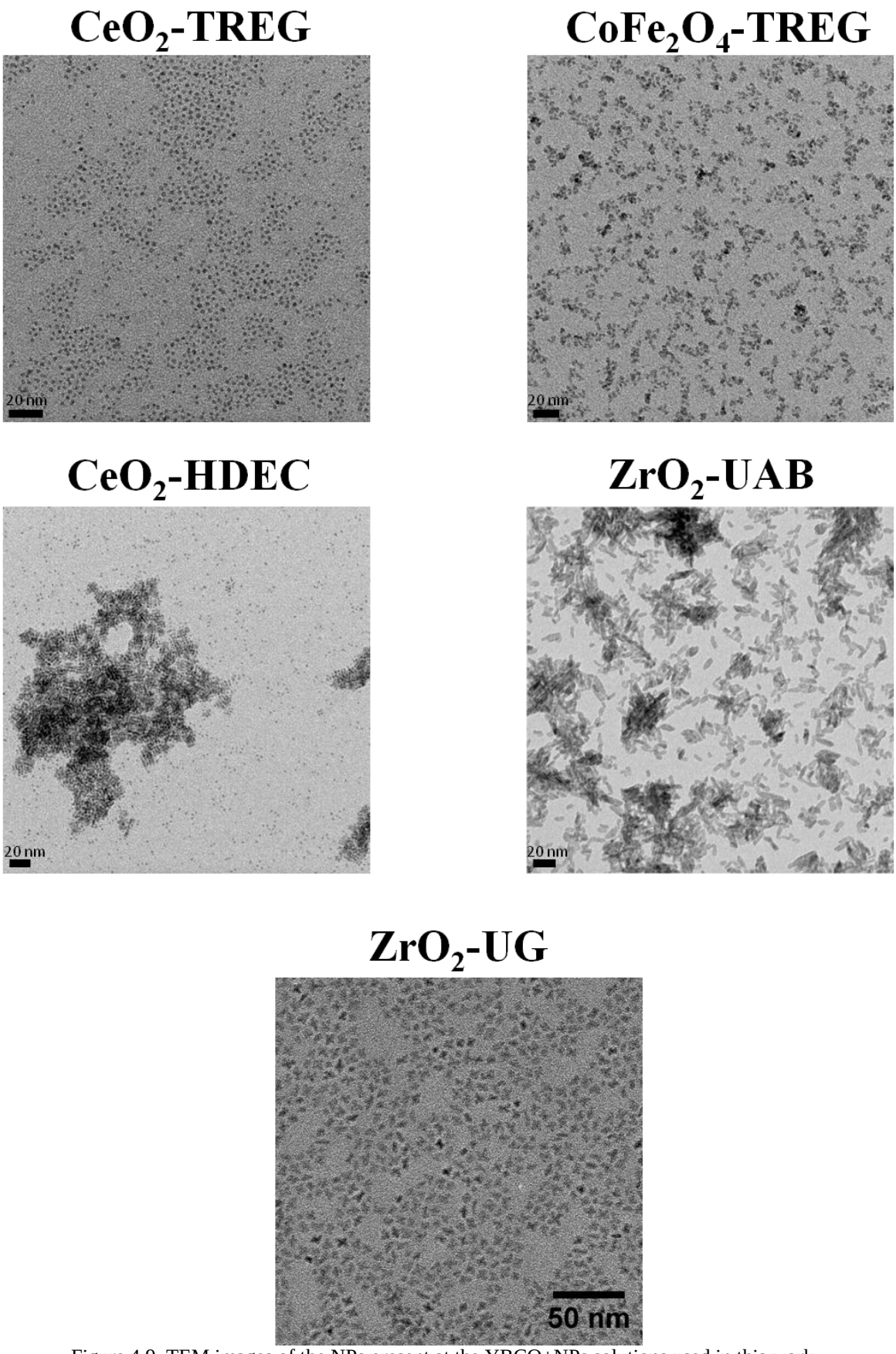

Figure 4.9. TEM images of the NPs present at the YBCO+NPs solutions used in this work.

4.2.1.5 Summary of NPs characterization

The table 4.2 serves as a summary of the synthesized NPs features in colloidal solution (YBCO+NPs solutions).

NPs	Stability	DLS size (nm)	TEM size (nm)	Agglomerates?
CeO_2 TREG	> 1 year	~3	2-3	No
CeO_2-HDEC	3-4 hours	~100	2-3	Yes (100 nm)
CFO-TREG	> 1 month	~8	4-5	No
ZrO_2-UAB	3-4 hours	~70	7-8 (long axis)	Yes (70 nm)
ZrO_2-UG	> 6 months	~11	8-10	No

Table 4.2 Features of the used NPs in colloidal solution (YBCO+NPs solutions).

It is noteworthy that it has been possible to synthesize NPs that are stable for a long time in the YBCO solution, for instance CeO_2-TREG NPs and ZrO_2-UG NPs. It is also remarkable (for the consequences in the final properties) that, despite all the NPs are below 10 nm, some of them tend to form big agglomerates, as in the case of CeO_2-HDEC NPs and ZrO_2-UAB NPs.

4.3 Magnetic NPs: $CoFe_2O_4$ NPs

The study of magnetic NPs is very interesting in order to prepare YBCO nanocomposites with enhanced pinning properties as compared to conventional NPs (structural pinning) because it is possible to add the "magnetic pinning" effect. Magnetic pinning is based on the coexistence of the superconductivity and ferromagnetism that may cause the enhancement of the critical currents in nanocomposites films[229, 230].

The structural and superconducting properties of YBCO+16%M CFO nanocomposite films will be studied. After that, the magnetic behavior, by SQUID and XMCD measurements, of the nanocomposites will be also investigated in order to compare with the behavior of NPs in powder and distinguish the possible difference between both cases.

4.3.1 YBCO+CFO NPs nanocomposites

4.3.1.1 Pyrolysis process

The nanocomposite films are prepared using a 0,125M YBCO+16%M CFO NPs solution resulting in a final thickness of 150±20 nm after complete YBCO processing. The solution is prepared using the procedure already explained in chapter 2. This solution is deposited on a LAO substrate and then spin-coated. Afterwards, the standard pyrolysis process is performed in order to remove the organic content of the film. This process leads to homogenous films (figure 4.10).

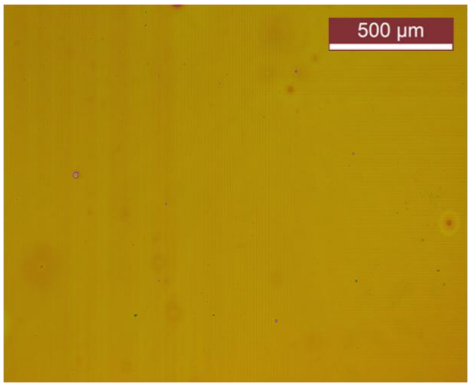

Figure 4.10. Optical microscope image of an YBCO+16%M CFO NPs thin film after the pyrolysis process showing an homogeneous surface.

4.3.1.2 Growth process

After the pyrolysis process the films are grown using the standard growth process already explained in chapter 2. The structural and superconducting properties of the films have been studied.

4.3.1.2.1 Structural characterization of the YBCO+CFO nanocomposites

XRD patterns of YBCO+16%M CFO nanocomposite film are shown in figure 4.11. The 2D frame and its integrated spectrum show the presence of the Bragg peaks corresponding to epitaxial YBCO, but also of other Bragg peaks that correspond to a-b grains and a ring that is assigned to randomly oriented YBCO grains. It is also noticeable the presence of a Bragg peak at 2θ~35,5º that corresponds to a double perovskite structure (DP) that, according to the 2θ angular position, corresponds to a similar or equivalent composition reported by Woodward et al. ($YBaFe_2O_5$)[231]. However, no trace of the original spinel ferrite structure of the CFO NPs was found.

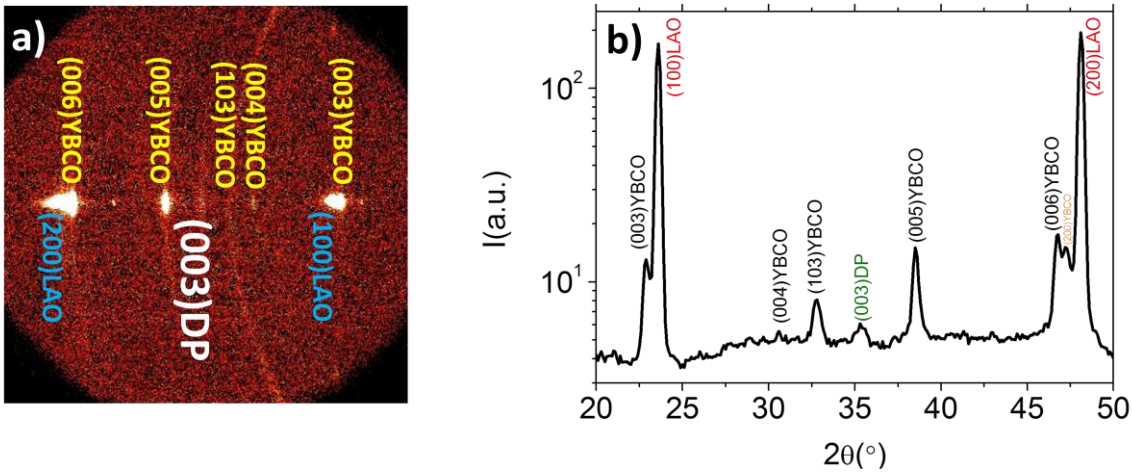

Figure 4.11. 2D XRD θ-2θ a) frame and b) integrated patterns of the YBCO+16%M CFO NPs nanocomposite fully grown. Presence of a double perovskite structure (similar or equivalent to $YBaFe_2O_5$) is detected.

The presence of the DP and not the spinel structure of the original CFO NPs, indicate that the NPs are reacting with the YBCO precursors forming the DP. It is suggested that the CFO NPs react with the BaF_2, obtained after the decomposition of BYF, forming the DP structure (note that the DP has Ba in its structure).

In order to minimize the reactivity of the CFO NPs with YBCO precursors, the heating profile has been modified by shortening the dwell time at high temperature. It was reported that at 810 ºC, after 10 min, the YBCO is already nucleated[232], so it was decided to quench the films at this stage of the process. Afterwards, in order to obtain the orthorhombic superconducting phase of the YBCO, the sample is oxygenated at 450 ºC during 2 hours in a fully O_2 atmosphere. However, as it observed in the XRD θ-2θ patterns showed in figure 4.12, the presence of YBCO and DP is already detected.

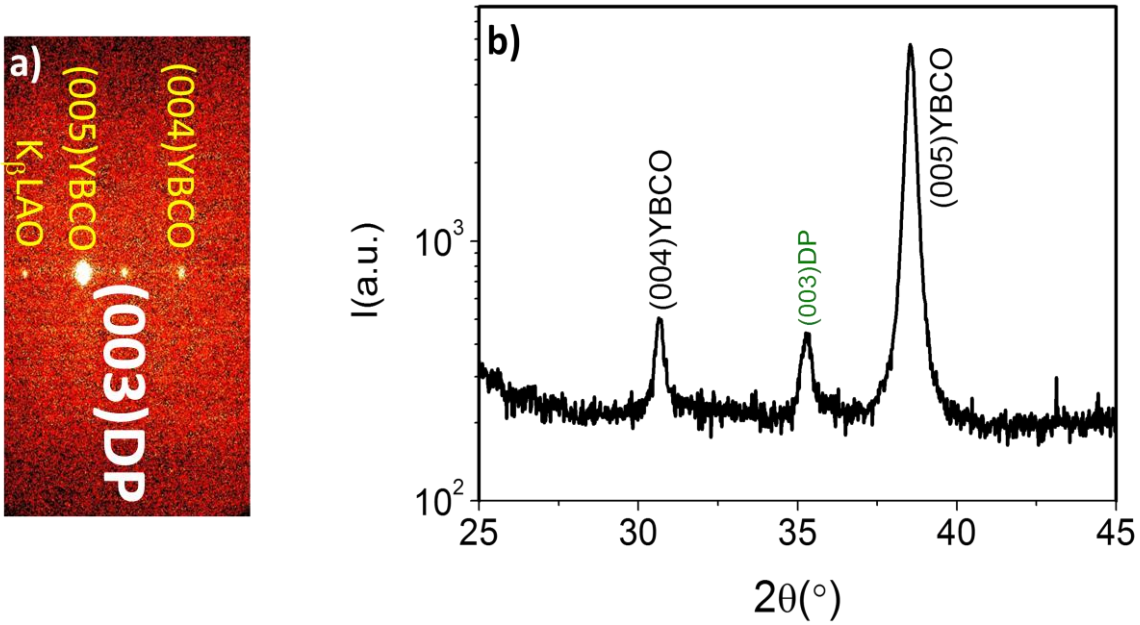

Figure 4.12. 2D XRD θ-2θ a) frame and b) integrated patterns of the YBCO+16%M CFO NPs nanocomposite fully grown. Presence of a double perovskite structure (DP) is detected.

HAADF TEM images of a fully grown YBCO+16%M CFO nanocomposite film were obtained in order to shed light on the nanocomposite microstructure. Figure 4.13 shows the presence of epitaxial YBCO and also the DP structure. Importantly, no CFO NPs are detected within the YBCO matrix. In order to elucidate the composition of the DP structure, EELS analysis was carried out. The analysis reveals the presence of Y, Ba, Fe, Co and O atoms. Therefore, the DP that appears in these films is a variant of that found by Woodward et al. ($YBaFe_2O_5$)[231] with the addition of Co to the structure ($YBa(Fe/Co)_2O_5$. TEM images of the quench oxygenated films show similar results: presence of DP but no sign of spinel CFO NPs. Therefore, the microstructural characterization suggests that CFO has fully reacted with YBCO forming a DP even when shortening the dwell time.

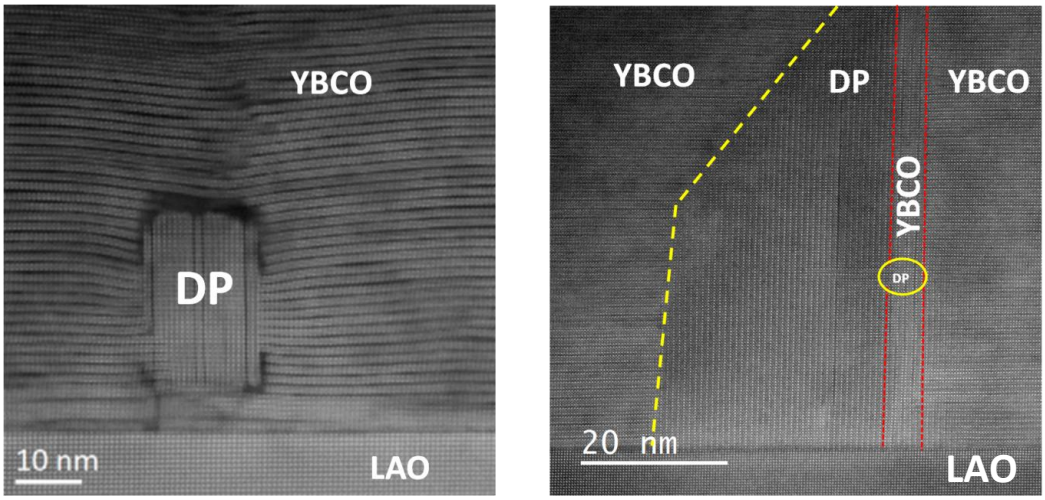

Figure 4.13. HAADF TEM images of the YBCO+16%M CFO NPs nanocomposite fully grown. Presence of a double perovskite structure (DP) is detected, but no sign of CFO NPs.

4.3.1.2.2 Superconducting properties of the YBCO+CFO nanocomposites

SQUID measurements of the YBCO+16%M CFO fully grown and quenched nanocomposites were carried out in order to study their superconducting properties. The T_c values are of most importance since it is well known that those films which contain Fe or Co atoms suffer a drastic reduction of T_c due to Fe or Co poisoning[233-236]. The T_c onset of a quenched YBCO+16%M CFO nanocomposite film observed in figure 4.14, of 40 K, clearly indicates that some Fe and/or Co atoms were introduced in the YBCO structure substituting some Cu atoms.

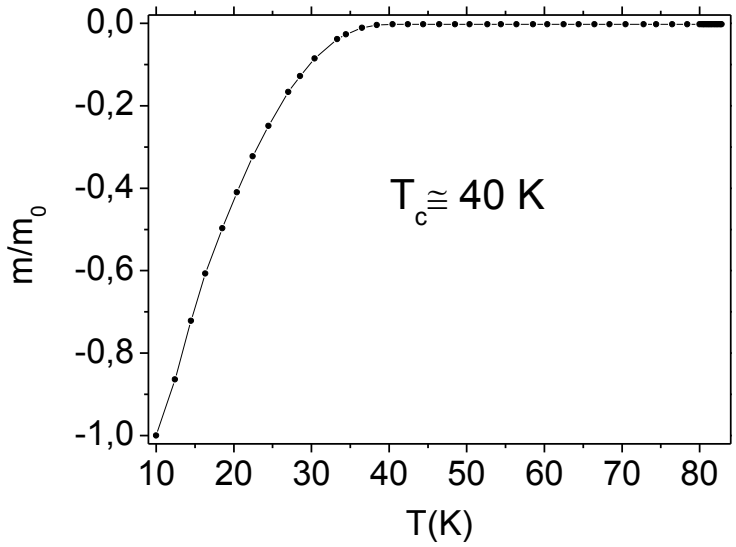

Figure 4.14. YBCO+16%M CFO quenched nanocomposite T_c measurement.

It is difficult to unambiguously identify if Co or Fe are responsible for the Cu substitution. By comparing this T_c value with the reported T_c values for $YBa_2(Cu_{1-x}Fe_x)O_{7-\delta}$ or $YBa_2(Cu_{1-x}Co_x)O_{7-\delta}$, the amount of Fe or Co incorporated can be determined[237]: amounts of Fe or Co of x~0,1 are enough to reduce the T_c to 40 K. These Fe and/or Co

atoms are located preferably in Cu-O chains but, since the amount of the incorporated Fe and/or Co is quite high, there are also other Fe and/or atoms that are incorporated in the CuO_2 planes[237].

4.3.2 Magnetic behavior: Bulk CFO vs. CFO nanocomposites

It was demonstrated by XRD and TEM measurements that the CFO NPs react during the growth process resulting in the formation of the DP structure. The quenched films, in which the time at high temperature was drastically reduced, show also the presence of the DP indicating the difficulty of avoiding the CFO reactivity with the use of the present processing parameters. It was also noticed that Fe and/or Co atoms tend to incorporate into the YBCO structure since a drastic reduction of the T_c onset was observed (T_c~40 K). The study of the magnetic properties can give more information about the moment in which the DP is formed.

4.3.2.1 SQUID measurements

The CFO NPs powder was exposed to the same thermal processes that are used to synthesize the YBCO+CFO nanocomposites films. The magnetic properties of this powder were measured using SQUID after the different steps and compared with the magnetic properties of the YBCO+16%M CFO films after the same steps.

Figure 4.15 shows the hysteresis loops measured with SQUID of the CFO NPs in powder at 10 and 300 K after the different thermal processes in comparison with the hysteresis loops of the films at 100 K processed under the same conditions.

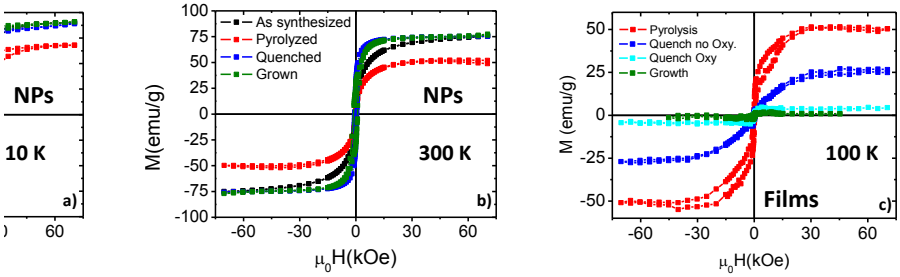

Figure 4.15. Hysteresis loops of the CFO NPs a) at 10 K and b) at 300 K and c) YBCO+16%M CFO nanocomposite films at 100 K exposed to different thermal treatments measured with the SQUID.

It is observed in figure 4.15 that at 10 K the CFO NPs have a ferromagnetic behavior (values of coercive field -H_{coer}- different from zero) as in the case of bulk CFO[238]. Note that the hysteresis loop corresponding to the pyrolyzed NPs is different from the others, in particular the saturation magnetization (M_{sat}) and H_{coer}. On the other hand, the loops corresponding to the quenched (the oxygenation step is not included) and grown (the oxygenation step is included) NPs are almost equivalent to the one from the synthesized NPs. The values of the remanent magnetization (M_{rem}) for the first two are higher than in the case of only synthesized NPs. The M_{sat} values of the synthesized, quenched and grown NPs (~90±5 emu/g) are in accordance with the reported values of bulk CFO[238].

To understand why the NPs have this behavior under the different thermal treatments, it has been proposed a model represented in figure 4.16. The as synthesized NPs (a) have the ligand (TREG) on their surface to prevent the aggregation. During the pyrolysis process at 310 ºC in a pure humid oxygen atmosphere the combustion of the ligand (organic compound) occurs (b). This causes the deterioration of the NP surface resulting on the reduction of the effective size of the NPs core and the appearance of a degraded shell. This induces a reduction of the M_{sat} value to ~68 emu/g. During the growth process, these NPs are exposed to humid N_2/O_2 atmosphere (200 ppm of O_2), but the ligand is not present now. Under these conditions the surface starts to reconstructs its original structure. The crystallinity of the samples is improved by the effect of the temperature (more definition of the peaks). The quench process (c) interrupts this reconstruction (not enough time at high temperature) and the values of M_{sat} are lower than in the case of complete grown NPs (d) in which the M_{sat} values are the same as in the case of synthesized NPs. The fact that both, the quenched and the grown NPs, have higher values of M_{rem} than in only synthesized NPs is because at high temperature the crystallinity of the NPs improves showing a similar behavior as the bulk CFO.

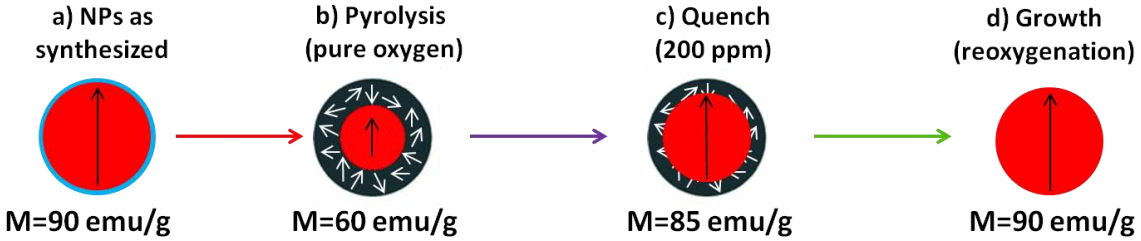

Figure 4.16. Sketch representing the evolution of the NPs under the different thermal treatments at 10 K.

At 300 K, the as synthesized and the pyrolyzed NPs show superparamagnetic behavior (H_{coer} almost zero) and the quenched and grown NPs show a ferromagnetic behavior with values of H_{coer} (less than 1 kOe) that are much lower than in the case of the NPs at 10 K. This indicates that the blocking temperature (temperature at which the transition from ferromagnetic state to superparamagnetic state occurs) was crossed in an intermediate point between 10 and 300 K making the transition from ferromagnetic to superparamagnetic behavior (at least in the case of synthesized and pyrolyzed NPs). Details of M_{sat}, M_{rem} and H_{coer} are listed in table 4.3.

	10K			300K		
	M_{sat} (emu/g)	**M_{rem} (emu/g)**	**H_{coer} (KOe)**	**M_{sat} (emu/g)**	**M_{rem} (emu/g)**	**H_{coer} (kOe)**
As synthesized	89,8	46,6	9,3	75,7	0,5	0,02
Pyrolysis	67,9	41,1	15,8	51,3	0,02	0,002
Quench	87,1	76,2	8,5	76,0	33,4	0,5
Growth	89,5	80,1	9,5	76,4	34,1	0,9

Table 4.3 Saturation magnetization (M_{sat}), remanent magnetization (M_{rem}) and coercive field (H_{coer}) values for the CFO NPs after to different thermal treatment. All the values in the table have a 5% of tolerance.

In the case of CFO nanocomposite films, figure 4.15 c) shows that the evolution of the magnetization is different. After the pyrolysis, the NPs maintain the values of the M_{sat} (M_{sat}=50,4 emu/g) near to the NPs in powder (note that the measurements in powder were done at 10 and 300 K and in the case of the films at 100 K to avoid the YBCO influence). However, the values of the M_{rem} and H_{coer} have decreased (M_{rem}=10,9 emu/g and H_{coer}=0,17 kOe). This indicates that the NPs in the film are about to change from the ferromagnetic to superparamagnetic state (incomplete transition as they still retain some of M_{rem} and H_{coer}) and, therefore, at 100 K, they are near to the blocking temperature (temperature at which the transition ferromagnetism-superparamagnetism occurs).

After the growth process, the films exhibit a very small magnetic signal (M_{sat}=0,9 emu/g). This indicates that, during the growth process, the CFO NPs suffer a transformation into other phases due to the reaction of the NPs with the YBCO precursors. By doing the quenching process, i.e., shortening the dwell time (quench no Oxy.), it is possible to preserve a higher magnetic signal (M_{sat}=26,6 emu/g). This is attributed to the use of shorter process leading to a minor amount of NPs that reacts losing their magnetic properties. At this stage, the NPs are in the superparamagnetic state (M_{rem}=0 and H_{coer}=0). However, when the quenched film is exposed to the oxygenation process (quench Oxy.), the magnetic signal decreases drastically (M_{sat}=4,5 emu/g) but still maintaining a higher value than in the case of complete growth process and the superparamagnetic behavior. The oxygen could affect the CFO NPs that do not react causing a similar effect than in the powder NPs after the pyrolysis process.

In view of the magnetization evolution, it is clear that the NPs have a different behavior when they are embedded in the YBCO matrix. In the films it is clear that the reaction of the CFO, which was detected by XRD and TEM and confirmed by the low values of M_{sat} the quenched and grown films, happens during the heating stage from room temperature to 810 ºC. It is very likely that it is produced by the reaction of the CFO NPs with the BaF_2 that is formed after the decomposition of BYF since Ba was detected in the DP structure that is formed.

4.3.2.1.1 Ferromagnetic-superparamagnetic transition

Superparamagnetism is a magnetic state which appears in small ferromagnetic or ferrimagnetic nanoparticles. In these conditions, as the temperature increase, the magnetization of each individual particle can randomly flip under the temperature influence. If the temperature is low enough, the system is in the so called “block state” and the magnetization of the NPs is fixed. In these conditions, the system behaves as a ferromagnet or ferrimagnet. However, when the temperature exceeds a certain value (blocking temperature), it induces random changes in the magnetization giving an average value for the global system of zero.

When a superparamagnetic sample is being measured, it is important the measurement time as it is a critical parameter. At a certain temperature, the average length of time that the NPs magnetization needs to randomly flip, as a result of thermal fluctuations, is known as Néel relaxation time and it is defined as follows (Eq 4-1):

$$\tau_N = \tau_0 e^{\left(\frac{KV}{K_B T}\right)} \quad \text{Eq. 4-1}$$

where τ_0 is a length of time, characteristic of the material, called the attempt time or attempt period and its typical value is 10^{-9}–10^{-10} seconds; K is the nanoparticle's magnetic anisotropy energy density; V is the volume of the NPs; K_B is the Boltzman constant and T is the temperature.

From the Néel relaxation time expression it is possible to define the Blocking Temperature, T_B (Eq. 4-2):

$$T_B = \frac{KV}{K_B \ln\left(\frac{\tau_m}{\tau_0}\right)} \quad \text{Eq. 4-2}$$

where τ_m is the measurement time.

Using a fixed measurement time (~20 s per point in this case), the T_B is defined as the temperature in which the τ_m is the same as the τ_N, i.e., is the temperature in which the measurement time is equal with the time in which the magnetization is blocked (no flips are detected). When the temperature is higher than T_B, during the measurement, the magnetization changes several times so, the average measured magnetization is zero and the system enters in the superparamagnetic state.

In order to study the transition between the ferromagnetism and the superparamagnetism of the NPs at different conditions and find out the blocking temperature, Field Cooled – Zero Field Cooled (FC-ZFC) curves were performed (figure.4.17).

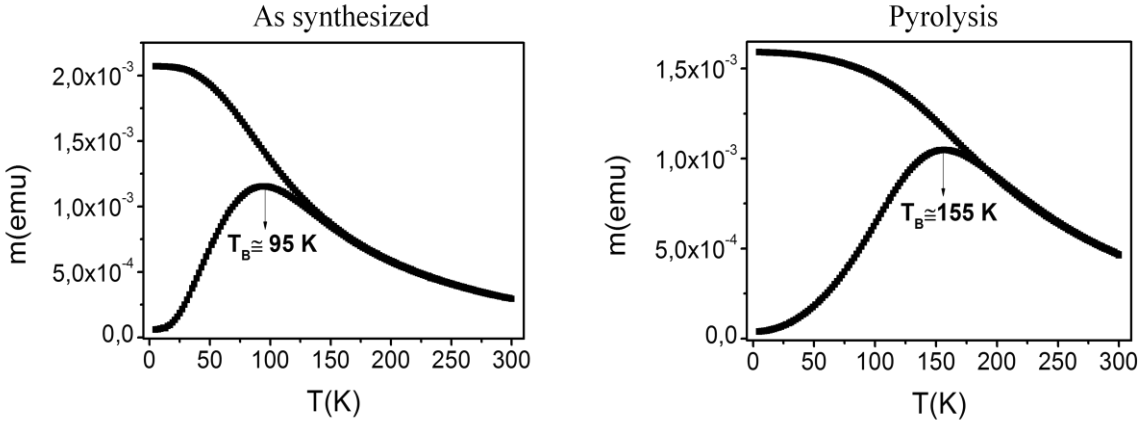

Figure 4.17. FC-ZFC curves of the CFO NPs exposed to different thermal treatments.

The T_B corresponds to the maximum of the ZFC curve. In the case of the synthesized NPs the T_B is 95 K while in the case of the pyrolyzed NPs the T_B is 155 K. Note that in the previous discussion it was said that the pyrolyzed NPs made the transition from ferromagnetic state to superparamagnetic state at a certain temperature between 10 and 300 K and that the pyrolyzed films are about to change to superparamagnetic state at 100 K because the M_{rem} and H_{coer} have drastically decreased. Therefore, the obtained value of the T_B from the FC-ZFC curves, which is 155 K for the pyrolyzed NPs, describes faithfully what it was observed previously. Also, these values of T_B are in agreement with the previous M(H) curves at 300 K in which it was observed that the synthesized and pyrolyzed NPs showed a superparamagnetic behavior (both T_B are below 300 K). In the

case of the quenched and the grown NPs, it has to be taken into account that the grain size is much larger due to the sintering process that takes place at high temperature. This causes that the ferromagnetic behavior is even observed at 300 K (V of the NPs in these two cases is high), so it is not necessary to perform the FC-ZFC curves, as it is known that the T_B will be higher than 300 K which is the maximum measured temperature.

The FC and ZFC curves have a different behavior below and above T_B. Both curves are modeled using different expressions depending on the temperature (below or above T_B)[239, 240].

Above T_B the thermal fluctuations dominate and the particles can spontaneously switch its magnetization from one easy axis to another. Such a system of superparamagnetic particles does not show hysteresis in the M(H) curves. In this case there are no differences between FC and ZFC curves. However, below T_B the NPs are in a blocked state and, therefore, the measurement time is not enough to see flips in the magnetization state. In this case there are differences between FC and ZFC curves due to previous magnetic history. Having this in mind, it is clear that T_B is defined as the moment in which FC and ZFC curves are separated.

This would correspond to the ideal case in which a very well defined and constant grain size is present. However, this is not the case in the NPs of this work. In this case there is a distribution of sizes. This causes a distribution of T_B (the T_B is defined for a specific value of grain size) which causes a separation between FC and ZFC curves that is not coincident with ZFC maximum. Therefore, the temperature of the maximum of the ZFC curve would correspond to the average T_B in the system.

4.3.2.2 Magnetic dichroism measurements

To understand better the magnetic properties of the CFO NPs under the different thermal processes, X-ray Absorption Spectroscopy (XAS) and X-ray Magnetic Circular Dichroism (XMCD) measurements were performed at ALBA synchrotron (Bellaterra, Spain) in collaboration with Dr. Elena Bartolomé. The oxidation state and site occupancy of the Fe and Co atoms in the NPs after the four different thermal processes were studied. These measurements were carried out using synchrotron radiation at 300 K and at a magnetic field of 6 T at which NPs are well saturated.

In figure 4.18 it is shown a) Fe $L_{2,3}$ XAS and b) XMCD spectra obtained from CFO NPs, as-synthesized and after the pyrolysis, after the quench at high temperature and after growth. Also the simulation for the Fe^{2+}Oh (octahedral), Fe^{3+}Td (tetrahedral) and Fe^{3+}Oh (octahedral) sites using the Ligand Field Multiplet (LFM) model and the CTM4XAS 5.0 program are presented (figure 4.18 c))[241].

Qualitatively, all the spectra shown in figure 4.18 a) and b) are very similar. The XAS spectra (figure 4.18 a)) show a negligible difference between the as synthesized NPs and the NPs after the quench and growth. Only the spectrum of the NPs after the pyrolysis changes a little bit as regards the intensity of the peaks. The XMCD at the $L_{2,3}$ edge (figure 4.18 b)) shows three characteristic peaks, typically found in CFO (spinel structure), each of them corresponding to an oxidation state/site in the structure: the lowest energy, negative peak corresponds to octahedral Fe^{2+}Oh, the positive peak to tetrahedral Fe^{3+}Td and the highest, negative peak to Fe^{3+}Oh. This result confirms the presence of the spinel structure of the CFO NPs after each step thermal process confirming observations made previously with SQUID measurements (SQUID measurements of CFO NPs in powder at 300 K

showed that the magnetization was the same as the initial one of the as-synthesized NPs after the quench and the growth and a small change was observed after the pyrolysis).

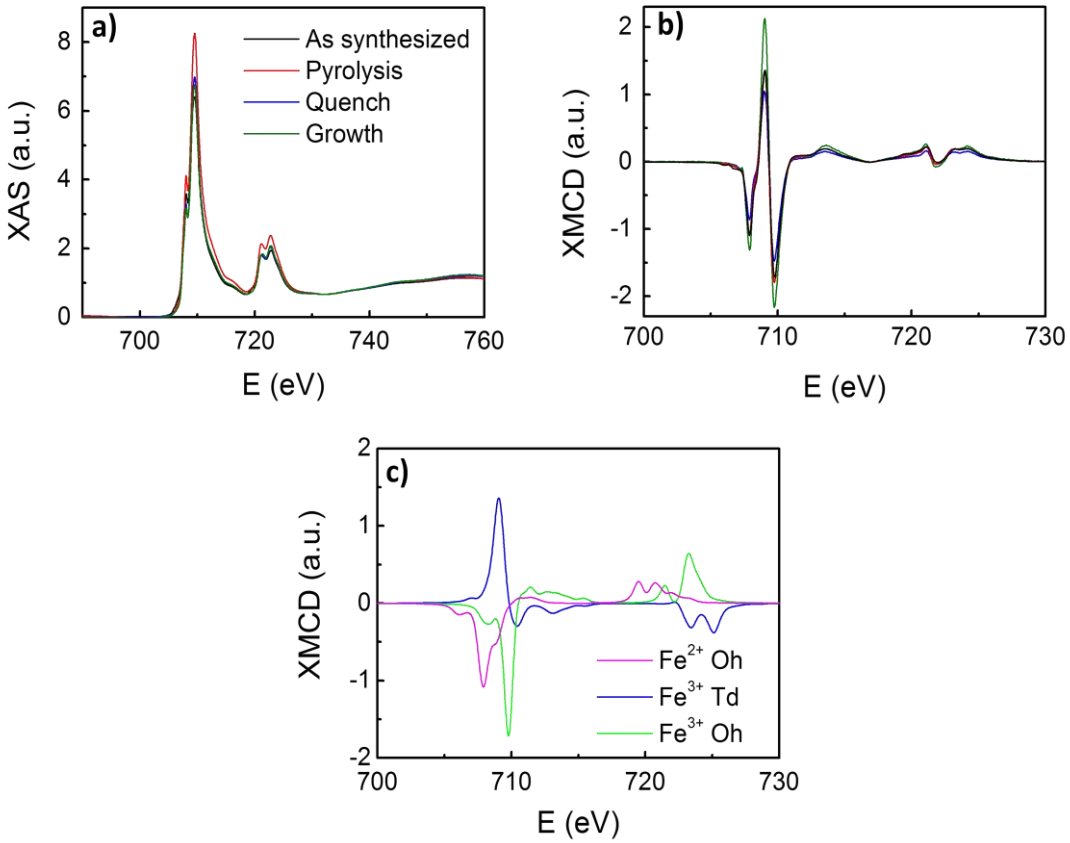

Figure 4.18. (a) XAS and (b) XMCD spectra at Fe $L_{2,3}$ edge of CFO NPs in 4 stages: as synthesized, after the pyrolysis, after the quench and after growth conditions; (c) LFM calculated XMCD spectra for Fe^{2+}Oh, Fe^{3+}Td and Fe^{3+}Oh of the as synthesized CFO NPs.

The same procedure is carried out in the case of the Co $L_{2,3}$ edge. The XAS and XMCD results are shown in figure 4.19. The XAS and XMCD measured at the Co $L_{2,3}$ edge shows a clear evolution from the synthesized to the grown NPs. In the XAS spectra, after the pyrolysis, the initial spectra are significantly modified, whereas, for the grown NPs, the spectra look similar to that of as synthesized NPs.

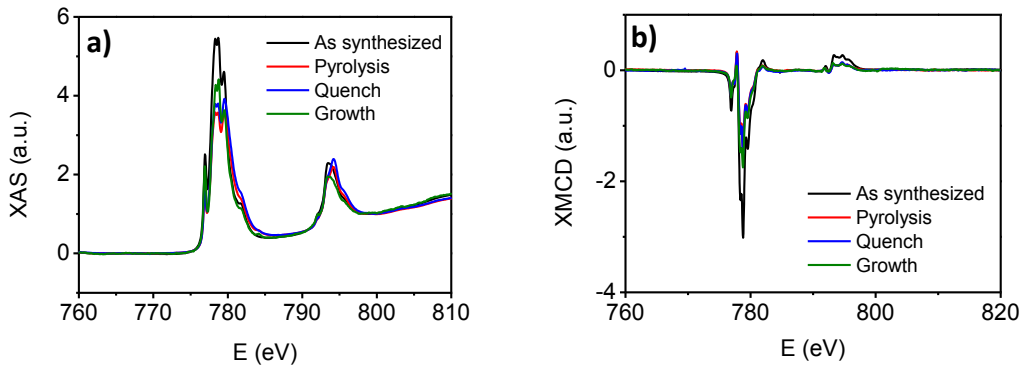

Figure 4.19. XAS and XMCD spectra at Co $L_{2,3}$ edge of $CoFe_2O_4$ NPs in 4 stages: as synthesized, after the pyrolysis, after the quench and after growth conditions.

In the case of Co, the site occupancy and oxidation state of Co was deduced by fitting the XMCD experimental spectra with a linear combination of the LFM calculated spectra for Co^{2+}Oh, Co^{2+}Td, Co^{3+} Oh and Co^{3+}Td. The aspect of the as synthesized NPs corresponds majorly (97%) to Co^{2+}Oh, with a minor contribution (3%) of Co^{2+} in Td sites. Remarkably, the spectra change significantly for the pyrolyzed and quench NPs, and to a less extend for the grown NPs, and cannot be fitted just considering Co^{2+} cations. LFM simulations show that an additional contribution of Co^{3+} in the three late heating stages is necessary to account for the experimental data. This observation was already mentioned when the hysteresis loops of the NPs were analyzed. After the pyrolysis, the Co^{+2} ions suffer an oxidation process to become Co^{3+} than modify the original spinel structure of the synthesized NPs. During the quench and the growth process, the Co^{3+} reduces again to its original oxidation state Co^{2+} obtaining similar magnetic properties than with the synthesized NPs.

The simulations permit the quantification of the site occupancy for Fe and Co. The estimated percentage is used to calculate the orbital (m_L), spin (m_S), and the total magnetic moment (m_L+ m_S) per average Fe ion (m_{Fe}) and Co ion (m_{Co}) from the XAS and XMCD spectra. With the magnetic moments m_{Fe} and m_{Co}, it is possible to determine the magnetic moment per formula unit as $m_{CFO}=2m_{Fe}+m_{Co}$. This last value can be compared to the value found with the SQUID measurements at 300 K (figure 4.20).

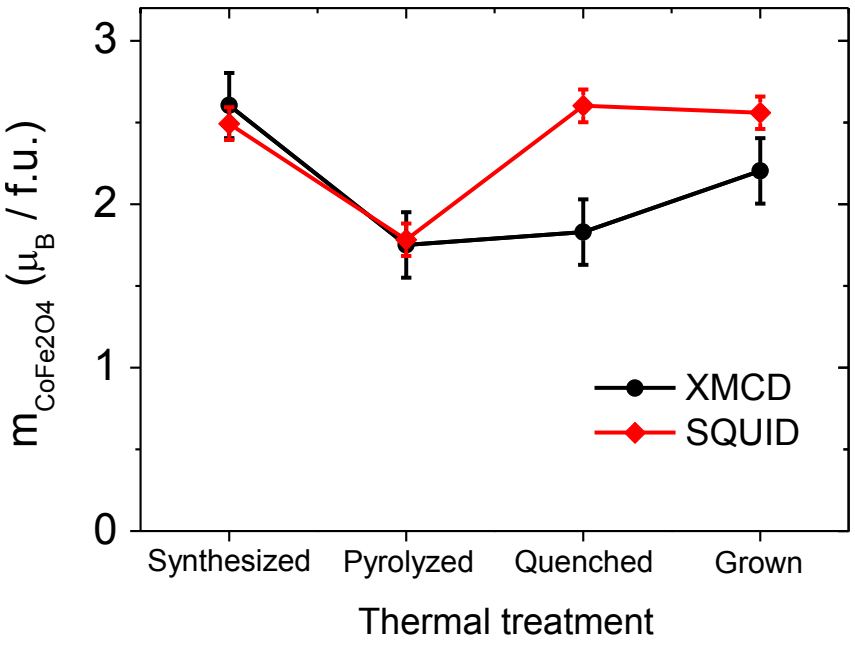

Figure 4.20 Comparison of the magnetic moment per formula unit at 300 K as determined from XMCD applying sum rules, and from SQUID measurements.

In order to interpret these results, it has to be taken into account that XMCD is just sensitive to the first ~6 nm of sample, whereas SQUID magnetometry is a macroscopic measurement. After the synthesis and the pyrolysis processes, the NPs are <5 nm in size. The XMCD and SQUID gives the same m_{CFO} values within the error, as both represent the average magnetic moment per formula unit of the whole NP. The decrease in m_{CFO} after the pyrolysis is observed by both techniques. After the quench and growth processes, the NP's size is >40 nm, according to XRD. Therefore, the m_{CFO} determined by XMCD

corresponds mainly to the surface, whereas the SQUID m_{CFO} is mainly due to core contribution. As shown in figure 4.20, after the quench and the growth, the m_{CFO} values found by XMCD are smaller than those obtained by SQUID, indicating that the thermal process mainly affects the NPs surface.

If similar XMCD measurements are carried out on the YBCO+CFO NPs nanocomposite films, the results are quite different. The XMCD spectrum shown in figure 4.21 only indicates the presence of the peak that corresponds to the atomic Fe^{3+}Oh. If this spectrum is compared with the spectra shown in figure 4.18 b), corresponding to the NPs in powder, the differences are clear. In the case of the spectra of the NPs in powder, they presented three different peaks corresponding to the three possible oxidation states/sites in the spinel structure. Therefore, it is evident that, at least in top layers (first 6 nm), no spinel CFO NPs have been detected in the YBCO+16%CFO NPs films confirming the previous results of TEM and XRD. The obtained XMCD spectrum could correspond to the Fe in the DP and/or to the Fe diffused in the matrix.

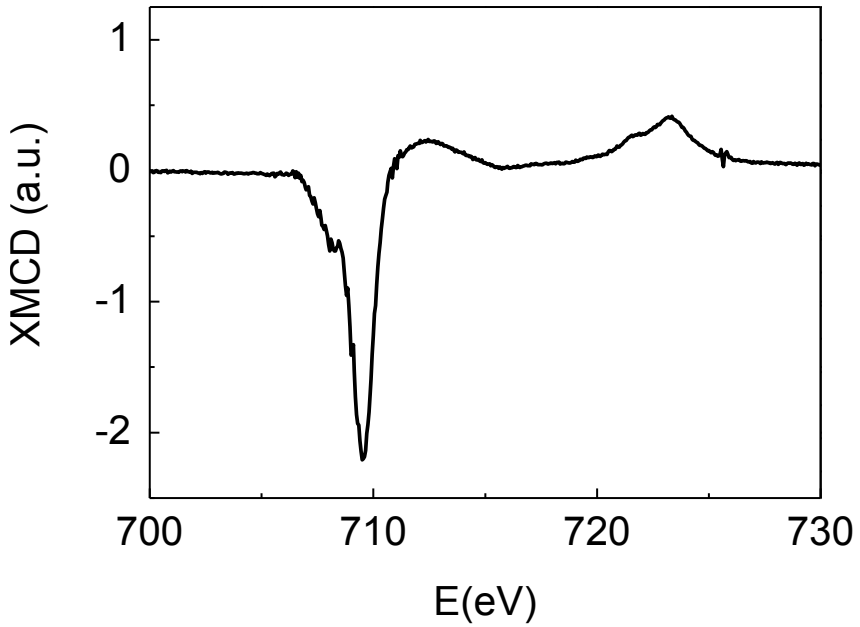

Figure 4.21. XMCD spectrum at Fe $L_{2,3}$ edge of quenched YBCO+16%CFO NPs nanocomposite film.

4.3.3 Summary

CFO NPs and YBCO+16%M CFO NPs nanocomposite films have been synthesized and deeply studied. The analysis of the XRD and TEM measurements reveal epitaxial YBCO with the presence of some a-b grains and also of a DP structure with unit formula $YBa(Fe/Co)_2O_5$, which indicates that the original CFO NPs react with the YBCO forming an alternative structure. The presence of CFO NPs after the growth process and, even, after the quench process could not be detected. The magnetic measurements helped to clarify that the reaction to form the DP structure starts during the heating process and it is very likely to occur by the interaction of BaF_2 coming from the decomposition of BYF and the CFO NPs. However, a small magnetic signal (M_{sat}=4,5 emu/g) is still identified in the films after the quench followed by oxygenation processes. Taking into account that no CFO NPs were detected, this signal should be attributed to the DP compound. However, the original structure reported by Woodward et al., $YBaFe_2O_5$, was demonstrated to be

antiferromagnetic, so it should not contribute to the magnetic moment. In the case of the structure identified in this work, it contains also Co, it might happen that the $YBa(Fe/Co)_2O_5$ structure displays some weak ferromagnetic behavior. In order to clarify if this magnetic signal could be caused by the DP compound, more local techniques should be used such as Lorentz microscopy[242], which uses the TEM to measure the local magnetic signal in the nanoscale.

The achievement of CFO nanocomposite films by CSD appears as a difficult task but it should not be considered to be impossible as the NPs, when they are outside the YBCO, maintain their structural and magnetic properties. The essential point is to avoid the reactivity. It was shown that, with the use of the standard growth process, it is not possible to avoid this reactivity, even by reducing the annealing time at high temperature. Increase the YBCO growth rate by, for example, working at low-pressures in such a way that the YBCO reaction was so fast that the NPs have no time to react with the BaF_2 would be a potential alternative. Another possibility could be to work at lower temperatures at which the reactivity should not be so favored.

4.4 Non-Magnetic NPs: CeO_2 and ZrO_2 NPs

This second part of the chapter is devoted to the study of the YBCO nanocomposites with the addition of non-magnetic NPs. Here, two different crystalline oxide NPs (ZrO_2 and CeO_2) were used. The two selected oxide phases are chemically compatible with YBCO, even if they react to form $BaZrO_3$ (BZO) and $BaCeO_3$ (BCO), respectively, as confirmed by the high superconducting transition temperatures achieved. However, other phenomena may occur that require a deep study of the structure and properties of these nanocomposites in order to achieve high quality epitaxial YBCO nanocomposite films.

4.4.1 YBCO+CeO_2 NPs nanocomposites

The solutions used to prepare the YBCO+CeO_2 NPs films were made following the steps already exposed in chapter 2. In this case, YBCO+6%M CeO_2 NPs in TREG and YBCO+8%M CeO_2 NPs in HDEC solutions from UAB were used.

4.4.1.1 Effect of the NPs´ ligand

The ligand is the basis of the steric stabilization and could also define the quality of the thin films. Figure 4.22 shows optical microscope images of a pristine YBCO film (figure 4.22 a) and an YBCO+6%M CeO_2-TREG films after the pyrolysis process (standard pyrolysis process). It is observed that the YBCO+6%M CeO_2-TREG film is not homogeneous.

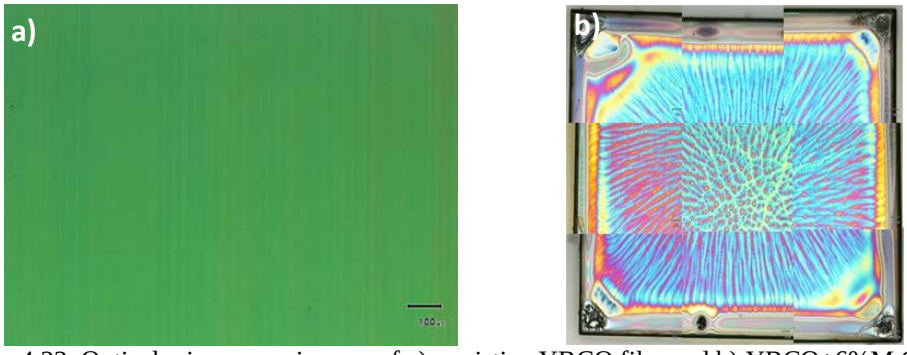

Figure 4.22. Optical microscope images of a) a pristine YBCO film and b) YBCO+6%M CeO_2-TREG film after the pyrolysis process.

From the profilometer measurement of YBCO+6%CeO_2-TREG pyrolyzed film (figure 4.23), it is observed a difference of 50 nm between the lower and the higher regions. Taking into account that the film thickness after the growth process is ~150 nm, this difference represents 30% of the thickness. Furthermore, it is well known that the inhomogeneities in the films deteriorate their final properties[178].

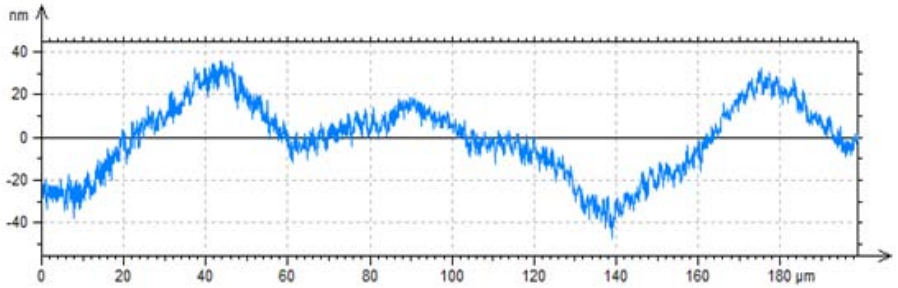

Figure 4.23. Height profile of the surface of an YBCO+6%M CeO_2-TREG film after the pyrolysis process obtained by a profilometer.

These films were grown following the standard growth process, in order to find out their properties and how the NPs affect the YBCO matrix. The 2D XRD θ-2θ patterns shown in figure 4.24 show the Bragg peaks corresponding to (00l)YBCO reflections indicating epitaxial orientation without the presence of other orientations of the grains. Also, it is observed the presence of the Bragg peaks corresponding to $BaCeO_3$ phase (BCO). The reflection (110) BCO shows a ring indicating the presence of randomly oriented NPs. The observation of BCO means that there is reactivity between the CeO_2 NPs and the BaF_2 during the YBCO reaction. It is the same phenomenon already mentioned in the case of the CFO. In this case, the CeO_2 NPs react during the growth process forming BCO. This reaction takes placed during the heating ramp in the growth process and it is quite difficult to avoid it. It is possible to reduce it by changing some of the processing parameters such as the heating ramp or the water pressure (making the YBCO reaction faster). Another alternative would be working with NPs that already contain Ba such as BCO. However, this is out of the scope of this thesis.

The nanostrain (ε) value of this film is 0,13±0,01 %. This value is much lower than those previously calculated for the in-situ nanocomposites in chapter 3. The calculated particle size (using Scherrer formula) of these films also differs from the values of the in-situ nanocomposite films. In this case the obtained value is 25±2 nm.

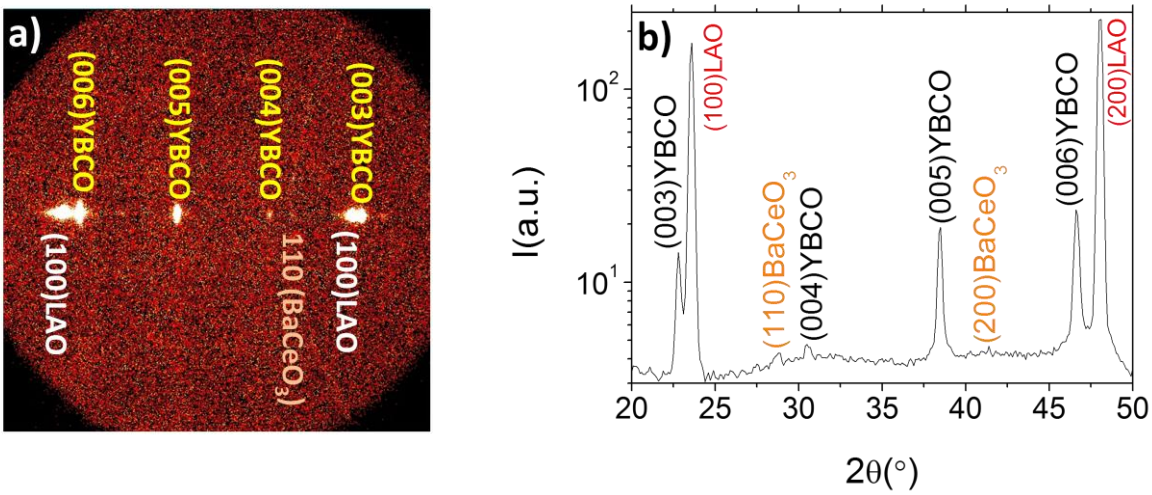

Figure 4.24. 2D XRD θ-2θ a) frame and b) integrated patterns of an YBCO+6%M CeO_2-TREG film after the growth process.

The physical properties (measured by SQUID) show similar values than in the case of the in-situ nanocomposites thin films (see chapter 3): T_c~90-91 K and J_c self-field (J_c^{sf}) at 77 K~3-4 MA/cm^2. On the other hand, by representing the J_c normalized by the J_c self-field (J_c/J_c^{sf}) dependence with the magnetic field for the pristine YBCO and the YBCO+6%M CeO_2-TREG (figure 4.25), it is possible to see that there is a small difference between both curves. The YBCO+6%M CeO_2-TREG curve is smoother but the improvement is small compare with the in-situ nanocomposites as it was shown in chapter 3. This indicates that, the effect of these CeO_2-TREG NPs is less than in the case of in-situ nanocomposites.

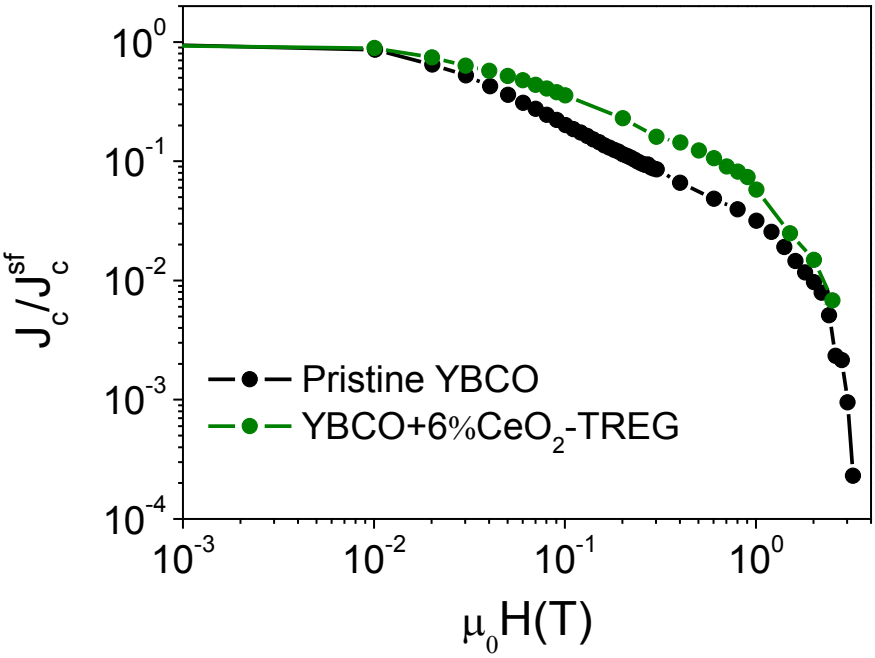

Figure 4.25. J_c/J_c^{sf} dependence with the magnetic field for the YBCO+6%M CeO_2-TREG NPs and pristine YBCO films

The microstructure of these films is studied by TEM. In figure 4.26 a) it is found that all the CeO_2 NPs are present on the top surface of the film and no NPs are found within the YBCO matrix. It is also observed in both figures 4.26 a) and b) that there are a large amount of Stacking Faults (SFs) near the top surface and the interface YBCO/LAO. This microstructural scenario can explain the low values of the ε and the similarity between curves in figure 4.25. Basically, what is observed in figure 4.26 is a pristine YBCO film with CeO_2 NPs in the top surface. The small difference between both curves in figure 4.25 is attributed to the presence of slightly higher amount of the SFs in the surface and interface surroundings (figure 4.26 b)) than in the pristine YBCO

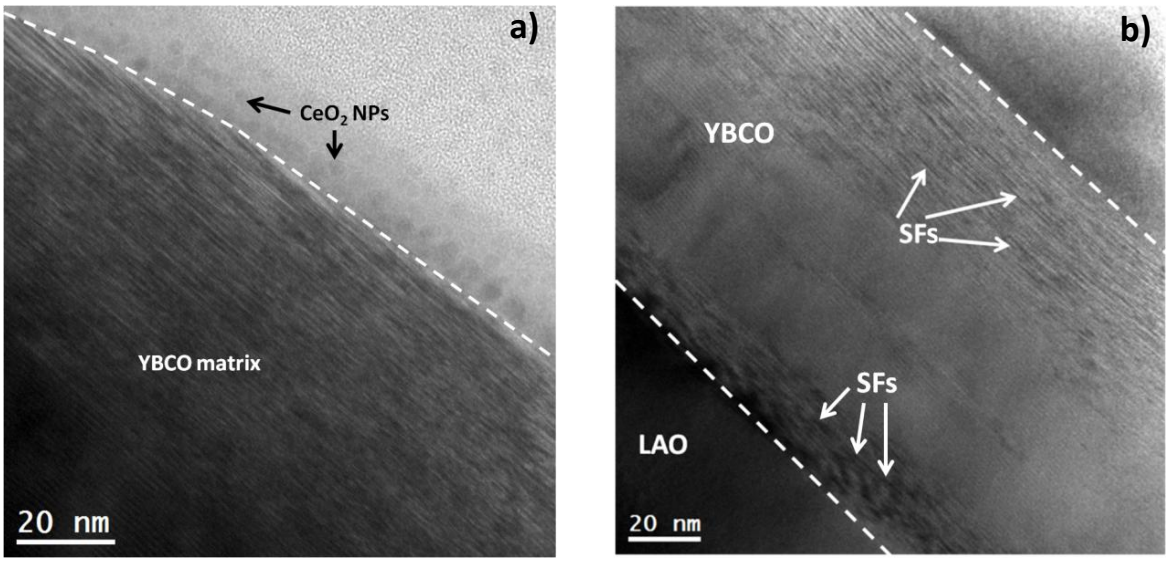

Figure 4.26. Cross-section HAADF TEM images of the one of the YBCO+6%M CeO_2-TREG thin films, showing a) the presence of the CeO_2 NPs in the surface of the films and b) the presence of the stacking faults (SFs) in the surroundings of the interface YBCO/LAO and the surface.

It is suggested that the inhomogeneous distribution of the NPs in the films is due to the presence of TREG. The high viscosity of TREG can favor these inhomogeneities in the spin-coating already because the TREG has a great tendency to place itself at the surface of the film, which would agree with the surface inhomogeneities observed in figure 4.22 b)

In order to confirm that surface inhomogeneities are due to TREG, it was prepared an YBCO with TREG solution (no NPs) using the same amount of TREG present in the NPs solution after the purification process. The as-prepared solution was deposited by spin-coating and pyrolyzed in the same conditions as the YBCO+CeO_2 NPs in TREG films. The optical microscope images after the pyrolysis shows the same morphology than in the case of the films with NPs proving that the TREG is the responsible for the inhomogeneities (figure 4.27 b)). Also the optical microscope images show that the inhomogeneities are already present just after the spin-coating before the pyrolysis process (figure 4.27 a)).

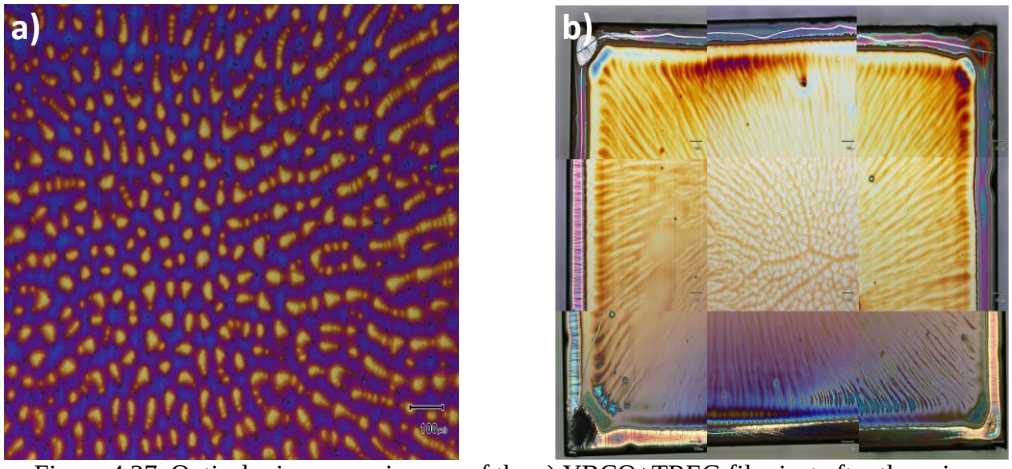

Figure 4.27. Optical microscope images of the a) YBCO+TREG film just after the spin-coating process and b) YBCO with TREG film after the pyrolysis process. These images prove that the responsible for the inhomogeneities in the films is the TREG.

When TREG is present in the solution, during spin-coating, it drags the NPs to the surface of the film. In order to avoid this effect, it is necessary to avoid the presence of TREG in the solution. For this reason a ligand exchange is carried out.

The procedure to perform the ligand exchange in the case of the UAB NPs was explained in section 4.2. In this case, the chosen ligand was the decanoic acid (HDEC) as it has a lower viscosity. A solution of YBCO+8%M CeO_2-HDEC was prepared and deposited by spin-coating. Then, it has been performed the standard pyrolysis process. After the pyrolysis the films show a homogenous surface as it can be observed in figure 4.28 (the effect of the LAO twins is also observed).

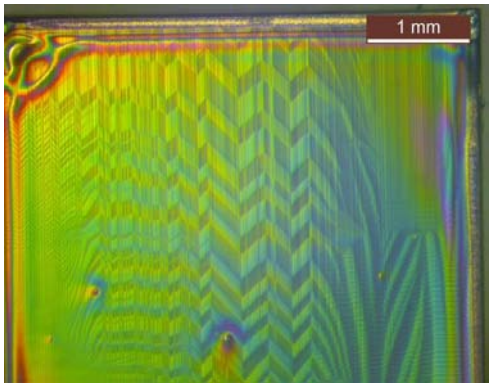

Figure 4.28. Optical microscope image of an YBCO+8%M CeO_2-HDEC film after pyrolysis showing inhomogeneities free surface.

Afterwards, it has been performed the standard growth process. The characterization of the grown films is performed in the same way as in the previous case. The 2D XRD θ-2θ patterns show the formation of epitaxial YBCO (figure 4.29). Again, the presence of BCO is detected suggesting the reaction between CeO_2 NPs and BaF_2. The results are very similar to the films obtained with TREG NPs. The most remarkable difference is that in this case no BCO ring is detected indicating that no randomly oriented NPs are present. The ε value is higher than in the previous case (0,18±0,01 %) while the NPs size is approximately the same (27±2 nm).

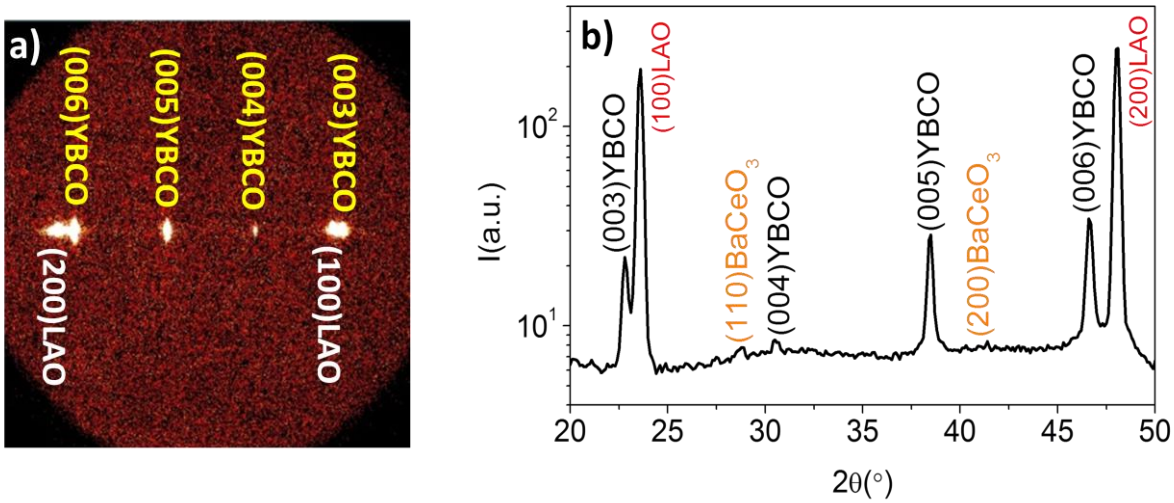

Figure 4.29. 2D XRD θ-2θ a) frame and b) integrated patterns of an YBCO+8%M CeO_2-HDEC film after the growth process.

The superconducting properties, the T_c and J_c^{sf} at 77 K values are lower than in the case of the NPs in TREG reaching 89-90 K and 1,5-2,5 MA/cm^2, respectively. Figure 4.30 presents the compared SQUID measurements of J_c/J_c^{sf}curves of the YBCO+8%M CeO_2-HDEC with the YBCO+6%M CeO_2-TREG and with the pristine YBCO film. It is observed that for both nanocomposites the behavior is almost the same. So, the higher value of ε does not entail a different behavior when the J_c/J_c^{sf} values are represented as a function of the magnetic field.

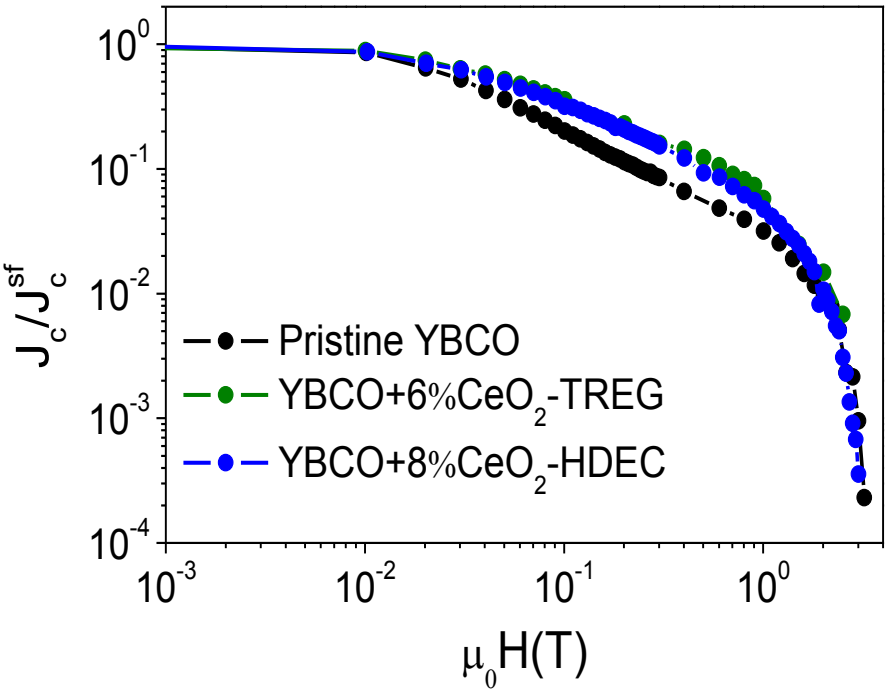

Figure 4.30. J_c/J_c^{sf} dependence with the magnetic field measured with SQUID for the pristine YBCO, YBCO+6%M CeO_2-TREG and YBCO+8%M CeO_2-HDEC.

This result is quite unexpected taking into account that the NPs in this case should be embedded YBCO matrix. To explore the reasons why the same results as in the case of TREG NPs are found, TEM images of one YBCO+8%M CeO_2-HDEC film are obtained. They are presented in figure 4.31.

Big particles (~100 nm) of BCO are observed mostly in the surface but also embedded in the YBCO matrix. These big blocks are created by the agglomeration of the NPs from the solution stage as it was already mention when the DLS measurements were presented (table 4.2). DLS measurements showed aggregates of more than 100 nm. These values are in accordance with the BCO particles observed in TEM images. These big particles are responsible for the low values of J_c in these films. They act as the unreacted phases already commented in the thick nanocomposites films, as "current blockers" lowering the effective thickness and hindering the current percolation.

It is also observed the presence of high amount of long SF in the film (figure 4.31 a)). This is the reason for the increase of the ε values. Most of them are created by these big BCO particles that, again, works as in the case of the unreacted phases in the thick films. These SFs are too long to have the desired effect in the films. For that reason the behavior of the J_c/J_c^{sf} vs. magnetic field curves are quite similar to the pristine YBCO films and the TREG NPs films.

On the other hand, figure 4.31 b) shows the presence of CeO_2 NPs at the surface of the film. But, in this case, this fact can not be attributed to ligand effect because the ligand is not TREG. The reason for this effect was related to the growth process and the most probable cause is the pushing effect.

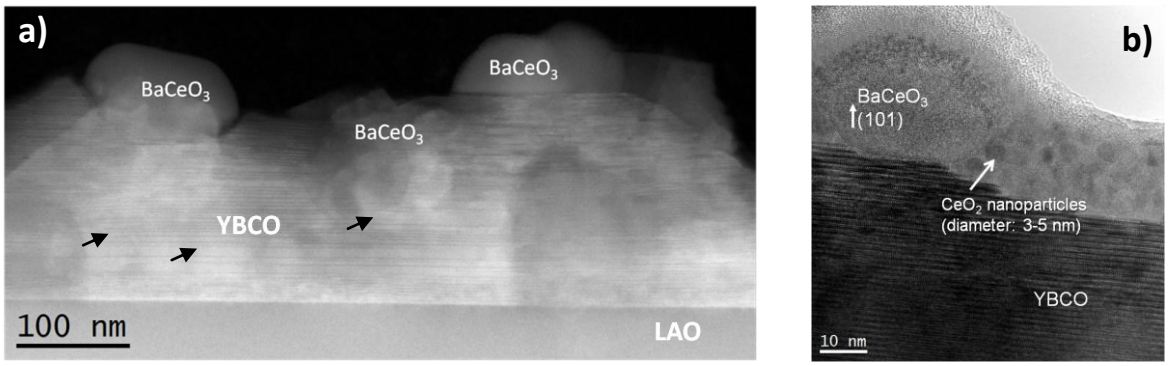

Figure 4.31. Cross-section HAADF TEM images of the one of the YBCO+8%M CeO_2-HDEC showing a) the presence of big particles of BCO and long SFs (black arrows) in the YBCO matrix and b) the presence of CeO_2 NPs in the surface of the film.

4.4.1.2 Pushing effect

The pushing effect was originally observed studying the behavior of an advancing solid–liquid interface during solidification. In this case, foreign particles are pushed out of the material matrix or trapped inside depending on the conditions of the system[243-247]. This theory was used also to explain the macrosegregation phenomenon of Y211 particles in YBCO crystals prepared by solidification processing[248]. It is possible to use the same principles to understand the behavior of the NPs when the YBCO growth front interacts with them.

According to the pushing/trapping theory, the critical size (r*) of a particle, larger than the trapped by the solid, is roughly determined by the critical growth rate (R*) and the interfacial energy ($\Delta\sigma_0$) by the following expression (Eq. 4-3):

$$r^* \propto \frac{\Delta\sigma_0}{\eta R^*} \qquad \text{Eq. 4-3}$$

where η is the melt viscosity.

In the case of a system in which the YBCO front interacts with NPs, the R* would be the YBCO growth rate, $\Delta\sigma_0$ the interfacial energy YBCO/NPs and η the "friction coefficient" of the amorphous phase formed by the YBCO precursors that the NPs have to cross to arrive to the surface.

The $\Delta\sigma_0$ and η have fixed values for the system YBCO/CeO_2 NPs so, among all the parameters, only the R* and the r* can be tuned. To change R* entails modifying the YBCO processing parameters which is not best option since the standard growth process that is being used contains all the optimized processing parameters for the YBCO growth. So, if pushing effect is observed with this R*, means that the radius of the NPs is smaller than the critical size for the trapping. Therefore, the strategy will be to synthesize new CeO_2 NPs with a larger radius in such a way that the new radius will be larger than the critical one.

New 4 nm diameter CeO_2 NPs were synthesized following the UAB synthesis process. They used the process presented in figure 4.3 but changing the Ce precursor from cerium acetylacetonate that gives 2 nm particles to cerium acetate that gives 4 nm particles. The change of the precursor modifies the conditions of the nucleation and growth of the NPs during the thermal process arriving to different size NPs.

The new 4 nm CeO_2 NPs have almost the same characteristics as the 2 nm NPs: the stability of the NPs in the YBCO is in the range of 3-4 hours, the DLS showed a peak in 100 nm meaning that they also tend to aggregate, TEM images reveal 4 nm diameter NPs with spherical shape and in the XRD the cubic structure was found as in the case of the 2 nm NPs (table 4.2). A new solution with these new NPs was prepared: YBCO+8%M CeO_2-HDEC 4 nm NPs. This solution is deposited on LAO substrate by spin-coating and then, the standard pyrolysis process is carried out. The film surface after the pyrolysis is homogeneous confirming that the use of HDEC as a ligand provides homogeneous films after the pyrolysis (figure 4.32).

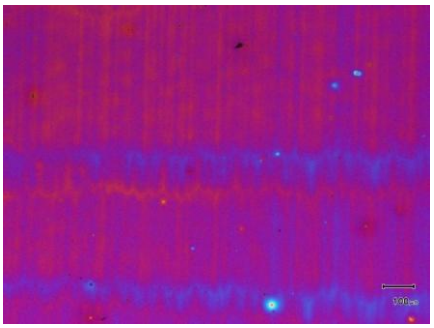

Figure 4.32. Optical microscope image of YBCO+8%M CeO_2-HDEC 4 nm NPs film after the pyrolysis process showing a homogeneous surface.

The XRD patterns of the grown films in figure 4.33 show the formation of epitaxial YBCO and the presence of BCO reflections. As in the case of 2 nm NPs, there is no ring of BCO NPs indicating that BCO tends to nucleate epitaxial. The ε and particle size values are maintained in the range of the previous films using the 2 nm NPs (0,19±0,01 and 30±2, respectively).

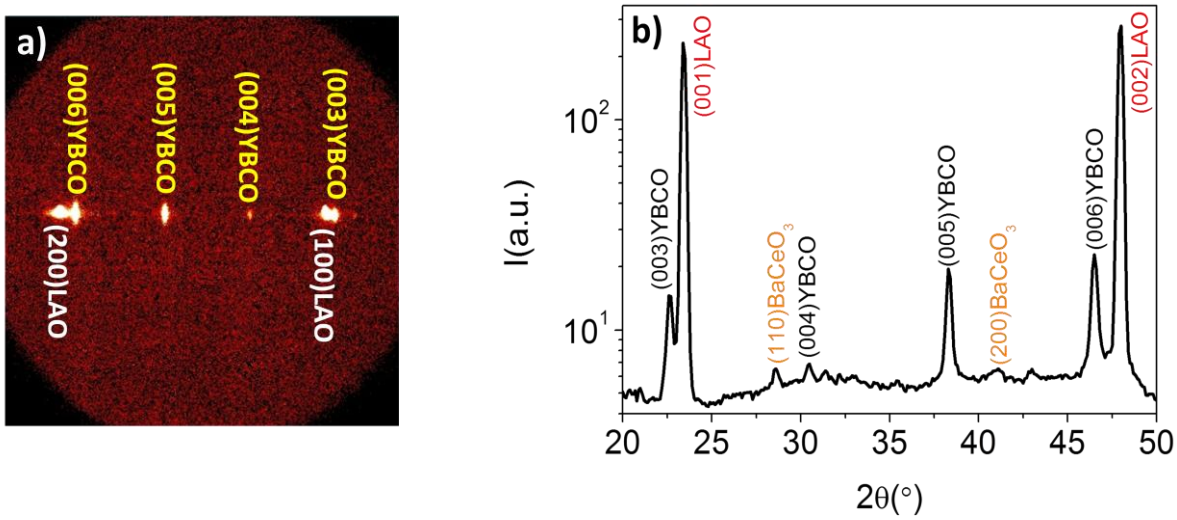

Figure 4.33. 2D XRD θ-2θ a) frame and b) integrated patterns of an YBCO+8%M CeO_2-HDEC 4 nm NPs film after the growth process.

The T_c and J_c^{sf} measured at 77 K of these films present a dramatic drop with respect to the previous films: 87-88 K and 0,5-1 MA/cm^2, respectively. In the J_c/J_c^{sf} dependence with the magnetic field (figure 4.34), it is observed that the curve for the 4 nm NPs drops at much lower fields than in other two cases (figure 4.34 red symbols).

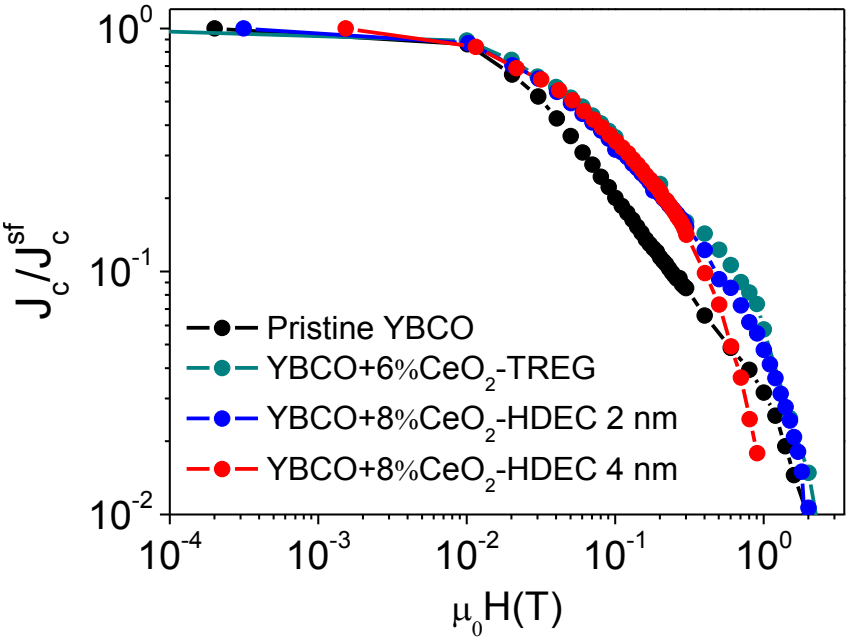

Figure 4.34. J_c/J_c^{sf} dependence with the magnetic field measured with SQUID for the pristine YBCO, YBCO+6%M CeO_2-TREG, YBCO+8%M CeO_2 NPs (2 nm) in HDEC and YBCO+8%M CeO_2 NPs (4 nm) in HDEC.

In order to clarify why this different behavior is observed in this case, TEM images of YBCO+8%M CeO_2 films with 4 nm NPs are investigated (figure 4.35). It is observed in figure 4.35 a) that there are big particles of BCO in the top surface of the film and also

occupy big parts of the YBCO matrix. Again, they act as "current blockers" disturbing the current flow. As in the case of 2 nm NPs films, these big particles come from the aggregated NPs already present in the solution (DLS peak at 100 nm, see table 4.2). Also in figure 4.35 a), it is possible to observe a huge amount of SF that, again, are the responsible for the increment of the ε but, as in the case of 2 nm NPs, they are too long to be effective pinning centers. This explains why, in this case, the J_c/J_c^{sf} vs. magnetic field curve had an identical behavior as in the case of 2 nm NPs films at intermediate fields. It is also observed that there are no NPs in the top surface so; the NPs were trapped in the YBCO matrix sustaining the hypothesis of the pushing/trapping effect. Actually, figure 4.35 b) shows two CeO_2 NPs embedded in the YBCO matrix confirming the trapping effect.

These results show that it is possible to achieve epitaxial YBCO films with trapped CeO_2 NPs in the YBCO matrix. However, the fact that the NPs are trapped could not be positive if the NPs tend to aggregate forming big cumulus as it observed in this case. These aggregates, which come from the initial solution, form big blocks of BCO after the growth process acting as "current blockers" and creating a non-uniform film microstructure that cause the observed drops in T_c and J_c and also in the J_c/J_c^{sf} vs. magnetic field curves. This was not the case working with the 2 nm NPs films because, in that situation, most of the NPs were in the surface so the big blocks were created mostly near to surface. They disturb a little bit the current flow causing a J_c decrease but the T_c remained constant at 90-91 K. This is the difference of having the big particles in the surface or in the middle of the matrix as in the 4 nm NPs films. Therefore, to have trapped NPs is beneficial as long as the NPs are small and homogenously distributed because, otherwise, the big block could deteriorate the properties. It is suggested, thus, that the use of non-aggregated NPs solution could further improve the YBCO nanocomposite properties.

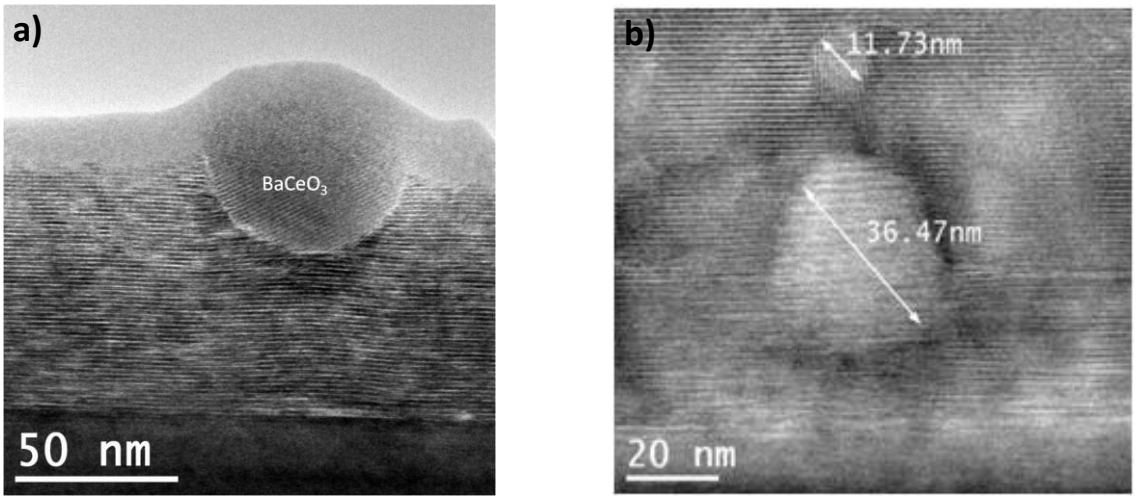

Figure 4.35. Cross-section HAADF TEM images of the one of the YBCO+8%M CeO_2-HDEC 4 nm NPs films showing a) the presence of big particles of BCO and plenty of long SFs in the YBCO matrix and b) the presence of CeO_2 NPs in the interface YBCO/LAO.

4.4.1.3 Summary

We have generated knowledge and the first advances on YBCO+CeO_2 nanocomposites using the ex-situ route with fairly good superconducting properties. It has been demonstrated that CeO_2 NPs with different ligands can be used to prepare epitaxial

YBCO nanocomposite films. It was shown the importance of the ligand choice to obtain homogeneous films after pyrolysis. Enhance pinning properties with respect to the pristine YBCO films has been achieved due to the generation of SFs observed in the YBCO+CeO_2 nanocomposite films. It was also shown that the pushing effect may appear if the size of the NPs is too small (i.e., 2 nm). The increase of the NPs diameter allowed the achievement of NPs trapping. However, there is still room for improvement. To synthesize colloidal solutions without NPs aggregates is absolutely necessary to avoid the big aggregates that place in the YBCO matrix deteriorating the superconducting properties.

4.4.2 YBCO+ZrO_2 NPs nanocomposites

In this section, it will be investigated YBCO nanocomposites using two different types of ZrO_2: ZrO_2-UAB NPs which are sterically stabilized by using HDEC as ligand and ZrO_2-UG NPs which are charge stabilized. Both types of stabilization results in NPs with different features (table 4.2). For ZrO_2-UAB NPs, we have performed a thorough study of YBCO+16%M ZrO_2. For the ZrO_2-UG NP, we have investigated different concentrations (6, 10 and 15%M) of NPs.

4.4.2.1 Pyrolysis process

Both type of solutions are deposited by spin-coating and pyrolyzed using the standard pyrolysis process. After the pyrolysis, the films present an homogeneous surface (figure 4.36).

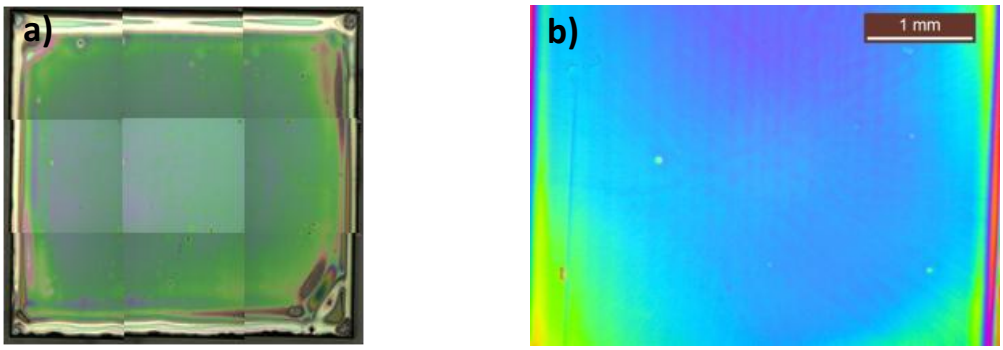

Figure 4.36. Optical microscope images of pyrolyzed films of a) YBCO+16%M ZrO_2-UAB NPs and b) YBCO+10%M ZrO_2-UG NPs. The pyrolyzed films show a homogeneous surface.

Based on the results obtained in YBCO+CeO_2 nanocomposites where it was observed that the distribution of the NP can vary, it has been studied, in the case of the ZrO_2 NPs films, the distribution of the nanoparticles by performing XPS depth profile studies (measure the chemical composition while the sputtering etches the film) after the pyrolysis, paying special attention to Zr(3p) region. The results are shown in figure 4.37. Figure 4.37 a) presents the spectra in the Zr(3p) region at different etch times for the case of the YBCO+16%M ZrO_2-UAB NPs. Figure 4.37 b) shows the evolution of the Zr content in the case of the YBCO+10%M ZrO_2-UG NPs. In this case it was possible to quantificate the Zr content by integrating the Zr peaks from the original XPS spectra with the etch time (the etch time is equivalent to the thickness because as the etch time increases

also the depth increases). These results reveal that, in both cases, most of the NPs tend to be allocated in the interface YBCO/LAO during the deposition/pyrolysis processes.

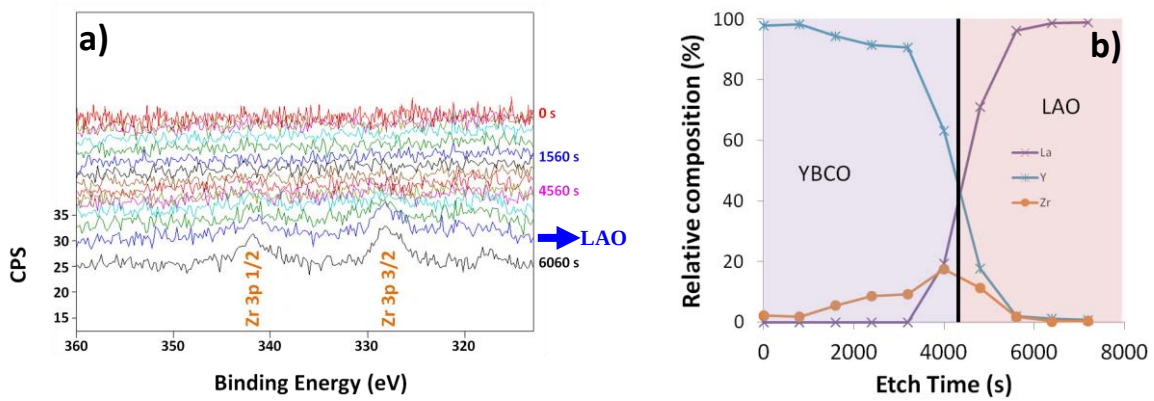

Figure 4.37. XPS depth profile studies of a) YBCO+16%M ZrO_2-UAB NPs and b) YBCO+10%M ZrO_2-UG NPs films.

4.4.2.2 Growth process

These films were grown using the standard growth process. From the XRD analysis it is observed that epitaxial YBCO is obtained in the UAB NPs films (figure 4.38 a)). However, this is not the case for the UG NPs films in which polycristalline YBCO is obtained (figure 4.38 b)). When the concentration of UG nanoparticles are reduced to 3 %M , then YBCO grows epitaxially (figure 4.38 c)). It is important to note that in all the cases, the presence of (200)BZO reflection is observed as a bright spot, indicating the reaction between the ZrO_2 and BaF_2 (same effect as in the case of of CFO and CeO_2 NPs) forming epitaxial BZO on the substrate surface. Indeed, the random fraction is in the range of the case of 200 nm in-situ BZO nanocomposites films (chapter 3, figure 3.6), reaching values of ~50%. The ε values in the case of the YBCO+16%M ZrO_2-UAB NPs film reach 0,23±0,01%, value which is very near to the values for the in-situ nanocomposites (chapter 3, figure 3.7)

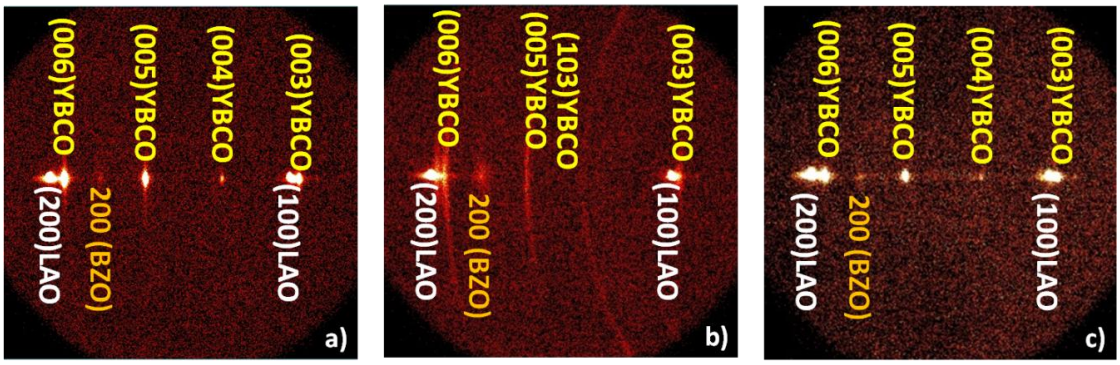

Figure 4.38. 2D XRD θ-2θ frames of a) YBCO+16%M ZrO_2-UAB NPs film, b) YBCO+10%M ZrO_2-UG NPs film and c) YBCO+3%M ZrO_2-UG NPs film.

In order to identify the location of the NPs after the growth process, XPS and TEM analysis were performed in the grown films. XPS depth profile studies were carried out in YBCO+15%M ZrO_2-UG NPs film showing that, after the growth process, the Zr

distribution throughout the thickness almost reproduce the distribution after the pyrolysis (figure 4.39). This means that the NPs remains at the interface YBCO/LAO after the growth process.

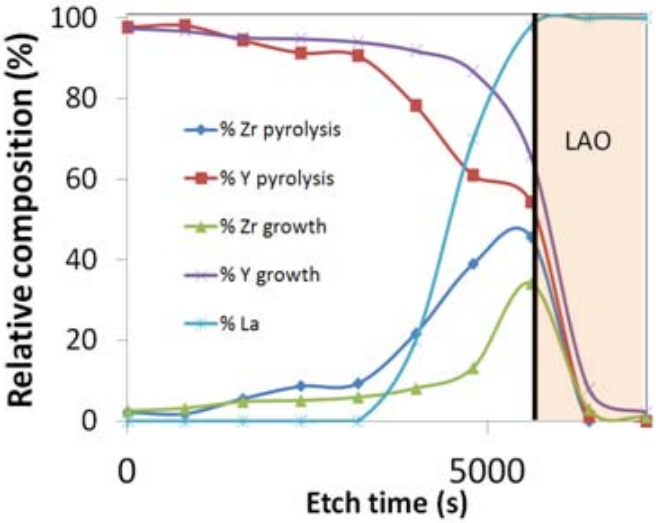

Figure 4.39. XPS depth profile study of YBCO+15%M ZrO_2-UG NPs of pyrolyzed and grown films.

This observation is confirmed by TEM images and EDX maps acquired from both UAB and UG ZrO_2 NPs grown films (figure 4.40).

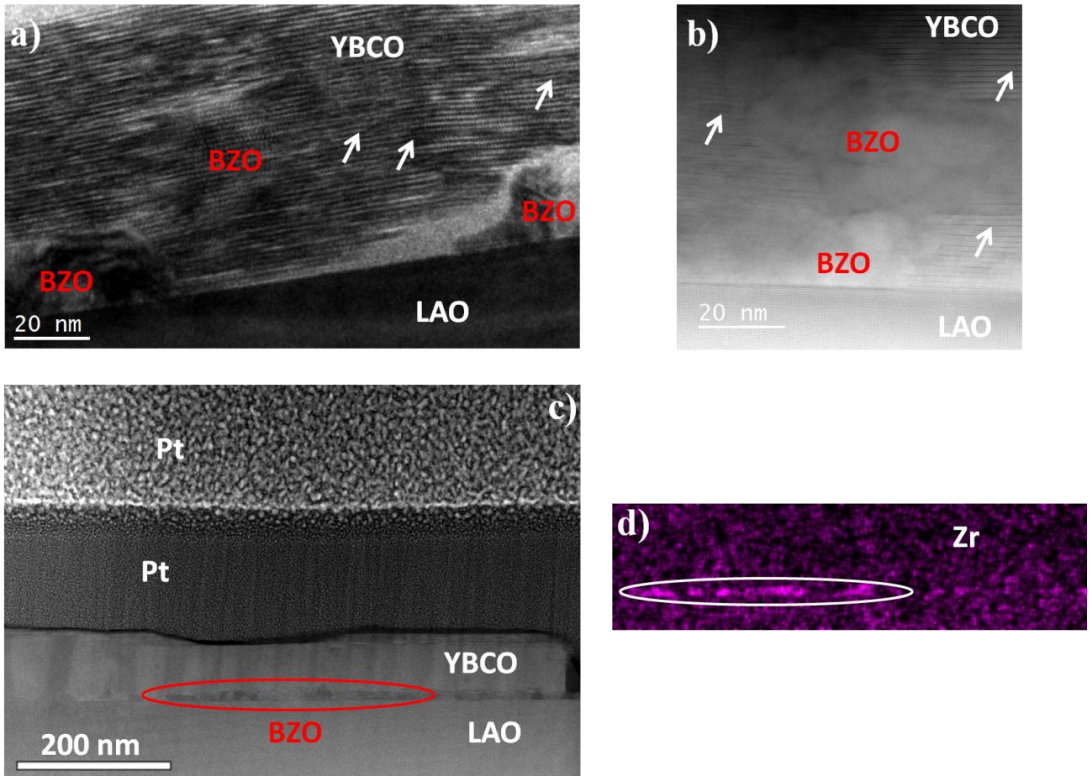

Figure 4.40. TEM images a) and b) of YBCO+16%M ZrO_2 UAB NPs film, c) YBCO+1%M ZrO_2 UG NPs film and d) EDX map of Zr of the YBCO+1%M ZrO_2 UG NPs film.

Figure 4.40 a) and b) show the images of an YBCO+16%M ZrO_2-UAB NPs film in which it is clearly observed the big amount of BZO particles in the YBCO/LAO interface. There are also big BZO particles in the matrix near the interface. Note that the size of these big BZO particles agrees with the size obtained by DLS from the colloidal solution of ZrO_2 NPs (70-80 nm). This film is full of SFs identified by white arrows in figure 4.40 a).

Figure 4.40 c) and d) correspond to YBCO+1%M ZrO_2 UG NPs. In this case, it is observed the presence of a ~10 nm BZO thin layer in the YBCO/LAO interface (figure 4.40 c)). In the EDX map of Zr is clearly observed a Zr accumulation in the YBCO/LAO interface (figure 4.40 d)).

From the comprehensive characterization presented above, it is suggested the following explanation for the ZrO_2 NPs distribution in the YBCO matrix, see figure 4.41. It was demonstrated that both type of NPs tend to aggregate in the interface during the deposition/pyrolysis processes. However, in the case of ZrO_2-UG NPs (they are well dispersed in the initial NPs solution) the NPs are placed individually at the interface forming a layer that covers part of the LAO (depends on the concentration they cover more or less space) while in the case of the UAB NPs (they are aggregated in the initial NPs solution), they form big aggregates that leave free space in the LAO. This fundamental difference affects the subsequent YBCO growth.

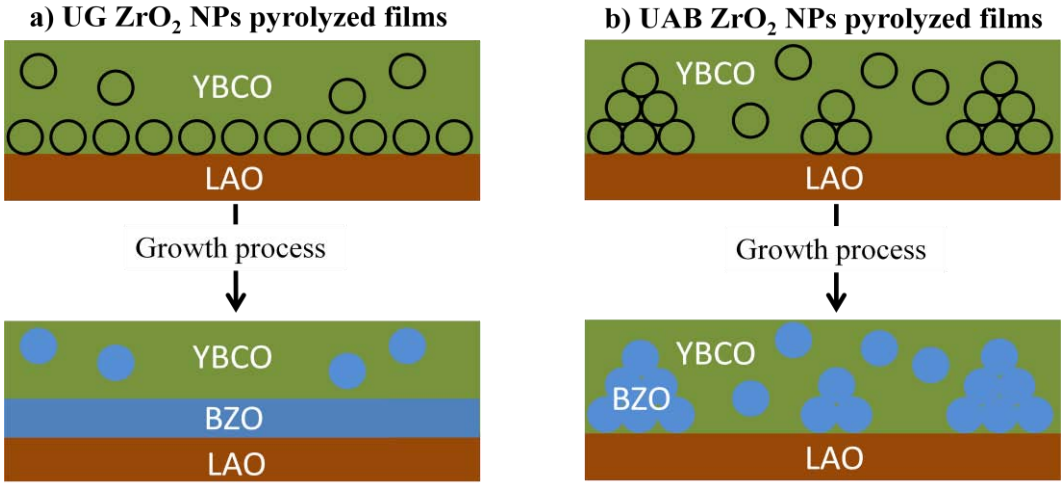

Figure 4.41. Sketch of the NPs evolution during the growth process for films using the two different types of NPs: a) ZrO_2-UG NPs and b) ZrO_2-UAB NPs

In the growth process, it was demonstrated that in both cases the NPs react forming BZO. However, in the case of the UG NPs films a ~10 nm thin layer of BZO is formed in the interface. Therefore, the YBCO have no space to epitaxially nucleate in the LAO surface and it nucleates on the top of the BZO layer (figure 4.41 a)). It was demonstrated by a quench study that the NPs reaction to form BZO, in this case, is formed at temperatures lower than 750 ºC, before the YBCO nucleation. So the YBCO nucleate on the top of the BZO layer and, since the mismatch between the the BZO and YBCO is large (+8,7%), the YBCO can not grow epitaxial. Epitaxial YBCO can be obtained only when low concentrations of ZrO_2 NPs (< 3%M) are used. At this concentration the amount of NPs is not enough to completely cover the LAO allowing the nucleation of epitaxial YBCO on the LAO.

In the case of UAB NPs, the BZO nucleates forming big aggregates that do not cover the entire LAO surface allowing the YBCO nucleation on LAO and, therefore,

obtaining epitaxial YBCO (figure 4.41 b)). In this case, it is also observed the presence of high amount of SFs. Their origin is the same as in the case of the CeO_2 NPs films: the big aggregates act as in the case of unreacted phases in the thick films creating high density of long SFs. This situation reveals the importance of the NPs colloidal solution quality and to perform DLS measurements to verify it as it strongly influences the growth process.

The consequences of this different behavior are clearly seen analyzing the physical properties of these films. Figure 4.42 shows the evolution of the J_c^{sf} at 77 K and T_c for the UG NPs films (figure 4.42 a)) and the UAB NPs films (figure 4.42 b)). The UG NPs films have poor values of J_c^{sf} at 77 K and also low values of T_c (compared with 90-91 K for the pristine YBCO) when the concentration is higher that 3%M as a consequence of the polycrystalline growth of YBCO. On the other hand, the UAB NPs films show good values of J_c at 77 K and T_c up to concentrations of 16%M.

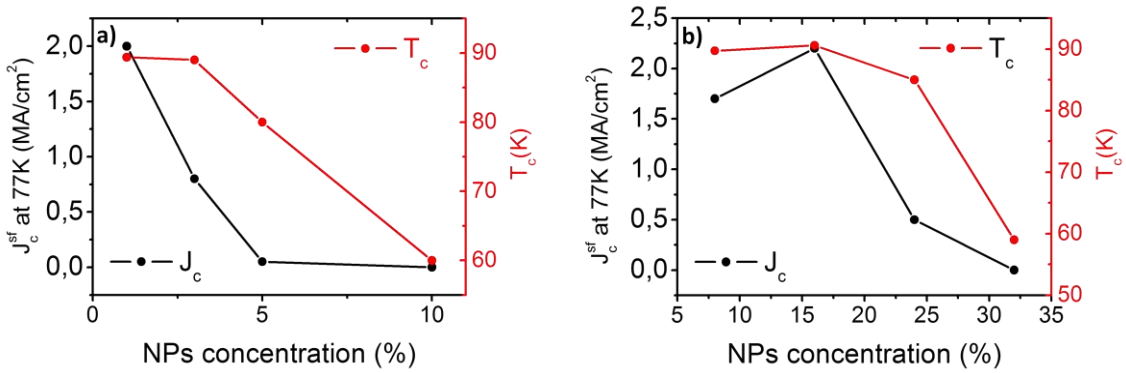

Figure 4.42. Evolution of the J_c and T_c for a) the UG NPs films and b) the UAB NPs films.

4.4.2.2.1 Transport measurements

Considering the different situations for the YBCO growth depending the NPs that being used, ZrO_2 UAB or UG NPs, the epitaxial film that showed the best physical properties, i.e., the YBCO+16%M ZrO_2-UAB, was chosen to carry out a detailed transport measurements. The results of this analysis are shown in figure 4.43.

Figure 4.43 a) shows the J_c at 77 K dependence with the magnetic field of the YBCO+16%M ZrO_2 UAB NPs film. First of all, it is observed that the J_c^{sf} at 77 K is comparable with the pristine YBCO values (reaching a value of 4,5 MA/cm^2). Apart from this, the shape of the curve is nanocomposite-like with the characteristic rounded shape at intermediate fields which leads to a higher values of H* than in the pristine YBCO films (larger vortex-defect region, see chapter 3). Finally, it can be seen that the drop of the J_c occurs at lower fields than in the pristine YBCO film, indicating that the twin boundaries effect in the nanocomposites is lower than in the pristine YBCO. This is due to presence of SF that breaks the coherence of the twin boundaries. So, the irreversibility line is also lower than in the pristine YBCO film, which is a characteristic of the nanocomposites.

In figure 4.43 b), the angular dependence of J_c at 65 K shows a more isotropic behavior of YBCO+16%M ZrO_2 UAB NPs film than in the pristine YBCO film. This figure also demonstrates the presence of SF as can be deduced from the width of the YBCO+16%M ZrO_2 UAB NPs film peaks at 90º. These peaks are much wider than the pristine YBCO peak in which the presence of SF is much lower. The SFs increase the width of this peak because their effect is relevant when the magnetic field is parallel to the ab-plane in which they act as pinning centers. At 180º, i.e., when the magnetic field is

parallel to c-axis, the pristine YBCO shows a peak related with the presence of the twin boundaries. This peak does not exist in the case of the YBCO+16%M ZrO_2 UAB NPs film since, as was mentioned before, the SFs break the coherence of the twin boundaries preventing their effect[183, 184]. The presence of the SFs, that cause a deformation in the YBCO in nanoscale regions, also explains the high value of the ε found in these films (ε=0,23±0,01%).

Finally figure 4.43 c) shows the isotropic collapse of the irreversibility line for the nanocomposite, measured at different magnetic field orientations. The collapse is reached with an effective gamma (γ_{eff}) value of 3, which is also a typical value of the in-situ nanocomposites.

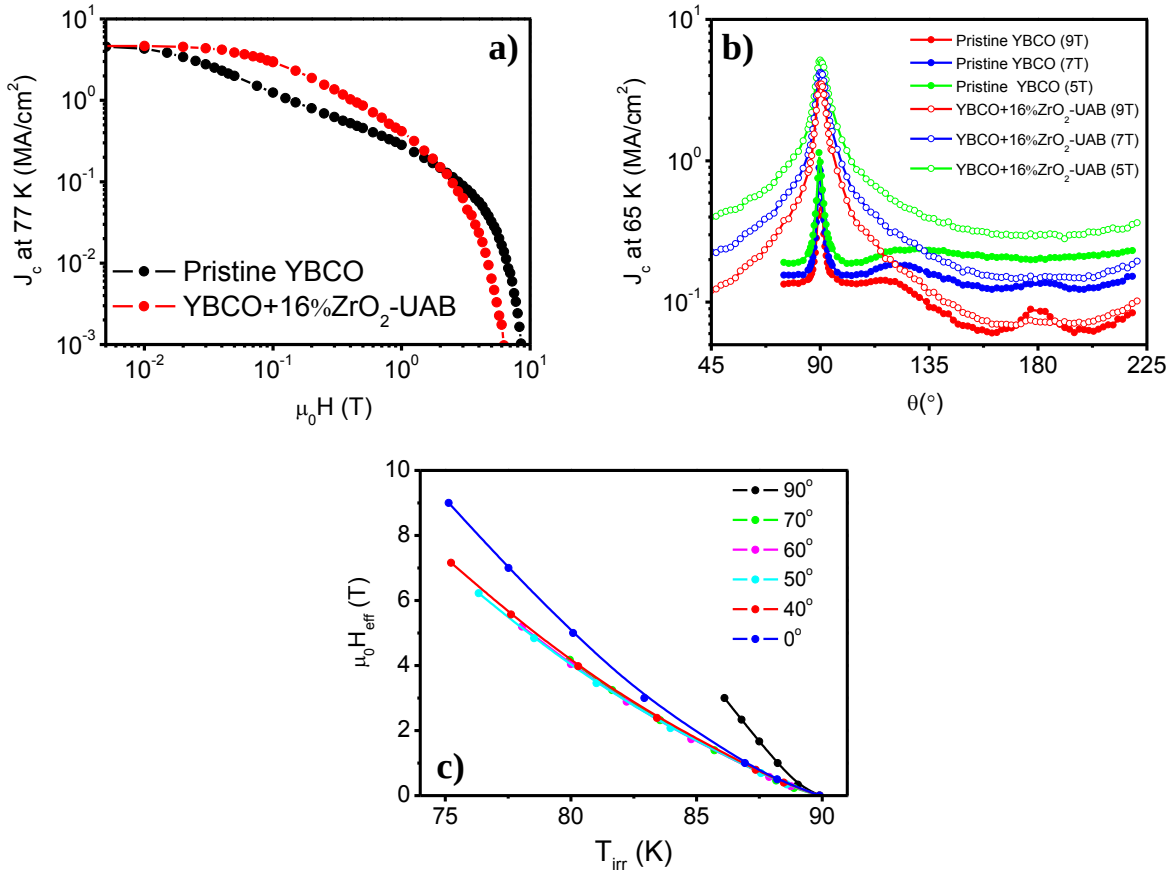

Figure 4.43. Results of the transport measurements in an YBCO+16%M ZrO_2 UAB NPs film. Graph a) shows the J_c at 77 K dependence with the magnetic field, graph b) the angular dependence of the J_c at 65 K for the YBCO+16%M ZrO_2-UAB film in comparison with a pristine YBCO film and graph c) the isotropic collapse of the irreversibility line for the nanocomposite, measured at different magnetic field orientations, with $\gamma_{eff} \sim 3$.

All the previous results demonstrate, again, the importance of controlling the initial colloidal solutions properties. The presence of aggregates could completely modify the final results. Despite that both type of NPs tend to go to the interface YBCO/LAO, they present different features. It was shown that, despite the UAB NPs tends to form big BZO cumulus in the films; they have excellent superconducting and pinning properties. On the other hand, the UG NPs, which are maintained aggregates-free in the solution, the nanocomposites show worse properties at high concentration of NPs due to the formation of a BZO layer which prevents the formation of epitaxial YBCO.

4.4.2.3 YBCO-ZrO_2 nanocomposite films with ultrathin YBCO interlayer

With the aim to further improve the quality of YBCO-ZrO_2-UG nanocomposite films and enhance their physical properties, an ultrathin pyrolyzed YBCO film is deposited on the LAO substrate prior to the nanocomposite films deposition in order to avoid the ZrO_2 NPs placement directly at the LAO surface.

To implement this strategy a 0,05M YBCO solution is used to deposit the initial pristine YBCO thin film on the LAO substrate. The pyrolysis of this diluted solution could be shorter than that used for 1,5M solutions due to its lower thickness (lower mass also). For this reason, the standard pyrolysis process is modified. When the temperature reaches 310 ºC, it automatically drops to room temperature (as fast as the furnace permits). Using this solution, 50 nm of pristine YBCO films are obtained after the growth process (100 nm after the pyrolysis process).

On top of the pyrolyzed pristine YBCO ultrathin film, YBCO+ZrO_2-UG solution with different concentrations of NPs (6, 10 and 15%M) are deposited. They are pyrolyzed using the standard pyrolysis process. At the end of the pyrolysis process, the films show excellent homogenity for all the different concentrations here studied, as it can be seen in figure 4.44.

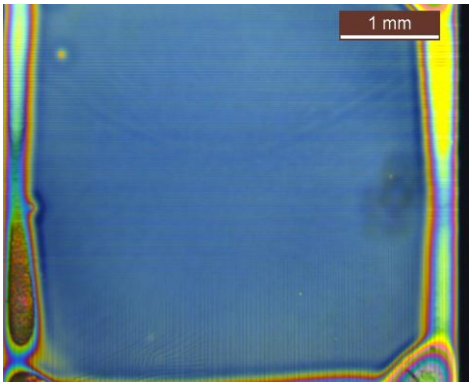

Figure 4.44. Representative optical microscope image of the YBCO+10% M ZrO_2 UG NPs pyrolyzed films on the top of the pristine YBCO interlayer.

In order to check the effectiveness of this strategy a XPS depth profile study, TEM images and EDX maps of Zr are carried out in YBCO+15%M ZrO_2-UG pyrolyzed film (figure 4.45). The evolution of the Zr content through the thickness measured with XPS using Zr(3p) core level is presented in figure 4.45 a). This plot demonstrates that the NPs are not located in the LAO surface, so the interlayer fulfills its function, at least, at this stage. Nonetheless, the NPs tend to go to the interface nancomposite/YBCO interlayer. This is confirmed by the TEM image and EDX map of Zr shown in figure 4.45 b) and c), respectively. The HAADF TEM image of the pyrolyzed film shows a brighter zone just in the interface nanocomposite/YBCO interlayer. Looking at the Zr EDX map, it is observed that the Zr is present throughout the film thickness but there is a big accumulation in the interface nanocomposite/YBCO interlayer. The thickness of this region in the interface is ~10 nm. This means that, as in the previous case, most of the NPs go to the interface forming a continuous layer of ZrO_2 (after the pyrolysis there is no BZO yet). There are also other ZrO_2 NPs embedded within the amorphous matrix. Therefore, it has been demonstrated that the YBCO interlayer prevents the disposition of the NPs on the top of the LAO.

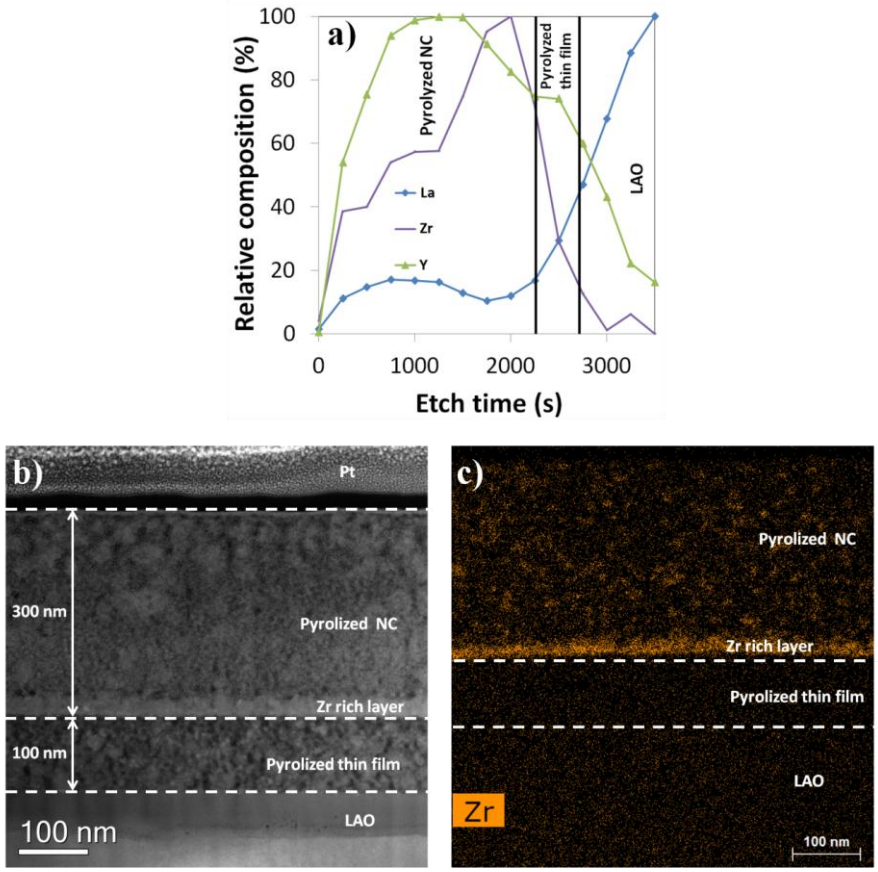

Figure 4.45. a) Depth profile XPS study, b) cross-section HAADF TEM image and c) Zr EDX map of YBCO+15%M ZrO_2-UG pyrolyzed film.

Having demonstrated that the interlayer is effective to avoid the acumulation of the NPs on the LAO surface, it is neccesary to prove that the growth of the YBCO takes place properly. From the XRD study (see figure 4.46), it is observed that epitaxial YBCO is obtained. It is also observed that, in contrast to the previous cases, both the (110)BZO and (200)BZO Bragg peaks are detected. Note that the presence of the (110)BZO ring indicates the presence of randomly oriented BZO NPs. Random fraction values are around 96%, as high as in the case of in-situ nanocomposites (chapter 3, figure 3.6). The nanostrain value, ε, is 0,22±0,01%, value which is also comparable with the in-situ BZO nanocomposites values (chapter 3, figure 3.7).

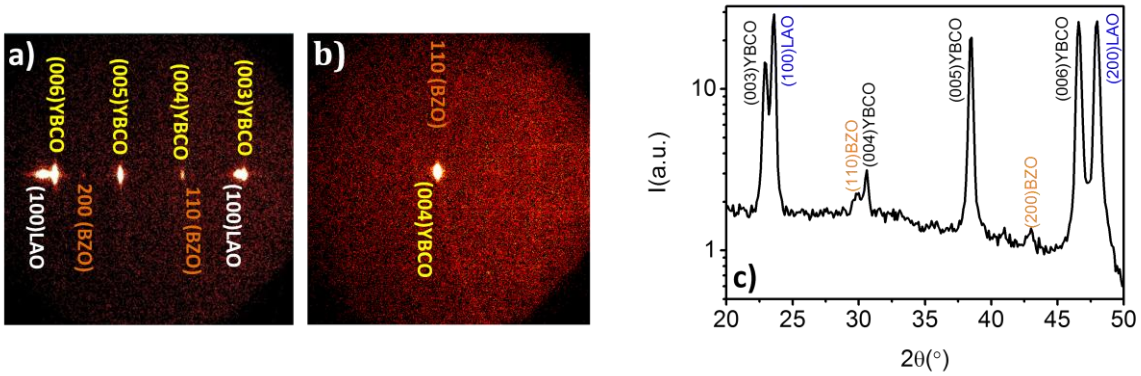

Figure 4.46. 2D XRD θ-2θ frames and integrated patterns of the YBCO+10%M ZrO_2-UG film. Image a) shows a general image of the film while image b) is focused in the region of the (110)BZO peak to get a better resolution. Finally graph c) correspond to the integrated spectrum from image a).

It is concluded that the introduction of the YBCO interlayer promotes the epitaxial growth of YBCO. In order to study the ZrO_2 distribution in the grown films, a XPS depth profile and TEM studies have been performed (figure 4.47).

The XPS study (figure 4.47 a)) show a homogeneous distribution of the Zr through the thickness of the nanocomposite film with no accumulation of Zr in the interface. Comparing it with the spectrum after pyrolysis (see figure 4.45 a)), it is clear that the distribution of Zr is completely different. This means that during the growth process it is possible to move the NPs from their initial position. Therefore, figure 4.47 a) reveals a completely different situation than before using the pristine YBCO interlayer.

From the TEM analysis it is also observed a homogenous distribution of Zr throughout the nanocomposite film. In figure 4.47 b) one can see BZO NPs distributed in the nanocomposite film with sizes ranging from 10 to 30 nm, very similar values to the BZO NPs found in the in-situ nanocomposites. This indicates that, although the NPs remain as isolated NPs in solution, during the growth process some coarsening occurs. It is also observed that no BZO NPs are detected in the interlayer demonstrating the efficiency of this strategy to avoid the NPs movement to the LAO surface. The Zr EDX map (figure 4.47 c)) also confirms the homogeneous distribution.

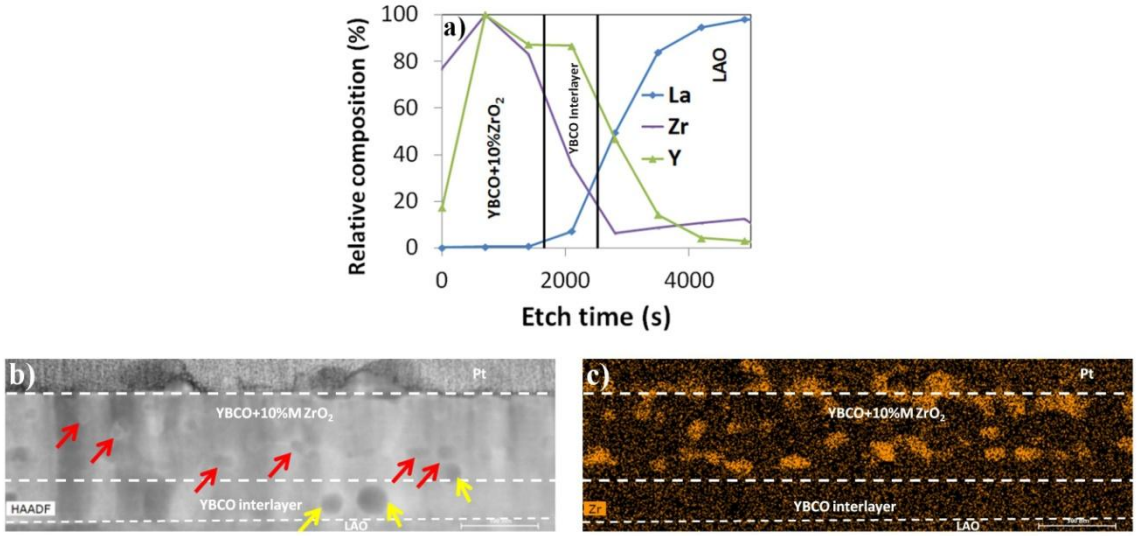

Figure 4.47. a) XPS+sputtering measurements, b) TEM image and c) Zr EDX map of YBCO+10%ZrO_2-UG grown film. Red arrows indicate the presence of BZO NPs and the yellow $Y_2Cu_2O_5$ particles.

In order to understand why the situation is different, it is necessary to take into account that in this case the BZO is formed on the top of a pristine YBCO layer. During the growth process, the BZO is formed before the nucleation of the YBCO (at 750-760 ºC). At 790 ºC, the YBCO nucleates and starts to grow. The heterogeneous nucleation of the YBCO occurs in the LAO surface and the growth front begins to move upwards. The growth front finds the NPs (in this moment the BZO NPs are still individual because there was no time to sinter and form a continuous layer), it starts to move the NPs from its initial position resulting BZO NPs homogeneously distributed in the final grown film. Although the way in which the BZO NPs are moved is not fully understood, it is suggested that it might be related to the size of the NP. After this process, the NPs are homogenously distributed favoring the epitaxial growth of the YBCO.

Further detail of the microstructure of YBCO-ZrO_2 nanocomposite films is obtained from TEM analysis. Figure 4.48 shows six different images in which BZO NPs are present. These images confirm that the sizes of the BZO NPs vary from 10 nm (NPs in

b), c) and d) images) to 30 nm (NPs in image a)) in the case of the YBCO+10M% ZrO_2-UG film. Images e) and f) show bigger NPs (up to 50 nm) for the case of YBCO+15%M ZrO_2-UG film because, in this case, the coarsening effect starts to be important[101]. It is observed the presence of SFs in images e) and f) although their density is quite low. It is also remarkable that the contrast observed in those two images indicates that both the NPs and the SFs are distorting the YBCO structure (the contrast on LAADF images comes from the strain) causing the observed ε increment.

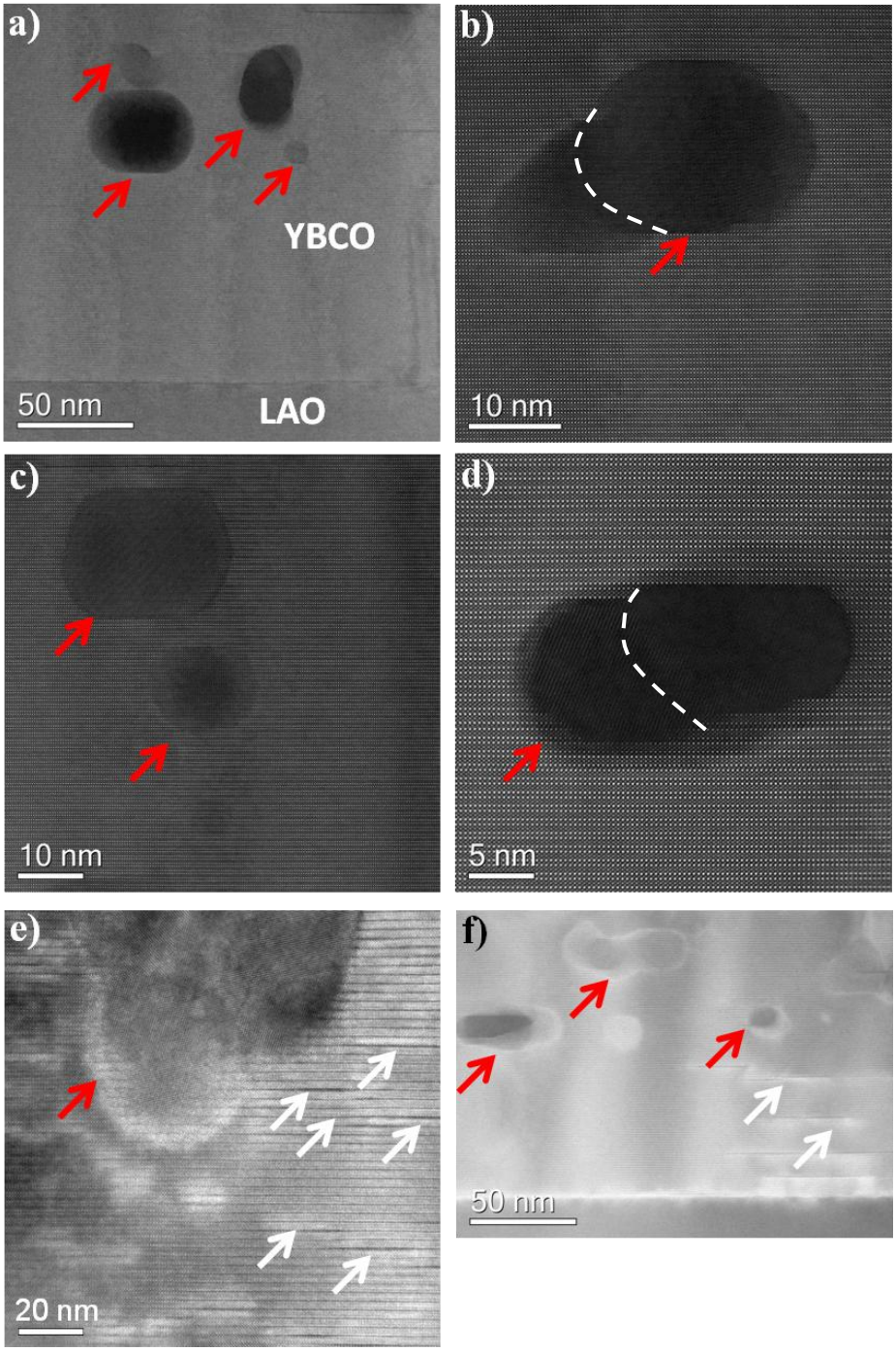

Figure 4.48. TEM images of YBCO+10%M ZrO_2-UG and YBCO+15%M ZrO_2-UG films. Red arrows indicate the presence of BZO NPs and withe arrows the presence of SFs. Images a), b), c) and d) were taken in HAADF mode and corresponds to a YBCO+10%M ZrO_2-UG NPs film and the images e) and f), obtained in the LAADF mode, to a YBCO+15%M ZrO_2-UG NPs film.

Up to know it has been observed that the introduction of the pristine YBCO interlayer improves the quality of the films and allows a homogeneous distribution of small BZO NPs.

Figure 4.49 shows the T_c and J_c^{sf} at 77 K values for the YBCO+ZrO_2-UG nanocomposites showing that the improvement of the crystalline quality of the films is reflected in a great improvement of the superconducting properties. The T_c remains constant around 90 K for all the studied concentrations. In the case of the J_c^{sf} at 77 K, the highest value (4,7 MA/cm^2) is reached for a 10%M of ZrO_2 NPs. It is observed that for a 15%M of ZrO_2 NPs, the J_c^{sf} at 77 K value decreases until 3,2 MA/cm^2. This is attributed to an excessive coarsening of NPs that, as in the case of the in-situ BZO or BYTO nanocomposites[97, 101], act as "current blockers" preventing a free current percolation.

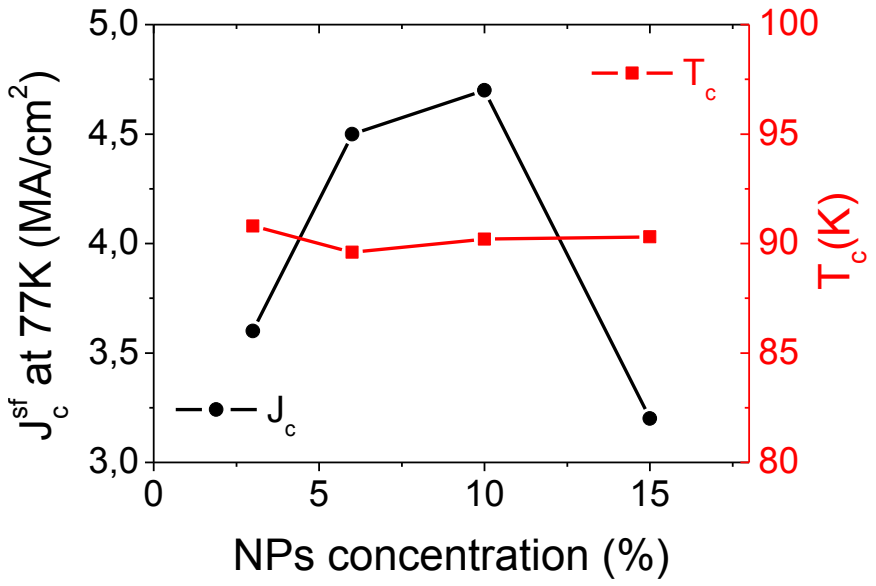

Figure 4.49. SQUID measurements of T_c and J_c^{sf} at 77 K values of ZrO_2-UG nanocomposites with different concentrations of NPs.

Transport measurements were carried out in the YBCO+ZrO_2-UG films in order to obtain detailed analysis of the pinning properties of these films. These measurements were done in films with the three different concentrations studied: 6%, 10% and 15%M. Figure 4.50 shows the results.

First of all, looking at figure 4.50 a) it is confirmed that the 10%M ZrO_2 films give the best J_c^{sf} at 77 K value, in agreement with the above measurements, reaching values of 5 MA/cm^2. This value is better than those obtained for the 6%M and 15%M of ZrO_2-UG NPs. It is also better than in the case of 16%M ZrO_2-UAB NPs (4,5 MA/cm^2) and the 8%M CeO_2 2 nm NPs in HDEC (2 MA/cm^2). The same figure shows that the YBCO+10%M ZrO_2-UG NPs film present almost the same behavior as the in-situ nanocomposite films (better J_c^{sf} at 77 K and similar behavior at intermediate fields and high fields). These results show that the YBCO+10%M ZrO_2-UG NPs can compete with the performances of the in-situ nanocomposites at 77 K.

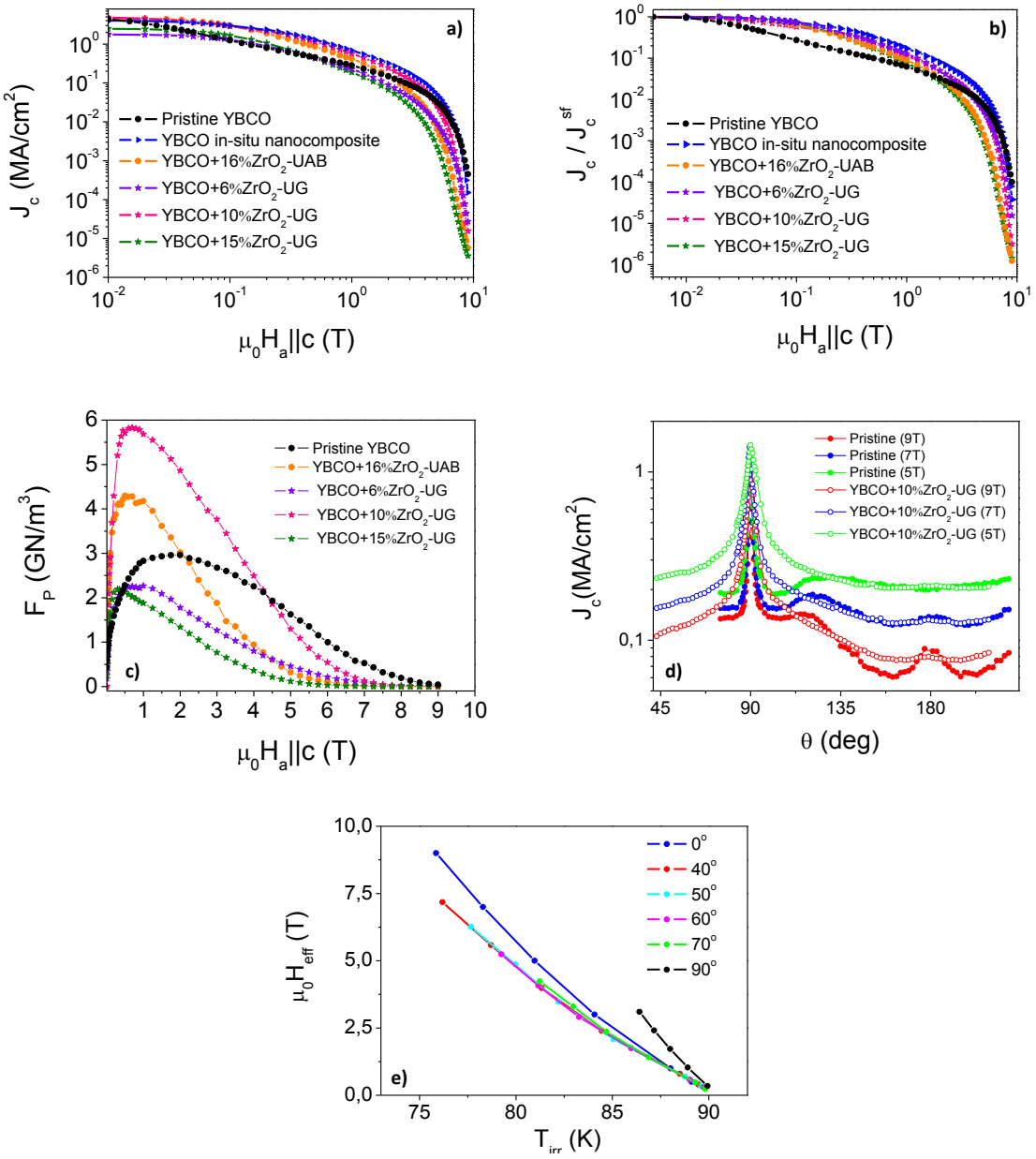

Figure 4.50. Results of the transport measurements analysis on the YBCO+ZrO_2 UG NPs films with different concentration of NPs in comparison with the previous YBCO+16%M ZrO_2-UAB NPs showing a) the J_c at 77 K dependence with magnetic field, b) J_c/J_c^{sf} dependence with the magnetic field, c) Pinning force with the magnetic field, d) the angular dependence of the J_c at 65 K for the YBCO+10%M ZrO_2 UG NPs film in comparison with a pristine YBCO film and e) the isotropic collapse of the irreversibility line for the YBCO+10%M ZrO_2 UG NPs, measured at different magnetic field orientations, with $\gamma_{eff} \sim 2{,}9$.

The evolution of the J_c/J_c^{sf} at 77 K with the magnetic field (figure 4.50 b)) stands out the differences that still are between the ex-situ and the in-situ nanocomposite films. The ex-situ films clearly shows H* values much lower than the in-situ nanocomposite films. From all the ex-situ nanocomposite films studied in this thesis, the highest performances at 77 K are observed for the YBCO+10%M ZrO_2-UG NPs film. The YBCO+16%M ZrO_2-UAB NPs shows similar behavior at low fields but, from ~0,3 T, the YBCO+10%M ZrO_2-UG NPs film clearly shows better performances. The pinning force

evolution with the magnetic field that is showed in figure 4.50 c) indicates that, once again, the YBCO+10%M ZrO_2-UG NPs film has the best performances.

Until now, it was shown that the YBCO+10%M ZrO_2-UG NPs films present the best performances at 77 K. However, this situation changes at lower temperatures. Figure 4.50 d) shows the angular dependence of the J_c at 65 K for the YBCO+10%M ZrO_2-UG NPs film in comparison with a pristine YBCO film. In this case, it is possible to see that the values for the nanocomposite films are similar to the pristine YBCO films. These values are much lower than in the case of the shown in figure 4.43 b). In this case, the peak at 90º associated with the SFs effect is much narrower. This is due to the lower density of SFs that these UG NPs films present that also could explain why the drop of the J_c at high fields observed in figure 4.50 a) occurs at higher fields than in the YBCO+16%M ZrO_2 UAB NPs films (if the density of SFs is low, the coherence of the twin boundaries is maintained acting as pinning centers at high fields at it was explained in chapter 3).

Finally, figure 4.50 e) presents the isotropic collapse of the irreversibility line for the YBCO+10%M ZrO_2-UG NPs, measured at different magnetic field orientations, with $\gamma_{eff} \sim 2{,}9$ which is a typical value for the in-situ nanocomposites. This value is very similar to that obtained for YBCO+16%M ZrO_2-UAB NPs.

4.4.3 Pinning performances in CeO_2 and ZrO_2 nanocomposite films

As it was mentioned in the introduction and in chapter 3, the pinning mechanism in CSD in-situ nanocomposites, first time proposed by the SUMAN group, is based on the effect of the SFs. The SFs are created in the surrounding of the NPs. In the ends of the SFs strained regions appear preventing the Cooper pair formation due to tensile strain. These nano-sized regions act as pinning centers[97]. This mechanism was used in chapter 3 to explain the consequences to change the SF scenario obtaining satisfactory results.

However, this is the first time that the pinning behavior of ex-situ nanocomposite films is studied. The advances that are exposed in this chapter regarding the processing of ex-situ nanocomposites, have allowed the achievement of films with sufficient quality to understand how the different microstructure found in each type ex-situ nanocomposite films affects the pinning performances. The results show that two different situations were found depending on the NPs used.

For YBCO nanocomposites with UAB NPs, there are agglomerates of NPs already in solution according to DLS measurements. These big agglomerations are present, after the growth process, in the YBCO matrix in form of big BCO or BZO particles. These big particles act as "current blockers" disturbing the current flow, providing inhomogeneity to the films and preventing higher values of J_c. They cause the appearance of long SFs that, as it was mentioned in chapter 4, are not as effective as the short SFs to improve the pinning properties. So, in this case, it is possible to say that what is being measured is a pristine YBCO film with big BCO or BZO particles acting as unreacted phases and full of long SFs. This is confirmed by the results of transport measurements: the J_c^{sf} at 77 K values are the same as in a pristine YBCO film. The difference in the J_c dependence with the magnetic field with respect to the pristine YBCO films can be attributed to the presence of high density of long SFs. The presence of the SFs also causes the increase of the nanostrain value reaching values of 0,18±0,01% in the case of YBCO+8%M CeO_2 NPs films and 0,23±0,01% in the case of YBCO+16%M ZrO_2 NPs So, in this case, the pinning mechanism will be similar than in the in-situ nanocomposites and attributed to the SFs

effect. The fact that these films do not reach the same performances as in the in-situ nanocomposites is because of the presence of big agglomerates.

For YBCO nanocomposites with UG NPs films, it was demonstrated that the NPs remains isolated until the growth process. The fact that these NPs tend to agglomerate in the interface YBCO/LAO preventing the epitaxial growth of the YBCO (the YBCO nucleate on the top of the BZO layer that is formed) made necessary to add a pristine YBCO interlayer. The films with the interlayer present epitaxial YBCO and homogeneous distribution of NPs, but still coarsening is detected. The distribution and size of these NPs is very similar to the in-situ nanocomposites scenario. These films showed excellent performances at 77 K, showing features that can even compete with the in-situ nanocomposites. However, at low temperatures, their properties decay below the YBCO nanocomposites using UAB NPs because lower density of SFs is detected. As it could be observed in the TEM images of UG NPs films, there are SFs but the amount of them is quite low compared with the UAB NPs films. This is responsible that the width of the peak at 90 º, in the $J_c(\theta)$ dependence, was narrower in the first case. The reason why the amount of SFs is lower in this case is under study.

It is known that most of the NPs are randomly oriented because it was shown that the random fraction is about 96% in these films. Therefore, they will cause distortion of the YBCO matrix in their surroundings, as it was observed in the TEM/LAADF images, and create interfacial energy. However, this interfacial energy, in this case, is not completely released by forming SFs. It is suggested that in this case the interfacial energy is not as high as in the case of the in-situ nanocomposites. The fact that the NPs already formed with defined crystalline structure are embedded in the YBCO matrix may facilitate the YBCO accommodation to them.

The differences between the ZrO_2-UG NPs ex-situ films and in-situ nanocomposite films properties are still significant, specially looking at the J_c/J_c^{sf} dependence with the magnetic field curves. These differences can be attributed to the lower amount of SFs which cause a lower number of pinning centers and, therefore, a decay in the performances with the magnetic field is observed.

4.5 Summary

From the study of this wide variety of compositions of ex-situ YBCO nanocomposites it is possible to identify a methodology of general validity to prepare epitaxial nanocomposite films using colloidal solutions, see figure 4.54. The green boxes indicate the correct path while the red arrows mean that, if this phenomenon is observed, one have to go back and change something of the process. Therefore, based on this scheme, the important parameters to succeed in the preparation of ex-situ YBCO nanocomposite are: to obtain stable NP solution with no aggregates that could lead to homogenous films after pyrolysis. Then, in the growth process, it is important to avoid reactivity and coarsening and achieve a homogeneous distribution of the NP embedded in the YBCO matrix (trapping).

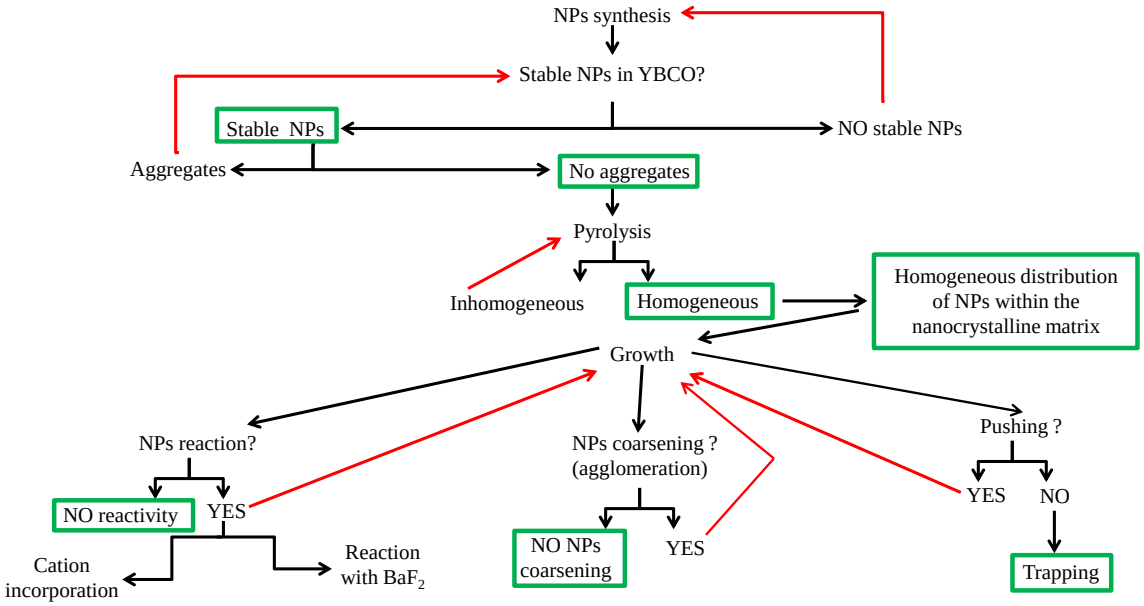

Figure 4.54. Ex-situ route pathway to achieve high quality nanocomposites thin films.

The properties of the obtained films can reach the T_c values of 90 K and J_c^{sf} at 77 K of 5 MA/cm^2 as in the case of YBCO+10%M ZrO_2–UG NPs films. The pinning performances are improved with respect to the pristine YBCO films and show potential to compete with the performances of the in-situ nanocomposites. The presence of randomly oriented NPs in these ex-situ nanocomposites, specially in the YBCO+ ZrO_2–UG NPs films (10%M), cause the increase of the incoherent interface and the generation of SFs that allow the increase of the nanostrain values that are in the range of the in-situ nanocomposites values (0,22-0,24%). Figure 4.55 shows that the nanostrain-incoherent interface dependence found in the in-situ nanocomposites is also followed by the ex-situ nanocomposites

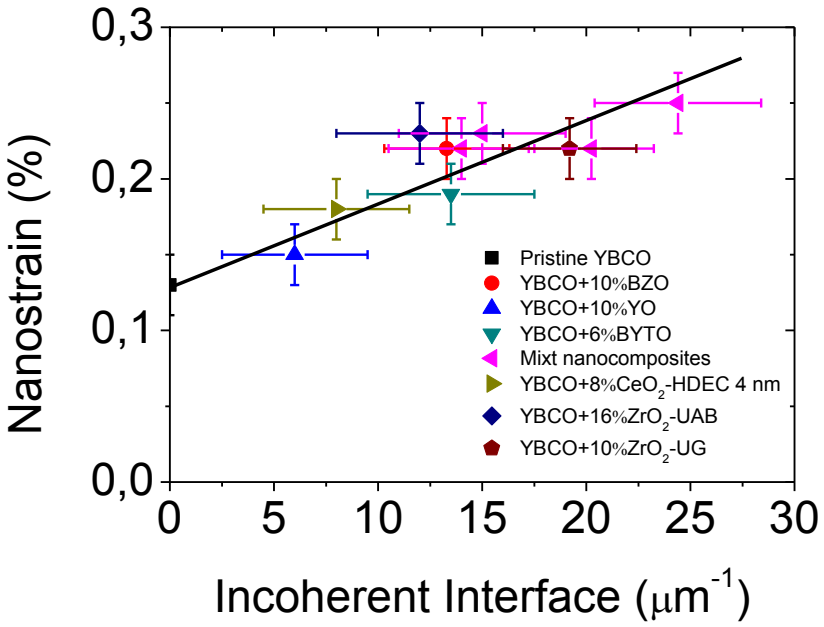

Figure 3.10 Dependence of the YBCO vertical nanostrain on the incoherent interface of NPs in the different in-situ (BZO, YO, BYTO and mixt) and ex-situ (CeO_2, ZrO_2-UAB and ZrO_2-UG NPs) nanocomposites

4.6 Conclusions

Throughout this chapter the first advances in the preparation of ex-situ nanocomposite thin films were exposed. It was shown that this is not an easy route as many parameters have to be kept under tight control. From the NPs synthesis to the growth process, there are many details that can make the difference between good and poor performances. Despite all the difficulties that were faced, first ex-situ nanocomposites epitaxial thin films showing competitive performances were achieved.

This chapter had two different parts: magnetic NPs (CFO) and non-magnetic NPs (CeO_2 and ZrO_2). The first part was mainly devoted to study the structural and magnetic properties of CFO NPs in powder under different thermal treatments and compared with the properties of the YBCO+CFO NPs nanocomposite films. This study was complemented with magnetic dichroism measurements carried out at ALBA synchrotron. The second part was devoted to the non-magnetic NPs (CeO_2 and ZrO_2). The influence of the ligand agent, the importance of the NPs size and the consequences of having aggregate or individual NPs on the YBCO nanocomposite properties have been investigated.

All this work has allowed the achievement of important conclusions:

- This work has evidenced for the first time that the use of colloidal solutions of oxide nanoparticles can lead to high quality epitaxial YBCO nanocomposite films. The properties of the NPs in the colloidal solution are critical for the final properties of the films. DLS measurements are very important to identify the NPs size and aggregation. If the NPs are aggregated in the solution, big particles will be found in the grown films. However, a small NPs size in DLS measurements is necessary but not sufficient to achieve the desired distribution and NPs size in the final YBCO film because other phenomena as NPs coarsening can occur during the thermal process resulting in a big NPs size.
- CFO NPs in powder maintain their magnetic properties under the YBCO processing conditions. It was observed that the pyrolysis process degrade the NPs surface causing a decrease of the saturation magnetization but, during the growth process, the surface is reconstructed by a reoxygenation process. Magnetic dichroism measurements of the CFO in powder suggested the presence of the spinel structure after the all the different thermal processes of the YBCO processing.
- YBCO-CFO nanocomposites are epitaxial with the presence of some of a-b grains. It was also identified a great reactivity between the CFO and the BaF_2 forming a double perovskite structure ($(YBa(Fe/Co)_2O_5$). The presence of the initial CFO NPs could not be detected even reducing the annealing time and, therefore, a drastic degradation of the magnetic properties was detected. It was also observed that in this kind of nanocomposite films the superconducting properties, specially the T_c, were dramatically reduced as compared with pristine YBCO films due to the incorporation of Fe and/or Co atoms to the YBCO structure.
- Epitaxial films were obtained when incorporated CeO_2 and ZrO_2 NPs. In these cases, the CeO_2 NPs tend to react with the BaF_2 to form BCO and also the ZrO_2 to form BZO. The simplest way to avoid this effect could be to synthesized directly BCO or BZO NPs.
- The ligand use to synthesize the NPs can determine the homogeneity of the pyrolyzed film. The use of TREG favors the formation of inhomogeneous films. The TREG present a great tendency to place in the top surface of the film and it drags the NPs to the upper part of the film after the deposition and pyrolysis process. This problem was

overcome by performing a ligand exchange process with the use of HDEC as the exchanged ligand.

- It was also demonstrated that the NPs size plays a key role during the growth process as it determines the pushing/trapping effect. It was proved that the use of 2 nm CeO_2 NPs leads to pushing effect (NPs in the surface of the films) while the use of the 4 nm NPs allows the trapping effect. The use of 4 nm CeO_2 NPs resulted in epitaxial YBCO films with higher nanostrain values (0,19±0,01%) as compared to pristine YBCO films. The improvement of the superconducting properties should be achieved by reducing the agglomerates in the initial solution.
- For ZrO_2 NPs, it was shown how the presence of aggregates can vary the YBCO growth tendency and the films features. Big aggregates in solution cause big particles in the films that will damage the films performances. Individual NPs makes necessary (at least in the case of ZrO_2 NPs) the use of a pristine YBCO interlayer to allow the epitaxial growth of YBCO. These films offer excellent superconducting properties. In particular, showed a T_c~90 K and a J_c~5 MA/cm^2 with a reduction of the γ_{eff} to similar values (~3) than in the in-situ nanocomposites. These properties make the YBCO+10%M ZrO_2-UG NPs films very competitive with the in-situ nanocomposites.

5

Oxygen Diffusion In YBCO Films: Surface Role

In all the previous chapters, it was commented the importance of achieving epitaxial YBCO to obtain films with good performances. The optimization of the processing parameters is crucial to achieve this objective and many research works during the last 20 years were devoted to these studies. However, the optimization of the YBCO and, in general, of all the functional oxides, does not end here. It is required a further research about the oxygen incorporation into the structure. And this study is indispensable because, as it was mentioned in chapter 1, the superconducting properties will depend on the oxygen content of the films.

The study of the oxygen role in the YBCO films can be divided in two parts: the kinetics of the oxygen incorporation to the YBCO structure, i.e., the oxygen diffusion process in YBCO films, and the analysis of how the oxygen content affects the physical and structural al properties of the YBCO films. The chapter covers these two parts.

The detailed analysis of the oxygen diffusion in YBCO that has been performed will be presented. The study of the oxygen diffusion is essential in order to find the optimal conditions for the oxygenation. The diffusion dependence with different YBCO processing parameters will be exposed. There are many reports in the literature about oxygen diffusion in YBCO but most of them focus on the bulk/volume oxygen diffusion. However, in this case, a different approach will be used. The role of the surface reactions in the oxygen diffusion will be discussed.

A different part of this chapter will be devoted to how the thickness of YBCO films and, therefore, the changes in the microstructure affect the oxygen diffusion. This study

includes a detailed analysis of the observed changes in the kinetics of the oxygen diffusion in YBCO films with different thicknesses. The thickness determines the strain (nanostrain/mesostrain) of the films, so the results are correlated with this parameter. The effect of the thickness on the oxygen content of the films will be also discussed. It will be shown how the thickness and, therefore, the strain and the microstructure could affect the final properties of the films. To do that, films of different thicknesses were exposed to the same oxygenation process in order to compare how the c-parameter and the physical properties evolve with the thickness

Another part of the chapter will be devoted to the role of the silver additions to the YBCO. It was demonstrated that the silver addition (mainly in the surface) in other materials have a catalytic effect favoring the oxygen diffusion. But this was not proved in YBCO thin films up to now. First results about how the silver presence modifies the oxygen diffusion in YBCO will be exposed. It was investigated which is the effect of silver when it is introduced in solution in form of precursor salt.

Finally, it was mentioned in previous chapters the importance of the nanocomposites in the field of superconductivity because of their properties, specially, at high magnetic fields. However, there are no studies about the oxygenation process in this kind of films. In this chapter, it will be introduced some results about how the oxygen diffusion process in YBCO+10%M BZO films is performed.

5.1 Introduction

The problem of the oxygen transfer from the gas phase to the crystalline structure of oxides is a complex phenomenon that has been widely investigated recently in the context of many applications such as fuel cells, resistive switching phenomenon, catalysis, etc. These studies have deeply advanced in the analysis of the problem and they become very useful in the analysis of YBCO films behavior.

The oxygenation process in HTS is crucial since it defines their final superconducting properties. In the particular case of YBCO, its structure is not fixed and it depends on the amount of oxygen in the Cu-O chains. The oxygen content in these chains will determine the amount of carrier doping because the content of oxygen establishes the value of δ in the unit formula $YBa_2Cu_3O_{6+\delta}$. The oxygen content in these chains will define if the structure is tetragonal where the material behaves as an insulator or orthorhombic where a metallic state is obtained leading to the superconducting behavior.

One important issue is that, before entering into the YBCO structure the oxygen has first to become trapped into the solid from the gas phase (O_2) and then diffuse within the crystalline structure in form of O^{2-} ions to fill the vacancies existing in the structure. These phenomena are not trivial events and, therefore, understanding which are the limiting factors for a correct oxygenation process is very challenging. This process can be studied experimentally as a macroscopic effect using different techniques. To understand the oxygen diffusion process is, therefore, the first step to comprehend how the oxygenation process can be carried out.

5.1.1 Structural changes in YBCO during oxygenation process: oxygen disposition in Cu-O chains

As it was mentioned in the introduction, once the oxygen enters into the YBCO structure, it is placed in the Cu-O chains where many vacancies exist. As oxygen is introduced in the Cu-O chains, the disposition of O atoms gradually changes. When no oxygen is present in the chains, the YBCO has a tetragonal structure and it behaves as an insulator. This structure is maintained until a value of δ about 0,3-0,35 in which the transition from the tetragonal structure to the orthorhombic structure occurs[249]. In the range of $0<\delta<0,35$ the oxygen is placed randomly in their sites in the Cu-O chains.

As the oxygen content is increased and $\delta>0,35$ the structure becomes orthorhombic and the oxygen atoms are placed periodically in the Cu-O chains forming superstructures (different arrangements of oxygen atoms in the Cu-O chains which extend into multiple unit cells) which have different periodicities along the a-axis[249]. Kinetic effects may preclude the formation of such type of oxygen ordered structures. De Fontaine et al proposed an equilibrium phase diagram in which it is possible to know the superstructure which is present in the system depending on the oxygen content[250].

5.1.2 Superconducting properties dependence with the oxygen content

As it was just discussed, the oxygen content in the YBCO will determine the structure and, therefore, its insulating or superconducting behavior. The dependence of T_c with oxygen content can be observed in figure 5.1 a)[251]. For δ (in figure 5.1 $\delta=x$) values below 0,35 the structure is tetragonal, so the YBCO behaves as an insulator and then the T_c is zero. For δ values above 0,35, orthorhombic structure is present and the T_c starts to increase with the enhancement of the oxygen content. This tendency is maintained until $\delta=0,92$ in which the T_c reaches a maximum of 94,3 K. In these conditions, it was proposed that there is an OIV superstructure extended to 3-6 YBCO unit cells[252]. For $\delta>0,92$ the T_c decreases again.

In the view of this behavior, it is possible to define three different regimes for the superconducting phase. The first one is called underdoped regime and it happens when $\delta<0,92$. In this regime, the oxygen content is not enough to reach the highest value of T_c. The optimum regime or the optimum oxygen doping is the second regime. It is reached when $\delta=0,92$. Here the T_c reaches its maximum value. The last one is called overdoped regime and it occurs when $\delta>0,92$. In this regime the T_c decreases again until 89 K approximately, for $YBa_2Cu_3O_7$[251].

The changes in the T_c as a function of the oxygen content are a consequence of the alterations that the oxygen atoms cause in the structure. In figure 5.1 b) it is presented the evolution of the T_c with the YBCO c-parameter. It can be observed that T_c increases as the c-parameter decreases. This happens until c=1,1695 nm approximately where T_c reaches the maximum of 94,3 K. Then, the T_c starts to decrease as the c-parameter continues to decrease[251].

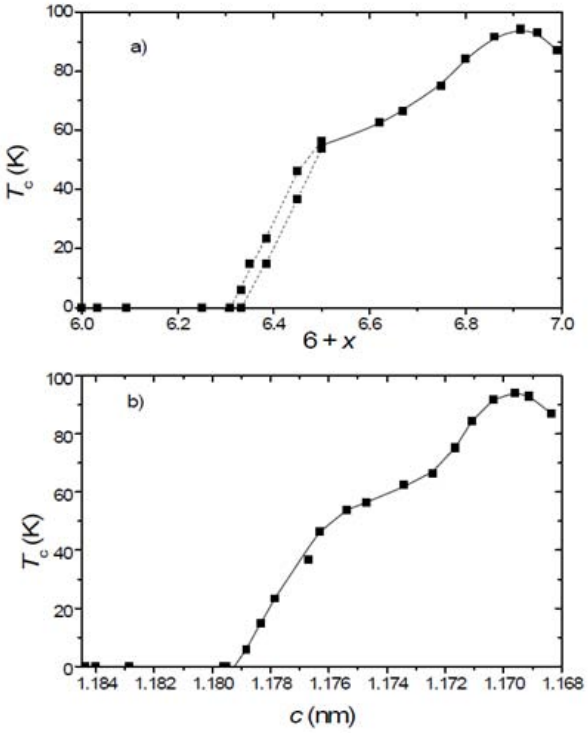

Figure 5.1. T_c evolution in YBCO as a function of a) oxygen content and b) c-parameter[251].

The alteration of the c-parameter that the oxygen content induces in YBCO is due to the change in the distance between Cu(1) and O(4) (apical oxygen) atoms caused by the oxygen atoms in Cu-O chains (figure 5.2).

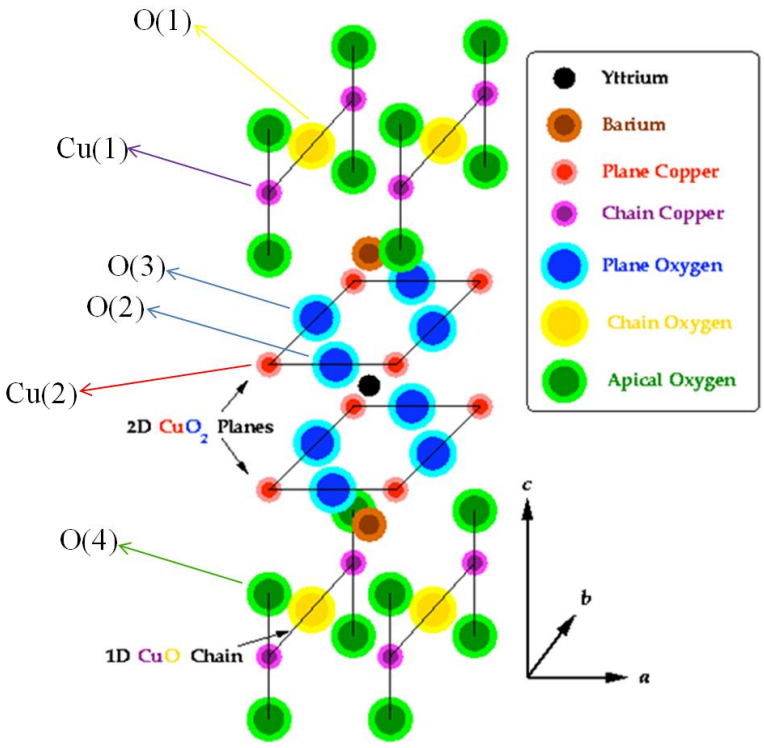

Figure 5.2. $YBa_2Cu_3O_7$ orthorhombic structure. The different oxygen and copper atoms are marked.

This produces changes in T_c since the carrier concentration in YBCO is controlled by changing the oxygen content that causes the movement of apical oxygen, O(4). Apical oxygen between the CuO_2 plane and the Cu–O chain is known to play an important role in the hole distribution between the two layers[253]. T_c decreases systematically if oxygen deficiency occurs. This happens because oxygen deficiency induces a shortening of the Cu(1)–O(4) bond length and, consequently, displacing the O(4) away from the CuO_2 plane impeding the hole transfer from the plane to the chain[254].

5.1.3 Oxygen diffusion in YBCO

The diffusion of oxygen, the mechanism by which oxygen atoms are incorporated into the YBCO structure, has been extensively studied. Oxygen diffusion in YBCO was analyzed using different techniques such as secondary ion mass spectrometry[255, 256], oxygen tracer[257], thermogravimetry[258], spectroscopic ellipsometry[259] or in-situ resistivity[260-266], The results from all the techniques showed that knowledge and control of the diffusion process is crucial in order to obtain good performances in YBCO samples.

Oxygen diffusion through YBCO is governed, as all the bulk diffusion processes, by Fick´s Laws (Eqs. 5-1 and 5-2):

$$\mathbf{j} = -\left(\mathbf{D_x}\frac{\partial \mathbf{C}}{\partial \mathbf{x}} + \mathbf{D_y}\frac{\partial \mathbf{C}}{\partial \mathbf{y}} + \mathbf{D_z}\frac{\partial \mathbf{C}}{\partial \mathbf{z}}\right) \qquad \text{Eq. 5-1}$$

$$\nabla \mathbf{j} = \frac{\partial \mathbf{C}}{\partial \mathbf{t}} = \mathbf{D_x}\frac{\partial^2 \mathbf{C}}{\partial \mathbf{x^2}} + \mathbf{D_y}\frac{\partial^2 \mathbf{C}}{\partial \mathbf{y^2}} + \mathbf{D_z}\frac{\partial^2 \mathbf{C}}{\partial \mathbf{z^2}}) \qquad \text{Eq. 5-2}$$

where j is the rate of mass transfer per cross-sectional area, C is the concentration of diffusing species, D is the diffusion coefficient and x, y and z are the distances travelled by the species in each direction (considering a unit cell, x=a, b=y and c=z).

Equation 5-1 is the first Fick´s law and it affirms that the rate of mass transfer per cross-sectional area is proportional to the concentration gradient. It describes the effect of a concentration potential gradient of one type of particle present in a particular media. Equation 5-2 is the seconds Fick´s law and it predicts how diffusion causes the concentration to change with time.

In the particular case of oxygen diffusion in YBCO, the diffusion coefficient is very anisotropic. In the c-axis direction the diffusion coefficient, D_c, is 10^4-10^6 smaller than along the a-axis or b-axis direction. Also, there is a difference between D_a and D_b since $D_b \approx 100 D_a$. This suggests that the diffusion may take place parallel to the Cu-O chains which are along the b-axis direction[257].

According to these assumptions, it is possible to transform, with great accuracy, the second Fick´s law into (Eq. 5-3):

$$\frac{\partial \mathbf{C}}{\partial \mathbf{t}} = \mathbf{D_{ab}}\left(\frac{\partial^2 \mathbf{C}}{\partial \mathbf{x^2}} + \frac{\partial^2 \mathbf{C}}{\partial \mathbf{y^2}}\right) \qquad \text{Eq. 5-3}$$

where D_{ab} is the mean value of the diffusion coefficient in the ab-plane which is taken, as an approximation, to be very similar in each direction of the plane.

It is possible to derive an expression for the concentration along one direction considering a one dimensional case (Eq. 5-4):

$$\mathbf{C_x(t,x) = \frac{4C_0}{\pi}\sum_{n=0}^{\infty}\frac{1}{2n+1}e^{-[\left(\frac{2n+1}{L}\right)\pi]^2} \times \sin\left(\frac{(2n+1)\pi}{L}x\right)} \quad \text{Eq. 5-4}$$

where C_0 is the initial concentration and L is the linear dimension of the average single-crystalline grain in the sample (the centre of the grains is located at L/2).

Integrating equation 5-4 from x=0 to x=L, it is obtained (Eq. 5-5):

$$\mathbf{C_x(t) = \frac{8C_0}{\pi^2}\sum_{n=0}^{\infty}\frac{1}{(2n+1)^2}e^{-[\left(\frac{2n+1}{L}\right)\pi]^2}} \quad \text{Eq. 5-5}$$

It is possible to simplify equation 5-5 considering long times ($t>t^*=0{,}044(L^2/D_{ab})$) because, in this case, only the first term of the infinite sum can be considered with an error lower than 1%. In this case equation 5-5 becomes (Eq. 5-6):

$$\mathbf{C_x(t) = \frac{8C_0}{\pi^2}e^{-\left(\frac{\pi^2 D_{ab}}{L^2}\right)t}} \quad \text{Eq. 5-6}$$

This is the solution in one dimension. But Eq. 5-3 is a two dimensional equation. To solve it, it is necessary to extract the expression for the concentration in the other direction. However, the initial assumption is that both directions have the same behavior. Therefore, the solution in y direction is (Eq. 5-7):

$$\mathbf{C_y(t) = \frac{8C_0}{\pi^2}e^{-\left(\frac{\pi^2 D_{ab}}{L^2}\right)t}} \quad \text{Eq. 5-7}$$

So, in conclusion, the solution for the two-dimensional diffusion equation 5-3 is (Eq. 5-8):

$$\mathbf{C_{xy} = C_x(t)C_y(t) = \frac{64{C_0}^2}{\pi^4}e^{-\left(\frac{t}{\tau_{ab}}\right)}} \quad \text{Eq. 5-8}$$

where $\tau_{ab} = \frac{L^2}{2\pi D_{ab}}$ is the diffusion relaxation time.

According to equation 5-8, the expected behavior of the oxygen concentration over time in YBCO is exponential both for the in-diffusion (introducing oxygen in the YBCO) and the out-diffusion (extracting the oxygen from inside the YBCO) because it will depend only on the concentration gradient no matter the direction. During many years, the oxygen diffusion in YBCO films was only interpreted as bulk diffusion process using Fick´s laws. Many different studies were devoted to comprehend how the oxygen goes in and out from the YBCO structure forgetting the surface phenomena.

5.1.3.1 In-situ resistance measurements

In this thesis, the oxygen diffusion phenomenon in YBCO was study by using in-situ resistance measurements (chapter 2 to see details about the equipment). The oxygen

concentration variations that are modeled with the second Fick´s law according to Eq. 5-8, can be related with resistivity values by Eq. 5-9 (assuming proportionality between small changes of concentration and resistivity)[267]:

$$\frac{\rho(t)-\rho_\infty}{\rho_0-\rho_\infty} \propto e^{-\left(\frac{t}{\tau_{ab}}\right)} \quad \text{Eq. 5-9}$$

where ρ_0 is initial resistivity, ρ_∞ is the saturation resistivity (when $t\rightarrow\infty$) and τ_{ab} the diffusion relaxation time.

In the literature is quite common that people use another expression which is nothing more than Eq.5-9 solved for $\rho(t)$ and normalized (Eq. 5-10):

$$\rho(t) \propto 1 - e^{-\left(\frac{t}{\tau_{ab}}\right)} \quad \text{Eq. 5-10}$$

Focusing in Eq. 5-9, it implies that, in terms of resistivity, the evolution of the diffusion processes is also governed by an exponential law which depends on the diffusion relaxation time. The diffusion relaxation time (τ_{ab}) is an important parameter related with the rate at which the oxygen is inserted or taken out from the structure. Large values of τ_{ab} imply a long time to insert or take out the oxygen from the YBCO structure and vice-versa. The values of τ_{ab} can be obtained by transforming Eq. 5-9 using natural logarithms (Eq. 5-11):

$$\ln\left(\frac{\rho(t)-\rho_\infty}{\rho_0-\rho_\infty}\right) \propto -\left(\frac{t}{\tau_{ab}}\right) \quad \text{Eq. 5-11}$$

By representing the left term of Eq. 5-11 as a function of time, a straight line is obtained. The slope of this line is $-(1/\tau_{ab})$. In this way, it is possible to obtain the diffusion relaxation time for a certain set of parameters.

Considering the oxygen diffusion as a thermally activated process, the temperature dependence of the diffusion relaxation time is expected to be given by an Arrhenius equation (Eq. 5-12):

$$\tau_{ab} = \tau_0 e^{\left(\frac{E_a}{K_B T}\right)} \quad \text{Eq. 5-12}$$

where E_a is the energy activation of the process, K_B is the Boltzmann´s constant and τ_0 is the frequency factor.

Knowing Eq. 5-12, it is possible to obtain the activation energy, E_a, of the process by calculating the τ_{ab} (τ from now) at different temperatures. Then, by plotting $\mathrm{Ln}(\tau_{ab})$ vs. $1/T$ a straight line is obtained. The slope of this line is E_a/K_B.

It is important to note that with the used setup, resistances are being measured instead of resistivity. The impossibility to change the connections configuration impedes measurements in Van der Pauw conditions so, only resistance values can be obtained instead of the resistivity values. However, equation 5-9 is equally valid. The relationship between resistivity and resistance consists in certain constants that depend on the measured films.

5.1.4 Surface reactions role

In the previous section, the oxygen diffusion process was presented as a bulk process governed by Fick´s laws. In this framework, the reactions that take place in the surface involving O_2 molecules are not considered. However, in recent years, the study of the diffusion process in functional oxides is no longer seen as only a volume phenomenon. Some works, in different functional oxides, have demonstrated that the reactions that the oxygen suffers in the surface of the materials play a key role in the diffusion process kinetics. Actually, as some authors claim, the surface reactions constitute the limiting factor of the kinetics of the diffusion process in different functional oxides[259, 264, 268-272].

Considering the surface reactions does not mean that the previous equations are not valid. Simply, the time spent in the surface reactions is included in the overall time of the diffusion. However, the explanation of diffusion mechanism has to be completed with the surface processes before entering in the bulk diffusion.

The studies in different functional oxides have demonstrated that there are several reactions that take place in the oxides surface. In the work of Kuklja et al[268] it has been proposed, in the case of the $(Ba,Sr)(Co,Fe)O_{3-\delta}$, four different reactions that the O_2 molecules have to complete before diffusing in the bulk. First of all, the chemisorption of O_2 molecules in the surface take place (figure 5.3 (I)). The O_2 molecules in the surface suffer ionization by taking two electrons and leaving two holes, becoming O_2^{2-} molecules. After that, the O_2^{2-} molecules diffuse in the surface until they find a vacancy (figure 5.3 (II)). Then, the molecules are dissociated and one of the O^- ions remains in the vacancy (figure 5.3 (III) while the other one have to find a new vacancy (figure 5.3 (IV)). The dissociation implies again charge transfer because the O^- ions are not stable and they need another electron to become O^{2-} ions. When this process finish both ions can diffuse in the bulk.

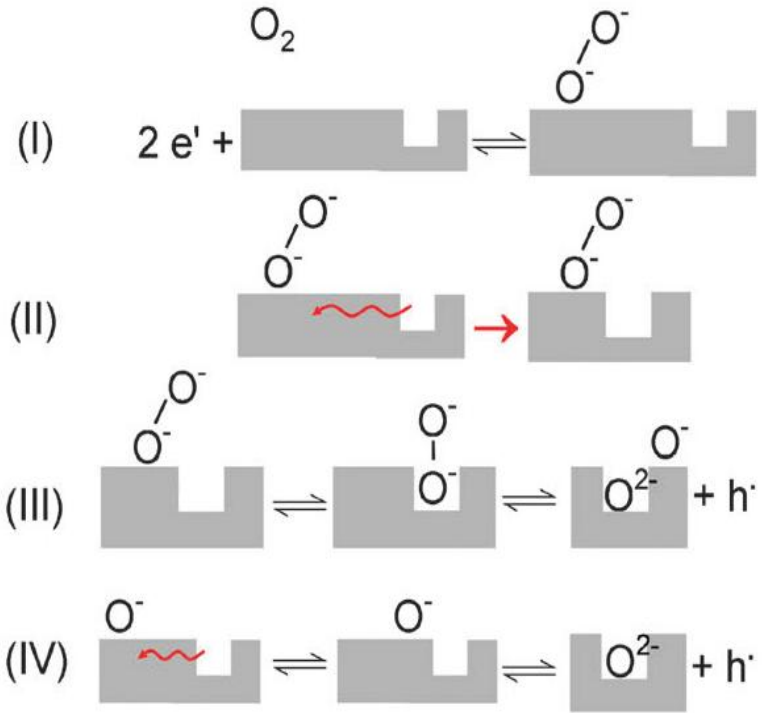

Figure 5.3. O_2 surface reactions that take place before oxygen ions diffuse in the bulk: (I) chemisorption of O_2 molecule and molecules ionization, (II) O_2^{2-} molecules surface diffusion to find a vacancy, (III) O_2^{2-} molecules dissociation, (IV) second O^- ion migration to other vacancy[268].

Considering the surface reactions, the problem of the diffusion is much more complicated. The complete scenario is presented in figure 5.4 including both the surface reactions and the bulk diffusion.

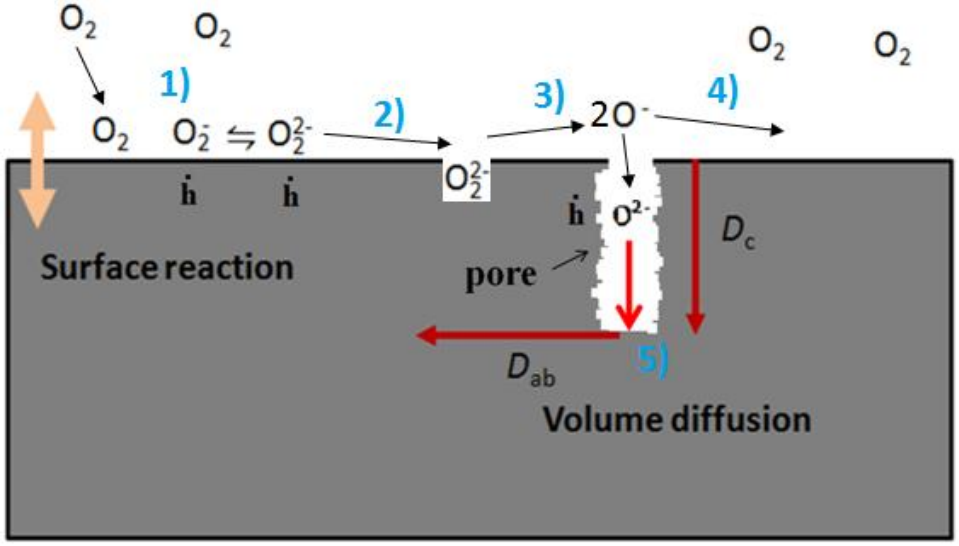

Figure 5.4. Complete picture of the diffusion process including the surface reaction and the bulk/volume diffusion. The complete process follows these steps: 1) Chemisorption of the O_2 molecule and ionization of the molecule, 2) surface diffusion to find a vacancy, 3) dissociation of O_2 molecules, 4) the second ion look for another vacancy and 5) volume diffusion.

Assuming that this is the complete diffusion process in the YBCO, there are two important issues to comment. The first one is that the different ionization processes of the O_2 molecules implies charge transfer which involve electron/holes (holes are symbolize as $\dot{h}$) interchange. Once the O_2 molecule is chemisorpted, it takes two electrons to become a O_2^{2-} molecule. This process creates two holes in the film. The dissociation of the O_2^{2-} molecule forms two O^- ions (unstable) that take another electron to become O^{2-} ions that can go in the bulk. So, in the whole process, four holes are created. It is not clear which are the species that acts as donors of electrons but is supposed to be the Cu ions that can exist as Cu^+, Cu^{2+} or Cu^{3+} in the YBCO structure[273-276].

The other point to take into account is that the bulk diffusion is mostly considered to be happening in the ab-plane. The diffusion coefficient in the c-axis direction, D_c, is 10^4-10^6 lower than in the ab-plane, D_{ab}. The O^{2-} ions initially penetrate in the YBCO through the pores or grain boundaries and then, they diffuse in the ab-planes ((step 5) in figure 5.4). It is contemplated in this way because if the diffusion in c-axis was considered, the oxygen diffusion would be much slower. With this in mind, it is possible to say that the diffusion process is divided in two processes: the surface reactions and the diffusion in the ab-plane. Therefore, the possible limiting factors of the process should be either the D_{ab} or the surface reaction rate constant, K.

If the surface reactions are taken into account and they are considered as the limiting factor for the whole diffusion process, it has no sense to use the τ as a reference for the process time. A new parameter, called "surface exchange coefficient (k_{chem} [cm/s])", appears and it has a similar role than the τ for the bulk diffusion. k_{chem} gives the rate of the surface reactions. It is related with τ by the following expression (Eq. 5-13)[264]:

$$k_{chem} = \frac{t}{\tau} \quad \text{Eq. 5-13}$$

where t is the thickness of the film and τ is the diffusion relaxation time found applying Eq. 5-11.

The k_{chem} has similar temperature dependence than τ, following an Arrhenius equation (Eq. 5-14):

$$\mathbf{k_{chem} = k_0 e^{\left(-\frac{E_a}{K_B T}\right)}} \quad \text{Eq. 5-14}$$

where E_a is the energy activation of the process, K_B is the Boltzmann´s constant and k_0 is the frequency factor which, in this framework, takes into account the probability of successful adsorption per collision (the higher the pre-exponential factor is, the larger the probability of molecule adsorption and the greater the reaction rate).

One of the major challenges, considering the diffusion mechanism represented in figure 5.4, is finding the slowest step in this process or, in other words, tracing the rate determining step (rds). If the surface reactions are considered as the limiting factor in the diffusion process, the rds is one of them. In the work of Kuklja et al[268] it was mentioned that the rds in (Ba,Sr)(Co,Fe)$O_{3-\delta}$ perovskites is the second step, i.e., the O_2 molecules surface diffusion but no studies about this issue in YBCO heve been reported up to now.

The aim of this study is to clarify which is the role of the surface in the YBCO oxygen diffusion kinetics. If the results suggest that the surface is an important factor, then, the rds will be pursued.

5.1.5 Oxygen in- and out-diffusion

Within the oxygen diffusion process, it is possible to carry out two different experiments: the in- and out-diffusion. The in-diffusion refers to the process by which the oxygen goes into the YBCO structure while the out-diffusion refers to the process by which the oxygen goes out from the YBCO structure.

There is much controversy in the scientific community about the equivalence, in terms of diffusion rate, of both processes. Considering pure bulk diffusion, it should not be expected any difference between in- and out-diffusion because bulk diffusion is just a matter of a concentration gradient in the YBCO structure and the direction of movement is not relevant. However, there is no unanimity on whether both processes are equivalent (same rate for each process) or if there is something more (surface reactions) than the bulk diffusion that causes a change in the rates in each case. Using in-situ resistance measurements, the situation is similar: some results show that both processes are symmetric while other results say the contrary.

However, using this last technique, one has to take into account the presence of the percolation phenomenon that can vary the results. This phenomenon consists on the presence of percolation currents flowing in the grain boundaries that can decrease the measured resistance creating a close circuit between the contacts in the sample (figure 5.5)[277].

When the oxygen goes into the film, the current flows in the "low resistance circuit" created through the grain boundaries, while the interior of the grains remains in a high resistance state. This causes an "electrical circuit" in which the grain boundaries and

the grains act as "parallel resistors". If both "resistors" are added, the major contribution comes from the low resistance state. So, in the in-diffusion, due to the percolation effect the diffusion rate increases.

The reverse phenomenon occurs in the out-diffusion. The oxygen goes out through the pores or the grain boundaries. Therefore, the resistance in the grain boundaries will increase due to the lack of oxygen while the grains are isolated in a low resistance state by these high resistance grain boundaries. In this case, both contributions are added as "series resistors" and the overall contribution will be affected mostly by the high resistance state. So, in the case of the out-diffusion, the resistance measurements take into account the slower of the two cases. A detailed discussion about the problem of the equivalence in the in- and out-diffusion will be exposed in section 5.2.3.

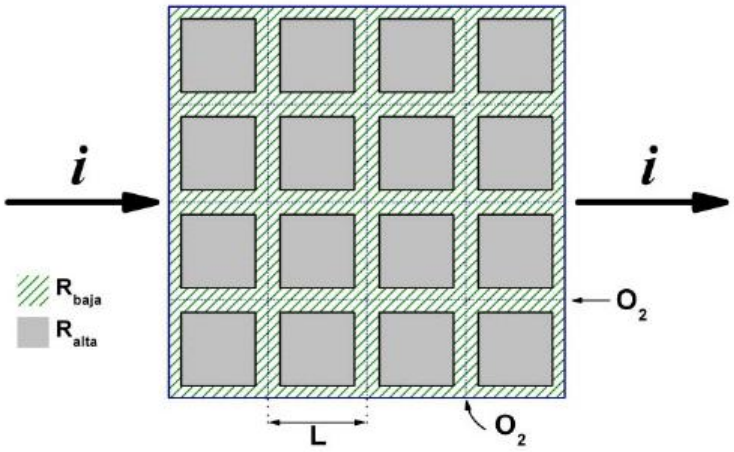

Figure 5.5. Sketch of the current percolation effect in YBCO thin films. The oxygen can diffuse easily in the grain boundaries creating a "low resistance circuit" that decrease the measured resistance. However, the grain remain in a high resistance state since the oxygen do not penetrate them[277].

5.2 YBCO processing parameters dependence on the oxygen diffusion

As it was discussed extensively during this thesis, the YBCO needs special conditions to nucleate and grow properly. However, there are no reported studies of how the processing parameters affect the oxygenation and the oxygen diffusion process of the YBCO. This is an important information in order to find out the optimal conditions for the oxygenation of these films.

The effect of the temperature, gas flow and oxygen partial pressure on the oxygen diffusion in 250 nm thick YBCO films will be described.

5.2.1 YBCO oxygen diffusion dependence with temperature

In this work, the study of the influence of the temperature was carried out in order to try to reproduce the results already obtained in previous work in the SUMAN group[277]

and to check that the measurement equipment was working properly. Also, the obtained results will be used as an explication of the work mode for the future analysis.

The evolution of the measured resistance with time for different temperatures is shown in figure 5.6. It is observed that consecutive increase and decrease of the resistance occur. These measurements correspond to alternative atmospheres A and B whose main difference is the oxygen partial pressure (P_{O_2}). Atmosphere A corresponds with a 1 atm of pure oxygen (O_2) flowing at 0,6 l/min while B implies an atmosphere formed by 1 atm of nitrogen (N_2) with 2.10^{-4} atm (200 ppm) of O_2 flowing at 0,6 l/min. The A atmosphere is called in-diffusion atmosphere because, when it is set, the resistance decreases (the oxygen tends to enter in the YBCO structure) while the B atmosphere is called the out-diffusion atmosphere because it causes a resistance increase (the oxygen tends to go out from the YBCO structure).

The way in which the results shown in figure 5.6 are obtained is as follows. First, the YBCO films are set at a certain temperature, for example 800 ºC. At this temperature atmosphere A is placed in order to decrease the resistance as much as possible. After 10 min with A, the atmosphere is changed into B during 60 min causing an increase of the resistance. After 60 min with B, the temperature is decreased to the next one with A atmosphere. When the next temperature is reached and after 10 more min with A atmosphere, B atmosphere is set again to observed the out-diffusion. This process is repeated each 50 ºC until 350 ºC.

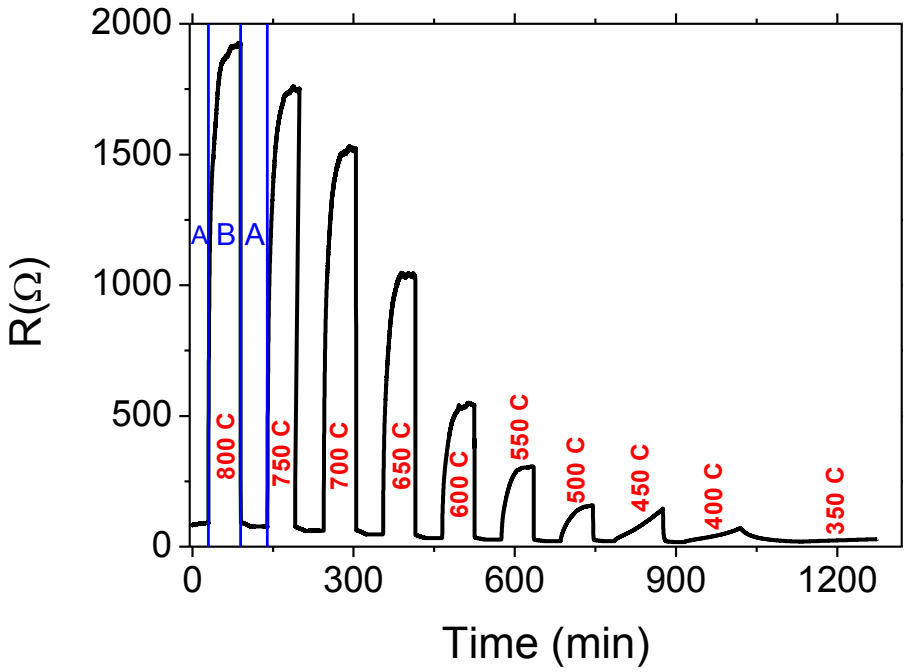

Figure 5.6. Evolution of the resistance with time for different temperatures following alternative changes of oxygen partial pressures (A: 1 atm and B: 2.10^{-4} atm).

The results shown in figure 5.6 are only valid to study the out-diffusion process since the in-diffusion curves are not measured in isotherms. The out-diffusion curves are presented in figure 5.7.

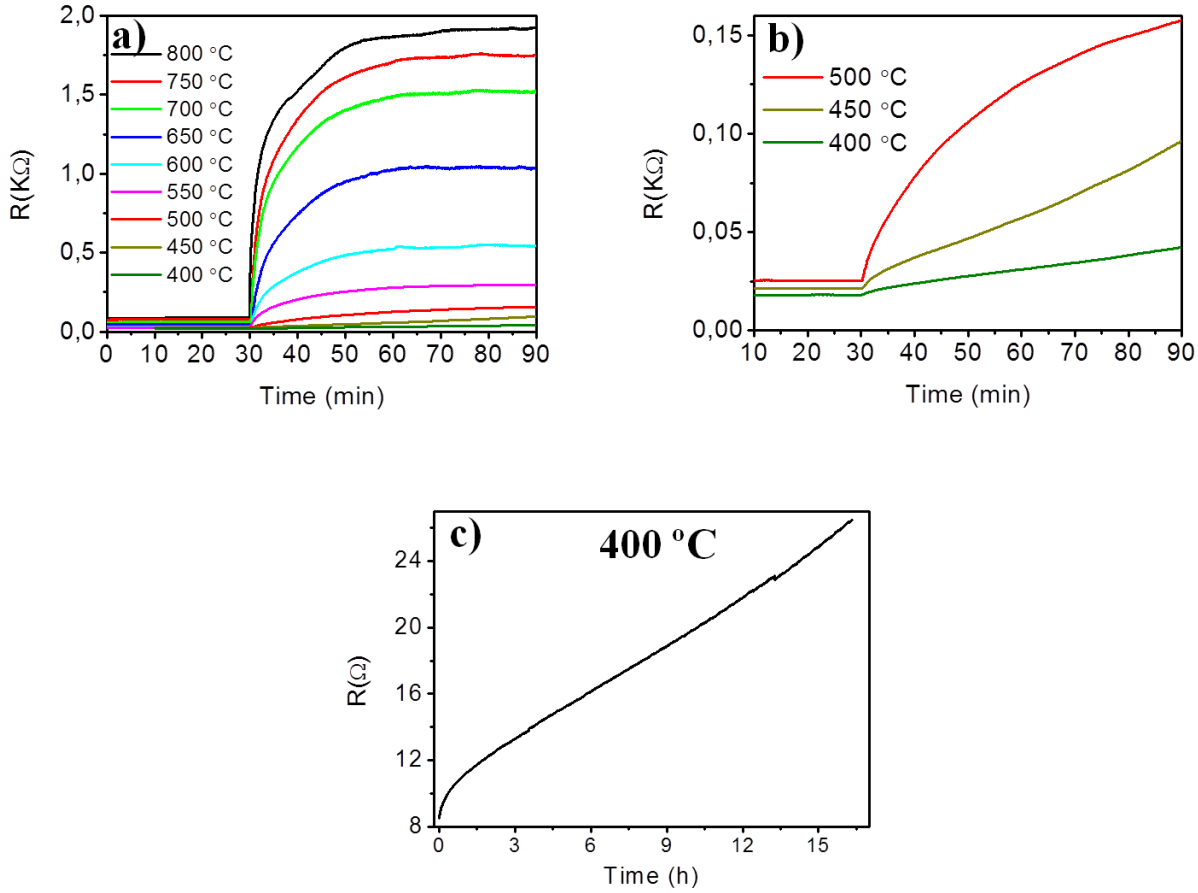

Figure 5.7. Out-diffusion curves at different temperatures. Graph a) shows a summary of all the curves while the graphs b) and c) are focused in the non-saturated curves at low temperatures.

Figure 5.7 a) shows the out-diffusion curves between 400 and 800 ºC. It is observed that as the temperature decreases, the saturation resistances decreases while the diffusion relaxation time (τ) increases (the curves arrive to the saturation resistances in a "smoother" way). This happens because in the equilibrium state, at a constant P_{O_2}, the number of carriers is different depending on the temperature. In the work of Shimoyama et al, the oxygen content (the more the oxygen content, the more the carriers) in the equilibrium state for a certain temperature and P_{O_2} conditions can be checked[278]. In this work, it is shown that, for a constant P_{O_2}, the oxygen content in the equilibrium state increases as the temperature decreases. If the oxygen content is higher, there are more carriers and, therefore, the resistance is lower. This is precisely what is observed in figure 5.7 a).

On the other hand, at low temperatures (below 550 ºC) the equilibrium is not reached (the curve do not arrive to a constant resistance value) as it can be seen in figure 5.7 b). One can think that the saturation is not reached because the measurement time is too short (only 60 min). However, this is not the case as is shown in figure 5.7 c) in which the equilibrium is not reached even after 15 hours at 400 ºC. The equilibrium is not observed at low temperatures because at these temperatures the kinetics of the process is really slow. The same effect is also observed in the in-diffusion process (doing the process in an isotherm) as it is shown in figure 5.8 for an in-diffusion process at 350 ºC.

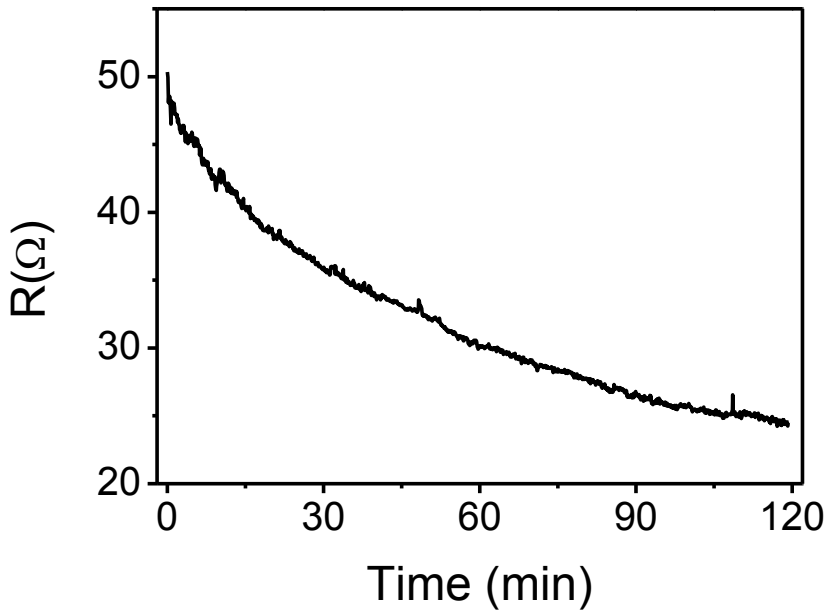

Figure 5.8. In-diffusion curve measured at 350 ºC. It is clearly seen that after 120 min the system do not arrive to the equilibrium state.

A consequence derived from the fact that the equilibrium is not reached is that Eq. 5-9 cannot be applied due to the impossibility to assign a value to ρ_∞. Therefore, the τ values can not be calculated at these temperatures. This entails that the analysis of temperature dependence of the τ (or the derived values such as k_{chem}), will contain only the values corresponding to saturated R(t) curves, both for the in- and out-diffusion.

The not-saturated curves can be modeled, however, by making a Taylor series expansion of Eq. 5-10 centered at t=0 (Eq. 5-15):

$$\boldsymbol{\rho(t) \propto 1 - e^{-\left(\frac{t}{\tau_{ab}}\right)} \approx \frac{t}{\tau_{ab}} - \frac{t^2}{2\tau_{ab}^2} + \cdots} \qquad \text{Eq. 5-15}$$

The first term of the Taylor expansion can be used to model the non-saturated curves and estimate the τ value if they are straight lines. The slope of this line would correspond to $1/\tau_{ab}$. For example the curve shown in figure 5.7 c) corresponding to the out-diffusion process at 400 ºC fits fairly well to a straight line obtaining a τ value of ~60 h. If the curve is not a line, more terms have to be used until the curve fit perfectly (500 ºC in figure 5.7 b)).

Once the conditions for the τ determination have been established, it is time to present the obtained values at each temperature for the out- and in-diffusions. Figure 5.9 contains the evolution of τ values, calculated using Eq. 5.10 and 5.11, with temperature. It is also plotted the $-Ln(k_{chem})$ vs. 1000/T curves used to calculate the E_a values (remember that k_{chem} is used considering the surface reactions) both for the out- and in-diffusions.

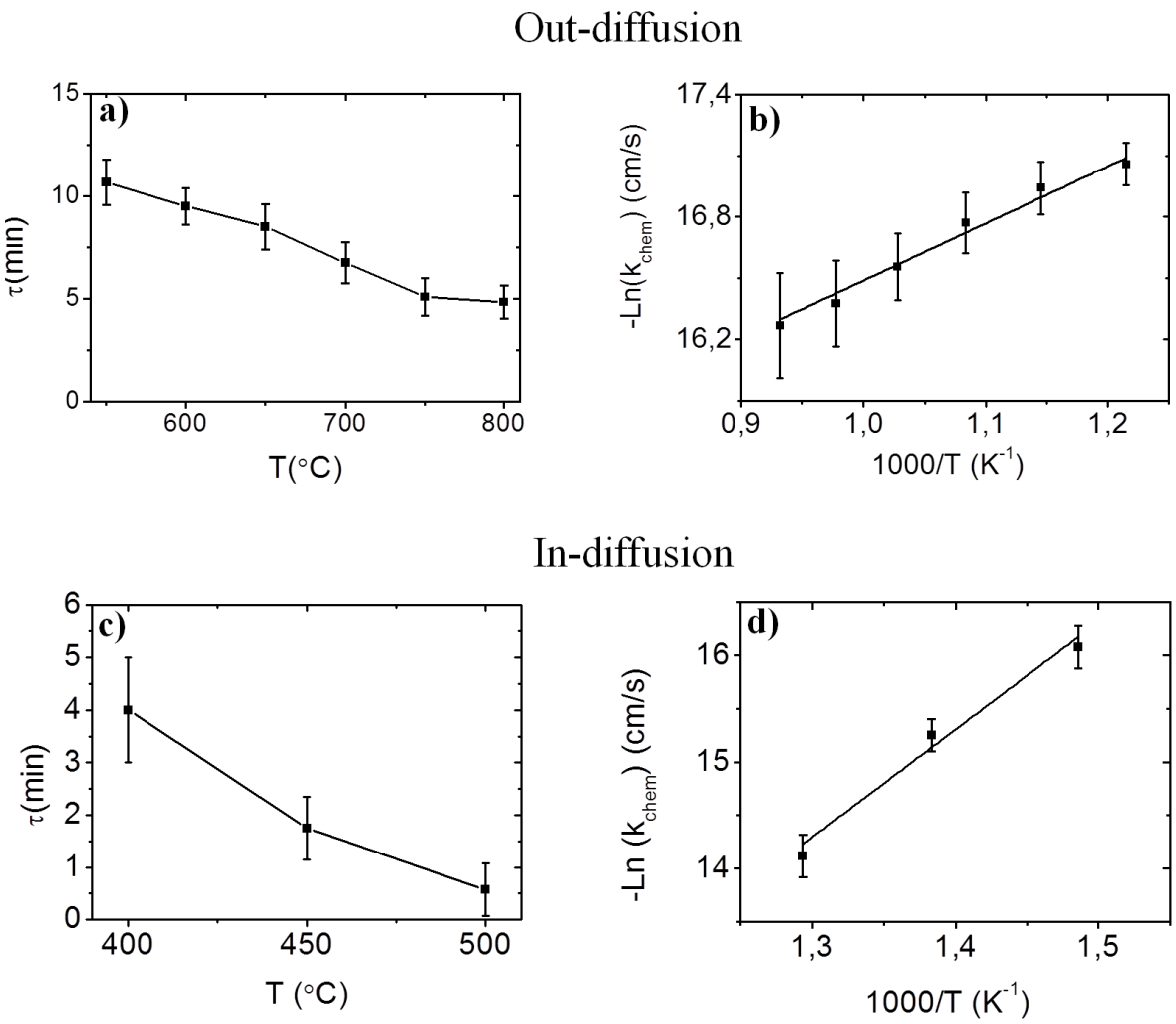

Figure 5.9. Evolution of τ values with the temperature and $-Ln(k_{chem})$ vs. 1000/T curves for the out-diffusion (a) and b)) and the in-diffusion (c) and d)) processes for a pristine YBCO film. Here a surface controlled diffusion was assumed.

The results shown in figure 5.9 a) and c) demonstrate, as it was mentioned before, that the τ value increases as the temperature decreases for both the out- and in-diffusions. This implies that as the temperature decreases the time needed to reach the equilibrium is longer. The curves presented in figure 5.9 b) and d) demonstrate that the out- and in-diffusions are thermally activated processes and that the τ values follow an Arrhenius equation (Eq.5-11). Finding the slope of these two lines, it is possible to calculate the E_a values for the out- and in-diffusions in this particular range of temperatures. The out-diffusion in the range of 550 to 800 ºC presents a E_a of 0,25±0,05 eV while in the case of the in-diffusion in the rage 400 to 500 ºC the E_a has a value of 0,8±0,2 eV. These values are in accordance with the reported ones[267, 266, 279]. The k_0 values can be calculated from the intercepts of the lines in figure 5.9 b) and d). The k_0 values are $1{,}5.10^{-6}\pm 8.10^{-7}$ eV and 0,29±0,09 cm/s for the out- and in-diffusion respectively. Note that there is a difference of five orders of magnitude between the k_0 values of the out- and in-diffusion.

It is very important to remark that, in the case of the in-diffusion, the E_a is only valid for this particular range of temperatures. Only three values of τ were used because

above 500 ºC the in-diffusion is so fast that it is very difficult, with the used experimental setup, to determine the τ values with accuracy.

With the information obtained until now, it is not possible to conclude which is the limiting factor of the diffusion, the surface or the volume. The graphs in figure 5.9 were made assuming a surface controlled process because k_{chem} was calculated. However, the observed evolution of the diffusion with temperature can be also interpreted as a bulk phenomenon. The graphs in figure 5.10 were made supposing that the diffusion is a bulk controlled phenomenon and the linearization of the Arrhenius equation for τ (not for k_{chem}) was plotted.

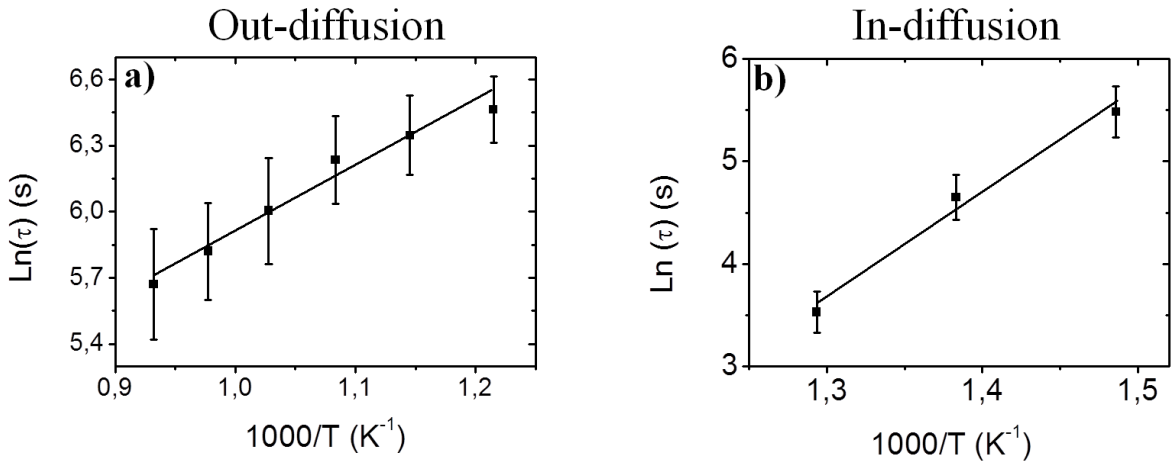

Figure 5.10. Ln(τ) vs. 1000/T curves for the out-diffusion a) and in-diffusion b) processes for a pristine YBCO film. Here volume controlled diffusion was assumed.

The E_a values obtained from figure 5.10 for the out- and in-diffusions are exactly the same (as it should be) as the previous ones obtained from k_{chem} values. The τ_0 values are 17,1±0,8 s for the out-diffusion and $8{,}5.10^{-5}\pm7.10^{-6}$ s. The value of τ_0 the in-diffusion (there are no reported values for τ_0 of the out-diffusion) is two orders of magnitude higher than the reported values[280], but it must to be considered that the changes P_{O_2} in this work are much larger than in the reported works. In view of these results, it is possible to conclude that the analysis of the diffusion dependence with the temperature do not give a definitive clue about the mechanism that controls the diffusion, the surface or the bulk. To elucidate that, more experiments are needed, in which other parameters have to be varied.

5.2.1.1 Physical properties after non-equilibrium oxygenation processes

It was previously mentioned that, under certain oxygenation conditions, the equilibrium state is not reached. First consequence is the impossibility of applying the equation 5.9 to obtain the τ value. However, there is another physical consequence: the performances of the YBCO films are not the optimal ones. If the equilibrium is not reached implies that, of all the amount of oxygen that is able to enter at this temperature and oxygen pressure, there is a part that is not inside yet. And, obviously, in this situation, the properties are not optimum for these particular conditions. In order to illustrate that, the physical properties of two different 250 nm pristine YBCO films subjected to different oxygenation processes will be analyzed.

Before detailing the results, it is important to clarify a concept that may cause confusion which is related with τ. When one says that a certain process have a τ of x min, it does not mean that the equilibrium is reached after these x min. The τ is only the time that the resistance takes to change a value of (1-1/e)= 0,6321→ 63,2%. So, after τ, the process is not completed. Usually, the criterion that it is used is that the process is nearly completed after 5τ because at this moment, (considering a perfect exponential behavior) the system reaches a 99,3% rate of the saturation value.

The first oxygenation process consisted on leaving the YBCO film at 450 ºC during 210 min with 1 atm of oxygen and 0,15 l/min of gas flow. Under these conditions, as it can be observed in figure 5.9 c), the τ value for the in-diffusion is approximately 6 min so, the 210 min are more than enough to reach the equilibrium (much more that the criterion 5τ). By calculating the c-parameter using the Nelson-Riley method (appendix A.2) after this oxygenation process, a value of $1{,}16926 \pm 6.10^{-5}$ nm is found. This value, according to figure 5.1, is equivalent to δ=0,94 and a T_c of 91K approximately. The experimental value of the T_c is 90,5 K, quite near of the theoretical value.

However, if the oxygenation process is carried out using the same gas conditions but at a different temperature, things change drastically. It was shown that the equilibrium state is not reached after 120 min at 350 ºC (figure 5.7). This means that the τ values for the in-diffusion below 400 ºC are huge (it was estimated a τ of 60 min for 350 ºC with gas flow of 0,6 l/min) so, the equilibrium will not be reached after 210 min. Under these assumptions, if the oxygenation process is performed at 300 ºC (here after 210 min the system is much below the equilibrium state). The c-parameter that is found is $1{,}17499 \pm 8.10^{-5}$ nm which corresponds to a δ of 0,62 and a T_c of approximately 59 K. In this case the experimental value is 60 K, again very near of the theoretical one.

In view of these results, it is clear that reaching the equilibrium state to achieve high oxygen contents in the films is of most importance. The incomplete process will cause the deterioration of the physical properties.

5.2.2 YBCO oxygen diffusion dependence with the gas flow

The gas flow during the oxygenation process is a parameter that plays an important role in the YBCO processing. In the case of the oxygenation process, the gas flow is set at a certain value, but there are no reported works of how the gas flow could affect the kinetics of the oxygen diffusion in the YBCO films. To elucidate this issue, measurements of the out- and in-diffusion processes were carried out at different temperatures and using different gas flows.

Atmosphere B ($P_{O_2}=2.10^{-4}$ atm) was used to carry out measurements of the out-diffusion process with the only change of the total gas flow in each case. The calculated values of τ for each temperature and gas flow and the resulting E_a and k_0 values for each gas flow are presented in figure 5.11.

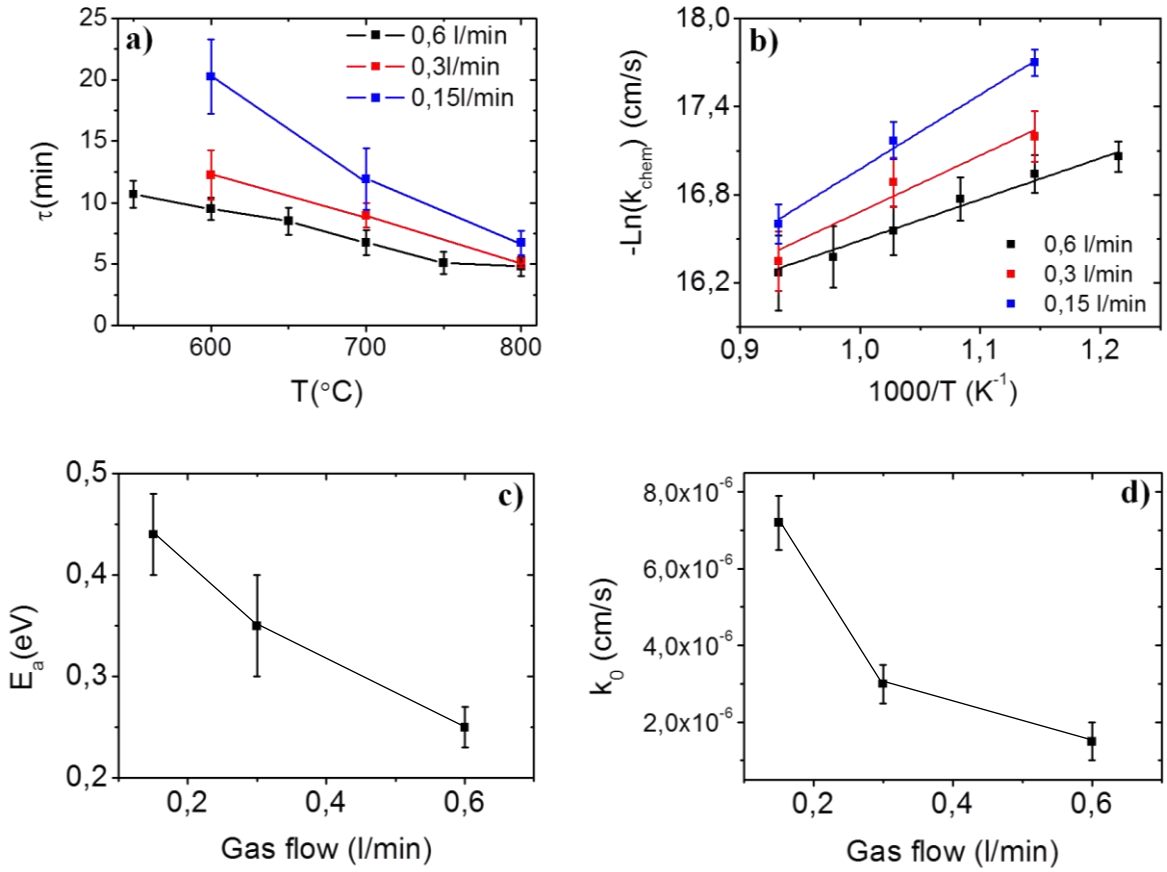

Figure 5.11. Measurements of the out-diffusion process showing a) the evolution of τ values with temperature for different gas flows, b) $-Ln(k_{chem})$ vs. 1000/T curves for different gas flows, c) the dependence of the E_a values with the gas flow and d) the dependence of the k_0 values with the gas flow.

First conclusion that can be extracted from figure 5.11 is that the τ values at each temperature depend on the gas flow that is being used in such a way that the lower the gas flow is, the higher the τ values. It is also observed that the increase of the gas flow cause a decrease of the E_a but a raise of the k_0 values. The fact that the k_0 decrease with the gas flow while the E_a increase indicate that, in this case, the parameter that governs the overall behavior is the E_a because, at the end, the τ vales increase with the gas flow in the same way as the E_a values do.

The fact that the E_a and the k_0 change with the gas flow is a relevant result because it is an unequivocal proof of the surface reactions influence in the kinetics of the oxygen diffusion in YBCO CSD films, as this dependence can not be explained in another way. Considering only volume diffusion, the only important parameter should be the concentration gradient between the borders and the center of the YBCO film. The gas flow should not have any influence in the diffusion kinetics in this framework because, avoiding surface reactions entails to consider that when the oxygen arrives to the surface it goes in the volume or to the atmosphere instantaneously without being affected by the surface in any way.

The same studies were performed in the case of the in-diffusion process. The results are presented in figure 5.12.

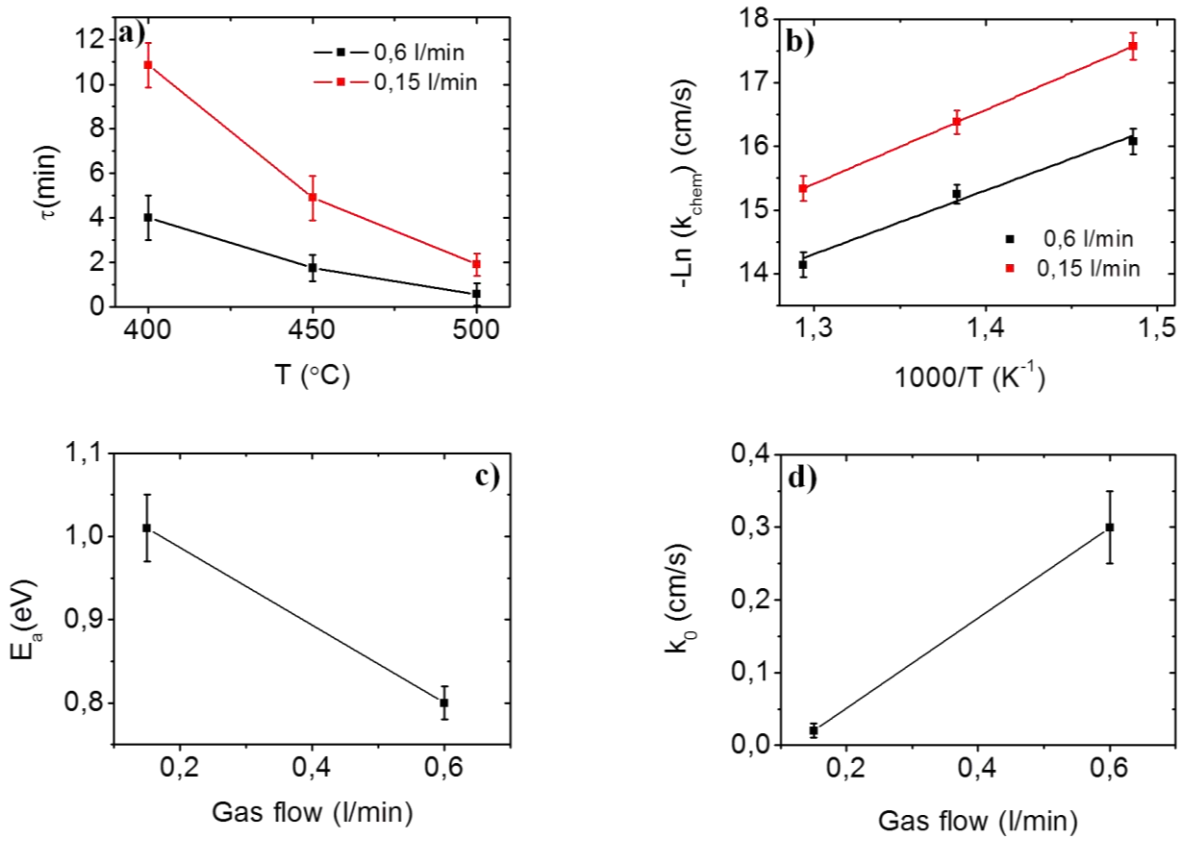

Figure 5.12. Measurements of the in-diffusion process showing a) the evolution of τ values with the temperature for different gas flows, b) $-Ln(k_{chem})$ vs. 1000/T curves for different gas flows, c) the dependence of the E_a values with the gas flow and d) the dependence of the k_0 values with the gas flow.

The situation in the case of the in-diffusion is similar than in the case of the out-diffusion. Figure 5.12 a) shows a change in τ values as the gas flow is changed in such a way that the diffusion process is faster as the gas flow is increased. It is also observed that the E_a values increase as the gas flow decrease while, in the case of the in-diffusion and unlike in the case of the out-diffusion, the k_0 decreases (the difference between both values of k_0 is the range of one order of magnitude). This means that the raise of the gas flow increase the probability of the molecules adsorption and reduce the energy barrier of the diffusion process. Therefore, in the case of the in-diffusion, both parameters go in the direction of reducing the τ values thus having an important influence on the final τ values.

This behavior is explained considering a simple model in which the oxygen molecules interact, in this particular case, with the YBCO films surface. As the O_2 molecules approach the surface, they experience an attractive potential. A fraction of the incident molecules are trapped, i.e., are adsorbed in the attractive potential well, and once adsorbed they can move in the surface by surface diffusion. The dynamics of the O_2 molecules/surface interactions are determined by the energy that is exchanged between the molecules and the surface atoms through the various energy transfer channels.

The adsorption rate constant (R_{ads}) is defined as the number of molecules that are adsorbed in the surface per unit area and time and it is measured in molecules/m^2.s. The adsorption rate constant can be obtained by the following expression (Eq. 5-16):

$$R_{ads} = S.F \quad \text{Eq. 5-16}$$

where S is the sticking probability (the probability that the molecule will be adsorbed upon the collision with the surface) and F is the molecular flux (the number of molecules crossing a unit surface in one direction during a unit of time).

The molecular flux is proportional to the macroscopic flux. So, according to Eq. 5.16, the adsorption rate increases with the flux. This implies that the overall time of the surface reaction will be lower as the flux increases. This is exactly what is shown in figures 5.11 and 5.12, the higher the oxygen flux, the lower the τ values, the higher the k_{chem} values and also the lower the E_a values implying a faster out- and in-diffusion processes.

5.2.3 YBCO oxygen diffusion dependence with the oxygen partial pressure

Another important parameter on the YBCO oxygenation process is the P_{O_2}. In this section, the effect of this parameter on the out- and in-diffusion processes will be investigated.

The procedure to perform these measurements was similar to the previous cases. The YBCO film is in atmosphere A (the P_{O_2}= 1 atm) to decrease the resistance as much as possible and then, the atmosphere is changed to B but varying the P_{O_2}. In the previous cases the P_{O_2} was always maintained at 2.10^{-4} atm. In this case the value is varied from 5.10^{-5} to 0,05 atm. The gas flow is always kept at 0,6 l/min. Similar procedure, with changes of P_{O_2} of orders of magnitude, was employed in melt textured YBCO samples[260].

Figure 5.13 a) shows the calculated τ values for the out-diffusion as a function of the temperature for different P_{O_2}. What is observed is that, as the final $P_{O_2}$is increased, the τ decreases at all temperatures. This means that, if the difference in P_{O_2}between A (1 atm) and B atmospheres decreases, the saturation resistance is reached much faster than in other cases. It is observed that, within the investigated time window, the saturation resistance is reached even at 420 ºC when P_{O_2}=0,05 atm, much lower temperature than in the other two cases (to calculate the E_a in the case of the 0,05 atm only the values until 500 ºC were used because below this temperature the values deviate from the linear trend).

As can be observed in figure 5.13 c), the E_a values decrease as the P_{O_2} increase meaning that the energy barrier for the diffusion decrease whit increasing the P_{O_2} and hence the low values of τ at higher P_{O_2}. On the other hand, the evolution of k_0 (figure 5.13 d)) shows that the higher value is obtained at 5.10^{-5} atm indicating that at low P_{O_2}, the τ are much more influenced by change in E_a (at low pressures the τ values are higher in the same way that the E_a values). However, when the P_{O_2}=0,05 atm, the k_0 increase with respect to the value at P_{O_2}=2.10^{-4} atm indicating that at this higher pressures, the τ values could be affected by both the E_a and the k_0 reducing the energy barrier and increasing the adsorption probability respectively thus resulting the observed lower values of τ.

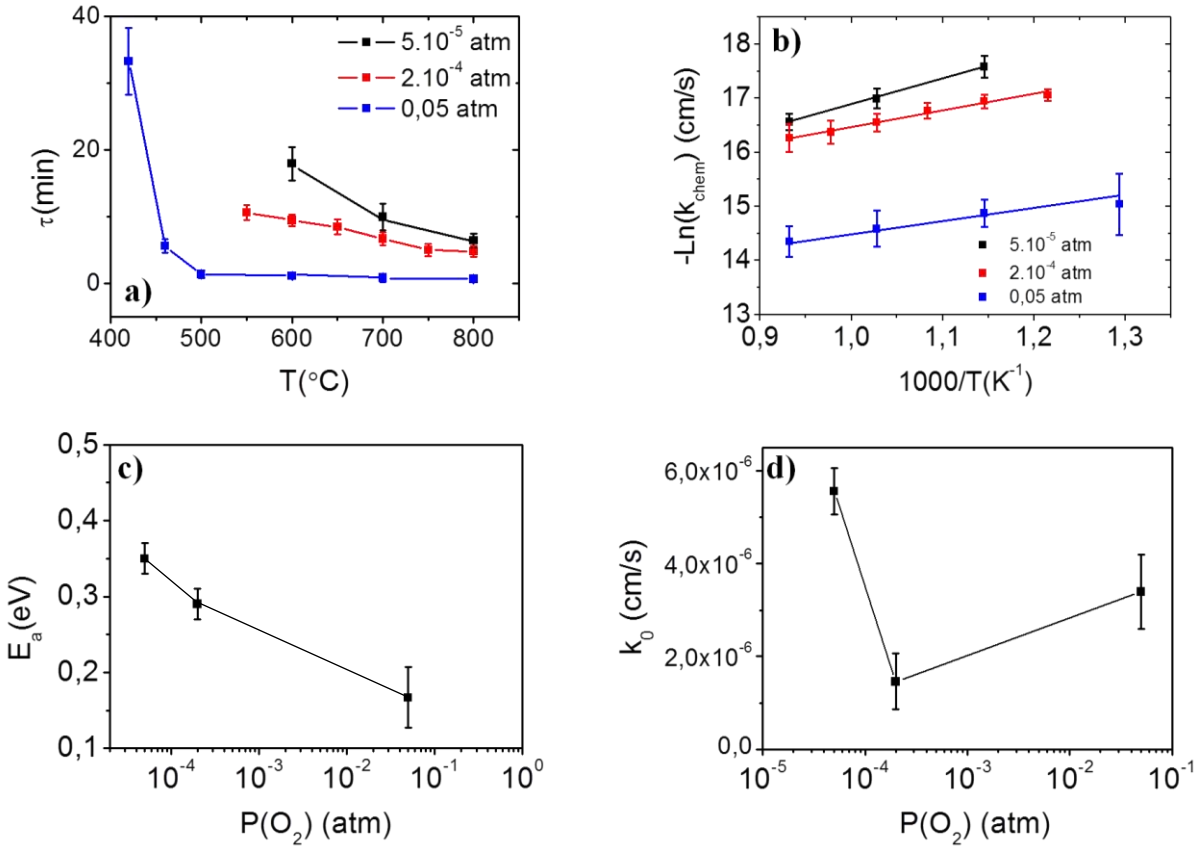

Figure 5.13. Measurements of the out-diffusion process showing a) the evolution of τ values with the temperature for different oxygen partial pressures, b) $-Ln(k_{chem})$ vs. 1000/T curves for different oxygen partial pressures, c) the dependence of the E_a values with the oxygen partial pressures and d) the dependence of the k_0 values with the oxygen partial pressures.

In the case of the in-diffusion, the dependence with the P_{O_2} was studied by choosing a temperature (600 ºC in this case) and obtaining the τ values changing from an atmosphere with a P_{O_2} of 5.10^{-5} atm of O_2 to another atmosphere with different values (always higher than 5.10^{-5} atm to induce the in-diffusion) of P_{O_2} (figure 5.14).

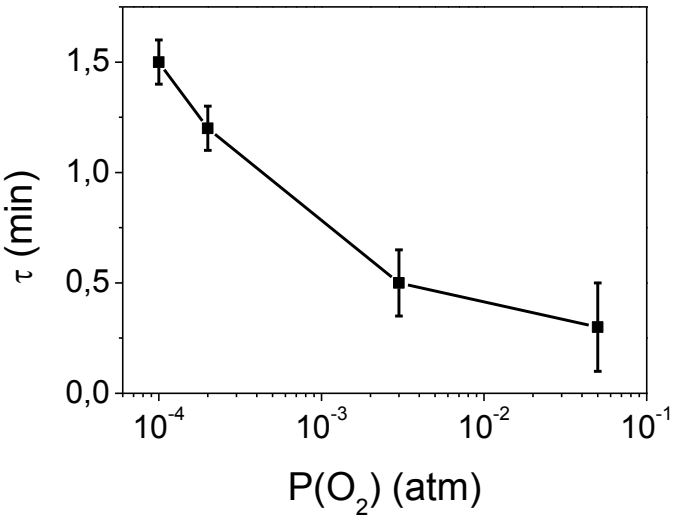

Figure 5.14. Evolution of the τ values for the in-diffusion process when the final P_{O_2} values are modified from an initial value of $P_{O_2}=5.10^{-5}$ atm for a pristine YBCO film at 600 ºC.

With this study it is not possible to calculate the E_a values, but it is enough to demonstrate that the P_{O_2} affects the in-diffusion process in the same way as in the case of the out-diffusion (the higher the P_{O_2}=0,05 atm is, the lower the τ value).

The results showed in figures 5.13 and 5.14 constitute another irrefutable proof of the surface reactions influence in the oxygen diffusion process in CSD YBCO films. The bulk diffusion could also depends on the P_{O_2} because, as it can be observed in the work of Shimoyama et al[278], the oxygen content in the equilibrium depends on the P_{O_2}. The higher the P_{O_2} is, the higher the oxygen content in the structure at the same temperature. And the oxygen content affects the diffusion coefficient in the bulk in such a way that, the higher the oxygen content is, the lower the diffusion coefficient and, therefore, the higher the diffusion relaxation time (the higher the oxygen content is, the lower the concentration difference). However, the experimental results obtained in this work go in the opposite direction i.e., both for the out- and in-diffusion processes, the higher the P_{O_2} is, the lower the τ values are. The only way to understand this behavior is assuming the relevance of the surface reaction effect.

Actually, the P_{O_2} effect in the surface reactions can be explained using the Langmuir model, a simple model that explains the adsorption of the gases in a certain surface. This model, that considers the adsorbate as an ideal gas at isothermal conditions, establishes that the fractional occupancy of the adsorption sites, θ_1, is related with α, the fraction of molecules that will condense and will be held by the surface forces and with μ, the number of gram molecules of gas striking each cm^2 per second, by the following equation (Eq. 5-17)[281]:

$$\boldsymbol{\theta_1 = \frac{\alpha\mu}{\nu_1 + \alpha\mu}} \qquad \text{Eq. 5-17}$$

where ν_1 is the rate at which the gas would evaporate if the surface were completely covered.

The number of gram molecules of gas striking each cm^2 per second, μ, is given by (Eq. 5-18):

$$\boldsymbol{\mu = 43,75.10^{-6}\frac{p}{\sqrt{MT}}} \qquad \text{Eq. 5-18}$$

where p is the pressure, M is the molecular weight of the adsorbed molecules and T is the temperature.

Looking at Eq. 5-17 and Eq. 5-18, it is clear that the adsorption of a certain gas on a surface depends on the pressure of this gas. So, it is clear that the variations in τ, E_a and k_0 shown in figures 5.13 and 5.14 are related with the change in the oxygen adsorption on the YBCO films surface. This dependence was also found previously for the oxygen incorporation in other functional oxides where the surface reaction is the dominating process[282].

Typically, the reaction rate that is found in the surface reactions is proportional to the $(P_{O_2})^{\alpha}$ where α depends on each particular reaction ($R \propto (P_{O_2})^{\alpha}$)[271, 270, 282]. In order to verify that the YBCO films follow the same law, a new experiment is designed. It consist on performing consecutives out-diffusion processes varying the P_{O_2} but maintaining constant the in-diffusion P_{O_2} at 1 atm (figure 5.15).

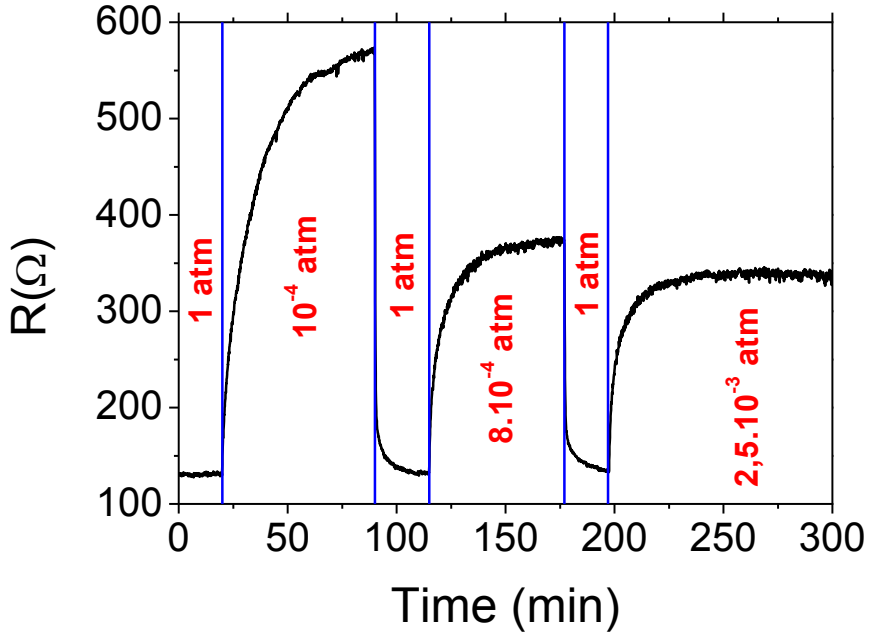

Figure 5.15. Evolution of the electrical resistance with time when different out-diffusion processes are carried out at different P_{O_2} and maintaining constant the P_{O_2} for the in-diffusion at 1 atm

By extracting the τ values for the out- and in-diffusion processes, it is possible to draw a graph with the ratio of τ values (τ is considered as rate so the ratio of τ values is also a rate) of the in- and out-diffusion vs. the square root of the ratio of P_{O_2} of the out- and in-diffusion (fixed at 1 atm). The exponent is chosen at ½ following the proposal for YBCO films of Ling Chen et al[264].

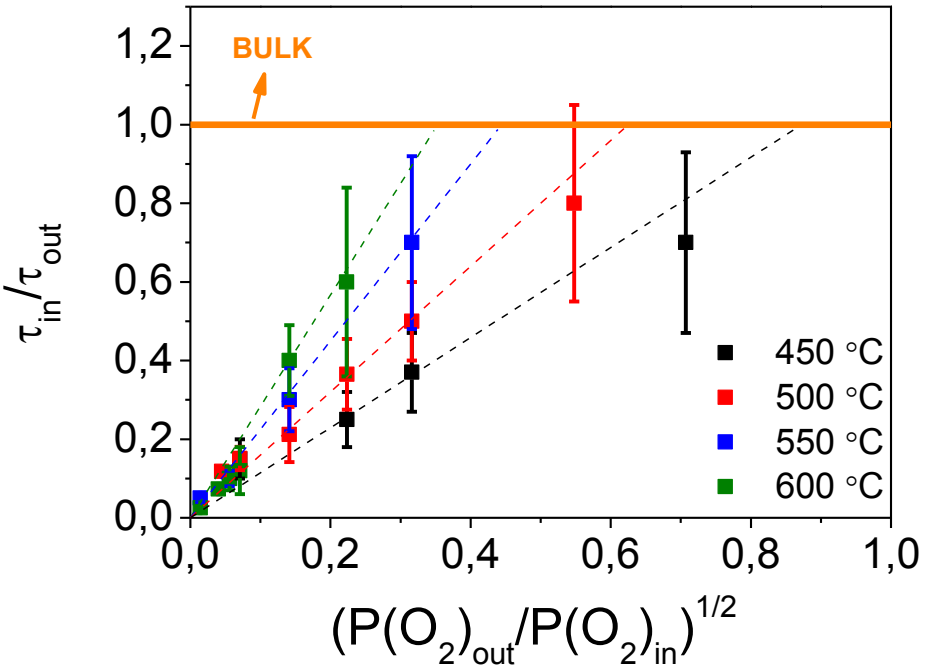

Figure 5.16. Graph of ratio of τ values of the in- and out-diffusion vs. the ratio of P_{O_2} of the out- and in-diffusion (P_{O_2} of the in-diffusion is fixed at 1 atm). The resulting lines confirm that the oxygen diffusion process in YBCO is surface controlled.

Figure 5.16 shows that the resulting curves are straight lines, which confirms the surface controlled process. The dashed lines are the extrapolation of the curves to the bulk behavior. Considering only the volume diffusion, the ratio of τ should not depend on the P_{O_2} in any way. Actually, the ratio should be equal to 1 at any P_{O_2} because the diffusion in two different directions should be equivalent since it is only the concentration gradient which matters.

In the case of the surface controlled process, at low pressures, the τ values for the in- and out-diffusion are really different but, as the $P_{O_2}$of the out-diffusion is increased, both values are increasingly similar. This happens because the difference in P_{O_2} between both processes become very small and the equilibrium state is reached very fast. Actually, this is in agreement with the reported τ values of in- and out-diffusion in single crystals when the changes in the conditions from the equilibrium are very small[267, 280]. At certain point, the equilibrium is reached so fast that, with the used experimental setup, it becomes impossible to detect any difference between the τ values of both processes.

The unmeasurable τ values are found at lower P_{O_2} as the temperature increases. Figure 5.17 shows that, for instance, at 700 ºC and at 0,05 atm for the out-diffusion, both the in- and out-diffusion are too fast to determine the τ values with an adequate accuracy. However, as the temperature is decreased, some differences between both processes start to appear (curvature of the line before reaching the equilibrium).

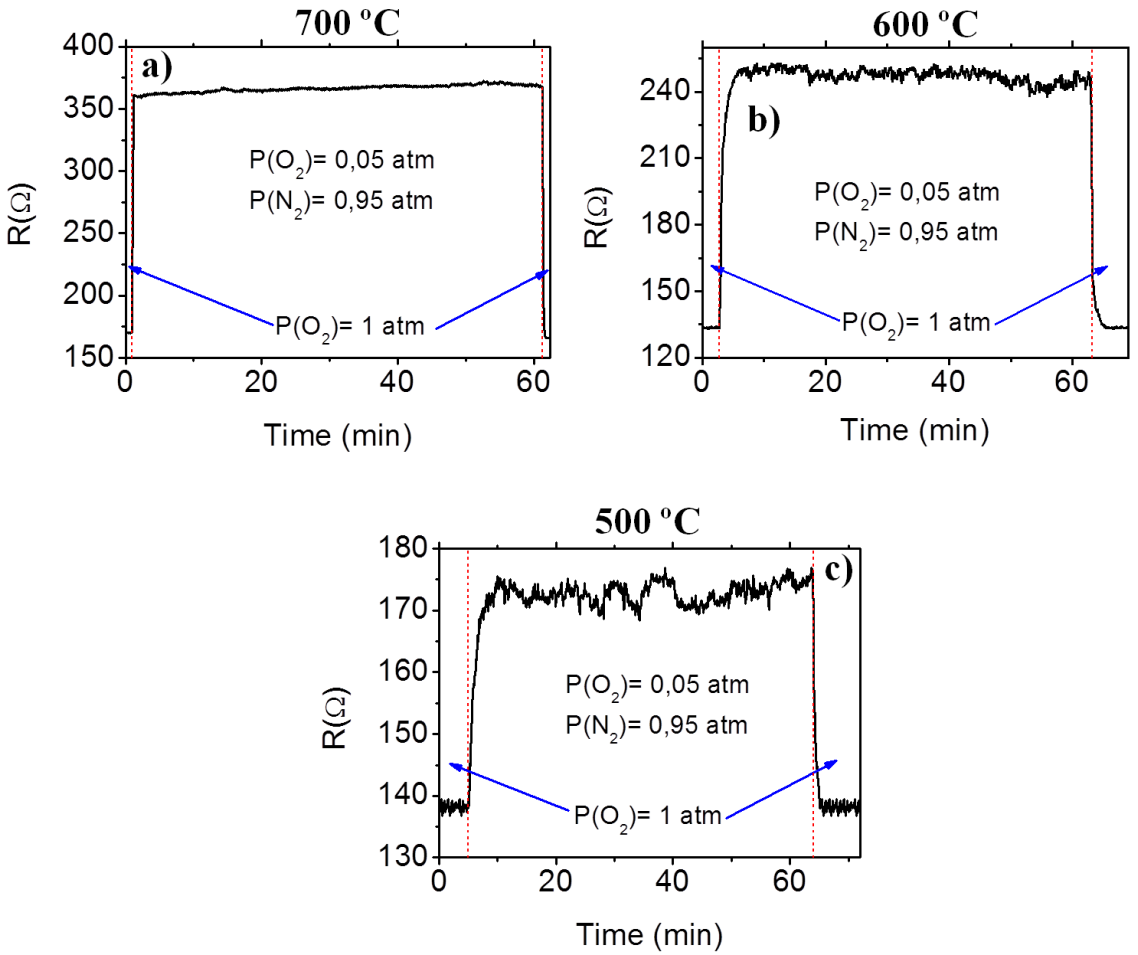

Figure 5.17. Resistance vs. time measurements for the out-diffusion process with a P_{O_2} of 0,05 atm showing that at 700 ºC the τ_{in} and τ_{out} are too small to measure them with an adequate accuracy while at lower temperatures it is possible to clearly distinguish between both of them.

Figures 5.16 and 5.17 serve as a demonstration of the low impact of the current percolation effect (described in section 5.1.5). If this effect was very important, the equivalence between in- and out-diffusion would never be reached in such a way that the lines in figure 5.16 do not extrapolate to 1. Current percolation effect, instead, would cause that the in-diffusion τ values were much lower than the out-diffusion ones, independently of the P_{O_2}.

Finally, the dependence of the in- and out-diffusion with the P_{O_2} allows, in some cases, the determination of the rds of the surface reactions. A complete explanation for that is described by Merkle and Maier in their study of the oxygen diffusion in $SrTiO_3$ films[271]. In this work, it was proposed that the equilibrium reaction rate (R^0) is related with the τ values of the in- and out-diffusion by the following expression (Eq. 5-19):

$$\boldsymbol{R^0 \propto \sqrt{k_{chem_{in}} k_{chem_{out}}} \rightarrow R^0 \propto \sqrt{\frac{1}{\tau_{in}\tau_{out}}}} \qquad \text{Eq. 5-19}$$

In the case of $SrTiO_3$ films, the relation of the R^0 with the P_{O_2} for each step of the surface reactions was described. Using the same relationships, by representing the obtained R^0 values in the CSD YBCO films at 500 ºC vs $P_{out}(O_2)^{0,53}$, it is obtained a straight line (figure 5.18). This suggests that the rds could be either the formation of O_2^{2-} molecule or the dissociation of the O_2^{2-} molecule to form two O^- ions.

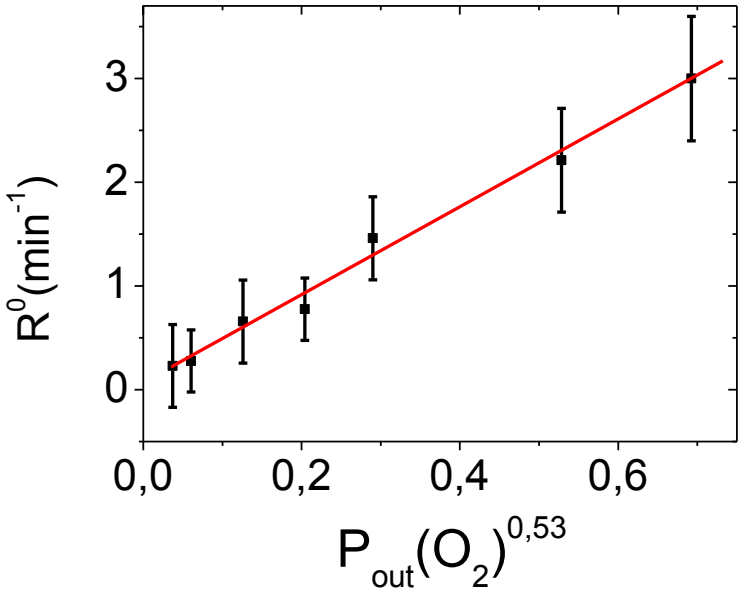

Figure 5.18. Plot of the equilibrium reaction rate R^0 for YBCO CSD films vs. $P_{out}(O_2)^{0,53}$.

It is important to note that the previous result obtained for the CSD YBCO film is based on the calculations on $SrTiO_3$ films[271]. These calculations are made assuming the adsorption equilibrium to be in the limit of low coverage and based on the bulk defect chemical data. With all these data in mind, it is clear that the determination of the rds in CSD YBCO films is only a first approximation to the problem and a deeper study of this issue is needed in order to obtain solid conclusions.

5.2.4 Discussion: Bulk controlled diffusion vs. surface controlled diffusion

The results shown in the last two sections, those devoted to the dependence of the P_{O_2} and gas flow in the diffusion processes, have provided unequivocal proofs of the surface reactions influence in the diffusion processes in the CSD YBCO films.

The main reason why the diffusion phenomenon is considered as a surface controlled process is because the surface reactions are slower than the later bulk diffusion in the ab-planes. A way to test if this is true in the CSD YBCO films is to compare the value of the diffusion coefficient in the ab-plane, D_{ab}, with the product k_{chem}*t (remind that t is the film thickness). If D_{ab} is larger than the product k_{chem}*t, then it is clear that the surface reactions are slower and, therefore, are the limiting factor of the diffusion processes. The determined values of k_{chem} for the CSD YBCO films in-diffusions are in the range of the 10^{-7} cm/s (T range of 400-500 ºC) and the thickness of the films is typically 250 nm (=250.10^{-7} cm). With these values, the product k_{chem}*t is equal to $2{,}5.10^{-12}$ cm^2/s. This value is 1-2 orders of magnitude smaller than the reported D_{ab} values (10^{-11}-10^{-10} cm^2/s)[257, 280, 283], thus confirming that the surface reactions are the limiting step in the oxygenation process in YBCO CSD films.

Previous analysis of oxygenation in melt textured ceramics and thin films have considered that bulk oxygen diffusion was the limiting step. Taking into account that bulk diffusion is faster in the YBCO CSD films than the surface processes, the obtained diffusion times in the YBCO CSD films can be used to establish an upper limit of the grain sizes and compare them with those previously determined in other YBCO samples. In the case of the samples in which the bulk diffusion is the limiting process, the grain size can be estimated using the following expression (Eq.5-20):

$$L = \sqrt{2\pi^2 \tau D_{ab}} \qquad \text{Eq. 5-20}$$

In the case of the CSD YBCO films (τ value for in-diffusion at 700 ºC), the values of L vary from 0,3-0,7 μm depending on the D_{ab} value that is chosen. As it was commented, these values correspond to an upper limit of the grain size. The grain sizes estimated for other YBCO samples were: 10^3-10^4 μm for melt textured YBCO[266], 10^1-10^2 μm for LPE films[279] or 0,2 μm for sputtering films[280]. The upper limit for the YBCO CSD films grain size is similar to the values reported in sputtering films.

Figure 5.19 shows the Ln($1/\tau$) vs. 1000/T curves for YBCO samples prepared in different ways. It is observed that the CSD film curve is situated in the top left part indicating that the τ values are the smallest in this range of temperature. The E_a values for the in-diffusion obtained for the CSD films presented in this work are not very different from those found in LPE, Sputtering or bulk ceramics. In the case of the YBCO CSD films, the values vary in the range 0,8-1 eV which are similar to the reported values (1,1-1,25 eV) in these systems. However, the τ_0 values obtained for each technique are quite different. The values of τ_0 for CSD and sputtering are in the range of 10^{-5}-10^{-7} s (depending on the changes of P_{O_2} that are used) while in the case of the LPE and MTG sample the τ_0 values are in the range of 10^{-2}-10^{-3} s. Despite the mechanism that limits the diffusion in sputtering films and in MTG and LPE samples is unknown, these differences in the τ_0 reveals that the mechanism that limits the diffusion process should be different and, probably, the surface reactions are the limiting factor (slower than the bulk diffusion) in

the CSD and sputtering films while the bulk diffusion is the limiting factor in the MTG and LPE samples (slower that the surface reactions). Therefore, it is suggested that in films with a thickness in the range of hundred of nm and with small grain size the surface reactions are the limiting factor while if the thickness increase above several μm and with large grain size, as in the case of the LPE samples (10 μm of thickness with large grains of 10^1-10^2 μm), the limiting factor is the bulk diffusion

The microscopic mechanism leading to these E_a values may arise from different sources depending on the phenomenon that controls the diffusion. In the case of a bulk controlled mechanism the E_a corresponds to the energy barrier that the oxygen atoms have to overcome to diffuse inside the YBCO structure. On the other hand, the E_a values in a surface controlled mechanism arise from the potential barrier that the oxygen molecules have to overcome to adsorb in the surface and start the surface reactions.

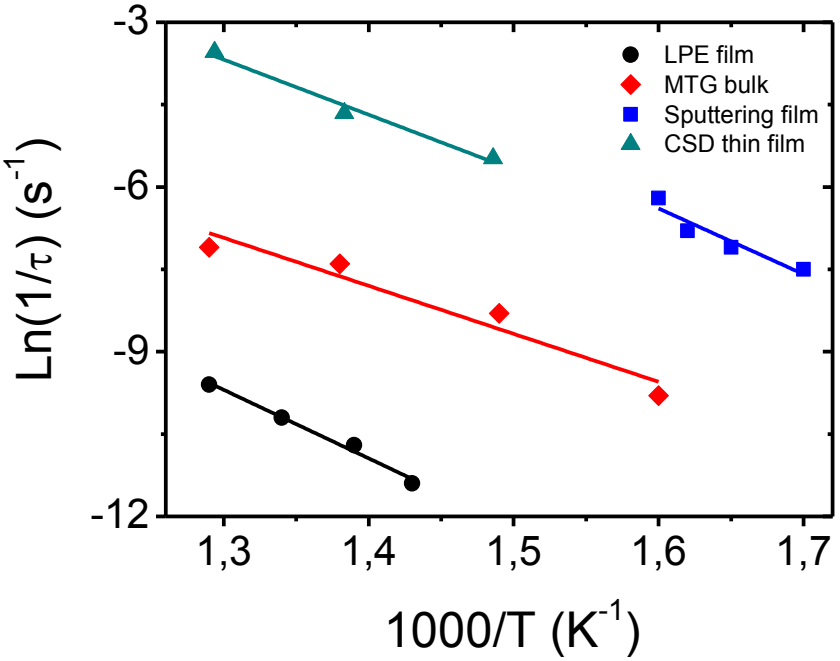

Figure 5.19. In-diffusion Ln(1/t) VS 1000/T curves for the LPE YBCO film[279], Sputtering film[267], MTG bulk[266] and CSD film.

5.3 Dependence of YBCO film thickness in the oxygen diffusion

Recent studies have revealed interesting thickness effects on the oxygen diffusion and, in particular, on the oxygen surface activity, in functional oxides. There is still not a satisfactory explanation for this effect, but the preliminary results indicate that the surface exchange coefficient, k_{chem}, vary widely. For example, in the case of $La_{0,8}Sr_{0,2}CoO_3$ films on yttria-stabilized zirconia (YSZ), it was found that k_{chem} increases with a decrease of the thickness of the films[284]. On the other hand, for $La_2NiO_{4+\delta}$[285] and gadolinium-doped ceria[286] films an increase in k_{chem} was observed with the thickness increase. In the case of the YBCO films, no systematic study about the effect of the thickness in the diffusion processes has been reported up to now.

In this work, three YBCO films with different thicknesses were prepared: 50, 130 and 250 nm. The three films were synthesized in the same way, using the standard TFA pyrolysis and growth processes used previously. The experiments consist of out- and in-diffusion measurements. The τ values and k_{chem} were calculated from these measurements to finally obtain the E_a and k_0 values for the out- and in-diffusion at each thickness. The results are shown in figure 5.20.

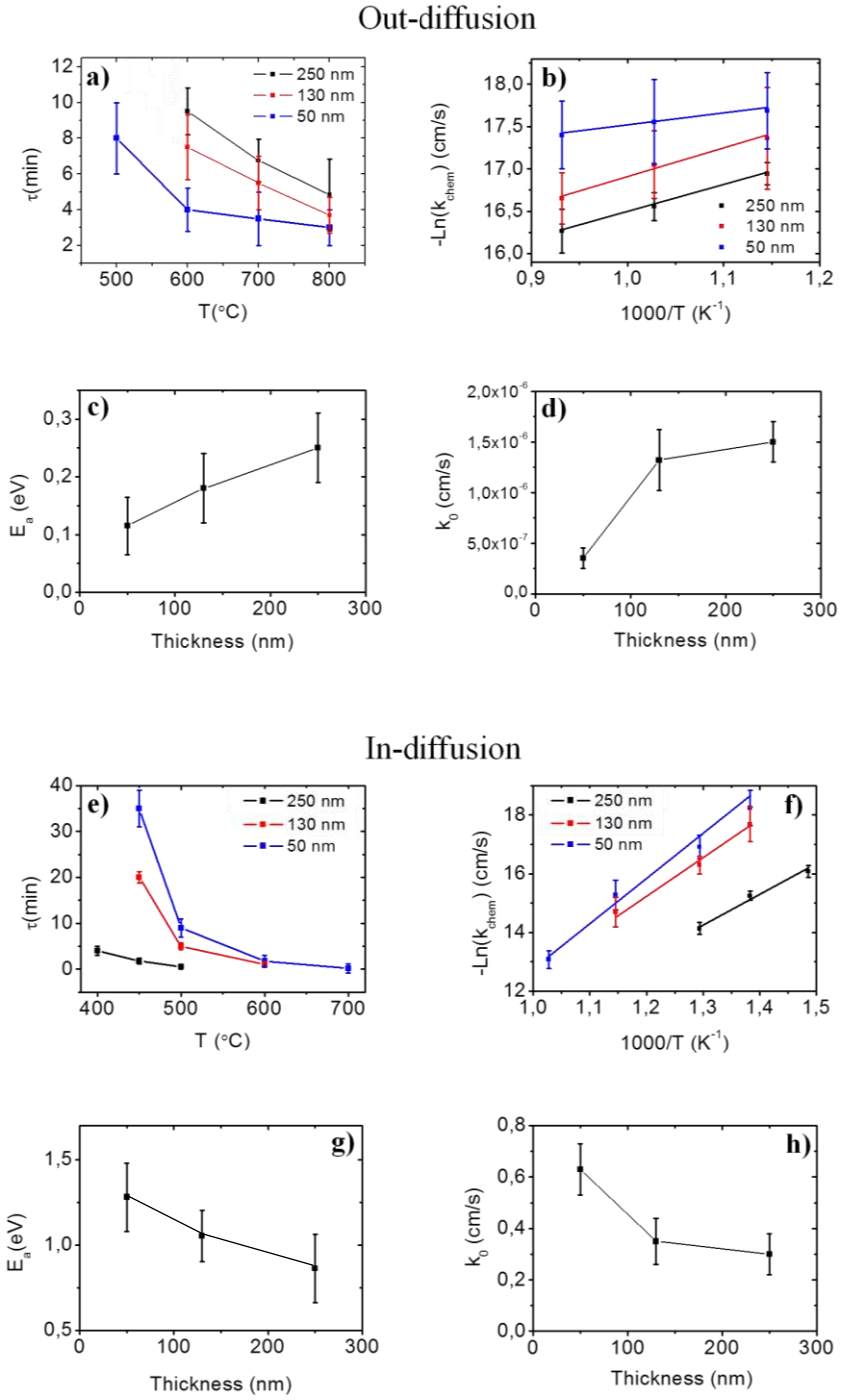

Figure 5.20. Results about the out- and in-diffusion experiments in different thickness YBCO films. Graphs a) and e) show the evolution of the τ values with the temperature for the out- and in-diffusion respectively. Graphs b) and f) present the $-Ln(k_{chem})$ vs. 1000/T curves for the out- and in-diffusion respectively. Graphs c) and g) show the E_a values dependence with the thickness of the films for the out- and in-diffusion process and, finally, graphs d) and h) the dependence of the k_0 values with the thickness.

The most important conclusion that can be extracted from the results shown in figure 5.20, is that the microstructural changes associated to the modification of film thickness vary the kinetics of the diffusion process. Figures 5.20 a) and e) show how the τ values (and therefore the k_{chem}) change with the thickness for the out- and in-diffusion process, respectively. These changes imply variations in the E_a and k_0 values. Figures 5.20 c) and g) present the evolution of the E_a values with the thickness of the films for the out- and in-diffusion respectively. It is observed that, in the case of the out-diffusion process, the higher the thickness is, the larger the E_a values. The opposite occurs in the case of the in-diffusion. In this case, the higher the thickness is, the lower the E_a values. In the case of the k_0 values, the same trends are maintained. In the case of the out-diffusion process, the higher the thickness is, the larger the k_0 values and in the case of the in-diffusion, the higher the thickness is, the lower the k_0 values. This means that, once again and similarly to some previous cases, the E_a has more influence to determine the τ values because in both cases the higher values of the adsorption probability correspond to the thickness with larger values of τ.

In order to find an explanation for this behavior, the main structural differences between the three films need to be investigated. The three films are epitaxial YBCO with no presence of other crystalline orientations or secondary phases. However, the strain values of the films are different. These differences in the strain values come from the fact that the granularity effect (already explained in chapter 3) increases as the thickness decreases (figure 5.21). This indicates that the growth process is not the optimum one for YBCO films which are below the 200-250 nm (actually, as it was mentioned before, the "standard growth process" was optimized for 250-300 nm YBCO films) and, therefore, the intergranular connectivity is not optimized, as it will be demonstrated also by superconducting properties measurements. The observation of granularity effects indicates that the calculated strain values probably arise from mesostrain contributions (grain boundaries localized strain).

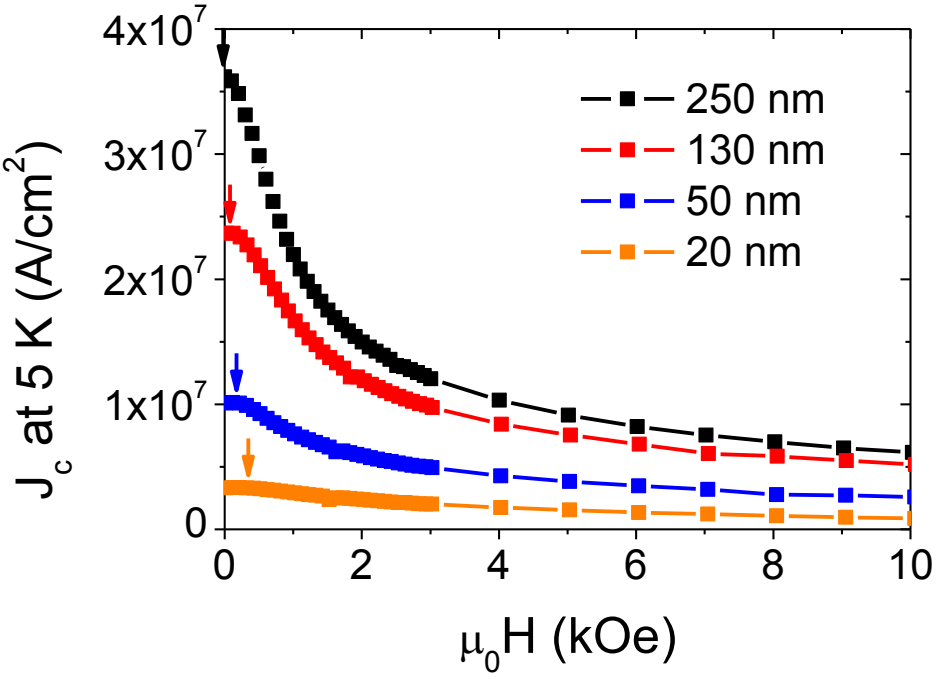

Figure 5.21. J_c at 5 K evolution with the magnetic field for pristine YBCO films of different thickness showing the displacement of the maximum (indicated with arrows) value of the J_c to magnetic fields $\neq 0$ as the thickness decreases.

If the E_a and k_0 values are represented as a function of the strain values (it would be nanostrain in the case of the 250 nm film and nanostrain+mesostrain in the other cases), a similar trend as in the case of the figures 5.20 c) and f) is obtained (figure 5.22).

Figure 5.22 clearly demonstrates that the strain of the films is a parameter that influences the kinetics of the diffusion processes. It is observed that while in the out-diffusion process high values of strain reduce the E_a (and reduce the k_0 but remind that it was said that the τ values are more influenced by the E_a values in this case) and, therefore, favor the out-diffusion process, in the in-diffusion process high values of strain increase the E_a values (and also the k_0 values) and, therefore, hinder the in-diffusion process. Thus, opposite tendency is found that may indicate that the rds is different for the out- and in-diffusion processes.

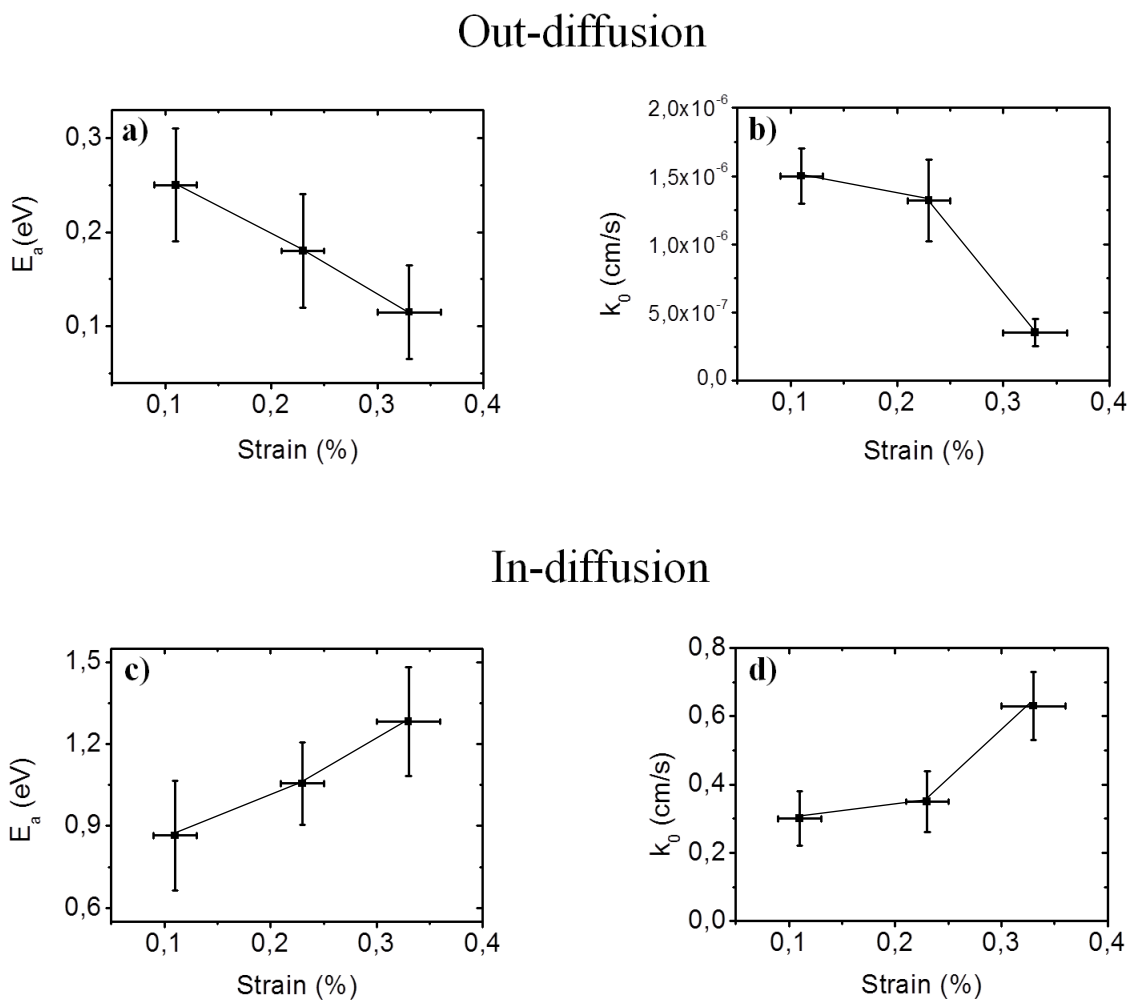

Figure 5.22. Evolution of a) and c) E_a values for the out- and in-diffusion respectively and b) and d) k_0 values for the out- and in-diffusion respectively with the strain values. The plotted strain values above 0,2 % (corresponding to 130 and 50 nm films) come from the nanostrain+mesostrain influence.

An explanation for a similar phenomenon was reported by Lu Yan and Paul A. Salvador in the case of $La_{0,7}Sr_{0,3}MnO_3$ (LSMO) thin films[287]. Their results about the oxygen in-diffusion in LSMO films confirms that as the thickness is increased, the E_a values decrease (from 1,5 eV for a 50 nm film to 0,75 eV for a 600 nm film). They attributed this effect to the relaxation of the films by a dislocation−mediated process, a

process that deeply modifies the physico-chemical properties of the films[288]. The thinnest films showed higher values of strain because they are coherently strained to accommodate with the substrate. As the thickness is increased, the strain is relaxed by the creation of dislocations that propagate from the surface to the interface. Therefore, the higher the thickness is, the larger the density of dislocations. They explained the reduction of the E_a values and the surface exchange rate at higher thickness due to the action of the dislocations. The surface is modified in such a way that the exchange of oxygen is favored in this situation. This mechanism if supported by various works that report the effect of the dislocations on the heterogeneous catalysis on solid surfaces[289, 290] or the increase of the oxygen mobility[291].

The case of the CSD YBCO films studied in this work is different. It is observed also a decrease of the strain values as the thickness increase but this is not caused by the increase of the dislocations but by the reduction of the mesostrain. This means that, as the thickness increases, the intergranular connectivity improves. The mechanism by which these changes in the strain modify the kinetics of the oxygen diffusion in YBCO thin films thin films is still unclear. However, what it is clear is that the difference in the diffusion kinetics is attributed to the different degree of distortion that is present in the films. Actually, it is proved that the distortions in the structure could modify both the structure[292] and the physic-chemical properties[293] of the thin film´s surface. And this change, considering a surface reaction diffusion mechanism, is enough to justify the changes in both the out- and in-diffusion for the different thicknesses of the YBCO films. Further investigations of the physico-chemical properties of films with different thickness need to be performed to discern how the rds is modified by the observed defect structure.

5.3.1 Thickness dependence on the oxygen content

It has been shown in the previous section that the film thickness and its associated microstructure changed both the oxygen out- and in-diffusion kinetics. To study the consequences of the thickness in the oxygenation process and, in particular, in the superconducting properties, pristine YBCO films of different thicknesses grown using an unique processing conditions (standard growth process) and exposed to the same oxygenation process have been studied. The c-parameter and the T_c were measured. The oxygenation process was set at 450 ºC during 210 min with 1 atm of oxygen and 0,15 l/min of gas flow. Under these conditions it is expected that the oxygenation is completed and homogeneous. However, as it will be shown, some differences in the superconducting properties are still detected. The results are shown in figure 5.23.

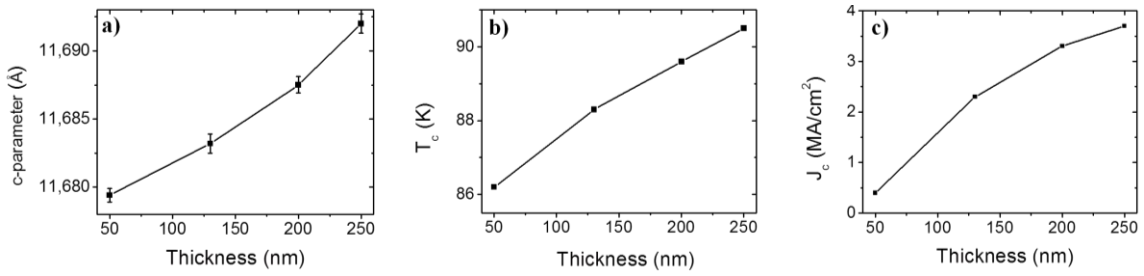

Figure 5.23. Evolution of the a) c-parameter, b) T_c, and c) J_c^{sf} at 77 K with the thickness of the pristine YBCO films oxygenated with the same process (450 ºC during 210 min with 1 atm of oxygen and 0,15 l/min of gas flow).

The results show that both the c-parameter and the T_c vary with the thickness of the film when they are grown under the same conditions. Actually, as it has been suggested before, both parameters are linked. According to the measured c-parameter values and assuming the general validity of the curve shown in figure 5.1[251], the results suggest that all the films are in the overdoped regime. The δ vary from almost 1 for the 50 nm film to 0,94 for the 250 nm film (optimum doping δ=0,92).

It was shown in the previous chapter that, for all the thicknesses, the equilibrium state was reached in these oxygenation conditions (these results are not exactly for the equilibrium state because after the 210 min at the oxygenation temperature, the temperature is decreased until room temperature at 2,5 ºC /min so the equilibrium conditions can be modified during the descent) . However, it is suggested in view of these results that the oxygen content in the equilibrium state varies with the thickness of the films, probably due to their modified microstructure. In the case of the 50 nm films, in the equilibrium state, almost all the oxygen vacancies have been eliminated, while in the case of the thicker films, there are still a few of them. The experimental T_c is also consistent with the overdoped regime in which the T_c decays below the optimum value.

If now the oxygenation process is performed at a different temperature, one would expect that the oxygen content at the equilibrium changes according to Shimoyama et al[278]. Actually, the oxygen content in the equilibrium decreases as the temperature is increased. This is exactly what is observed in figure 5.24 when the oxygenation process is changed from 450 ºC to 550 ºC.

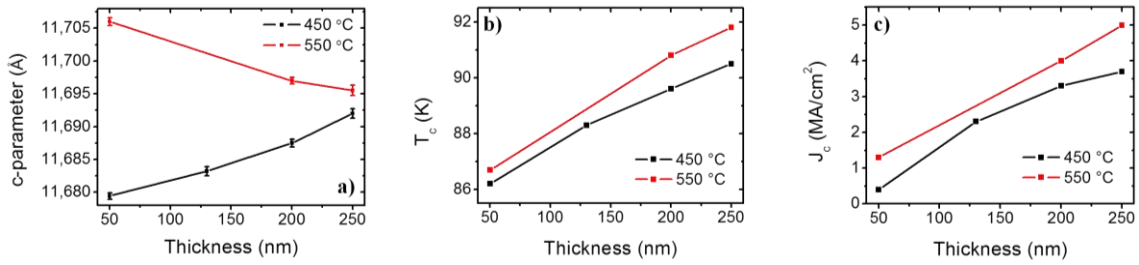

Figure 5.24. Evolution of the a) c-parameter, b) T_c and c) J_c^{sf} at 77 K with the thickness of the pristine YBCO films oxygenated with the different processes: 450 ºC during 210 min with 1 atm of oxygen and 0,15 l/min of gas flow (black line) and 550 ºC during 210 min with 1 atm of oxygen and 0,15 l/min of gas flow (red line) and.

When the oxygen process is changed to a higher temperature (550 ºC), the c-parameters for all the thicknesses increase. This means that the oxygen content inside the films is now lower than before. Actually, the 50 and 130 nm films change to the underdoped regime (δ<0,92), as it can be observed in figure 5.25. The T_c values are higher for all the thicknesses (figure 5.24 b)) because δ is nearer to the optimum doping (δ=0,92) in all the cases. Actually, for the oxygenation at 550 ºC, the film of 250 nm is very close to the optimum doping (δ=0,92), as it observed in figure 5.25 and the T_c and the J_c^{sf} at 77 K are the highest (91,5 K and 5,1 MA/cm^2 respectively).

It is important to remark that, as it was explained in chapter 3, the increase of the mesostrain could also decrease the J_c values whatever the thickness. So, probably the J_c^{sf} at 77 K are influenced to a greater or lesser extent by this effect.

It is observed that the response to the change in oxygenation conditions is higher as the thickness decreases as it can be seen also in (figure 5.24 a)). This entails that, as the

thickness decrease, the sensitivity to the oxygenation conditions is higher and small changes in the conditions may cause large variation in the c-parameter and therefore in the superconducting properties. This is an expected behavior since the number of oxygen vacancies in the thinner films is lower. This is not so severe in the case of the thicker films due to the higher number of oxygen vacancies and small changes will not affect so much the overall behavior of the film.

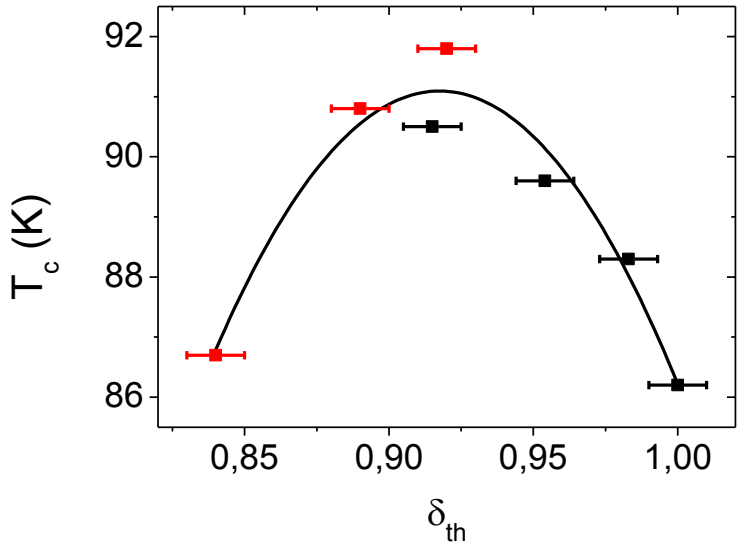

Figure 5.25. T_c as a function of the theoretical δ values (δ_{th}) of the films with different thickness and oxygenated at 450 ºC (black squares) and at 550 ºC (red squares).

In order to ensure the validity of the results, the experimental c-parameters values were compared with the theoretical values that should be obtained according the T_c experimental values taking figure 5.1 as a reference. Figure 5.26 shows that both values fit reasonably well to a straight line demonstrating the validity of the presented results.

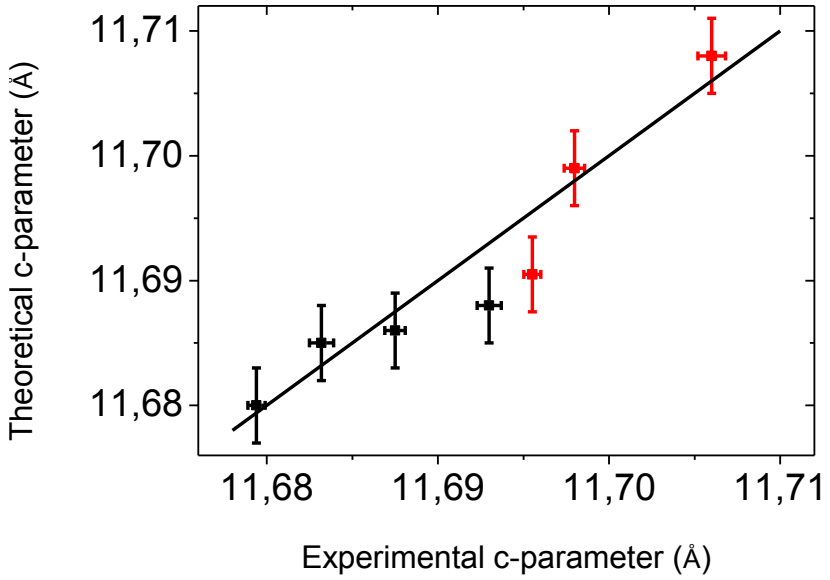

Figure 5.26. Theoretical c-parameter determined from the observed T_c values (taken curve in figure 5.1 as reference) vs. experimental c-parameter. Black squares correspond to 450 ºC and red squares to 550 ºC oxygenation processes.

5.4 Oxygen diffusion in YBCO films with silver addition

It was demonstrated in previous sections that in CSD YBCO films the surface reactions are the limiting factor in the diffusion processes. It was also found that at low temperatures (below 550 ºC in the case of the out-diffusion and below 400 ºC in the case of the in-diffusion) the diffusion processes are too slow to reach the equilibrium state within the used measuring window time, with the consequence of the properties degradation.

Looking at the equilibrium phase diagram reported by Shimoyama et al[278], one realizes that, as the temperature decreases, the oxygen content in the equilibrium state increases. This fact increases also the number of carriers and, therefore, the superconducting properties are improved[294, 295]. For this reason, to achieve the equilibrium in the oxygenation process at the lowest possible temperature is beneficial for the final performances of the YBCO films. However, in the case of the pristine YBCO, it was shown that there is a limit at 400 ºC.

Researchers have been looking for a path to overcome this limit. One solution to the problem, proved in other functional oxides, is using silver as a catalyst to enhance the whole process. The use of silver as a catalyst for selective oxidation processes in different fields, especially in the hydrocarbon industry, is well-known[296, 297]. The role of the silver is to facilitate the O_2 molecules dissociation and reduction. When an O_2 molecule is adsorbed in the silver surface, there is an electron transfer from the silver to the π^* orbitals of the O_2 molecules. This causes a decrease in the binding energy of the O=O bond facilitating its rupture[298].

This strategy was tested successfully in $SrTiO_3$ (STO)[269]. A layer of silver (100 nm, annealed at 1023 K during 7 days) was deposited on top of the STO by sputtering. After this long annealing process, the silver layer transforms into NPs in the surface. The STO films with these silver NPs on the top showed lower E_a and also much higher k_0 values than the pristine samples[269].

This approach has been applied to YBCO CSD films. In this case, however, the silver was introduced directly in the YBCO solution. A YBCO+5%M Ag solution is prepared by adding Ag-TFA salt to the YBCO solution and some films were synthesized. The final result is similar to the previous reported results in SUMAN group[131]. The Ag shows a tendency to be placed in the films´ surface before its sublimation and at 810 ºC is it supposed that some traces of silver remains in the surface (at 720 ºC some silver NPs are still seen in the surface after the growth) although the element can not be easily detected[131]. Under these conditions, the evolution of the resistance both for the out-diffusion and the in-diffusion processes has been measured in these 250 nm YBCO+5%M Ag films. The results, concerning the relaxation times and the surface exchange coefficient, are shown in figure 5.27.

Figure 5.27 a) shows the evolution of the τ values as a function of the temperature for the out-diffusion of the YBCO+5%M Ag compared with the pristine YBCO film. One can see that the τ values slightly differ in both cases. In the case of the pristine YBCO films the E_a value is 0,25±0,05 and in the case of the YBCO+5%M Ag film the value is 0,42±0,08 eV. The k_0 values also differ: $1{,}5.10^{-6}\pm 8.10^{-7}$ cm/s for the pristine films and $3{,}2.10^{-5}\pm 7.10^{-6}$ cm/s.

More interesting results are shown in figure 5.27 c). Here, the τ values for the in-diffusion are presented. It is observed that the YBCO+5%M Ag reaches the equilibrium

state down to lower values than in the case of the pristine YBCO film (below 400 ºC the black line is plotted to see clearly the time difference with the Ag addition films). The equilibrium is even reached at 300 ºC.

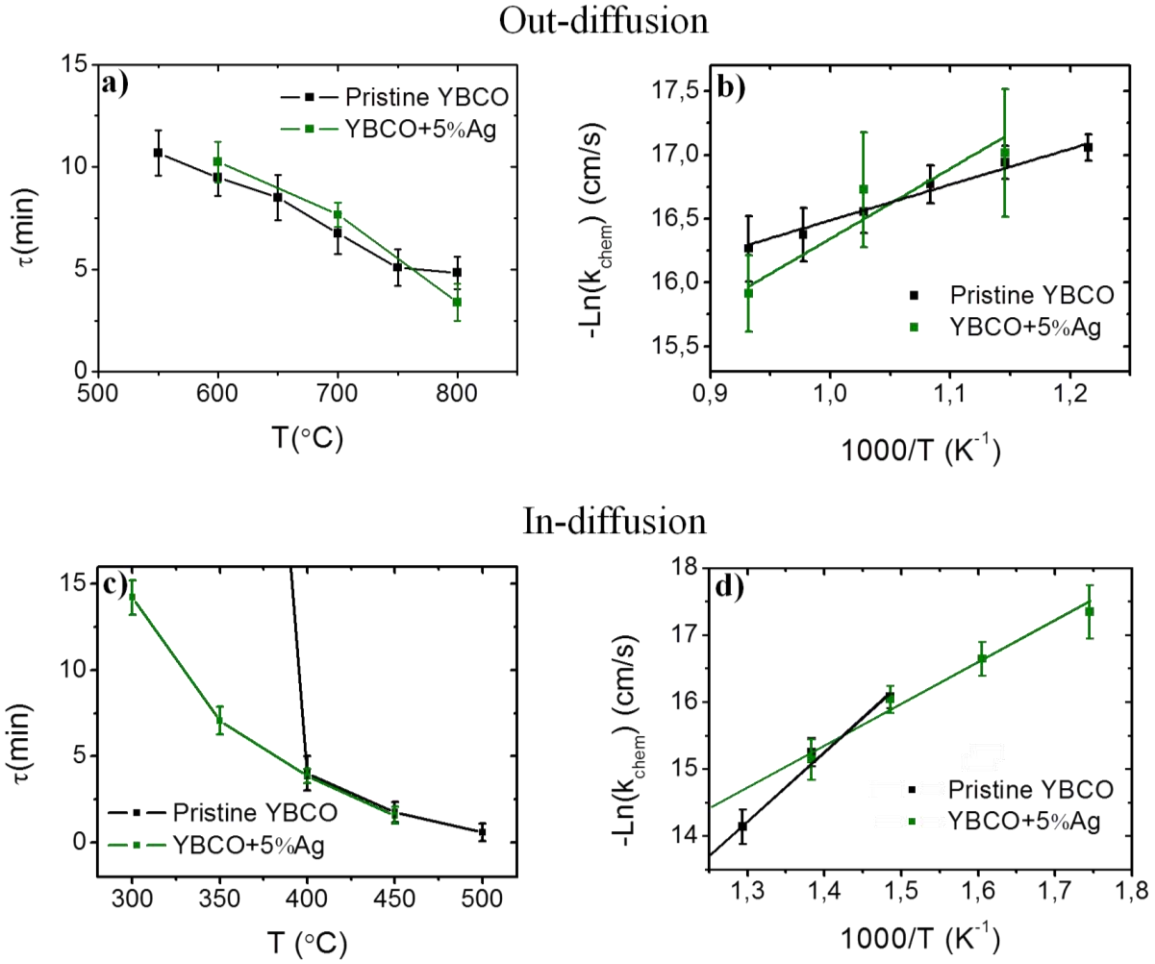

Figure 5.27. Evolution of τ values with the temperature and $-Ln(k_{chem})$ vs. 1000/T curves for the out-diffusion (a) and b)) and the in-diffusion (c) and d)) for a YBCO+5%M Ag film in comparison with a pristine YBCO film.

The observed behavior of the YBCO+5%M Ag films can be modeled as two channel oxygen diffusion process having different temperature dependences (different E_a and also k_0 values). Above 400 ºC the τ values of the pristine and the YBCO+5%M Ag films are similar indicating almost equivalent temperature dependences (same E_a and k_0 for both films with the same values obtained for the in-diffusion in pristine films). However, below 400 ºC, the τ values differ widely suggesting a change in the kinetics of process of both films. In this case the reaction rate of the pristine films, it becomes extremely low resulting in large values of τ. On the other hand, the reaction rate in the YBCO+5%M Ag films remains in respectable values below 400 ºC due to the effect of the silver as catalytic agent which lead to measurable values of τ. In these conditions, a reduction of the E_a is observed in YBCO+5%M Ag films (E_a=0,51±0,09 eV) while the $k_0=5{,}2.10^{-4}\pm 8.10^{-5}$ cm/s. In the same conditions (below 400 ºC), it is expected a larger value of E_a and a lower value of k_0 for the pristine films

These last results demonstrate that the oxygen in-diffusion process is favored at low temperatures by the silver presence in the surface. When silver is on the surface of the

YBCO, the number of O_2 molecules that are adsorbed and dissociated is larger due to the reduction of the bond energy and, probably, due to an enhancement of the sticking probability. It has been suggested that the oxygen atoms diffuse into the silver bulk and arrive to the films (see complete path in figure 5.28). This oxygen path was proposed for a silver membrane kept at temperatures above 310ºC. Below this temperature, the atomic oxygen is found to be locked at the silver surface of the silver without diffusion into the silver layer[299-301]. The overall result of this phenomenon is the acceleration of the surface reactions. Probably the silver is able to fasten the rds, which was suggested to be the dissociation of the O_2^{2-} molecule (or the formation of O_2^{2-}). However, at higher temperatures this effect is negligible because the number of O_2 molecules potentially influenced by the Ag is smaller than those which are unaffected (value of k_0 below 400 ºC is much smaller that the calculated k_0 above 400 ºC). For this reason, the silver effect is only noticed at low temperature where the energy to split and reduce the O_2 molecules in standard conditions (with no silver) is very large and the silver acts reducing these energies and maintaining the reaction rate at reasonable values.

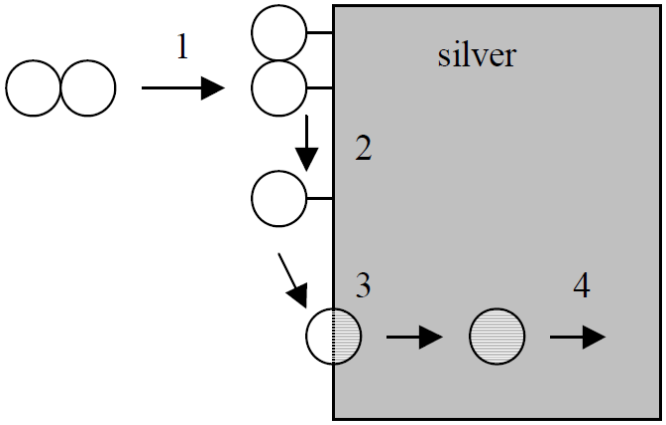

Figure 5.28. Path that the oxygen follows through a silver membrane. The O_2 molecule is 1) absorbed in the silver surface and 2) dissociated. After that the oxygen atoms 3) migrate in the first layers of the silver and then 4) they diffuse in the bulk to arrive to the YBCO layer.

The changes in the low temperature oxygen diffusion rate al in YBCO+5%M Ag films have important consequences when the superconducting performances are analyzed. It has been demonstrated in a previous work in the SUMAN group that the best superconducting performances in the YBCO+5%M Ag films (T_c=90,7 K and J_c=5,0 MA/cm^2) were obtained by performing an oxygenation process at 350 ºC during 210 min. This implies a drastic decrease of the optimum oxygenation temperature with respect to the pristine YBCO films (550 ºC)[277]. This confirms that the oxygen in-diffusion process in YBCO+5%M Ag films is more effective than in pristine films at low temperatures.

On the other hand, the out-diffusion does not suffer any change by the silver presence or it becomes even less favorable than in the case of the pristine YBCO films. This happens because the catalytic effect of the silver is effective only in one direction, i.e., reduce the binding energy of the O_2 bond. The catalytic reaction starts with O_2 molecules which have to be reduced while the out-diffusion starts with O^{2-} ions that have to be oxidized to go out from the YBCO structure and thus, the catalytic cycle is not effective. The out-diffusion process can be actually disturbed because the silver can block some of the pores and grain boundaries from which the O^{2-} ions reach the surface.

5.5 Oxygen diffusion in YBCO nanocomposites

The studies of the diffusion process that were carried out in pristine YBCO thin films have confirmed that the surface reactions play a key role in the diffusion process. However, as it was commented in previous chapters, the field of superconductivity is, nowadays, very interested in nanocomposite films due to their superior performances in some applications. For that reason, the oxygen diffusion process in 250 nm YBCO+10%M BZO films was also studied.

The study, in this case, was not as deep as in the case of the pristine YBCO films. Only a simple analysis of the out- and in-diffusion processes as a function of the temperature was performed. However, this study is the first one about diffusion issues in nanocomposites and the result gives the first idea of how the diffusion process works in nanocomposites.

The out-diffusion experiments were performed by setting A atmosphere (P_{O_2}=1 atm) and then measuring the resistance with B atmosphere (P_{O_2}=2.10^{-4} atm) at different temperatures. The in-diffusion experiments were carried out applying B atmosphere and then measuring the resistance with A atmosphere. The results for the out- and in-diffusion are shown in figure 5.29.

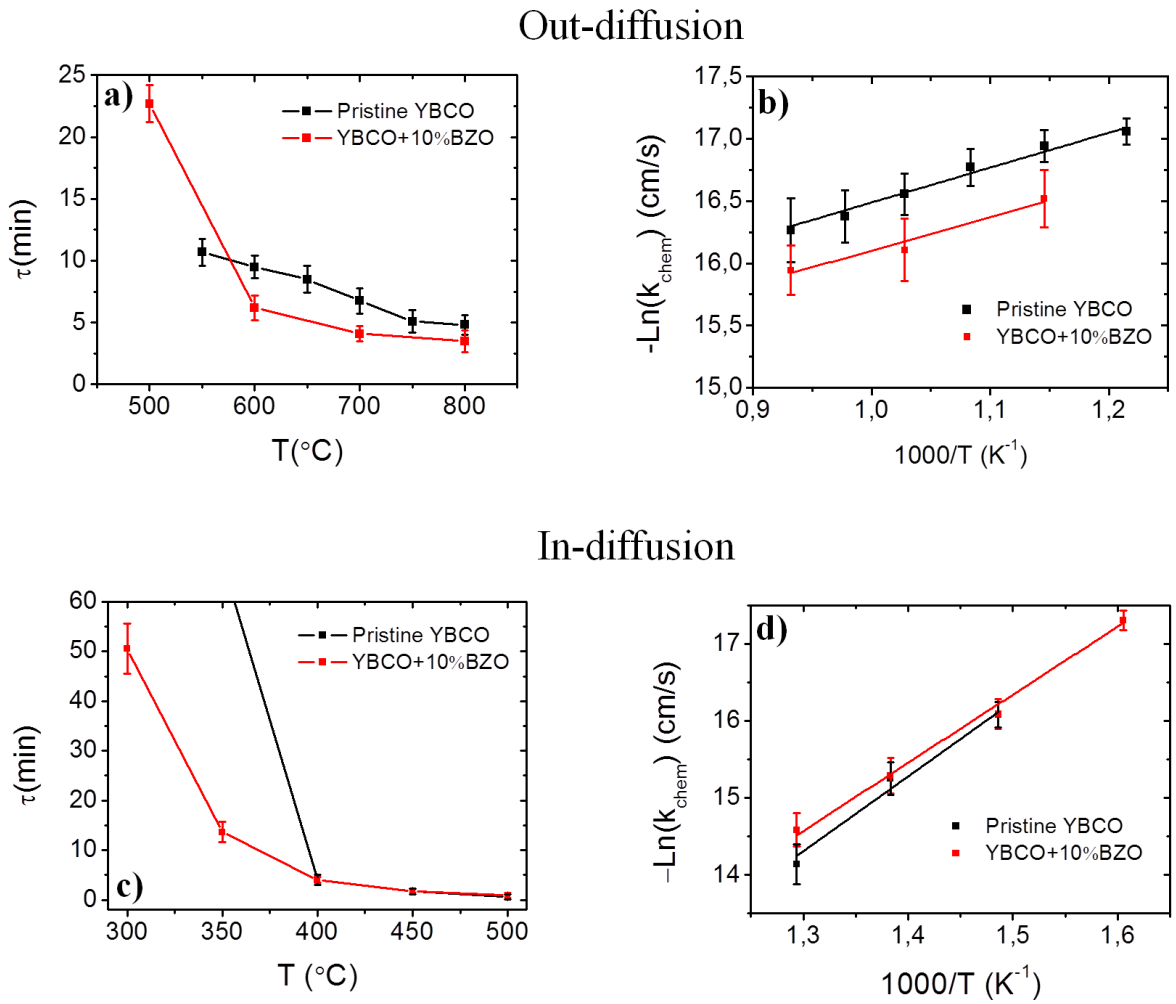

Figure 5.29. Evolution of τ values with the temperature and $-Ln(k_{chem})$ VS 1000/T curves for the out-diffusion (a) and b)) and the in-diffusion (c) and d)) for a YBCO+10%M BZO film.

Looking at the τ values plotted in figure 5.29 a) and c) (out-diffusion and in-diffusion respectively) it is possible to see that the equilibrium state (saturation resistance) is reached until lower temperatures for the YBCO+10%M BZO than in the case of the pristine YBCO films. Actually, in the case of the in-diffusion, at 300 ºC degrees a saturation resistance is still seen (the black line below 400 ºC in the case of the pristine YBCO films is added just to see the time difference). This indicates that, at low temperatures (below 550 ºC for the out-diffusion and below 400 ºC for the in-diffusion), both oxygen diffusion processes are faster in the case of the nanocomposites than in the case of the pristine YBCO films.

However, figure 5.29 b) and d) shows that the slopes of the lines are quite similar in both cases in the represented temperature ranges. For the YBCO+10%M BZO film the E_a values are 0,23±0,04 eV for the out-diffusion and 0,8±0,1 for the in-diffusion. These values are calculated between 550 and 800 ºC in the case of the out-diffusion and between 350-400 ºC (350 ºC for the nanocomposite and 400 ºC in the case of the pristine YBCO) and 500 ºC in the case of the in-diffusion. Focusing in the case of in-diffusion process, it is noted that the k_0 values for both kind of films are also quite similar: 0,29±0,09 cm/s for the pristine film and 0,06±0,01 cm/s for the nanocomposite films.

The above results show that both the E_a and k_0 values are similar in both cases and this should entail that the diffusion dynamics were similar in both cases. However, in the case of in-diffusion, it can be observed that the equilibrium is reached at lower temperatures in the nanocomposite films. It is particularly important because this implies that the oxygenation temperature can be decreased with respect to the case of pristine YBCO obtaining a complete diffusion process (remember that if the equilibrium is not reached, this means that the oxygen continues to move and the diffusion process is not completed). This difference is probably related to do the microstructure influence on the surface reactions (all the results indicate that, in both cases, the surface reactions dynamics are similar).

These changes in the diffusion rates could be also associated to the fact that in the nanocomposite films the nanostrain values are higher than in the pristine YBCO films. The strain values in the case of BZO nanocomposites (contribution of nanostrain+mesostrain) are in the range of 0,2-0,25% which implies a higher degree of distortion of the YBCO structure than in the case of the pristine YBCO (ε = 0,11±0,01%). As it was mention in section 5.2, the change in the microstructure results in differences in the diffusion kinetics. A more thorough investigation of the relationship between the nanostructure and oxygenation kinetics in nanocomposite YBCO films is therefore required

5.6 Conclusions

This chapter was devoted to the study of oxygen diffusion processes in YBCO and nanocomposite films. In the field of HTS, there is a lack of knowledge about the mechanisms of the oxygen diffusion processes in thin films that this work has faced. Some questions remain still unclear about the liming factors of the diffusion, but we have clearly shown that the surface exchange rates are the dominant ones. The role of the different processing parameters in the oxygen incorporation into YBCO and also the role of the microstructure of the films have been studied.

The use of the some catalytic agents (silver in this case), which were previously used successfully in other functional oxides to accelerate oxygen transfer, was also

investigated here for the first time in YBCO and the way in which the catalyst works was also explained.

Finally, the diffusion in YBCO nanocomposites was also studied for the first time. The first clues about how the diffusion processes work in this kind of thin films was discussed.

Through this chapter the main conclusions that were extracted are the following:

- It has been demonstrated that the oxygen diffusion processes are limited by the surface reactions. Irrefutable proofs were given to show this. The diffusion dependence found here with gas flow and P_{O_2} can not be explained without consideration of the diffusion as a surface controlled process. It was demonstrated that both parameters affect the oxygen adsorption in the YBCO surface.
- It was also proved that the percolation effect has not a strong influence in the experimental analysis of the diffusion processes by means of in-situ electrical resistance measurements.
- The rate determining step (rds) for the YBCO in-diffusion process was suggested to be either the formation of O_2^{2-} molecule or the dissociation of the O_2^{2-} molecule to form two O^- ions.
- The microstructure and the degree of distortion in the YBCO have some influence on the oxygen diffusion kinetics.
- The used of silver as a catalytic agent was demonstrated to be very effective. The reduction of E_a was quite significant at low temperatures allowing to oxygenate films containing Ag at much lower temperatures than pristine films. It is suggested that silver helps to reduce the strength of O=O bond reducing drastically the overall surface reaction time.
- Oxygen diffusion in nanocomposite films is strongly influenced by the presence of defects in its structure as it was demonstrated by the observed changes in the E_a in films with different strain (nanostrain+mesostrain) values.

6
General conclusions

This work has been focused on the preparation and detailed characterization of $YBa_2Cu_3O_{7-\delta}$ (YBCO), $GdBa_2Cu_3O_{7-\delta}$ (GdBCO) and different YBCO and GdBCO nanocomposites thin films by Chemical Solution Deposition (CSD), a scalable, versatile and low cost technique.

We have demonstrated through these pages that it is possible to enhance the performances of the pristine YBCO films by a fine control of its microstructure. The work that we have done with in-situ nanocomposites has shown that the use of novel combinations of NPs lead to a nanostructured YBCO microstructure which presents different features with respect to the pristine films but also with respect to the single phase nanocomposites. These mixt YBCO nanocomposite films allows the increase of the NPs concentration up to 15% minimizing the coarsening effect observed in the single phase nanocomposites films at so high NPs concentration. It has been also evidenced that in the case of the mixt nanocomposites a shortening of the SFs is produced which causes a strong enhancement of the pinning properties. In particular, it is observed a large increase of the H*, i.e., the crossover magnetic field from single vortex pinning to the collective pinning, with respect to the pristine YBCO and single phase nanocomposite films. This could be explained by the effect of the stacking faults that cause strained regions, in which the Cooper-pair formation is suppressed, in their perimeter by partial dislocations that act as pinning centers enlarging the single vortex pinning regime.

Our work with YBCO in-situ nanocomposite films has also paid attention to thick films. The development of thick films is really important from the industrial point of view to enlarge the current capabilities of the Coated Conductors. However, the increase of the film thickness by using the CSD process has to face with several problems in the pyrolysis

process. Inhomogeneities may appear related with the stress released during the huge shrinkage of the films. The crystallization process also requires a tuning of the processing parameters due to the changes in the supersaturation conditions associated to the thickness increase. We have deeply studied the evolution of the structural and superconducting properties of the nanocomposite thick films and we have identified that some hindrances may occur. For instance, the mesostrain associated to the granularity effects limits the nanostrain contribution to the pinning enhancement. Also, the presence of unreacted phases acting as current blockers may have an adverse effect in the current flow.

Within our objective of developing in-situ nanocomposite films, we have also devoted an extended effort to the preparation of GdBCO thin films. GdBCO thin films may offer some advantages with respect to the YBCO films due to the T_c enhancement. However, the synthesis of the GdBCO thin film by CSD is not easy and has required the development of a new Low-Fluorine Solution which allows the growth of homogeneous thin films with a high reproducibility. It was also necessary to define a new growth process that we called "Flash-Heating" process in order to achieve epitaxial GdBCO films. Once the novel processes for the GdBCO pristine films were established, we have been able to synthesize GdBCO+20%M Gd_2O_3 nanocomposite thin films that showed promising superconducting properties and enhanced pinning performances as compared to the pristine GdBCO thin films and a similar behavior to YBCO nanocomposites.

We have also established the basis for a novel ex-situ approach to prepare CSD YBCO nanocomposite based on the use of colloidal solutions. This approach was born with the idea of overcoming certain limits, related with the NPs size and reaction control, that are intrinsic to the in-situ approach. As it is common in the first stages of challenging projects, we have dealt with many different difficulties (stability of NPs, ligand incompatibilities, NP pushing, NP coarsening, reactivity, etc). However, we have succeeded in fully overcoming all these difficulties by proposing adequate solutions for each of them. We have achieved the first ex-situ nanocomposite thin films that can compete with the in-situ nanocomposite films performances. This part of the work has required a big effort to integrate knowledge on NPs preparation with thin film growth ideas.

Our final objective was to investigate the oxygenation process in the case of the CSD YBCO films in order to comprehend the role of the surface reactions in this process. We developed in our group a homemade device to measure in-situ the electrical resistance during the thermal processes. This equipment allows monitoring the nucleation, growth rate and oxygen diffusion processes of the CSD superconducting films. In particular, we have studied the effect of different processing parameters on the oxygen diffusion of YBCO films. We have realized that the oxygen diffusion in YBCO follows, actually, a surface controlled mechanism and, therefore, the surface reactions are the limiting factor of the diffusion kinetics. We have also initiated the analysis of the film thickness and the nanocomposite structures on the oxygen diffusion kinetics. Finally, the analysis of the oxygen diffusion process in YBCO thin films with some silver addition has lead to the important conclusion that silver addition benefits the YBCO oxygenation kinetics through catalytic effects, thus allowing to carry out the oxygenation processes at lower temperatures than in pristine YBCO films with the possible enhancement of the charge carriers and, therefore, of the superconducting properties that this entails.

FUTURE WORK

As we have mentioned in the conclusion section included in each chapter as well as in the general conclusions, our work has reached significant advancement in the different parts that we have dealt with. However, several issues require further investigation.

We have demonstrated that we can produce short stacking faults using mixt composition nanocomposites. However, the reason why these stacking faults remain short is still unclear and requires a deeper study on these mixt nanocomposites. During this work the growth process has not been modified so, it would be worth to investigate if some tuning of the YBCO processing parameters may allow the enhancement of the short stacking faults formation and hence improve the pinning performances.

The Flash-Heating process used to crystallize the pristine GdBCO and GdBCO nanocomposite thin films is still in its early stages and requires further optimization of the processing parameters. By doing this, the reproducibility and performances of pristine GdBCO and GdBCO nanocomposite films should increase.

Similar effort is required with the YBCO nanocomposite thick films. In this work we have identified the problems that appear when the thickness increases. This problem requires a drastic change in the standard growth process that allows the variation of the supersaturation conditions. Nowadays, this is a hot topic in our group and there are several people trying to optimize the growth process in thick films. It is very likely that reducing the total should allow to achieve further control of the supersaturation conditions.

With respect to the ex-situ approach, we have explained that we have made the first steps. We have identified the main troubles that can be found and we have achieved the first films with excellent performances. However, as it was remarked, the potential of this route is enormous and it exists still a long way to maximize the performances. We should expect a large improve of the superconducting properties and pinning performances by optimizing of each step of the process. NPs synthesis control (smaller NPs without agglomeration), prevention of reactivity (BZO or BCO for example) and optimization of growth process to prevent coarsening are issues which should allow to achieve much higher performances.

Finally, we have made a complete and detailed analysis of how the oxygen diffusion in YBCO films takes place. However, there are still some open questions to clarify. For instance, the equivalence of the in- and out-diffusion processes which should help to elucidate the percolating effect role. It must be also investigated in more detail which is the rate determining step (rds) within the surface reactions. Here, we have provided some hints but we could not achieve a definitive answer. On the other hand, the study of oxygenation on nanocomposites, in films with different thicknesses and in YBCO with silver additions should be completed (change the processing parameters) in order to assure that they follow the same trend that in the pristine thin films. Finally, it is necessary to use the generated knowledge to optimize the oxygenation process and to test if YBCO films with different degrees of doping can be achieved.

APPENDICES

Appendix A: Nanostrain, c-parameter and random fraction determination from XRD spectra

A.1) Strain determination: Williamson-Hall method

As it was mention in chapter 2, the nanostrain determination is made using Siemens or Rigaku spectra taken with longer acquisition times per point and a higher density of measured points to increase the accuracy of the diffraction patterns. Afterwards, the Williamson-Hall method is used.

The broadening of the peaks of an X-ray spectrum is caused principally by two sources: the crystallite size and the strain (nanostrain for nanoscale or mesostrain for the mesoscale).

The crystallite size broadening is given by the Scherrer formula (Eq. A.1)[302, 303]:

$$\beta_L = \frac{K\lambda}{L\cos\theta} \qquad \text{Eq. A-1}$$

where L is the crystallite size, θ is the Bragg angle, λ is the radiation wavelength and K is a constant which depends on the assumptions made in the theory (e.g. the peak shape and crystallite habit, spherical crystallites being the easiest case to interpret) but, anyway, it is close to 1 and its value is often taken as 0,9.

β is defined as the width of a rectangle that has the same height an area as the peak. The relation between β and the width of the peak at half of the height (FWHM) is a simple multiplication factor (β = A* FWHM) which depends also on the shape of the peak. For a Gaussian fitting A = $\frac{\pi}{2}$ (approximately 1,57).

According to Eq. A-1, it is clear that β and L are reciprocally related: the greater the broadening the smaller the crystallite size and vice-versa.

The second main source of XRD peak broadening is the strain, or more specifically, the inhomogeneous strain. In figure A.1 it can clearly be observed why only the inhomogeneous strain can cause the broadening. If the strain is completely homogeneous (for example in the case of homogeneous compression of the sample) the only effect that can be observed is a peaks displacement due to the changes in the interplanar distance, d, but not a peaks broadening (figure A.1 b)). However, in the case of the inhomogeneous strain caused by structural defects (interstitials, vacancies, etc) or the addition of secondary phases in the nanocomposites case, the degree of strain within a crystallite is obviously greater at distances close to the defect. This causes a continuous change in the interplanar distance and, therefore, a broadening in the peak (figure A.1 c)).

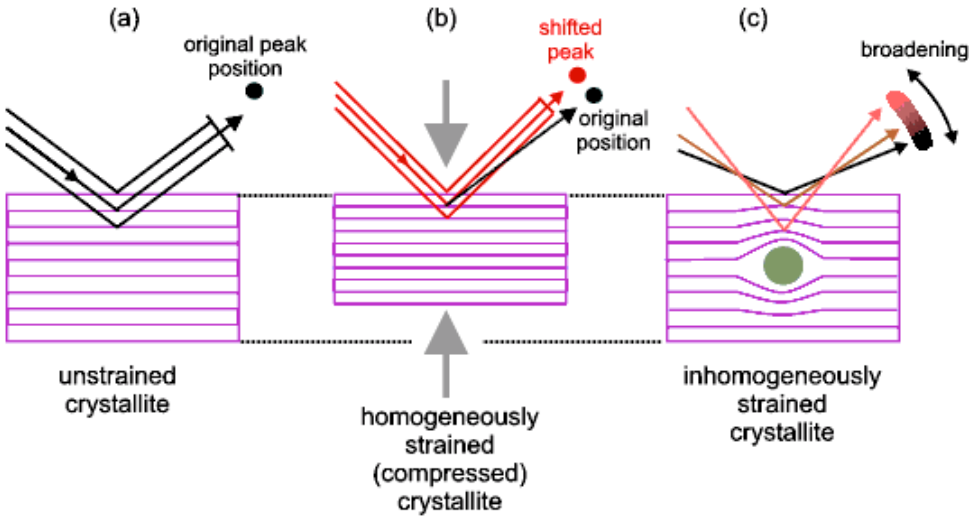

Figure A.1. Sketch of homogeneous strain and inhomogeneous strain.

The peak broadening cause by the strain is given by (Eq. A-2):

$$\boldsymbol{\beta_e = C\varepsilon tan\theta} \qquad \text{Eq. A-2}$$

where C is a constant that depends on the assumptions made concerning the nature of the inhomogeneous strain, but is typically ≈ 4 or 5 and ε is the inhomogeneous strain.

The Williamson-Hall method is based on the principle that the approximate formulae for size broadening, β_L, and strain broadening, β_e, vary quite differently with respect to Bragg angle, θ. One contribution varies as 1/cosθ and the other as tanθ. If both contributions are present, then their combined effects should be determined by convolution. The simplification proposed by Williamson and Hall was to assume that the convolution is either a simple sum or a sum of squares.

For Gaussian functions, the convolution is done using the sum of squares. This results in (Eq. A-3):

$$\boldsymbol{\beta_{Total}{}^2 = \beta_L{}^2 + \beta_e{}^2 = \left(\frac{K\lambda}{Lcos\theta}\right)^2 + (C\varepsilon tan\theta)^2} \qquad \text{Eq. A-3}$$

Multiplying by cosθ and reorganizing the terms, the following expression is obtained (Eq. A-4):

$$\boldsymbol{\beta_{Total}{}^2 cos\theta = \left(\frac{K\lambda}{L}\right)^2 + (C\varepsilon sin\theta)^2} \qquad \text{Eq. A-4}$$

Eq. A-3 looks like the equation of a straight line y=a+mx. In this case $y=\beta_{Total}{}^2 cos\theta$, $a=\left(\frac{K\lambda}{L}\right)^2$, $m=(C\varepsilon)^2$ and $x=(sin\theta)^2$. Therefore, the ε values can be extracted by plotting the $\beta_{Total}{}^2 cos\theta$ vs. $(sin\theta)^2$ obtaining a straight line with a slope equal to $(C\varepsilon)^2$.

In practice, once the spectra have been obtained, β and the position, 2θ, of each peak are extracted for each (00l) Bragg peak of YBCO using the gaussian fit with the FullProf_Suite software. Afterwards, the instrumental value is subtracted from the experimental value. The instrumental value is found by obtaining the spectrum of a

reference sample of LaB_6. After that, the values of ${\beta_{Total}}^2 cos\theta$ and $(sin\theta)^2$ are calculated and plotted (figure A.2). From the slope of the line the ε value is obtained considering C=4.

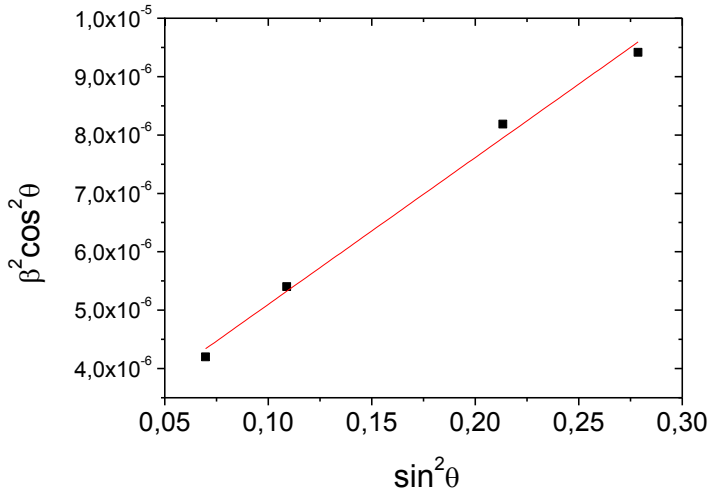

Figure A.2. Typical plot of ${\beta_{Total}}^2 cos\theta$ and $(sin\theta)^2$ to calculate the strain.

In this work, the calculated values of nanostrain are only for the c-parameter. So, these values give the deformation caused parallel to the c-axis.

A.2) c-parameter determination: Nelson-Riley method

It was mention in chapter 2 that the spectra needed for the c-parameter determination are obtained with Siemens or Rigaku using higher density of measured points to increase the accuracy of the spectrum.

When one tries to determine the unit-cell dimensions (in this case c-parameter) from θ-2θ scans, it is necessary to take into account systematic errors that appear as a consequence of:

- Absorption of the X-ray beam in the specimen,
- Displacement of the rotation axis of the specimen relative to the geometric centre of the cylindrical film (usually called the eccentricity error),
- Inaccurate determination of the diffractometer constants.

These three effects vanish at θ=90º, corresponding to the extreme back-reflection along the path of the incident beam. Taking this into account, the procedure usually adopted is the calculation of the c-parameter from a number of peaks on the spectrum, plot these values as a function of some expresion of the Bragg angle θ, and then extrapolate to a value corresponding to θ=90º.

The function that Nelson and Riley proposed as the best to make the extrapolation is (Nelson-Riley function, Eq. A-8)[165, 166]:

$$\frac{1}{2}\left(\frac{\boldsymbol{cos^2\theta}}{\boldsymbol{sin\theta}} + \frac{\boldsymbol{cos^2\theta}}{\boldsymbol{\theta}}\right) \qquad \text{Eq. A-8}$$

In practice, from the obtained spectrum, the 2θ position of each peak is extracted. Then, for each peak, the c-parameter is calculated.

It is well known that the interplanar distance, d, for an orthorhombic structure is given by (Eq. A-6):

$$\frac{1}{d^2} = \left(\frac{h}{a}\right)^2 + \left(\frac{k}{b}\right)^2 + \left(\frac{l}{c}\right)^2 \qquad \text{Eq. A-6}$$

where h, k and l represent the Miller indices of the peaks and the a, b and c are the unit-cell dimensions.

For an epitaxial film (h=k=0) the c-parameter for each peak can be calculated as (Eq. A-7):

$$c = ld \qquad \text{Eq. A-7}$$

Once the c-parameter for each peak is calculated, it is necessary to calculate the value of the Nelson-Riley function for each peak using the position previously calculated using the FullProf_Suite software. Finally, a plot with the c-parameter values in the y-axis and the Nelson-Riley function values in the x-axis is done (figure A.3). The data is adjusted to a straight line which intercepts to the desired c-parameter.

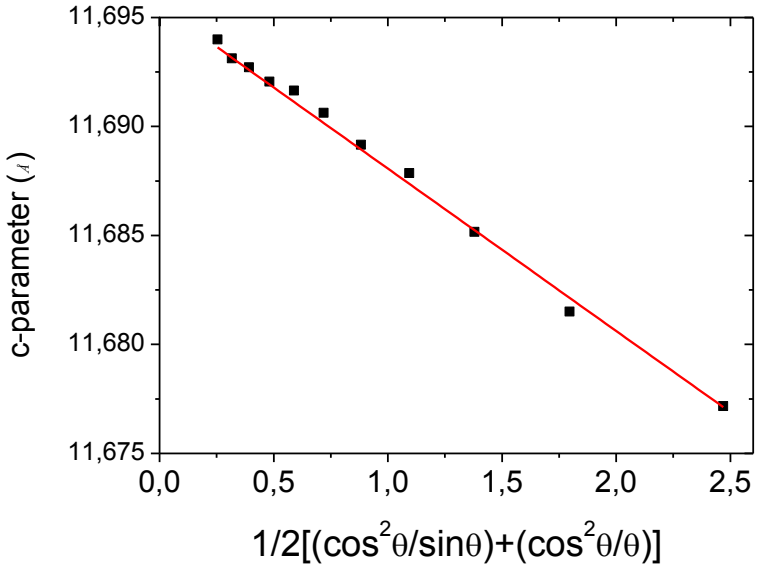

Figure A.3. Typical plot of c-parameter vs. Nelson-Riley function to find unit-cell c dimension as the intercept of the line.

A.3) Random fraction determination

The methodology that was used in this work to determine the random fraction was developed by A. Llordes is her thesis[304]. In her work, this method was used to quantify the random/epitaxial fraction of a nanoparticulated phase (the NPs that are introduced in the

nanocomposites). The random fraction has important consequences when analyzing the microstructure of the nanocomposites thin films.

This method is based on the simultaneous out-of-plane measurement of both the diffracted pole (from the epitaxial fraction) and the diffracted ring (from the randomly oriented fraction) using the GADDS diffractometer. Figure A.4 shows the pattern obtained for BZO nancomposite. To perform these measurements, the incident angle ω is fixed to the value of the corresponding maximum intense reflection of the NPs phase and the detector is centered at the χ value of the same reflection. The ϕ angle was fixed and optimized in order to assure the maximum intensity. For example, in the case of BZO NPs these conditions are: ω=15°, χ=45° and φ=0° for the (110) reflection. Longer measurement times with respect to standard scans are required (from 15 min to 1 h) due to the fact that the volume fraction of the nanoparticles is really low compared to the whole volume of the sample.

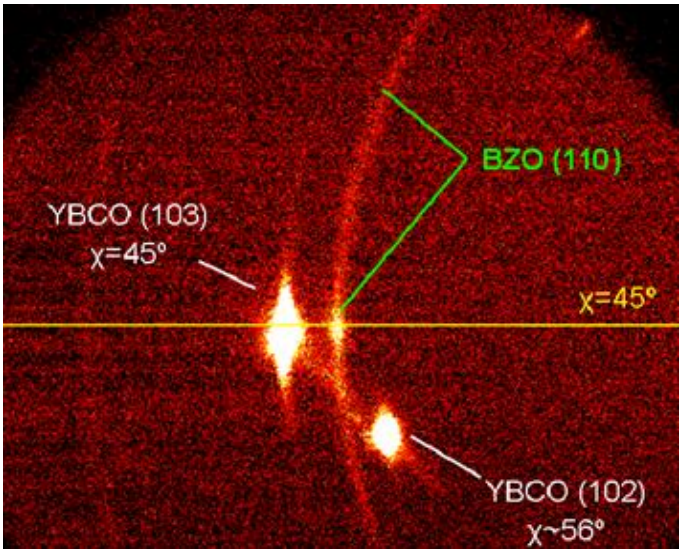

Figure A.4. 2D θ-2θ XRD patterns of the nanocomposites measured at fixed ω and centered at the maximum intense line of BZO[304].

Once the XRD pattern is obtained, it is necessary to integrate the epitaxial part of the NPs reflection (the spot located at χ=45º), the random or polycrystalline part (ring) and the background. The integration is done using GADDS software. To integrate the epitaxial part, a small range of 2θ is selected leaving the spot in the center (1,5-2º) and also a small range of χ (10-20º) again leaving the spot in the center (χ=45º). The intensity enclosed in these ranges is quantified and the intensity of the peak is extracted (the fitting of the NPs peak has to be done carefully because, although ω was optimized to fulfill the Bragg condition for the (110)BZO, the tails of nearby YBCO poles are also detected due to the bidimensionality of the detector). To select the polycrystalline part, the 2θ and χ ranges are maintained but the center of the integration area is displacing up or down to other value of χ (figure A.5). Finally, for the background, the integration area is displaced to other 2θ maintaining the χ of the polycrystalline part.

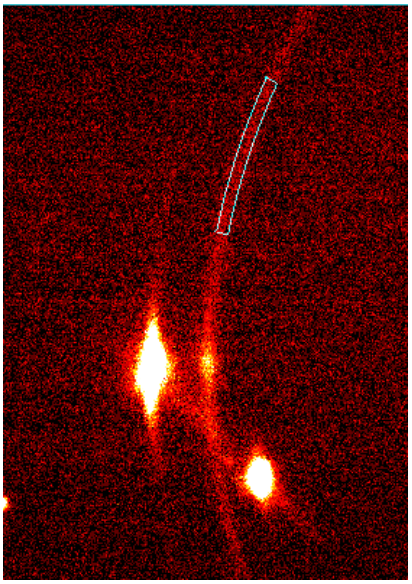

Figure A.5. XRD diffraction pattern showing the integration of the polycrystalline part[304].

Once the intensities of the epitaxial part, the polycrystalline part and the background are obtained, it is necessary to subtract the background intensity from the epitaxial part and the polycrystalline part. Afterwards, the polycrystalline intensity is subtracted from the epitaxial one to assure that only the epitaxial part is taken into account in the calculation. With the intensities of the epitaxial and the polycrystalline contributions it is possible to obtain the random fraction taking into account that the sum of the epitaxial part and the random part percentages is equal to 100 % and applying the following expression (Eq. A-9):

$$\frac{I_{random}}{I_{epitaxial}} = \frac{I_{ring}^{exp}\left(\frac{360}{\Delta\chi}\right)4\pi}{8I_{pole}^{exp}} \qquad \text{Eq. A-9}$$

Appendix B: SQUID measurements

This appendix is devoted to explain in detail how the different SQUID measurements are carried out and which kind of information can be extracted from them.

B.1) Magnetization measurements as a function of the temperature

One of the properties that can be extracted from the m(T) curves is the critical temperature of the thin films. For this measurements, the films are placed with the c-axis parallel to the magnetic field (H//c) and then cooled down under Zero Field Cooled (ZFC) conditions (no magnetic field is applied during the cooling process) to 10 K. Then, a weak magnetic field of 2Oe is applied to maintain the sample in Meissner state. Afterwards, the temperature is slowly increased and the magnetization values (m) are measured over T

until the transition to normal state is observed. This transition happens due to the fact that when the film is in the superconducting state there are supercurrents that induce high magnetization values. However, in the moment in which the film makes the transition to normal state, these supercurrents vanish and the magnetization values become zero. Figure 7.6 shows a typical m(T) curve obtained with SQUID. The T_c is reached in the moment that m=0 (T_c onset, marked with a red square in figure A.6).

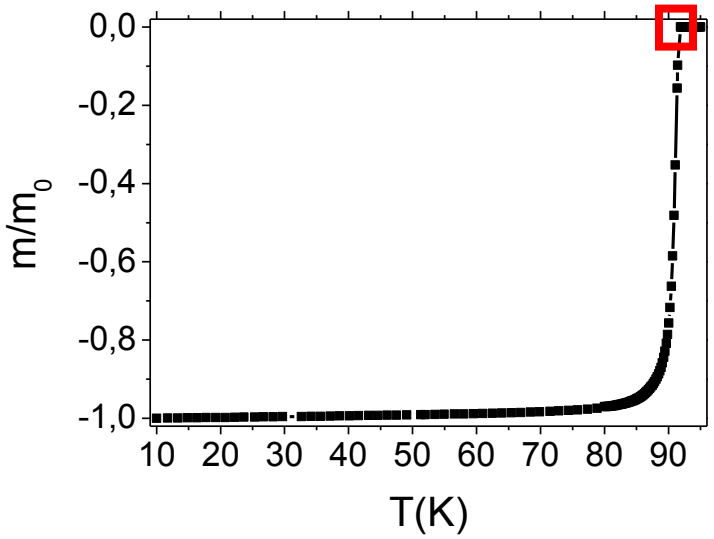

Figure A.6. Typical m(T) curve obtained with the SQUID of pristine YBCO thin films. In this case the m values were normalized by the maximum value (m_0).

To obtain the values of the critical currents (J_c) of the thin films at each temperature, m(T) curves are also carried out in (H//c) configuration . In this case, the films are cooled to 5 K again under ZFC conditions. Afterwards, the magnetic field is increased up to 3 T and again decreased to 0 T. In these conditions the films change to the remanence state (full of trapped vortices). Further, the temperature is increased measuring m values over T. With the m values is possible to calculate the J_c vales at each temperature using the Bean´s model. Figure A.7 shows the typical J_c(T) curve.

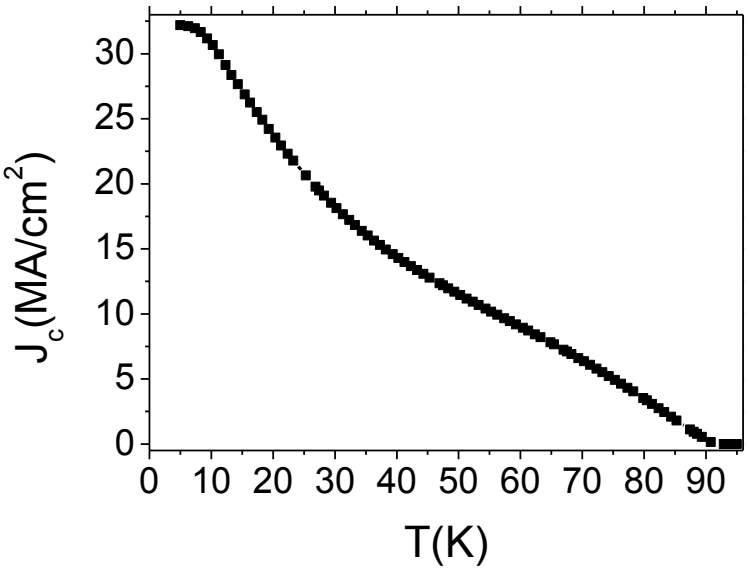

Figure A.7. Typical J_c(T) curve obtained with the SQUID of a pristine YBCO thin film.

Another option of this type of measurements is the FC-ZFC curves that are used to extract information about the NPs magnetic behavior. These kind of measurements are composed by two different combined curves. First, the ZFC curve is obtained after cooling the sample in zero field from high temperature and then by measuring the magnetization at stepwise increasing temperatures in a small applied field (100 Oe) (curve 1 in figure A.8). On the other hand, the FC curve is obtained by measuring m in the cooling process in the same small applied field (curve 2 in figure A.8). With these curves, the blocking temperature of the magnetic NPs can be obtained. The blocking temperature is the temperature at which the NPs change from a ferromagnetic behavior to a superparamagnetic behavior (marked with a red square in figure 7.8).

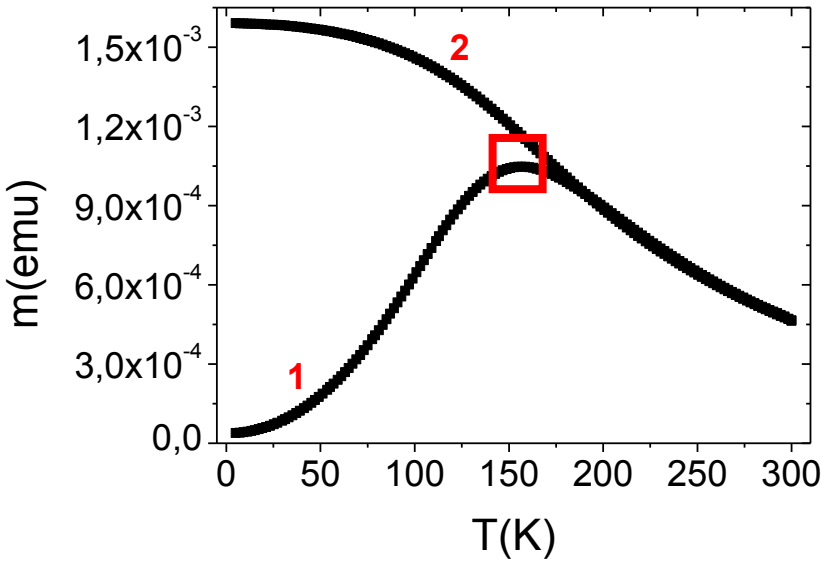

Figure A.8. Typical m(T) curve FC-ZFC obtained with the SQUID to study the magnetic features of magnetic NPs.

B.2) Magnetization measurements as a function of the magnetic field

The m(H) curves are carried out in thin films in (H//c) configuration to observe the evolution of the critical current with the increment of the magnetic field. In this case, the films are cooling down in ZFC conditions. Afterwards, the magnetic field is increased up to a maximum of 7 T while the m values are being measured and further decreased to close the hysteresis loop. The Bean´s model is used to transform the m values in J_c values in order to obtain the final $J_c(H)$ curve (figure A.9 a)). To present these results and further appreciate the features of the curves, it is usually taken the branch in the first quadrant plot in a log-log scale (figure A.9 b)).

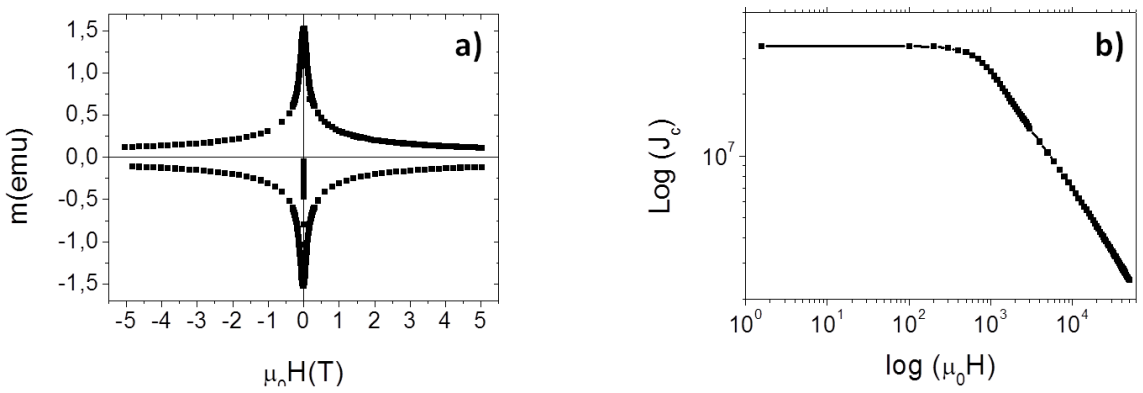

Figure A.9. Typical m(H) curve obtained with the SQUID for a pristine YBCO thin film a) in normal scale and b) in log –log scale after calculating the J_c values.

To measure the magnetic properties of magnetic NPs m(H) curves are also performed. In this case, the NPs are cooled down in ZFC conditions and then the magnetic field is increased until the saturation of the sample or up to 7 T. The same procedure is performed to observe the magnetic features of these NPs when they are embedded in the YBCO matrix. But in this case, as the volume fraction of NPs is really low compare to the total volume of the film, it is necessary to subtract the diamagnetic contribution of the substrate in order to obtain the real signal of the NPs.

Appendix C: Electrical transport measurements

As it was also mention in chapter 2, generally two types of transport measurements are performed in order to analyze the superconducting properties of the thin films: resistivity measurements to determine the critical temperature and irreversibility line, and V(I) curves for J_c analysis.

C.1) Resistivity measurements

In order to find the transition from normal to superconducting states at different applied magnetic fields, the resistance as a function of temperature is measured. According to Eq.A-10, the resistivity is expressed as:

$$\boldsymbol{\rho} = \frac{\boldsymbol{V^+ - V^-}}{\boldsymbol{I}} \frac{\boldsymbol{t_s \omega}}{\boldsymbol{l}} \qquad \text{Eq. A-10}$$

where $V^+ - V^-$ is the voltage drop provided by the nanovoltimeter, I is the applied current, t_s is the sample thickness, and ω and l are the bridge width and length respectively.

Measurements were carried out using an AC-current of 10 μA and 33Hz. When no magnetic field is applied, ρ(T) curves provide the value of the T_c. On the other hand, in the

presence of an external magnetic field, the ρ(T) curves allow the determination of the irreversibility temperature, T_{irr}.

In figure 7.10 a typical ρ(T) curve at zero applied magnetic field is presented. Figure 7.10 a) shows the whole ρ(T) curve measured from 300K to 80K where the ohmic behavior is observed for T > 100 K. T_c and T_{irr} are defined as $\rho(T_c, T_{irr})/\rho(100\ K) = 10^{-3}$. The T_c^{onset} represents the temperature at which the resistivity diverges from the linear ohmic behavior. The T_c^{drop} represents the temperature at which the resistivity achieves the experimental offset (figure 7.10 b)).

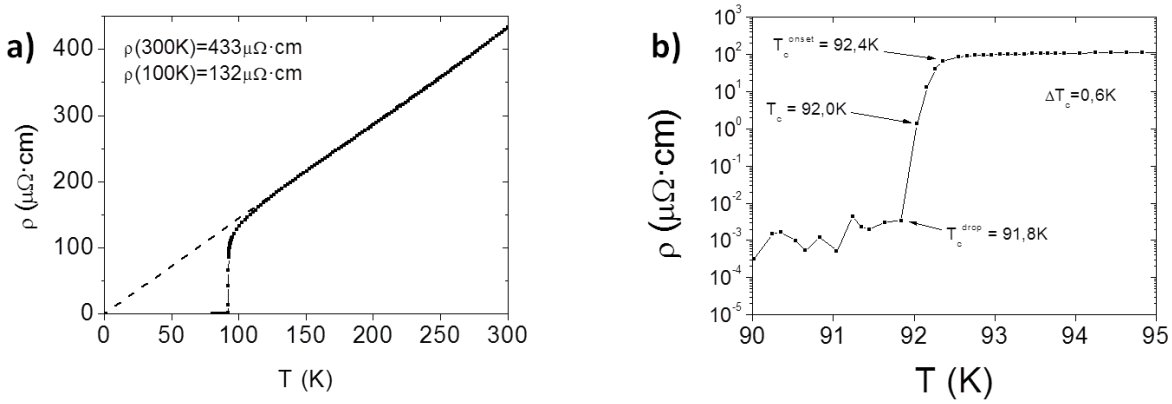

Figure 7.10. Typical ρ(T) curve a) from 300 K to 80 K and b) centered in the transition from superconducting to normal state.

C.2) V(I) curves

V(I) curves are measured in order to determine the critical current density of the thin films. Electrical current is increased in small steps from 0 to I_{max}. In order to avoid damaging the sample by injecting too much electrical current, the voltage drop is limited at 5-7 μV during the measurements.

The V(I) curves of a superconducting material are non linear, and typically are described by a power law behavior (figure A.11). The critical current (I_c) is defined as the maximum current that can go through the superconductor without dissipation. Experimentally, voltage drops at the nanometric scale are always measured due to offset-measurement devices and so, a criterion should be used to determine I_c.

The most common criterion used to define I_c is the current needed to obtain an electrical field of 1μV/cm where the electric field is E = V/l, being l the distance between voltage connections. However, if the bridges are short enough to be able to perform homogenous patterns along them, a different criterion can be used. The criterion chosen for this thesis was 10μV/cm (figure 7.11).

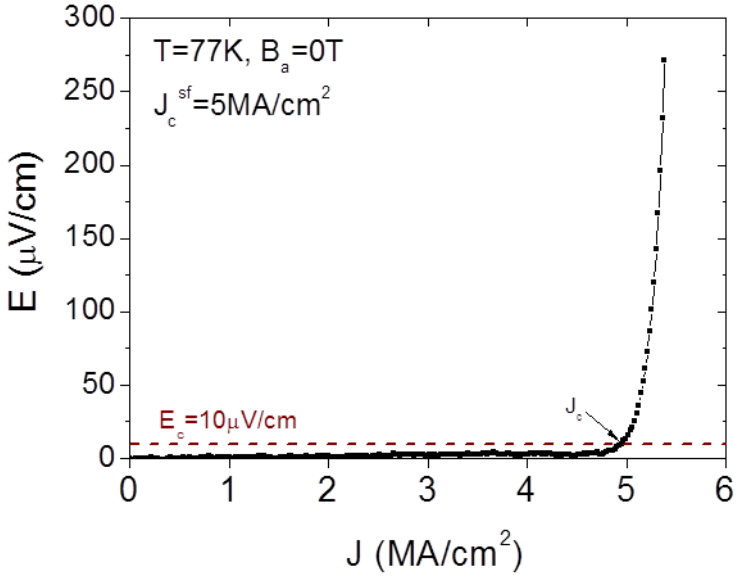

Figure A.11. E(J) curve of a YBCO thin film at 77K and self field showing a critical current density of 5 MA/cm^2.

In this thesis, E(J) curves are measured at different values of applied magnetic field, temperature, and sample orientation with respect to the c-axis of the YBCO or nanocomposites films in order to obtain different dependences of J_c at different conditions.

BIBLIOGRAPHY

1 Z. L. Wang and Z. C. Kang, 'Functional and Smart Materials Structural Evolution and Structure Analysis' (New York: Plenum Press, 1998).

2 M. Izumi, Y. Murakami, Y. Konishi, T. Manako, M. Kawasaki, and Y. Tokura, 'Structure Characterization and Magnetic Properties of Oxide Superlattices $La_{0.6}Sr_{0.4}MnO_3/La_{0.6}Sr_{0.4}FeO_3$', *Physical Review B*, 60 (1999), 1211-15.

3 R. Asahi, T. Morikawa, T. Ohwaki, K. Aoki, and Y. Taga, 'Visible-Light Photocatalysis in Nitrogen-Doped Titanium Oxides', *Science*, 293 (2001), 269-71.

4 J. Mizusaki, 'Nonstoichiometry, Diffusion, and Electrical Properties of Perovskite-Type Oxide Electrode Materials', *Solid State Ionics*, 52 (1992), 79-91.

5 H. Tanaka, J. Zhang, and T. Kawai, 'Giant Electric Field Modulation of Double Exchange Ferromagnetism at Room Temperature in the Perovskite Manganite/Titanate P/N Junction', *Physical review letters*, 88 (2001), 027204.

6 M. G. Blamire, J. L. MacManus-Driscoll, N. D. Mathur, and Z. H. Barber, 'The Materials Science of Functional Oxide Thin Films', *Advanced Materials*, 21 (2009), 3827-39.

7 J.A. Rodríguez and M. Fernández-García, 'Synthesis, Properties, and Applications of Oxide Nanomaterials', (Wiley, 2007).

8 H. Hahn, 'Microstructure and Properties of Nanostructured Oxides', *Nanostructured Materials*, 2 (1993), 251-65.

9 A. Martínez-Arias, M. Fernández-García, J.C. Hanson, J.A. Rodriguez, 'Nanostructured Oxides in Chemistry: Characterization and Properties', *Chemical Reviews*, 104 (2004), 4063−104.

10 C. M. Lieber, 'One-Dimensional Nanostructures: Chemistry, Physics &Amp; Applications', *Solid State Communications*, 107 (1998), 607-16.

11 W. V. Hassenzahl, D. W. Hazelton, B. K. Johnson, P. Komarek, M. Noe, and C. T. Reis, 'Electric Power Applications of Superconductivity', *Proceedings of the IEEE*, 92 (2004), 1655-74.

12 M. K. Wu, J. R. Ashburn, C. J. Torng, P. H. Hor, R. L. Meng, L. Gao, Z. Huang, Y. Wang, and C. Chu, 'Superconductivity at 93 K in a New Mixed-Phase Y-Ba-Cu-O Compound System at Ambient Pressure', *Physical review letters*, 58 (1987), 908-10.

13 J. Gutierrez, A. Llordes, J. Gazquez, M. Gibert, N. Roma, S. Ricart, A. Pomar, F. Sandiumenge, N. Mestres, T. Puig, and X. Obradors, 'Strong Isotropic Flux Pinning in Solution-Derived $YBa_2Cu_3O_{7-\delta}$ Nanocomposite Superconductor Films', *Nat Mater*, 6 (2007), 367-73.

14 J. L. MacManus-Driscoll, S. R. Foltyn, Q. X. Jia, H. Wang, A. Serquis, L. Civale, B. Maiorov, M. E. Hawley, M. P. Maley, and D. E. Peterson, 'Strongly Enhanced Current Densities in Superconducting Coated Conductors of Yba2cu3o7-X + Bazro3', *Nat Mater*, 3 (2004), 439-43.

15 Kaname Matsumoto, and Paolo Mele, 'Artificial Pinning Center Technology to Enhance Vortex Pinning in YBCO Coated Conductors', *Superconductor science & technology*, 23 (2010), 014001.

16 H. K. Onnes, 'The Liquefaction of Helium', *Proceedings of the Section of sciences Koninklijke Nederlandse akademie van wetenschappen*, 11 (1908), 168-85.

17 H. K. Onnes, 'Further Experiments with Liquid Helium D - on the Change of the Electrical Resistance of Pure Metals at Very Low Temperatures, Etc V the Disappearance of the Resistance of Mercury', *Proceedings of the Section of sciences Koninklijke Nederlandse akademie van wetenschappen*, 14 (1911), 113-15.

18 W. Meissner, and R. Ochsenfeld, 'Short Initial Announcements', *Naturwissenschaften*, 21 (1933), 787-88.

19 F. London, and H. London, 'The Electromagnetic Equations of the Supraconductor', *Proceedings - Royal Society. Mathematical, physical and engineering sciences*, 149 (1935), 71-88.

20 J. N. Rjabinin, and L. W. Shubnikow, 'Magnetic Properties and Critical Currents of Supra-Conducting Alloys', *Nature*, 135 (1935), 581-82.

21 A. A. Abrikosov, 'The Magnetic Properties of Superconducting Alloys', *Journal of physics and chemistry of solids*, 2 (1957), 199-208.

22 A. A. Abrikosov, 'On the Magnetic Properties of Superconductors of the Second Group', *Soviet physics, JETP*, 5 (1957), 1174-83.

23 J. Bardeen, L. N. Cooper, and J. R. Schrieffer, 'Theory of Superconductivity', *Physical review*, 108 (1957), 1175-204.

24 'Collected Papers of L.D. Landau', (Oxford: Pergamon Press, 1965).

25 L. P. Gorkov, 'Microscopic Derivation of the Ginzburg-Landau Equations in the Theory of Superconductivity', *Soviet physics, JETP*, 9 (1959), 1364-67.

26 B. D. Josephson, 'Possible New Effects in Superconductive Tunnelling', *Physics letters*, 1 (1962), 251-53.

27 J. G. Bednorz, and K. A. Müller, 'Possible Hight C Superconductivity in the Ba-La-Cu-O System', *Zeitschrift für Physik. B, Condensed matter*, 64 (1986), 189-93.

28 Y. Kamihara, H. Hiramatsu, M. Hirano, R. Kawamura, H. Yanagi, T. Kamiya and H. Hosono, 'Iron-Based Layered Superconductor: LaOFeP', *Journal of the American Chemical Society*, 128 (2006), 10012-13.

29 P. Monthoux, A. V. Balatsky, and D. Pines, 'Weak-Coupling Theory of High-Temperature Superconductivity in the Antiferromagnetically Correlated Copper Oxides', *Physical Review B*, 46 (1992), 14803-17.

30 S. Chakravarty, A. Sudbø, P. W. Anderson, and S. Strong, 'Interlayer Tunneling and Gap Anisotropy in High-Temperature Superconductors', *Science*, 261 (1993), 337-40.

31 H. Fröhlich, 'Theory of the Superconducting State. I. The Ground State at the Absolute Zero of Temperature', *Physical review*, 79 (1950), 845-56.

32 C. A. Reynolds, B. Serin, and L. B. Nesbitt, 'The Isotope Effect in Superconductivity. I. Mercury', *Physical review*, 84 (1951), 691-94.

33 A. Brown, M. W. Zemansky, and H. A. Boorse, 'The Superconducting and Normal Heat Capacities of Niobium', *Physical review*, 92 (1953), 52-58.

34 U. Essmann, and H. Träuble, 'The Direct Observation of Individual Flux Lines in Type II Superconductors', *Physics Letters A*, 24 (1967), 526-27.

35 John Bardeen, and M. J. Stephen, 'Theory of the Motion of Vortices in Superconductors', *Physical review*, 140 (1965), A1197-A207.

36 M. P. A. Fisher, 'Vortex-Glass Superconductivity: A Possible New Phase in Bulk High-T_c oxides', *Physical review letters*, 62 (1989), 1415-18.

37 V. Foglietti, G. Koren, A. Gupta, R. H. Koch, and W. J. Gallagher, 'Experimental Evidence for Vortex-Glass Superconductivity in Y-Ba-Cu-O', *Physical review letters*, 63 (1989), 1511-14.

38 B. Dam, J. M. Huijbregtse, F. C. Klaassen, R. C. F. Van der Geest, G. Doornbos, J. H. Rector, A. M. Testa, S. Freisem, J. C. Martinez, B. Stauble-Pumpin and R. Griessen, 'Origin of High Critical Currents in $YBa_2Cu_3O_{7-\delta}$ Superconducting Thin Films', *Nature*, 399 (1999), 439-42.

39 A.I. Larkin, 'Effect of Inhomogeneities on the Structure of the Mixed State of Superconductors', *Journal Name: Zh. Eksp. Theor. Fiz. 58: 1466-70(Apr 1970).; Other Information: Orig. Receipt Date: 31-DEC-70* (1970), Medium: X.

40 Alex Gurevich, 'To Use or Not to Use Cool Superconductors?', *Nat Mater*, 10 (2011), 255-59.

41 D. Larbalestier, A. Gurevich, D. M. Feldmann, and A. Polyanskii, 'High-T_c Superconducting Materials for Electric Power Applications', *Nature*, 414 (2001), 368-77.

42 C. P. Bean, 'Magnetization of Hard Superconductors', *Physical review letters*, 8 (1962), 250-53.

43 Charles P. Bean, 'Magnetization of High-Field Superconductors', *Reviews of Modern Physics*, 36 (1964), 31-39.

44 K. Fossheim and A. Sudbo, 'Superconductivity: Physics and Applications', (ed. by Wiley, 2004).

45 H. A. Blackstead, D. B. Chrisey, J. D. Dow, J. S. Horwitz, A. E. Klunzinger, and D. B. Pulling, 'Superconductivity in $PrBa_2Cu_3O_7$', *Physics Letters A*, 207 (1995), 109-12.

46 J. Klamut, T. Glowiak, Z. Henkie, A. Zygmunt and Z. Bukowski, 'Thermal Vibrations in $YBa_2Cu_3O_{6+x}$ and $PrBa_2Cu_3B_{6+x}$', *Acta physica Polonica. A*, 73 (1988), 759-65.

47 J. R Waldram, 'Superconductivity of Metals and Cuprates', (ed. by Institut of Physics Publishing, 1996).

48 C. P. Poole, Jr., H. A. Farach, R. J. Creswick and R. Prozorov, 'Superconductivity' (ed. by London: Academic, 2007).

49 S. Maekawa, M. Sato, 'Physics of High-Temperature Superconductors', (ed. by Springer, 1992).

50 M. Murakami, N. Sakai, T. Higuchi, and S. I. Yoo, 'Melt-Processed Light Rare Earth Element - Ba - Cu - O', *Superconductor science & technology*, 9 (1996), 1015-32.

51 B. J. Kim, S. W. Lim, H. J. Kim, G. W. Hong, and H. G. Lee, 'New MOD Solution for the Preparation of High Jc REBCO Superconducting Films', *Physica C: Superconductivity*, 445–448 (2006), 582-86.

52 Y. Yoshida, T. Ozaki, Y. Ichino, Y. Takai, K. Matsumoto, A. Ichinose, M. Mukaida, and S. Horii, 'Progress in Development of Advanced PLD Process for High J_c REBCO Film', *Physica C: Superconductivity*, 468 (2008), 1606-10.

53 R. Pinto, S. P. Pai, A. S. Tamhane, P. R. Apte, L. C. Gupta, R. Vijayaraghavan, K. I. Gnanasekar, and H. V. Keer, 'Superconductivity at 86 K In $LuBa_2Cu_3O_{7-\delta}$ Thin Films', *Physical review. B, Condensed matter*, 46 (1992), 14242-44.

54 J. Shibata, T. Hirayama, K. Yamagiwa, I. Hirabayashi, X. L. Ma, and Y. Ikuhara, 'Characterization of $YbBa_2Cu_3O_{7-y}$ Superconducting Thin Films Prepared by Chemical Solution Deposition on $SrTiO_3$ (001) and $LaAlO_3$ (001) Substrates', *Physica status solidi. A, Applied research*, 173 (1999), 441-50.

55 J. Xiong, X. M. Cui, B. W. Tao, X. Z. Liu, and Y. R. Li, 'YBCO Superconducting Film Coated on $LaAlO_3$ Substrate by TFA-MOD Process', *Journal of superconductivity*, 18 (2005), 291-94.

56 L. H. Jin, Y. F. Lu, W. W. Yan, Z. M. Yu, Y. Wang, and C. S. Li, 'Fabrication of $GdBa_2Cu_3O_{7-x}$ Films by TFA-MOD Process', *Journal of alloys and compounds*, 509 (2011), 3353-56.

57 A. Di Trolio, G. Grimaldi, G. Mattei, and A. M. Testa, 'Structural and Superconducting Properties of $EuBa_2Cu_3O_{7-x}$ thin Films Grown by Off-Axis Pulsed Laser Deposition', *Superconductor science & technology*, 17 (2004), 1009-13.

58 S. H. Wee, A. Goyal, P. M. Martin, and L. Heatherly, 'High in-Field Critical Current Densities in Epitaxial $NdBa_2Cu_3O_{7-\delta}$ Films on Rabits by Pulsed Laser Deposition', *Superconductor science & technology*, 19 (2006), 865-68.

59 R. Suryanarayanan, R. Nagarajan, H. Selig, and L. Ben Dor, 'Preparation by Sol–Gel, Structure and Superconductivity of Pure and Fluorinated $LaBa_2Cu_3O_{7-\delta}$', *Physica. C, Superconductivity*, 361 (2001), 40-44.

60 C. Andreouli, and A. Tsetsekou, 'Synthesis of HTSC $Re(Y)Ba_2Cu_3O_x$ Powders: The Role of Ionic Radius', *Physica C: Superconductivity*, 291 (1997), 274-86.

61 M. S. Islam, and R. C. Baetzold, 'Atomistic Simulation of Dopant Substitution In $YBa_2Cu_3O_7$', *Physical review. B, Condensed matter*, 40 (1989), 10926-35.

62 J. L. MacManusDriscoll, 'Materials Chemistry and Thermodynamics of $ReBa_2Cu_3O_{7-x}$', *Advanced Materials*, 9 (1997), 457-73.

63 T. P. Beales, J. Jutson, L. Le Lay, and M. Molgg, 'Comparison of the Powder-in-Tube Processing Properties of Two $(Bi_{2-x}Pb_x)Sr_2Ca_2Cu3O_{10+\delta}$ Powders', *Journal of Materials Chemistry*, 7 (1997), 653-59.

64 C.L. Briant, E.L. Hall, K.W. Lay, and I.E. Tkaczyk, 'Microstructural Evolution of the BSCCO-2223 During Powder-in-Tube Processing', *Journal of Materials Research*, 9 (1994), 2789-808.

65 U. Balachandran, A. N. Iyer, J. Y. Huang, R. Jammy, and P. Haldar, 'Recent Advances in Bismuth-Based Superconductors', *JOM*, 46 (1994), 23-25.

66 Y. Iijima, N. Tanabe, Y. Ikeno, and O. Kohno, 'Biaxially Aligned $YBa_2Cu_3O_{7-x}$ Thin Film Tapes', *Physica. C, Superconductivity*, 185 (1991), 1959-60.

67 M. P. Paranthaman, and T. Izumi, 'High-Performance YBCO-Coated Superconductor Wires', *MRS bulletin*, 29 (2004), 533-41.

68 A. Goyal, M. Parans Paranthaman, and U. Schoop, 'The Rabits Approach: Using Rolling-Assisted Biaxially Textured Substrates for High-Performance YBCO Superconductors', *MRS bulletin*, 29 (2004), 552-61.

69 N. F. Heinig, R. D. Redwing, I. Fei Tsu, A. Gurevich, J. E. Nordman, S. E. Babcock, and D. C. Larbalestier, 'Evidence for Channel Conduction in Low Misorientation Angle [001] Tilt $YBa_2Cu_3O_{7-x}$ Bicrystal Films', *Applied physics letters*, 69 (1996), 577-79.

70 Rajiv K. Singh, and D. Kumar, 'Pulsed Laser Deposition and Characterization of High-T_c $YBa_2Cu_3O_{7-x}$ Superconducting Thin Films', *Materials science & engineering. R, Reports*, 22 (1998), 113-85.

71 M. Lorenz, H. Hochmuth, D. Natusch, H. Börner, G. Lippold, K. Kreher, and W. Schmitz, 'Large-Area Double-Side Pulsed Laser Deposition of $YBa_2Cu_3O_{7-x}$ Thin Films on 3-In. Sapphire Wafers', *Applied physics letters*, 68 (1996), 3332-34.

72 F. A. List, A. Goyal, M. Paranthaman, D. P. Norton, E. D. Specht, D. F. Lee, and D. M. Kroeger, 'High J_c YBCO Films on Biaxially Textured Ni with Oxide Buffer Layers Deposited Using Electron Beam Evaporation and Sputtering', *Physica. C, Superconductivity*, 302 (1998), 87-92.

73 H. M. Christen, 'Pulsed Electron Deposition of Fluorine-Based Precursors for YBa_2Cu3O_{7-x}-Coated Conductors', *Superconductor science & technology*, 18 (2005), 1168-75.

74 I. M. Watson, 'Metal-Organic CVD of the High-T_c Superconductor $YBa_2Cu_3O_{7-\delta}$', *Chemical vapor deposition*, 3 (1997), 9-26.

75 F. A. List, P. G. Clem, L. Heatherly, J. T. Dawley, K. J. Leonard, D. F. Lee, and A. Goyal, 'Low-Pressure Conversion Studies for YBCO Precursors Derived by PVD and MOD Methods', *IEEE Transactions on Applied Superconductivity*, 15 (2005), 2656-58.

76 C. Klemenz, and H. J. Scheel, 'Flat $YBa_2Cu_3O_{7-x}$ Layers for Planar Tunnel-Device Technology', *Physica. C, Superconductivity*, 265 (1996), 126-34.

77 H. J. Scheel, C. Klemenz, F. K. Reinhart, H. P. Lang, and H. J. Güntherodt, 'Monosteps on Extremely Flat $YBa_2Cu_3O_{7-x}$ Surfaces Grown by Liquid-Phase Epitaxy', *Applied physics letters*, 65 (1994), 901-03.

78 N. Newman, B. F. Cole, S. M. Garrison, K. Char, and R. C. Taber, 'Double Gun Off-Axis Sputtering of Large Area $YBa_2Cu_3O_{7-\delta}$ Superconducting Films for Microwave Applications', *IEEE Transactions on Magnetics*, 27 (1991), 1276-79.

79 A. Usoskin, A. Rutt, J. Knoke, H. Krauth, and T. Arndt, 'Long-Length YBCO Coated Stainless Steel Tapes with High Critical Currents', *IEEE Transactions on Applied Superconductivity*, 15 (2005), 2604-07.

80 A. Usoskin, L. Kirchhoff, J. Knoke, B. Prause, A. Rutt, V. Selskij, and D. E. Farrell, 'Processing of Long-Length YBCO Coated Conductors Based on Stainless Steel Tapes', *IEEE Transactions on Applied Superconductivity*, 17 (2007), 3235-38.

81 P. Pahlke, M. Hering, M. Sieger, M. Lao, M. Eisterer, A. Usoskin, J. Stromer, B. Holzapfel, L. Schultz and R. Huhne, 'Thick High J(c) YBCO Films on Abad-YSZ Templates', *IEEE Transactions on Applied Superconductivity*, 25 (2015), 1-4.

82 P. M. Mankiewich, J. H. Scofield, W. J. Skocpol, R. E. Howard, A. H. Dayem, and E. Good, 'Reproducible Technique for Fabrication of Thin Films of High Transition Temperature Superconductors', *Applied physics letters*, 51 (1987), 1753-55.

83 M. Paranthaman, C. Park, X. Cui, A. Goyal, D. F. Lee, P. M. Martin, T. G. Chirayil, D. T. Verebelyi, D. P. Norton, D. K. Christen, and D. M. Kroeger, '$YBa_2Cu_3O_{7-y}$−Coated

Conductors with High Engineering Current Density', *Journal of Materials Research*, 15 (2000), 2647-52.

84 X. Obradors, and T. Puig, 'Coated Conductors for Power Applications: Materials Challenges', *Superconductor science & technology*, 27 (2014), 044003.

85 M. A. Kirk, 'Structure and Flux Pinning Properties of Irradiation Defects in $YBa_2Cu_3O_{7-x}$', *Cryogenics*, 33 (1993), 235-42.

86 T. Terai, K. Kusagaya and Y. Takahashi, 'Modification of the High-T_c Superconductor $YBa_2Cu_3O_{7-x}$ by Particle-Beam Irradiation', *Physica. C, Superconductivity*, 190 (1991), 116-18.

87 J. C. Barbour, E. L. Venturini, D. S. Ginley, and J. F. Kwak, 'Irradiation Effects in High Temperature Superconductors', *Nuclear instruments & methods in physics research. Section B, Beam interactions with materials and atoms*, 65 (1992), 531-38.

88 T. Aytug, M. Paranthaman, K. J. Leonard, S. Kang, P. M. Martin, L. Heatherly, A. Goyal, A. O. Ijaduola, J. R. Thompson, D. K. Christen, R. Meng, I. Rusakova, and C. W. Chu, 'Analysis of Flux Pinning In $YBa_2Cu_3O_{7-x}$ Films by Nanoparticle-Modified Substrate Surfaces', *Physical review*, 74 (2006).

89 T. Aytug, M. Paranthaman, K. J. Leonard, K. Kim, A. O. Ijaduola, Y. Zhang, E. Tuncer, J. R. Thompson, and D. K. Christen, 'Enhanced Flux Pinning and Critical Currents in $YBa_2Cu_3O_{7-\delta}$ Films by Nanoparticle Surface Decoration: Extension to Coated Conductor Templates', *Journal of applied physics*, 104 (2008), 043906.

90 M. Sparing, E. Backen, T. Freudenberg, R. Huehne, B. Rellinghaus, R. Hühne, L. Schultz, and B. Holzapfel, 'Artificial Pinning Centres in YBCO Thin Films Induced by Substrate Decoration with Gas-Phase-Prepared Y_2O_3 nanoparticles', *Superconductor science & technology*, 20 (2007), S239-S46.

91 P. Mikheenko, A. Sarkar, V. S. Dang, J. Tanner, M. M. Tanner, J. S. Awang Kechik, and A. Abell, 'Pinning Centers Induced in YBCO Films by Nano-Dots in Substrate Decoration and Quasi-Superlattice Approaches', *IEEE Transactions on Applied Superconductivity*, 19 (2009), 3491-94.

92 P. Mele, K. Matsumoto, T. Horide, A. Ichinose, M. Mukaida, Y. Yoshida, S. Horii, and R. Kita, 'Ultra-High Flux Pinning Properties of $BaMO_3$-Doped $YBa_2Cu_3O_{7-x}$ Thin Films (M = Zr, Sn)', *Superconductor science & technology*, 21 (2008), 032002.

93 T. Kotaki, Y. Uraguchi, T. Makihara, M. Suenaga, T. Sueyoshi, T. Fujiyoshi, F. Mitugi, and T. Ikegami, 'Influence of Nano-Particle Diameter on Superconducting Properties in $BaMO_3$(M=Sn, Hf)/$YBa_2Cu_3O_y$ Quasi-Multilayered Films', *Physica C: Superconductivity and its Applications*.

94 P. Mele, K. Matsumoto, A. Ichinose, M. Mukaida, Y. Yoshida, S. Horii, and R. Kita, 'Systematic Study of the $BaSnO_3$ Insertion Effect on the Properties of $YBa_2Cu_3O_{7-x}$ Films Prepared by Pulsed Laser Ablation', *Superconductor science & technology*, 21 (2008), 125017.

95 M. Erbe, J. Haenisch, R. Huehne, T. Freudenberg, A. Kirchner, J. Hänisch, R. Hühne, L. Molina Luna, C. Damm, G. Van Tendeloo, S. Kaskel, L. Schultz, and B. Holzapfel, '$BaHfO_3$ artificial Pinning Centres in TFA-MOD-Derived YBCO and GdBCO Thin Films', *Superconductor science & technology*, 28 (2015), 114002.

96 I. Birlik, M. Erbe, T. Freudenberg, E. Celik, L. Schultz, and B. Holzapfel, 'Flux Pinning Improvement of YBCO Superconducting Films with $BaZrO_3$ Nanoparticles Prepared by Chemical Solution Deposition Method', *Journal of physics. Conference series*, 234 (2010), 012004.

97 A. Llordes, A. Palau, J. Gazquez, M. Coll, R. Vlad, A. Pomar, J. Arbiol, R. Guzmán, S. Ye, V. Rouco, F. Sandiumenge, S. Ricart, T. Puig, M. Varela, D. Chateigner, J. Vanacken, J. Gutiérrez, V. Moshchalkov, G. Deutscher, C. Magen, and X. Obradors, 'Nanoscale Strain-Induced Pair Suppression As a Vortex-Pinning Mechanism in High-Temperature Superconductors', *Nature Materials*, 11 (2012), 329-36.

98 D. Kumar, C. Cantoni, M. Varela, A. A. Gapud, S. K. Viswanathan, J. Abiade, S. J. Pennycook, and D. K. Christen, 'Enhancement of Flux Pinning in $YBa_2Cu_3O_7$ Thin Films

Embedded with Epitaxially Grown Y_2O_3 Nanostructures Using a Multi-Layering Process', *Superconductor science & technology*, 18 (2005), 1502-05.

99 Y. Chen, V. Selvamanickam, Y. Zhang, Y. Zuev, C. Cantoni, E. Specht, M. P. Paranthaman, T. Aytug, A. Goyal, and D. Lee, 'Enhanced Flux Pinning by BaZrO3 and $(Gd,Y)_2O_3$ Nanostructures in Metal Organic Chemical Vapor Deposited GdYBCO High Temperature Superconductor Tapes', *Applied physics letters*, 94 (2009), 062513.

100 T. Haugan, P. N. Barnes, R. Wheeler, F. Meisenkothen, and M. Sumption, 'Addition of Nanoparticle Dispersions to Enhance Flux Pinning of the $YBa_2Cu_3O_{7-x}$ Superconductor', *Nature*, 430 (2004), 867-70.

101 M. Coll, R. Guzman, P. Garces, J. Gazquez, V. Rouco, P. Garcés, A. Palau, S. Ye, C. Magen, H. Suo, H. Castro, T. Puig, and X. Obradors, 'Size-Controlled Spontaneously Segregated Ba_2YTaO_6 nanoparticles in $YBa_2Cu_3O_7$ nanocomposites Obtained by Chemical Solution Deposition', *Superconductor science & technology*, 27 (2014), 044008.

102 S. A. Harrington, J. H. Durrell, B. Maiorov, H. Wang, S. C. Wimbush, A. Kursumovic, J. H. Lee, and J. L. MacManus Driscoll, 'Self-Assembled, Rare Earth Tantalate Pyrochlore Nanoparticles for Superior Flux Pinning in $YBa_2Cu_3O_{7-x}$ Films', *Superconductor science & technology*, 22 (2009), 022001.

103 S. R. Foltyn, L. Civale, J. L. MacManus-Driscoll, Q. X. Jia, B. Maiorov, H. Wang, and M. Maley, 'Materials Science Challenges for High-Temperature Superconducting Wire', *Nat Mater*, 6 (2007), 631-42.

104 X. Obradors, T. Puig, S. Ricart, M. Coll, J. Gazquez, A. Palau, and X. Granados, 'Growth, Nanostructure and Vortex Pinning in Superconducting $YBa_2Cu_3O_7$ thin Films Based on Trifluoroacetate Solutions', *Superconductor science & technology*, 25 (2012), 123001.

105 H. Y. Zhai, and W. K. Chu, 'Effect of Interfacial Strain on Critical Temperature of $YBa_2Cu_3O_{7-\delta}$ Thin Films', *Applied physics letters*, 76 (2000), 3469-71.

106 Y. Yamada, K. Takahashi, H. Kobayashi, M. Konishi, T. Watanabe, A. Ibi, T. Muroga, S. Miyata, T. Kato, T. Hirayama, and Y. Shiohara, 'Epitaxial Nanostructure and Defects Effective for Pinning in $Y(Re)Ba_2Cu_3O_{7-x}$ Coated Conductors', *Applied physics letters*, 87 (2005), 132502.

107 A. Goyal, S. Kang, K. J. Leonard, P. M. Martin, A. A. Gapud, M. Varela, M. Paranthaman, A. O. Ijaduola, E. D. Specht, J. R. Thompson, D. K. Christen, S. J. Pennycook, and F. A. List, 'Irradiation-Free, Columnar Defects Comprised of Self-Assembled Nanodots and Nanorods Resulting in Strongly Enhanced Flux-Pinning in $YBa_2Cu_3O_{7-\delta}$ Films', *Superconductor science & technology*, 18 (2005), 1533-38.

108 P. Mele, R. Guzman, J. Gazquez, T. Puig, X. Obradors, S. Saini, Y. Yoshida, M. Mukaida, A. Ichinose, K. Matsumoto, and M. Idries Adam, 'High Pinning Performance of $YBa_2Cu_3O_{7-x}$ Films Added with Y_2O_3 Nanoparticulate Defects', *Superconductor science & technology*, 28 (2015), 024002.

109 M. Haruta, T. Fujiyoshi, T. Sueyoshi, K. Dezaki, D. Ichigosaki, K. Miyahara, R. Miyagawa, M. Mukaida, K. Matsumoto, Y. Yoshida, A. Ichinose, and S. Horii, 'Flux Pinning Properties of $ErBa_2Cu_3O_y$ thin Films with $BaZrO_3$ nanorods', *Superconductor science & technology*, 19 (2006), 803-07.

110 T. Nishiyama, K. Kaneko, K. Yamada, R. Teranishi, T. Kato, T. Hirayama, T. Izumi, and Y. Shiohara, 'Microstructural Characterization of TFA-MOD Processed $Y_{1-x}Gd_xBa_2Cu_3O_{7-y}$ with $BaZrO_3$', *Micron*, 52-53 (2013), 1-7.

111 K. P. Ko, S. M. Choi, Y. C. Kim, J. W. Lee, S. H. Moon, C. Park, and S. I. Yoo, 'Strongly Enhanced Flux Pining of GdBCO Coated Conductors with $BaSnO_3$ Nanorods by Pulsed Laser Deposition', *Physica. C, Superconductivity*, 471 (2011), 940-43.

112 P. Mele, K. Matsumoto, A. Ichinose, M. Mukaida, Y. Yoshida, S. Horii, and R. Kita, 'Systematic Study of $BaSnO_3$ Doped $YBa_2Cu_3O_{7-x}$ Films', *Physica. C, Superconductivity*, 469 (2009), 1380-83.

113 Guy Deutscher, 'Origin of Weak-Link Behavior of Grain Boundaries in Superconducting Cuprates and Pnictides', *Applied physics letters*, 96 (2010), 122502.

114 M. Coll, S. Ye, V. Rouco, A. Palau, R. Guzman, J. Gazquez, J. Arbiol, H. Suo, T. Puig, and X. Obradors, 'Solution-Derived $YBa_2Cu_3O_7$ Nanocomposite Films with a Ba_2YTaO_6 Secondary Phase for Improved Superconducting Properties', *Superconductor science & technology,* 26 (2013), 015001.

115 I. Bretos, T. Schneller, M. Falter, M. Bäcker, E. Hollmann, R. Wördenweber, L. Molina-Luna, G. Van Tendeloo. and O. Eibl, 'Solution-Derived $YBa_2Cu_3O_{7-\delta}$ (YBCO) Superconducting Films with $BaZrO_3$ (BZO) Nanodots Based on Reverse Micelle Stabilized Nanoparticles', *Journal of Materials Chemistry C: Materials for optical and electronic devices,* 3 (2015), 3971-79.

116 K. Kimura, R. Hironaga, Y. Takahashi, T. Nakanishi, T. Koizumi, T. Hasegawa, K. Higashikawa, M. Inoue, T. Kiss, T. Kato, T. Nakamura, M. Yoshizumi, T. Izumi, and Y. Shiohara, 'Development of REBCO Coated Conductors by TFA-MOD Method with High Characteristic in Magnetic Field', *IEEE Transactions on Applied Superconductivity,* 23 (2013), 6601704-04.

117 M. Miura, M. Yoshizumi, T. Izumi, and Y. Shiohara, 'Formation Mechanism of BaZrO3 Nanoparticles in $Y_{1-x}Sm_xBa_2Cu_3O_y$ Coated Conductors Derived from Trifluoroacetate Metal–Organic Deposition', *Superconductor science & technology,* 23 (2010), 014013.

118 M. Miura, B. Maiorov, S. A. Baily, N. Haberkorn, J. O. Willis, K. Marken, T. Izumi, Y. Shiohara, and L. Civale, 'Mixed Pinning Landscape in Nanoparticle-Introduced $YGdBa_2Cu_3O_y$ Films Grown by Metal Organic Deposition', *Physical Review B Condensed matter and materials physics,* 83 (2011).

119 F. F. Lange, 'Chemical Solution Routes to Single-Crystal Thin Films', *Science,* 273 (1996), 903-09.

120 R. W. Schwartz, T. Schneller, and R. Waser, 'Chemical Solution Deposition of Electronic Oxide Films', *Comptes rendus. Chimie,* 7 (2004), 433-61.

121 N. Roma, S. Morlens, S. Ricart, K. Zalamova, J. M. Moreto, A. Pomar, T. Puig, and X. Obradors, 'Acid Anhydrides: A Simple Route to Highly Pure Organometallic Solutions for Superconducting Films', *Superconductor science & technology,* 19 (2006), 521-27.

122 N. Sahu, 'Fundamental Understanding and Modeling of Spin Coating Process : A Review', *Indian Journal of Physics and Proceed of the Indian Association for the Cultivation of Science,* 83 (2009), 493-502.

123 F. Sánchez, C. Ocal, and J. Fontcuberta, 'Tailored Surfaces of Perovskite Oxide Substrates for Conducted Growth of Thin Films', *Chemical Society reviews,* 43 (2014), 2272-85.

124 J. M. Huijbregtse, J. H. Rector, and B. Dam, 'Effect of the Two (100) $SrTiO_3$ Substrate Terminations on the Nucleation and Growth of $YBa_2Cu_3O_{7-\delta}$ Thin Films', *Physica. C, Superconductivity,* 351 (2001), 183-99.

125 P. C. McIntyre and M. J. Cima, 'Preparation of Highly Textured Oxide Superconducting Films from MOD Precursor Solutions', US Patent, 1993).

126 T. Araki, K. Yamagiwa, and I. Hirabayashi, 'Fabrication of $YBa_2Cu_3O_{7-x}$ Film by Metalorganic Deposition Method Using Trifluoroacetates and Its Process Conditions', *Cryogenics,* 41 (2001), 675-81.

127 X. Palmer, C. Pop, H. Eloussifi, B. Villarejo, P. Roura, J. Farjas, A. Calleja, A. Palau, X. Obradors, T. Puig, and S. Ricart, 'Solution Design for Low-Fluorine Trifluoroacetate Route to $YBa_2Cu_3O_7$ Films', *Superconductor Science and Technology,* 29 (2016), 024002.

128 X. Obradors, T. Puig, A. Pomar, F. Sandiumenge, N. Mestres, X. Obradors, M. Coll, A. Cavallaro, N. Romà, J. Gázquez, J. C. González, O. Castaño, J. Gutierrez, A. Palau, K. Zalamova, S. Morlens, A. Hassini, M. Gibert, S. Ricart, J. M. Moretó, S. Piñol, D. Isfort and J. Bock, 'Progress Towards All-Chemical Superconducting $YBa_2Cu_3O_{7-\delta}$ Coated Conductors', *Superconductor science & technology,* 19 (2006), S13-S26.

129 T. Araki, and I. Hirabayashi, 'Review of a Chemical Approach to $YBa_2Cu_3O7_x$-Coated Superconductors—Metalorganic Deposition Using Trifluoroacetates', *Superconductor science & technology,* 16 (2003), R71-R94.

130 O. Castano, A. Cavallaro, A. Palau, J. C. Gonzalez, M. Rossell, T. Puig, J. C. Gonzalez, F. Sandiumenge, N. Mestres, S. Piñol, A. Pomar, and X. Obradors, 'High Quality $YBa_2Cu_3O_7$

thin Films Grown by Trifluoroacetates Metalorganic Deposition', *Superconductor science & technology*, 16 (2003), 45-53.

131 X. Obradors, F. Martínez-Julián, K. Zalamova, V. R. Vlad, A. Pomar, A. Palau, A. Llordés, H. Chen, M. Coll, S. Ricart, N. Mestres, X. Granados, T. Puig, and M. Rikel, 'Nucleation and Mesostrain Influence on Percolating Critical Currents of Solution Derived $YBa_2Cu_3O_7$ Superconducting Thin Films', *Physica. C, Superconductivity*, 482 (2012), 58-67.

132 X. Obradors, T. Puig, A. Pomar, F. Sandiumenge, N. Mestres, T. Obradors, A. Puig, F. Pomar, N. Sandiumenge, M. Mestres, A. Coll, N. Cavallaro, J. Romà, J. C. Gázquez, O. González, J. Castaño, A. Gutierrez, K. Palau, S. Zalamova, A. Morlens, M. Hassini, S. Gibert, J. M. Ricart, S. Moretó, D. Piñol, and J. Isfort, 'Progress Towards All-Chemical Superconducting $YBa_2Cu_3O_{7-\delta}$ Coated Conductors', *Superconductor science & technology*, 19 (2006), S13-S26.

133 T. Kumagai, T. Manabe, W. Kondo, H. Minamiue and S. Mizuta, 'Effects of Heat Treatment Conditions on the Critical Current Densities of $Ba_2YCu_3O_{7-y}$ Films Prepared by the Dipping-Pyrolysis Process', *Japanese journal of applied physics*, 29 (1990), L940-L42.

134 F Parmigiani, G Chiarello, N Ripamonti, H Goretzki, and U Roll, 'Observation of Carboxylic Groups in the Lattice of Sintered $Ba_2YCu_3O_{7-y}$ High-T_c Superconductors', *Physical Review B*, 36 (1987), 7148.

135 A. Gupta, R. Jagannathan, E. I. Cooper, E. A. Giess, J. I. Landman, and B. W. Hussey, 'Superconducting Oxide Films with High Transition Temperature Prepared from Metal Trifluoroacetate Precursors', *Applied physics letters*, 52 (1988), 2077-79.

136 K. Zalamova, A. Pomar, A. Palau, T. Puig, and X. Obradors, 'Intermediate Phase Evolution in YBCO Thin Films Grown by the TFA Process', *Superconductor science & technology*, 23 (2010), 014012.

137 C. Apetrii, H. Schlorb, M. Falter, I. Lampe, L. Schultz, and B. Holzapfel, 'YBCO Thin Films Prepared by Fluorine-Free Polymer-Based Chemical Solution Deposition', *IEEE Transactions on Applied Superconductivity*, 15 (2005), 2642-44.

138 Yuanqing Chen, Chuanbao Wu, Gaoyang Zhao, and Caiyin You, 'An Advanced Low-Fluorine Solution Route for Fabrication of High-Performance YBCO Superconducting Films', *Superconductor science & technology*, 25 (2012), 062001.

139 Yuanqing Chen, Zheng Liu, Lifeng Bai, and Fuxue Yan, 'High-Performance $GdBa_2Cu_3O_{7-x}$ Superconducting Film Prepared Using an Advanced Low-Fluorine Solution', *IEEE Transactions on Applied Superconductivity*, 22 (2012), 6601204-04.

140 R. Roy, 'Gel Route to Homogeneous Glass Preparation', *Journal of the American Ceramic Society*, 52 (1969), 344-44.

141 T. G. Holesinger, Q. Jia, B. Maiorov, L. Civale, P. C. Dowden, and B. J. Gibbons, 'Ultrafine Multilayers of Complex Metal Oxide Films', *Advanced Materials*, 19 (2007), 1917-20.

142 V. F. Solovyov, 'Nucleation of $YBa_2Cu_3O_7$ from Precursor Films Using the Barium Fluoride Process', *IEEE Transactions on Applied Superconductivity*, 15 (2005), 2739-42.

143 J. Gazquez, J. Gàzquez, F. Sandiumenge, M. Coll, A. Pomar, N. Mestres, T. Puig, X. Obradors, Y. Kihn, M. J. Casanove, and C. Ballesteros, 'Precursor Evolution and Nucleation Mechanism of $YBa_2Cu_3O_x$ Films by TFA Metal−Organic Decomposition', *Chemistry of materials*, 18 (2006), 6211-19.

144 F. M. Granozio, and U. S. diUccio, 'Simple Model for the Nucleation of (001) and (100) Oriented Grains in YBCO Films', *Journal of Crystal Growth*, 174 (1997), 409-16.

145 F. M. Granozio, M. Salluzzo, U. S. di Uccio, I. Maggio Aprile, and O. Fischer, 'Competition between a-axis and c-axis Growth in Superconducting $RBa_2Cu_3O_{7-x}$ Thin Films', *Physical Review B Condensed matter and materials physics*, 61 (2000), 756-65.

146 Y. Ichino, K. Sudoh, K. Miyachi, Y. Yoshida, and Y. Takai, 'Orientation Mechanism of $ReBa_2Cu_3O_y$ (Re=Nd, Sm, Gd, Y, Yb) Thin Films Prepared by Pulsed Laser Deposition', *IEEE Transactions on Applied Superconductivity*, 13 (2003), 2735-38.

147 T. Endo, K. Yoshii, S. Iwasaki, H. Kohmoto, H. Saratani, S. Shiomi, M. Matsui, and Y. Kurosaki, 'Oxygen Partial Pressure Dependences Of a-c phase Ratio, Crystallinity, Surface Roughness and in-Plane Orientation in YBCO Thin Film Depositions by Ibs', *Superconductor science & technology*, 16 (2003), 110-19.

148 Y. Q. Cai, X. Yao, and Y. J. Lai, 'Mechanism of Transition between a-Axis and c-Axis Growth of $YBa_2Cu_3O_x$ Thick Films Grown on $NdGaO_3$ Substrate', *Journal of applied physics*, 99 (2006), 113909.

149 V. F. Solovyov, H. J. Wiesmann, Q. Li, David, O. Welch and M. Suenaga, 'Three- and Four-μm-Thick $YBa_2Cu_3O_7$ Layers with High Critical-Current Densities on Flexible Metallic Substrates by the BaF_2 Process', *Journal of applied physics*, 99 (2006), 013902.

150 H. Chen, K. Zalamova, A. Pomar, X. Granados, T. Puig, and X. Obradors, 'Nucleation and Growth Rate Influence on Microstructure and Critical Currents of TFA-$YBa_2Cu_3O_7$ under Low-Pressure Conditions', *Journal of Materials Research*, 25 (2010), 2371-79.

151 M. Yoshizumi, I. Seleznev, and M. J. Cima, 'Reactions of Oxyfluoride Precursors for the Preparation of Barium Yttrium Cuprate Films', *Physica. C, Superconductivity*, 403 (2004), 191-99.

152 D. E. Wesolowski, M. Yoshizumi, and M. J. Cima, 'Trajectory-Property Relationships in MOD-Derived YBCO Films', *Physica. C, Superconductivity*, 450 (2006), 76-82.

153 V. F. Solovyov, H. J. Wiesmann, and M. Suenaga, 'Nucleation of $YBa_2Cu_3O_{7-x}$ on Buffered Metallic Substrates in Thick Precursor Films Made by the BaF_2 Process', *Superconductor science & technology*, 18 (2005), 239-48.

154 T. Puig, J. C. González, A. Pomar, N. Mestres, O. Castaño, M. Coll, J. Gázquez, F. Sandiumenge, S. Piñol, and X. Obradors, 'The Influence of Growth Conditions on the Microstructure and Critical Currents of TFA-MOD $YBa_2Cu_3O_7$ Films', *Superconductor science & technology*, 18 (2005), 1141-50.

155 V. Solovyov, I. Dimitrov, and Q. Li, 'Growth of Thick $YBa_2Cu_3O_7$ Layers Via a Barium Fluoride Process', *Superconductor science & technology*, 26 (2013), 013001.

156 K. F. Kelton, and A. L. Greer, 'Chapter 2 - the Classical Theory', in *Pergamon Materials Series*, (ed. by Pergamon, 2010), pp. 19-54.

157 K. F. Kelton, and A. L. Greer, 'Chapter 6 - Heterogeneous Nucleation', in *Pergamon Materials Series*, (ed. by Pergamon, 2010), pp. 165-226.

158 M. C. Flemings, *Solidification Processing*. ed. by McGraw-Hill (New York, 1974).

159 A. Calleja, S. Ricart, X. Palmer, R. F. Luccas, T. Puig, and X. Obradors, 'Water Determination of Precursor Solutions with Oxidant Cations by the Karl Fischer Method: The YBCO-TFA Case', *Journal of sol-gel science and technology*, 53 (2010), 347-52.

160 G. Strom, G. Ström, M. Fredriksson and P. Stenius, 'Contact Angles, Work of Adhesion, and Interfacial Tensions at a Dissolving Hydrocarbon Surface', *Journal of colloid and interface science*, 119 (1987), 352-61.

161 Y. Rotenberg, L. Boruvka, and A. W. Neumann, 'Determination of Surface Tension and Contact Angle from the Shapes of Axisymmetric Fluid Interfaces', *Journal of colloid and interface science*, 93 (1983), 169-83.

162 J. F. Boyce, S. Schürch, Y. Rotenberg, and A. W. Neumann, 'The Measurement of Surface and Interfacial Tension by the Axisymmetric Drop Technique', *Colloids and surfaces*, 9 (1984), 307-17.

163 W. H. Bragg, 'The Reflection of X-Rays by Crystals', *Proceedings - Royal Society. Mathematical, physical and engineering sciences*, 88 (1913), 428-38.

164 G. K. Williamson and W. H. Hall, 'X-Ray Line Broadening from Filed Aluminium and Wolfram', *Acta metallurgica*, 1 (1953), 22-31.

165 J. B. Nelson, and D. P. Riley, 'An Experimental Investigation of Extrapolation Methods in the Derivation of Accurate Unit-Cell Dimensions of Crystals', *Proceedings of the Physical Society*, 57 (1945), 160-77.

166 J. B. Nelson, and D. P. Riley, 'The Thermal Expansion of Graphite from 15 ºC to 800 ºC: Part I. Experimental', *Proceedings of the Physical Society*, 57 (1945), 477-86.

167 X. Hao, C. Kuang, Z. Gu, Y. Wang, Y. Ku, Y. Li, J. Ge and X. Liu, 'From Microscopy to Nanoscopy Via Visible Light', *Light: Science & Applications*, 2 (2013), e108.

168 P.J. Hirst and R.G. Humphreys, *Handbook of Superconducting Materials, Vol. 1: Superconductivity, Materials and Processes* (Institute of Physics: Publishing Bristol and Philadelphia, 2003).

169 Víctor Rouco Gómez, 'Controlling Vortex Pinning and Dynamics of Nanostructured YBCO Thin Films Grown by Chemical Solution Deposition', Universitat Autonoma de Barcelona (UAB), 2014).

170 Eduardo Solano Minuesa, 'Synthesis and Characterisation of Ferrite Nanoparticles for $YBa_2Cu_3O_{7-\delta}$ Nanocomposite Superconducting Layers: A Neutron and Synchrotron Study', Universitat Autonoma de Barcelona (UAB), 2013).

171 N. M. Strickland, N. J. Long, E. F. Talantsev, P. Hoefakker, J. Xia, M. W. Rupich, T. Kodenkandath, W. Zhang, X. Li, and Y. Huang, 'Enhanced Flux Pinning by $BaZrO_3$ Nanoparticles in Metal-Organic Deposited YBCO Second-Generation HTS Wire', *Physica C: Superconductivity*, 468 (2008), 183-89.

172 P. Garcés, M. Coll, H. Castro, T. Puig, and X. Obradors, 'Development of $YBa_2Cu_3O_7$-Ba_2YTaO_6 Nanocomposites by Chemical Solution Deposition', *Journal of physics. Conference series*, 568 (2014), 022015.

173 V. Solovyov, H. Wiesmann, L. Wu, Y. Zhu and M.Suenaga, 'Kinetics of $YBa_2Cu_3O_7$ Film Growth by Postdeposition Processing', *Applied physics letters*, 76 (2000), 1911-13.

174 V. Solovyov, H. Wiesmann and M. Suenaga, 'Growth Rate Limiting Mechanisms of $YBa_2Cu_3O_7$ Films Manufactured by Ex Situ Processing', *Physica. C, Superconductivity*, 353 (2001), 14-22.

175 R. Feenstra, A. A. Gapud, F. A. List, E. D. Specht, D. K. Christen, T. G. Holesinger, and D. M. Feldmann, 'Critical Currents I_c (77 K) > 350 A/Cm-Width Achieved in Ex Situ YBCO Coated Conductors Using a Faster Conversion Process', *IEEE Transactions on Applied Superconductivity*, 15 (2005), 2803-07.

176 R. Feenstra, F. A. List, Y. Zhang, D. K. Christen, V. A. Maroni, D. J. Miller, and D. M. Feldmann, 'Characterization of Phase Evolution in YBCO Coated Conductors Produced by the Ex Situ BaF_2 Process', *IEEE Transactions on Applied Superconductivity*, 17 (2007), 3254-58.

177 R. Feenstra, F. List, X. Li, M. Rupich, D. Miller, J. R. Thompson, V. A. Maroni, and D. K. Christen, 'A Modular Ex Situ Conversion Process for Thick MOD-Fluoride RBCO Precursors', *IEEE Transactions on Applied Superconductivity*, 19 (2009), 3131-35.

178 Katerina Zalamova, Neus Roma, Alberto Pomar, Stephanie Morlens, and Teresa Puig, 'Smooth Stress Relief of Trifluoroacetate Metal-Organic Solutions for $YBa_2Cu_3O_7$ Film Growth', *Chemistry of materials*, 18 (2006), 5897-906.

179 T. Yoshida, A. Ibi, T. Takahashi, M. Yoshizumi, T. Izumi, and Y. Shiohara, 'Fabrication of 93,7m Long PLD-EuBCO+$BaHfO_3$ Coated Conductors with 103 A/Cm-w at 77 K under 3T', *Physica. C, Superconductivity*, 518 (2015), 54-57.

180 T. Nakamura, K. Nakahata, M. Yoshizumi, T. Izumi, Y. Shiohara, K. Kimura, T. Hasegawa, T. Kato, and T. Hirayama, 'Development of BZO Doped YGdBCO Thick Films Using TFA-MOD Process', *Physics Procedia*, 45 (2013), 153-56.

181 N. Pellerin, P. Odier, P. Simon, and D. Chateigner, 'Nucleation and Growth Mechanisms of Textured YBaCuO and the Influence of Y_2BaCuO_5', *Physica. C, Superconductivity*, 222 (1994), 133-48.

182 A. Palau, T. Puig, J. Gutierrez, X. Obradors, and F. de la Cruz, 'Pinning Regimes of Grain Boundary Vortices in $YBa_2Cu_3O_{7-x}$ Coated Conductors', *Physical Review B Condensed matter and materials physics*, 73 (2006).

183 R. Guzman, J. Gazquez, V. Rouco, A. Palau, C. Magen, M. Varela, J. Arbiol, X. Obradors, and T. Puig, 'Strain-Driven Broken Twin Boundary Coherence in $YBa_2Cu_3O_{7-\delta}$ Nanocomposite Thin Films', *Applied physics letters*, 102 (2013), 081906.

184 V. Rouco, A. Palau, R. Guzman, J. Gazquez, M. Coll, X. Obradors, and T. Puig, 'Role of Twin Boundaries on Vortex Pinning of CSD YBCO Nanocomposites', *Superconductor science & technology*, 27 (2014), 125009.

185 T. Izumi, M. Yoshizumi, M. Miura, Y. Sutoh, T. Nakanishi, A. Nakai, Y. Ichikawa, Y. Yamada, T. Goto, A. Yajima, Y. Aoki, T. Hasegawa, and Y. Shiohara, 'Research and Development of Reel-to-Reel TFA-MOD Process for Coated Conductors', *Physica. C, Superconductivity*, 468 (2008), 1527-30.

186 R. Teranishi, J. Matsuda, K. Nakaoka, H. Fuji, Y. Aoki, Y. Kitoh, S. Nomoto, Y. Yamada, A. Yajima, T. Izumi and Y. Shiohara, 'High-I_c Processing for YBCO Coated Conductors by TFA-MOD Process', *Physica. C, Superconductivity*, 426 (2005), 959-65.

187 T. Izumi, M. Yoshizumi, J. Matsuda, K. Nakaoka, Y. Kitoh, Y. Sutoh, T. Nakanishi, A. Nakai, K. Suzuki, Y. Yamada, A. Yajima, T. Saitoh, and Y. Shiohara, 'Progress in Development of Advanced TFA-MOD Process for Coated Conductors', *Physica. C, Superconductivity*, 463 (2007), 510-14.

188 Y. Shiohara, M. Yoshizumi, T. Izumi, and Y. Yamada, 'Current Status and Future Prospects of Japanese National Project on Coated Conductor Development and Its Applications', *Physica C: Superconductivity*, 468 (2008), 1498-503.

189 M. Vilardell, X. Granados, S. Ricart, R. Cobas, M. Arjona, T. Puig, X. Obradors, S. C. Hopkins, B. A. Glowacki, J. Bennewitz, M. Falter, and M. Bäcker, 'Ink Jet Printing for Functional Ceramic Coatings', *The Journal of imaging science and technology*, 55 (2011), 040304.

190 I. Van Driessche, J. Feys, S. C. Hopkins, P. Lommens, X. Granados, B. A. Glowacki, S. Ricart, B. Holzapfel, M. Vilardell, A. Kirchner, and M. Bäcker, 'Chemical Solution Deposition Using Ink-Jet Printing for YBCO Coated Conductors', *Superconductor science & technology*, 25 (2012), 065017.

191 J. Feys, P. Vermeir, P. Lommens, S. Hopkins, X. Granados, B. Glowacki, M. Baecker, E. Reich, S. Ricard, B. Holzapfel and I. Van Driessche, 'Ink-Jet Printing of $YBa_2Cu_3O_7$ Superconducting Coatings and Patterns from Aqueous Solutions', *Journal of Materials Chemistry*, 22 (2012), 3717-26.

192 T. J. Haugan, P. N. Barnes, and D. C. van der Laan, 'Effect of a Compressive Uniaxial Strain on the Critical Current Density of Grain Boundaries in Superconducting $YBa_2Cu_3O_{7-\delta}$ Films', *Physical review letters*, 103 (2009), 027005.

193 A. Palau, T. Puig, X. Obradors, E. Pardo, C. Navau, A. Sanchez, A. Usoskin, H. C. Freyhardt, L. Fernández, B. Holzapfel, and R. Feenstra, 'Simultaneous Inductive Determination of Grain and Intergrain Critical Current Densities of $YBa_2Cu_3O_{7-x}$ Coated Conductors', *Applied physics letters*, 84 (2004), 230-32.

194 A. Palau, T. Puig, X. Obradors, and Ch Jooss, 'Simultaneous Determination of Grain and Grain-Boundary Critical Currents in $YBa_2Cu_3O_{7-\delta}$ Coated Conductors by Magnetic Measurements', *Physical Review B Condensed matter and materials physics*, 75 (2007).

195 Y. Iye, T. Tamegai, H. Takeya, and H. Takei, 'Critical-Field Anisotropy of a Single-Crystal $GdBa_2Cu_3O_x$ and $Hoba_2cu_3o_x$', *Japanese Journal of Applied Physics Part 2-Letters*, 26 (1987), L1850-L52.

196 Toshihiro Iguchi, Takeshi Araki, Yutaka Yamada, Izumi Hirabayashi, and Hiroshi Ikuta, 'Fabrication of Gdbacuo Films by the Metal Organic Deposition Method Using Trifluoroacetates', *Superconductor science & technology*, 15 (2002), 1415-20.

197 D. A. Cardwell, N. H. Babu, and N. Hari Babu, 'Processing and Properties of Single Grain (Re)–Ba–Cu–O Bulk Superconductors', *Physica. C, Superconductivity*, 445 (2006), 1-7.

198 J. H. Durrell, A. R. Dennis, J. Jaroszynski, M. D. Ainslie, E. E. Hellstrom, D. A. Cardwell, A. M. Campbell, J. Hull, and M. Strasik, 'A Trapped Field of 17,6 T in Melt-Processed, Bulk Gd-Ba-Cu-O Reinforced with Shrink-Fit Steel', *Superconductor science & technology*, 27 (2014), 082001.

199 R. Krupke, G. Ulmer, R. Schneider, M. Kurzmeier, G. Linker, and J. Geerk, 'Superconducting, Structural and Surface Properties of GdBaCuO Thin Films Deposited by

Electron Cyclotron Resonance Supported Sputtering', *Physica. C, Superconductivity*, 279 (1997), 153-64.

200 W. Andra, R. Hergt, W. Michalke, K. Steenbeck, and W. Andrä, 'Rotational Hysteresis Losses in Sputtered REBCO Films of Different Structure', *Physica. C, Superconductivity*, 185 (1991), 2169-70.

201 L. Qiang, L. L. Fei, X. G. Na, L. Y. Jie, Y. J. Li, Q. Luo, L. F. Liu and G. N. Xiao, 'Effect of the O_2/Ar Pressure Ratio on the Microstructure and Surface Morphology of Epi-MgO/IBAD-MgO Templates for $GdBa_2Cu_3O_{7-\delta}$ Coated Conductors', *Chinese Physics Letters*, 31 (2014), 037402.

202 Y. Wang, D. Xu, Y. Li and L. Liu, 'Dependencies of Microstructure and Stress on the Thickness of $GdBa_2Cu_3O_{7-\delta}$ Thin Films Fabricated by RF Sputtering', *Nanoscale Research Letters*, 8 (2013), 304.204

203 S. Lee, N. Chikumoto, T. Yokoyama, T. Machi, K. Nakao and K. Tanabe, 'Development of in-Plume Pulsed Laser Deposition of High-I_c GdBCO Films for Coated Conductors', *IEEE Transactions on Applied Superconductivity*, 19 (2009), 3192-95.

204 W. Li, G. Li, B. Zhang, P. Chou, S. Liu, and X. Ma, 'Fabrication of $GdBa_2Cu_3O_{7-\delta}$ Films by Photo-Assisted-MOCVD Process', *Physica. C, Superconductivity*, 501 (2014), 1-6.

205 J. W. Lee, G. M. Shin, S. H. Moon, and S. I. Yoo, 'High-J_c $GdBa_2Cu_3O_{7-\delta}$ Films Fabricated by the Metal–Organic Deposition Process', *Physica. C, Superconductivity*, 470 (2010), 1253-56.

206 G. Kim, A. R. Jeong, W. Jo, D. Y. Park, H. Cheong, G. M. Shin, and S. I. Yoo, 'Optimal Growth Conditions for $GdBa_2Cu_3O_7$ Thin-Film Coated Conductors Characterized by Polarized Raman Scattering Spectroscopy', *Physica. C, Superconductivity*, 470 (2010), 1021-24.

207 P. Vermeir, I. Cardinael, M. Baecker, J. Schaubroeck, E. Schacht, M. Bäcker, S. Hoste and I. Van Driessche, 'Fluorine-Free Water-Based Sol-Gel Deposition of Highly Epitaxial $YBa_2Cu_3O_{7-\delta}$ Films', *Superconductor science & technology*, 22 (2009), 075009.

208 P. Vermeir, I. Cardinael, J. Schaubroeck, K. Verbeken, M. Bäcker, P. Lommens, W. Knaepen, J. D'Haen, K. De Buysser, I. Van Driessche, M. Bäcker and J. D'haen, 'Elucidation of the Mechanism in Fluorine-Free Prepared $YBa_2Cu_3O_{7-\delta}$ Coatings', *Inorganic chemistry*, 49 (2010), 4471-77.

209 J. Zhang, S. Morlens, L. H, Pfalzgraf and D,Luneau, 'Synthesis, Characterization and Molecular Structures of Yttrium Trifluoroacetate Complexes with O- and N-Donors: Complexation vs. Hydrolysis', *European journal of inorganic chemistry*, 2005 (2005), 3928-35.

210 L. H. Jin, Y. Zhang, Z. M. Yu, G. Yan, C. S. Li, and Y. F. Lu, 'Effect of Relative Humidity on Morphology of YBCO Films Prepared by CSD Method', *Physica. C, Superconductivity*, 470 (2010), 1257-60.

211 P. Cayado, 'Preparation of $GdBa_2Cu_3O_7$ Superconducting Films by Chemical Solution Deposition' (Master Thesis, Universitat Autonoma de Barcelona (UAB), 2012).

212 J. W. Lee, S. M. Choi, J. H. Song, S. H. Moon and S. I. Yoo, 'Stability Phase Diagram of $GdBa_2Cu_3O_{7-\delta}$ in Low Oxygen Pressures', *Journal of alloys and compounds*, 602 (2014), 78-86.

213 M. Erbe, J. Haenisch, T. Freudenberg, A. Kirchner, I. Mönch, S. Kaskel, J. Hänisch, L. Schultz and B. Holzapfel, 'Improved $ReBa_2Cu_3O_{7-X}$ (Re = Y, Gd) Structure and Superconducting Properties by Addition of Acetylacetone in TFA-MOD Precursor Solutions', *Journal of Materials Chemistry A: Materials for energy and sustainability*, 2 (2014), 4932-44.

214 J. E. Evetts and B. A. Glowacki, 'Relation of Critical Current Irreversibility to Trapped Flux and Microstructure in Polycrystalline $YBa_2Cu_3O_7$', *Cryogenics*, 28 (1988), 641-49.

215 M. Erbe, J. Hänisch, R. Hühne, T. Freudenberg, A. Kirchner, L. Molina Luna, C. Damm, G. Van Tendeloo, S. Kaskel, L. Schultz, and B. Holzapfel, 'BaHfO3 Artificial Pinning

Centres in TFA-MOD-Derived YBCO and GdBCO Thin Films', *Superconductor science & technology*, 28 (2015), 114002.

216 F. Martinez-Julián, S. Ricart, A. Pomar, M. Coll, P. Abellán, F. Sandiumenge, M. J. Casanove, X. Obradors, T. Puig, I. Pastoriza-Santos and L. M. Liz-Marzán, 'Chemical Solution Approaches to $YBa_2Cu_3O_{7-\delta}$-Au Nanocomposite Superconducting Thin Films', *Journal of nanoscience and nanotechnology*, 11 (2011), 3245-55.

217 A. Garzón-Manjón, E. Solano, M. de la Mata, R. Guzman, J. Arbiol, T. Puig, X. Obradors, R. Yáñez, S. Ricart, and J. Ros, 'Induced Shape Controllability by Tailored Precursor Design in Thermal and Microwave-Assisted Synthesis of Fe_3O_4 Nanoparticles', *Journal of nanoparticle research*, 17 (2015).

218 E. Solano, R. Yáñez, S. Ricart and J. Ros, 'New Approach Towards the Polyol Route to Fabricate MFe_2O_4 Magnetic Nanoparticles: The Use of MCl_2 and $Fe(Acac)_3$ as Chemical Precursors', *Journal of Magnetism and Magnetic Materials*, 382 (2015), 380-85.

219 E. Solano, L. Perez-Mirabet, F. Martinez-Julián, R. Guzmán, J. Arbiol, T. Puig, X. Obradors, R. Yañez, A. Pomar, S. Ricart, and J. Ros, 'Facile and Efficient One-Pot Solvothermal and Microwave-Assisted Synthesis of Stable Colloidal Solutions of MFe_2O_4 Spinel Magnetic Nanoparticles', *Journal of nanoparticle research*, 14 (2012).

220 E. Solano, C. Frontera, I. Puente, T. Puig, X. Obradors, S. Ricart and J. Ros, 'Neutron and X-Ray Diffraction Study of Ferrite Nanocrystals Obtained by Microwave-Assisted Growth. A Structural Comparison with the Thermal Synthetic Route', *Journal of applied crystallography*, 47 (2014), 414-20.

221 L. Perez-Mirabet, E. Solano, F. Martinez-Julián, R. Guzmán, J. Arbiol, T. Puig, X. Obradors, A. Pomar, R. Yáñez, J. Ros and S. Ricart, 'One-Pot Synthesis of Stable Colloidal Solutions of MFe_2O_4 Nanoparticles Using Oleylamine as Solvent and Stabilizer', *Materials research bulletin*, 48 (2013), 966-72.

222 J. De Roo, K. De Keukeleere, J. Feys, P. Lommens, Z. Hens and I. Van Driessche, 'Fast, Microwave-Assisted Synthesis of Monodisperse HfO_2 Nanoparticles', *Journal of nanoparticle research*, 15 (2013).

223 K. De Keukeleere, J. Feys, M. Meire, J. De Roo, K. De Buysser, P. Lommens and I. Van Driessche, 'Solution-Based Synthesis of BaZrO3 Nanoparticles: Conventional Versus Microwave Synthesis', *Journal of nanoparticle research*, 15 (2013).

224 J. De Roo, F. Van den Broeck, K. De Keukeleere, I. Van Driessche, J. Martins and Z. Hens, 'Unravelling the Surface Chemistry of Metal Oxide Nanocrystals, the Role of Acids and Bases', *Journal of the American Chemical Society*, 136 (2014), 9650-57.

225 M. Niederberger and G. Garnweitner, 'Organic Reaction Pathways in the Nonaqueous Synthesis of Metal Oxide Nanoparticles', *Chemistry - A European Journal*, 12 (2006), 7282-302.

226 M. Baghbanzadeh, L. Carbone, P. D. Cozzoli and C. O. Kappe, 'Microwave-Assisted Synthesis of Colloidal Inorganic Nanocrystals', *Angewandte Chemie (International ed.)*, 50 (2011), 11312-59.

227 J. Park, J. Joo, S. Kwon, Y. Jang and T. Hyeon, 'Synthesis of Monodisperse Spherical Nanocrystals', *Angewandte Chemie (International ed.)*, 46 (2007), 4630-60.

228 H. Imagawa, A. Suda, K. Yamamura and S. Sun, 'Monodisperse CeO_2 Nanoparticles and Their Oxygen Storage and Release Properties', *The Journal of Physical Chemistry C*, 115 (2011), 1740-45.

229 S. Wimbush, J. Durrell, R. Bali, R. Yu, H. Wang, S. A. Harrington and J. L. MacManus-Driscoll, 'Practical Magnetic Pinning in YBCO', *IEEE Transactions on Applied Superconductivity*, 19 (2009), 3148-51.

230 L. N. Bulaevskii, E. M. Chudnovsky and M. P. Maley, 'Magnetic Pinning in Superconductor-Ferromagnet Multilayers', *Applied physics letters*, 76 (2000), 2594-96.

231 P. Woodward and Pavel Karen, 'Mixed Valence in $YBaFe_2O_5$', *Inorganic chemistry*, 42 (2003), 1121-29.

232 C. F. Sánchez-Valdés, T. Puig and X. Obradors, 'In Situ Study through Electrical Resistance of Growth Rate of Trifluoroacetate-Based Solution-Derived $YBa_2Cu_3O_7$ Films', *Superconductor science & technology,* 28 (2015), 024006.

233 K. Yanagisawa, Y. Matsui, Y. Kodama, Y. Yamada and T. Matsumoto, 'Effects of Fe and Ni Substitutions on the 1-2-4 Structure of YBCO Superconductors Studied by High-Resolution Transmission Electron Microscopy', *Physica. C, Superconductivity,* 191 (1992), 32-42.

234 B. Ullmann, R. Wordenweber, K. Heinemann, R. Wördenweber and H. C. Freyhardt, 'Aspects of Substitution of Magnetic Ions Fe, Ni and Gd in YBCO-HTSC', *Physica. C, Superconductivity,* 170 (1990), 71-79.

235 Y. Ren, E. Brecht, H. Fuess, and W. W. Schmahl, 'Intergrain Flux-Pinning in Relation to Structural Phase Transformation and Tweed Formation in $YBa_2(Cu_{1-X}Fe_x)_3O_{7-y}$ and $NdBa_2(Cu_{1-X}Fe_x)_3O_{7-y}$', *Physica. C, Superconductivity,* 199 (1992), 414-24.

236 W. Zhou, A. Mackenzie, C. T. Lin, S. X. Li, and W. Y. Liang, 'Cobalt-Doped YBCO Single Crystals and Their Accurate Characterisation', *Physica. C, Superconductivity*, 176 (1991), 285-94.

237 J. M. S. Skakle, 'Crystal Chemical Substitutions and Doping of $YBa_2Cu_3O_x$ and Related Superconductors', *Materials science & engineering. R, Reports,* 23 (1998), 1-40.

238 B.D. Cullity and C.D. Graham, *Introduction to Magnetic Materials*. (ed. by Wiley, 2009).

239 M. Knobel, P. Panissod, J. C. Denardin, A. L. Brandl, A. B. Pakhomov, H. Liu and X. X. Zhang, 'Thermoremanence and Zero-Field-Cooled/Field-Cooled Magnetization Study of $Co_x(SiO_2)_{1-x}$ Granular Films', *Physical review. B, Condensed matter,* 65 (2002).

240 M. Suzuki, S. Fullem and I. Suzuki, 'Scaling Form of Zero-Field-Cooled and Field-Cooled Susceptibility in Superparamagnet', *Journal of Magnetism and Magnetic Materials,* 322 (2010), 3178-85.

241 E. Stavitski and F. M. F. de Groot, 'The CTM4XAS Program for EELS and XAS Spectral Shape Analysis of Transition Metal L Edges', *Micron,* 41 (2010), 687-94.

242 A. K. Petford-Long and J. N. Chapman, 'Lorentz Microscopy', in *Magnetic Microscopy of Nanostructures*, ed. by Herbert Hopster and HansPeter OepenSpringer Berlin Heidelberg, 2005), pp. 67-86.

243 B. Chalmers, D. R. Uhlmann and K. A. Jackson, 'Interaction between Particles and a Solid-Liquid Interface', *Journal of applied physics,* 35 (1964), 2986-&.

244 G. F. Bolling and J. Cissé, 'A Theory for the Interaction of Particles with a Solidifying Front', *Journal of Crystal Growth,* 10 (1971), 56-66.

245 J. Cissé and G. F. Bolling, 'A Study of the Trapping and Rejection of Insoluble Particles During the Freezing of Water', *Journal of Crystal Growth,* 10 (1971), 67-76.

246 A. A. Chernov, D. E. Temkin and A. M. Melnikova, 'Theory of Solid Inclusions Capture During Crystal-Growth from a Melt', *Kristallografiâ,* 21 (1976), 652-60.

247 J. Pötschke and Volker Rogge, 'On the Behaviour of Foreign Particles at an Advancing Solid-Liquid Interface', *Journal of Crystal Growth,* 94 (1989), 726-38.

248 Y. Shiohara and A. Endo, 'Crystal Growth of Bulk High-T_c Superconducting Oxide Materials', *Materials science & engineering. R, Reports,* 19 (1997), 1-86.

249 N. H. Andersen, M. von Zimmermann, T. Frello, M. Käll, D. Mønster, P. A. Lindgård, J. Madsen, T. Niemöller, H. F. Poulsen, O. Schmidt, J. R. Schneider, T. Wolf, P. Dosanjh, R. Liang and W. N. Hardy, 'Superstructure Formation and the Structural Phase Diagram of $YBa_2Cu_3O_{6+x}$', *Physica C: Superconductivity,* 317–318 (1999), 259-69.

250 D. de Fontaine, V. Ozolins, Z. Islam and S. C. Moss, 'Origin of Modulated Structures In $YBa_2Cu_3O_{6,63}$: A First-Principles Approach', *Physical review,* 71 (2005)

251 R. Liang, D. A. Bonn and W. N. Hardy, 'Evaluation of CuO2 Plane Hole Doping in $YBa_2Cu_3O_{6+x}$ Single Crystals', *Physical review,* 73 (2006).

252 X. Liu, Z. Islam, S. K. Sinha, J. C. Lang, S. C. Moss, D. Haskel, G. Srajer, P. Wochner, D. R. Lee, D. R. Haeffner and U. Welp, 'Four-Unit-Cell Superstructure in the Optimally Doped $YBa_2Cu_3O_{6,92}$ superconductor', *Physical review letters,* 93 (2004), 157008.

253 D. Ha, S. Byon and K. Lee, 'On the Role of Apical Oxygen in the Charge Transfer of YBCO Superconductors', *Physica. C, Superconductivity,* 340 (2000), 243-50.

254 P. F. Miceli, J. M. Tarascon, L. H. Greene, P. Barboux and F. J. Rotella, 'Role of Bond Lengths in the 90-K Superconductor - a Neutron Powder-Diffraction Study of $YBa_2Cu_{3-x}Co_xO_{7-y}$', *Physical review. B, Condensed matter,* 37 (1988), 5932-35.

255 S. Tsukui, R. E. Koritala, M. Li, K. C. Goretta, M. Adachi, J. E. Baker and J. L. Routbort, 'Oxygen and Cation Diffusion in YBCO Coated Conductors', *Physica C: Superconductivity,* 392–396, Part 2 (2003), 841-46.

256 R. Mogilevsky, R. Levisetti, B. Pashmakov, K. Zhang, R. Levi Setti, Li Liu, H. M. Jaeger, D. B. Buchholz and B. W. Veal, 'Direct Measurements of Room-Temperature Oxygen Diffusion in $YBa_2Cu_3O_x$', *Physical review. B, Condensed matter,* 49 (1994), 6420-23.

257 S. J. Rothman, J. L. Routbort, U. Welp and J. E. Baker, 'Anisotropy of Oxygen Tracer Diffusion in Single-Crystal $YBa_2Cu_3O_7$', *Physical Review B,* 44 (1991), 2326-33.

258 Tong B. Tang and Wai Lo, 'Oxygen Diffusion in YBCO: An Isothermal Thermogravimetric Study', *Physica C: Superconductivity,* 174 (1991), 463-66.

259 A. Michaelis, O. Auciello, E. A. Irene, and A. R. Krauss, 'A Study of Oxygen Diffusion in and out of $YBa_2Cu_3O_{7-\delta}$ Thin Films', *Journal of applied physics,* 83 (1998), 7736-43.

260 G. S. Grader, P. K. Gallagher, J. Thomson and M. Gurvitch, 'Rates of Change in High Temperature Electrical Resistivity and Oxygen Diffusion Coefficient in $Ba_2YCu_3O_x$', *Applied Physics A,* 45, 179-83.

261 S. H. Lee, S. C. Bae, J. K. Ku and H. J. Shin, 'Oxygen Diffusion in Epitaxial $YBa_2Cu_3O_{7-x}$ Thin Films', *Physical review. B, Condensed matter,* 46 (1992), 9142-46.

262 S. Kittelberger, U. Bolz, B. Holzapfel, L. Mex and R. P. Huebener, 'Oxygen Diffusion in $YBa_2Cu_3O_{7-\delta}$ Films with Different Microstructures', *Physica. C, Superconductivity,* 302 (1998), 93-101.

263 C. Krauns and H. U. Krebs, 'Comparison of the Oxygen Diffusion in $Y_1Ba_2Cu_3O_y$ Bulk Materials and Thin Films', *Zeitschrift für Physik. B, Condensed matter,* 92 (1993), 43-46.

264 C. L. Ling Chen, A. J. Chen and Jacobson, 'Electrical Conductivity Relaxation Studies of Oxygen Transport in Epitaxial $YBa_2Cu_3O_{7-\delta}$ Thin Films', *IEEE Transactions on Applied Superconductivity,* 13 (2003), 2882-85.

265 T. Qu, Y. Xue, F. Feng, R. Huang, W. Wu, K. Shi and Z. Han, 'Study on the Oxygenation Process During the Heat Treatment of TFA-MOD YBCO Thin Films by in Situ Resistance Measurement', *Physica. C, Superconductivity,* 494 (2013), 148-52.

266 H. Zhang, H. Ye, K. Du, X. Y. Huang and Z. H. Wang, 'Electric Resistance Relaxation and Oxygen Diffusion in Melt-Texture Grown YBCO Bulk Post-Annealed at High Temperature', *Superconductor science & technology,* 15 (2002), 1268-74.

267 S. Kittelberger, U. Bolz, R. P. Huebener, B. Holzapfel and L. Mex, 'Oxygen Diffusion in $YBa_2Cu_3O_{7-\delta}$ Films with Different Microstructures', *Physica C: Superconductivity,* 302 (1998), 93-101.

268 M. M. Kuklja, E. A. Kotomin, R. Merkle, Yu A. Mastrikov and J. Maier, 'Combined Theoretical and Experimental Analysis of Processes Determining Cathode Performance in Solid Oxide Fuel Cells', *PCCP. Physical chemistry chemical physics,* 15 (2013), 5443-71.

269 M. Leonhardt, R. A. De Souza, J. Claus and J. Maier, 'Surface Kinetics of Oxygen Incorporation into $SrTiO_3$', *Journal of the Electrochemical Society,* 149 (2002), J19-J26.

270 R. Merkle and J. Maier, 'How Is Oxygen Incorporated into Oxides? A Comprehensive Kinetic Study of a Simple Solid-State Reaction with Srtio3 as a Model Material', *Angewandte Chemie (International ed.),* 47 (2008), 3874-94.

271 R. Merkle and J. Maier, 'Oxygen Incorporation into Fe-Doped $SrTiO_3$: Mechanistic Interpretation of the Surface Reaction', *PCCP. Physical chemistry chemical physics,* 4 (2002), 4140-48.

272 L. Wang, R. Merkle and J. Maier, 'Surface Kinetics and Mechanism of Oxygen Incorporation into $Ba_{1-x}Sr_xCo_yFe_{1-y}O_{3-\delta}$ Soft Microelectrodes', *Journal of the Electrochemical Society,* 157 (2010), B1802-B08.

273 T. Suzuki, H. Okada and T. Takeuchi, 'Effect of Complex Dopants (Li^{+} with Al^{3+}) Substituted for Cu Ions in Preparing the Superconducting YBCO', *Solid State Communications*, 77 (1991), 587-92.

274 H. Ihara, M. Hirabayashi, N. Terada, Y. Kimura, K. Senzaki, M. Akimoto, K. Bushida, F. Kawashima and R. Uzuka, 'Electronic Structures and Superconducting Mechanism of $Ba_2Y_1Cu_3O_7$', *Japanese journal of applied physics*, 26 (1987), L460-L62.

275 D. H. Kim, D. D. Berkley, A. M. Goldman, R. K. Schulze and M. L. Mecartney, 'Electronic Structure Changes and Superconductivity in $YBa_2Cu_3O_{7-x}$', *Physical review. B, Condensed matter*, 37 (1988), 9745-48.

276 N. Savvides, S. X. Dou, H. K. Liu, A. J. Bourdillon, J. P. Zhou, and C. C. Sorrell, 'Labile Cu^{3+} Ions Correlated with Superconducting Properties in $YBa_2Cu_3O_{7-x}$', *Solid State Communications*, 68 (1988), 221-25.

277 César Fidel Sánchez Valdés, 'Crecimiento Epitaxial De Películas Delgadas De $YBa_2Cu_3O_{7-\delta}$ Mediante Soluciones Químicas: Análisis in-Situ De La Nucleación, El Crecimiento Y La Oxigenación.', UNIVERSIDAD AUTONOMA DE BARCELONA, 2013).

278 J. I. Shimoyama, S. Horii, K. Otzschi, K. Kishio and M. P. Paranthaman, 'How to Optimize Critical Current Performance of Re123 Materials by Controlling Oxygen Content Materials for High-Temperature Superconductor Technologies', 689 (2002), 265-69.

279 H. Zhang, X. Yao, and X. H. Zeng, 'Oxygen in-Diffusion in LPE Thick Films of YBCO by Electrical Resistance Relaxation', *Physica status solidi. A, Applied research*, 201 (2004), 2305-11.

280 S. Kittelberger, O. M. Stoll and R. P. Huebener, 'Oxygen Diffusion in Thin Films Studied from Isothermal Electric Resistivity Measurements', *Superconductor science & technology*, 11 (1998), 744-50.

281 I. Langmuir, 'The Adsorption of Gases on Plane Surfaces of Glass, Mica and Platinum', *Journal of the American Chemical Society*, 40 (1918), 1361-403.

282 Y. Mastrikov, R. Merkle, E. Heifets, E. Kotomin and Joachim Maier, 'Pathways for Oxygen Incorporation in Mixed Conducting Perovskites: A DFT-Based Mechanistic Analysis for (La, Sr)$MnO_{3-\delta}$', *The journal of physical chemistry. C*, 114 (2010), 3017-27.

283 G. A. Emelchenko, S. Carter, S. I. Bredikhin, J. A. Kilner, V. S. Shechtman, A. A. Zhokhov, and R. J. Chater, 'Anisotropy of Oxygen Self-Diffusion in $YBa_2Cu_{3O7-\delta}$ Single Crystals', *Physica. C, Superconductivity*, 179 (1991), 286-90.

284 G. J. la O, S. J. Ahn, E. Crumlin, Y. Orikasa, M. Biegalski, Y. S. Horn and H. M. Christen, 'Catalytic Activity Enhancement for Oxygen Reduction on Epitaxial Perovskite Thin Films for Solid-Oxide Fuel Cells', *Angewandte Chemie (International ed.)*, 49 (2010), 5344-47.

285 M. Rossell, G. Van Tendeloo, A. Figueras, M. Burriel, J. Santiso and Gemma Garcia, 'Enhancing Total Conductivity of $La_2NiO_{4+\delta}$ Epitaxial Thin Films by Reducing Thickness', *The journal of physical chemistry. C*, 112 (2008), 10982-87.

286 A. Karthikeyan and S. Ramanathan, 'Oxygen Surface Exchange Studies in Thin Film Gd-Doped Ceria', *Applied physics letters*, 92 (2008), 243109.

287 L. Yan and P. A. Salvador, 'Substrate and Thickness Effects on the Oxygen Surface Exchange of $La_{0,7}Sr_{0,3}MnO_3$ Thin Films', *ACS applied materials & interfaces*, 4 (2012), 2541-50.

288 G. A. Ovsyannikov, A. M. Petrzhik, I. V. Borisenko, A. A. Klimov, Yu Ignatov, V. V. Demidov and S. A. Nikitov, 'Magnetotransport Characteristics of Strained $La_{0,7}Sr_{0,3}MnO_3$ Epitaxial Manganite Films', *Journal of experimental and theoretical physics*, 108 (2009), 48-55.

289 L. Cratty and A. Granato, 'Dislocations as Active Sites in Heterogeneous Catalysis', *The Journal of chemical physics*, 26 (1957), 96-97.

290 I. Uhara, S Yanagimoto, K. Tani, T. Kazuo and G. Adachi, , 'Dislocations as Active Centres in Heterogeneous Catalysis', *Nature*, 192 (1961), 867-68.

291 K. Szot, W. Speier, G. Bihlmayer and R. Waser, 'Switching the Electrical Resistance of Individual Dislocations in Single-Crystalline $SrTiO_3$', *Nature Materials*, 5 (2006), 312-20.

292 R. Bertacco, A. Barthelemy, J. Olivier, J. P. Contour, and A. Barthélemy, 'Evidence for Strontium Segregation in $La_{0,7}Sr_{0,3}MnO_3$ Thin Films Grown by Pulsed Laser Deposition: Consequences for Tunnelling Junctions', *Surface science*, 511 (2002), 366-72.

293 T. Fister, D. Fong, J. Eastman, P. Baldo, M. Highland, P. Fuoss, K. Balasubramaniam, J. Meador and P. Salvador, 'In Situ Characterization of Strontium Surface Segregation in Epitaxial $La_{0,7}Sr_{0,3}SnO_3$ Thin Films as a Function of Oxygen Partial Pressure', *Applied physics letters*, 93 (2008), 151904.

294 J. L. Tallon, 'Thermodynamics and Critical Current Density in High-T_c Superconductors', *Applied Superconductivity, IEEE Transactions on*, 25 (2015), 1-6.

295 E. F. Talantsev, S. C. Wimbush, N. M. Strickland, J. A. Xia, P. D'Souza, J. G. Storey, J. L. Tallon, B. Ingham, R. Knibbe, and N. J. Long, 'Oxygen Deficiency, Stacking Faults and Calcium Substitution in MOD YBCO Coated Conductors', *IEEE Transactions on Applied Superconductivity*, 23 (2013), 7200205-05.

296 H. Knözinger, G. Ertl, F. Schüth and J. Weitkamp *Handbook of Heterogeneous Catalysis*Wiley, 2008.

297 R. A. Vansanten, Hpce Kuipers, and R. A. Van Santen, 'The Mechanism of Ethylene Epoxidation', *Advances In Catalysis*, 35 (1987), 265-321.

298 S. Chavadej, S. Rojluechai, J. W. Schwank and V. Meeyoo, 'Chapter 9 - Effect of Support on Ethylene Epoxidation on Ag, Au, and Au-Ag Catalysts', in *Mechanisms in Homogeneous and Heterogeneous Epoxidation Catalysis*, ed. by S. Ted Oyama (Amsterdam: Elsevier, 2008), pp. 283-96.

299 C. Backx, C. P. M. Degroot, and P. Biloen, 'Adsorption of Oxygen on Ag(110) Studied by High Resolution ELS and TPD', *Surface science*, 104 (1981), 300-17.

300 I. P. Prosvirin, V. I. Bukhtiyarov and V. V. Kaichev, 'Oxygen Adsorption on Ag(111): X-Ray Photoelectron Spectroscopy (XPS), Angular Dependent X-Ray Photoelectron Spectroscopy (ADXPS) and Temperature-Programmed Desorption (TPD) Studies', *The Journal of chemical physics*, 111 (1999), 2169-75.

301 B. Sexton and R. Madix, 'Vibrational Spectra of Molecular and Atomic Oxygen on Ag(110)', *Chemical Physics Letters*, 76 (1980), 294-97.

302 P. Scherrer, 'Bestimmung Der Gröss Und Der Inneren Struktur Von Kolloidteilchen Mittels Röntgenstrahlen, Nachrichten Von Der Gesellschaft Der Wissenschaften, Göttingen', *Mathematisch-Physikalische Klasse*, Vol. 2 (1918), 98-100.

303 A. L. Patterson, 'The Scherrer Formula for X-Ray Particle Size Determination', *Physical review*, 56 (1939), 978-82.

304 Anna Llordés i Gil, 'Superconducting Nanocomposite Films Grown by Chemical Solution Deposition: Synthesis, Microstructure and Properties', Universitat Autonoma de Barcelona (UAB), 2010).

NOMENCLATURE

γ_{eff}	Effective Anisotropic Parameter
λ	Penetration Depth
Φ_0	Flux Quantum
ε	Nanostrain
ξ	Coherence length
AFM	Atomic Force Microscopy
B	Magnetic Field Induction
BCO	$BaCeO_3$
BYTO	Ba_2YTaO_6
BZO	$BaZrO_3$
CC	Coated Conductor
CFO	$CoFe_2O_4$
CSD	Chemical Solution Deposition
DLS	Dynamic Light Scattering
E_a	Activation Energy
FC	Field Cooled
F_L	Lorentz Force
F_p	Pinning Force
GdBCO	$GdBa_2Cu_3O_{6+\delta}$
H	Magnetic Field
H_{c_1}	Lower Critical Field
H_{c_2}	Upper Critical Field
H_{coer}	Coercive Magnetic Field of
H_c	Critical Field
HAADF	High Annular Angle Dark Field
HTS	High Temperature Superconductors
I_c	Critical Current
IL	Irreversibility Line
J_c	Critical Current Density
J_c^{sf}	Critical Current Density at self-field
K_B	Boltzmann constant
k_0	Frequency factor
LAADF	Low Annular Angle Dark Field
LAO	$LaAlO_3$
LTS	Low critical-Temperature Superconductor
M	Magnetization
M_{sat}	Saturated Magnetization
M_{rem}	Remanent Magnetization
NPs	Nanoparticles
REBCO	$REBa_2Cu_3O_{6+\delta}$
SEM	Scanning Electron Microscopy
SFs	Stacking Faults
SQUID	Superconducting Quantum Interference Device
T	Temperature
T_c	Critical Temperature
TB	Twin Boundary

TEM	Transmission Electron Microscopy
TFA	Trifluoroacetate Route
Y248	$Y2Ba_4Cu_8O_{16}$
YBCO	$YBa_2Cu_3O_{6+\delta}$
YO	Y_2O_3
ZFC	Zero Field Cooled